Universiteit Leiden
The Netherlands

Ingredients of the planet-formation puzzle: Gas substructures and kinematics in transition discs

Wölfer, L.B.

Citation

Wölfer, L. B. (2023, March 28). *Ingredients of the planet-formation puzzle: Gas substructures and kinematics in transition discs*. Retrieved from https://hdl.handle.net/1887/3589823

Version:	Publisher's Version
License:	Licence agreement concerning inclusion of doctoral thesis in the Institutional Repository of the University of Leiden
Downloaded from:	https://hdl.handle.net/1887/3589823

Note: To cite this publication please use the final published version (if applicable).

Ingredients of the planet-formation puzzle

- Gas substructures and kinematics in transition discs -

Proefschrift

ter verkrijging van
de graad van doctor aan de Universiteit Leiden,
op gezag van rector magnificus prof.dr.ir. H. Bijl,
volgens besluit van het college voor promoties
te verdedigen op dinsdag 28 maart 2023
klokke 11:15 uur
door

Lisa Berenice Wölfer

geboren te Münster, Duitsland
in 1993

Promotores:

Prof. dr. E. F. van Dishoeck	
Prof. dr. B. Ercolano	Ludwig-Maximilians-Universität München

Co-promotor:

Dr. S. Facchini	Università degli Studi di Milano

Promotiecommissie:

Prof. dr. I. A. G. Snellen	
Prof. dr. M. R. Hogerheijde	Universiteit Leiden
	Universiteit van Amsterdam
Prof. dr. C. J. Clarke	University of Cambridge
Prof. dr. J. P. Williams	University of Hawaii
Dr. R. Dong	University of Victoria

ISBN: 978-94-6419-744-0

Cover and cartoon design: Marta Paula Tychoniec

It's a dangerous business, going out your door. You step onto the road, and if you don't keep your feet, there's no knowing where you might be swept off to.

J.R.R. Tolkien, The Lord of the Rings

Contents

1 Introduction **1**
1.1 Star and planet formation 2
1.2 Protoplanetary discs 4
1.2.1 Disc evolution 4
1.2.2 Disc dispersal 5
1.2.2.1 Photoevaporation 6
1.2.3 Transition discs 8
1.2.4 Planet formation 8
1.3 Disc observations 11
1.3.1 ALMA 11
1.3.2 Dust substructures 12
1.3.3 Gas substructures 14
1.4 Kinematics 15
1.4.1 Kinematical signatures of planets 17
1.5 This thesis 19
1.5.1 Future outlook 21

PART I Models of photoevaporative disc winds **25**

2 Radiation-hydrodynamical models of X-ray photoevaporation in carbon-depleted circumstellar discs **27**
2.1 Introduction 29
2.2 Methods 30
2.2.1 Thermal Calculations 30
2.2.2 Hydrodynamics 32
2.2.2.1 Primordial Discs 34
2.2.2.2 Transition Discs 34
2.2.3 Calculation of the mass-loss rates and $\dot{\Sigma}$ profiles 35
2.3 Results 37
2.3.1 Mass-loss rates for the primordial disc simulations 38
2.3.2 Hole radius dependency 42
2.3.3 Mass-loss profiles $\dot{\Sigma}$ 45
2.3.4 Rapid disc dispersal of carbon-depleted discs 47

2.4 Conclusions 48
Appendices 51
2.A Temperature error 51
2.B Choice of the (internal) disc radius of the streamlines calculation 51
2.C Test for radiative equilibrium 52
2.D Mass-loss rates of the transition disc simulations 53
2.E Additional $\dot{\Sigma}$ profiles 56

PART II Gas substructures observed with ALMA 61

3 A highly non-Keplerian protoplanetary disc. Spiral structure in the gas disc of CQ Tau 63
3.1 Introduction 65
3.2 Observations 66
3.2.1 Target 66
3.2.2 Data reduction 67
3.3 Observational results 68
3.3.1 Integrated intensity and brightness temperature maps . . . 68
3.3.2 Radial and azimuthal cuts 70
3.4 Analysis 72
3.4.1 Temperature structure 72
3.4.2 Velocity structure 73
3.4.2.1 Analysis of the gas rotation velocity 74
3.4.2.2 Razor-thin disc model 75
3.4.3 Analysis of the spiral structure 77
3.5 Discussion 81
3.6 Summary 83
Appendices 86
3.A ALMA observing log 86
3.B Channel maps 86
3.C Beam dilution 88
3.D Posterior distributions of the modelling 88

4 Kinematics and brightness temperatures of transition discs. A survey of gas substructures as seen with ALMA 91
4.1 Introduction 93
4.2 Observations 95
4.3 Observational results 101
4.3.1 Brightness temperature 101
4.3.2 Rotation velocity 103
4.3.3 Radial profiles 104
4.4 Analysis 106
4.4.1 Brightness temperature structure 106
4.4.2 Velocity structure 107

4.5 Discussion . . . 110
4.5.1 Clear spiral or arc-like features . . . 114
4.5.2 Tentative spiral or arc-like features . . . 114
4.5.3 No spiral or arc-like features . . . 114
4.5.4 Conclusive remarks . . . 115
4.6 Summary . . . 116
Appendices . . . 117
4.A Continuum . . . 117
4.B Thick disc residuals of the main lines . . . 118
4.C Uncertainties of the rotation velocity . . . 119
4.D Re-imaged and archival data products comparison . . . 120
4.E Additional lines . . . 122
4.E.1 Characteristics . . . 122
4.E.2 Brightness temperature maps . . . 125
4.E.3 Rotation velocity maps . . . 127
4.E.4 Brightness temperature residuals . . . 129
4.E.5 Rotation velocity residuals . . . 132
4.F Radial profiles of the integrated intensity . . . 134

5 Spirals and meridional flows in the planet-forming disc around HD 100546. A multi-line study of its gas kinematics 137
5.1 Introduction . . . 139
5.2 Observations . . . 141
5.2.1 The HD 100546 system . . . 141
5.2.2 ALMA observations . . . 143
5.2.3 Observational results . . . 145
5.3 Analysis . . . 150
5.3.1 Model setup . . . 150
5.3.2 Fitting procedure . . . 151
5.3.3 Fitting Results . . . 152
5.3.3.1 Channel maps . . . 154
5.3.3.2 Observables . . . 156
5.4 Results . . . 156
5.4.1 Kinematics . . . 156
5.4.2 Peak intensities and line widths . . . 160
5.4.3 Emission heights . . . 161
5.4.4 Azimuthal averages . . . 162
5.5 Discussion . . . 164
5.5.1 On the planet candidate at 50 au . . . 164
5.5.2 On the planet candidate between 70–150 au . . . 165
5.5.3 Origin of the asymmetry in emission heights . . . 165
5.6 Summary . . . 166
Appendices . . . 168
5.A Comparison of the ^{12}CO 3-2 data sets . . . 168
5.B Best-fit parameters blue- and redshifted sides . . . 169
5.C Comparison of the data and model channels . . . 172

5.D Logarithmic spirals 174
5.E Peak intensity and line width residuals 175

Bibliography **175**

Nederlandse samenvatting **193**

English summary **203**

Deutsche Zusammenfassung **211**

Publications **221**

Curriculum Vitae **223**

Acknowledgements **225**

Equipped with his five senses,
man explores the universe around him
and calls the adventure science.

Edwin Powell Hubble

Chapter 1

Introduction

Since time immemorial, people have wondered about the origin and structure of our world as well as our place in the cosmos. How did the Earth form and which laws of nature does it follow? Are we alone, sitting on a tiny oasis surrounded by lifeless wasteland, or does life flourish in many corners of the universe? First observations of the night sky were captured already in the earliest history of humanity in the form of cave paintings and over centuries better instruments reaching far beyond the human eye were developed. Nowadays, there exist remarkable observatories both on Earth and in space that are capable of resolving the cosmos even on its smallest scales. At the same time, dedicated theoretical efforts have invoked mechanisms to explain the physics behind the observations. The question of extraterrestrial life reached a new era when the first exoplanet – a planet orbiting another star than our Sun – was discovered in 1992 (Wolszczan & Frail 1992) around a pulsar and in 1995 around a solar-type star (Mayor & Queloz 1995). To date, 5323 exoplanets[1] have been confirmed through various detection techniques, a number that is steadily growing and will be outdated already by the time you read this thesis. These planetary systems appear to come in an enormous variety, including the stellar and planetary masses or sizes but also the system architectures in terms of the number, species, or distribution of planets. In this comparison, the Solar System itself presents to be rather atypical (e.g., Raymond et al. 2020), raising questions of whether there may be an observational bias or if the occurrence of life itself is uncommon. To understand the formation of planets and the diversity of developed planetary systems, it is crucial to take a step back and set the focus on their nursery stages in the circumstellar material. Here, dense remnants of the star formation process called protoplanetary or planet-forming discs provide the gaseous and dusty building blocks to assemble planets. These discs are not static objects but they evolve and eventually disperse over time with the evolutionary processes not only shaping the disc's appearance but also influencing (and putting a limit on) the planet-formation mechanisms. Vice versa, planets

[1] `http://www.exoplanet.eu`, as of 26 February 2023

interact with their environment, impact disc evolution, and are expected to alter their host disc's structure, for example in terms of density, temperature, or velocity. Even though such young embedded planets may be hidden from the direct eye of our telescopes, their planet–disc interactions still leave marks observable to us depending on their mass and location. Modelling the dynamic processes taking place in discs together with characterizing the observed substructures represent key pieces in assembling the planet-formation puzzle.

1.1 Star and planet formation

Stars are formed in giant molecular clouds, an interstellar accumulation of mainly molecular hydrogen gas (H_2) and some small sub-μm-sized dust grains, which make up only about 1 % of the total mass (Draine 2003). Under certain conditions, the dense ($n > 10^4\,\mathrm{cm}^{-3}$) and cold ($T \sim 10 - 20\,\mathrm{K}$) cores of these clouds can collapse under their own gravity, forming a prestellar core in the centre (e.g., review of Evans 1999). In the subsequent evolution, young stellar objects (YSOs) are theoretically divided into four evolutionary stages (Shu et al. 1987) and observationally categorized into four classes based on the spectral slope of their spectral energy distribution (SED; Lada 1987; André et al. 1993; Greene et al. 1994; Fig. 1.1). In this context, infrared to submillimetre wavelengths are usually best to identify the class of a YSO: High-energy radiation from the star (UV and optical) heats the surrounding dust which re-emits at lower energies and consequently longer wavelengths. The four theoretical stages and observed classes roughly correspond to each other, but it is important to note that the SED depends on the geometry of the protostellar system such as the inclination (e.g., Crapsi et al. 2008) and thus deviations may occur.

In the initial stage after the formation of the prestellar core, the latter has collapsed into a protostar surrounded by an infalling envelope (Stage 0). At the same time, a disc begins to form around the protostar due to angular momentum conservation. Stage 0 is marked by a high envelope mass that significantly exceeds the stellar mass. The emission of a Class 0 YSO is thus dominated by the envelope. In the following, the mass of the protostar increases due to accretion, and it grows larger than the envelope mass within $\sim 10^5\,\mathrm{yr}$ (Stage I). As the envelope begins to dissipate both due to accretion and bipolar outflows, emission from the star and disc starts to become visible (Class I). These processes continue and after $\sim 10^5 - 10^6\,\mathrm{yr}$, the embedded star formation stage is over, and instead, a pre-main-sequence star surrounded by a gas-rich protoplanetary disc (Stage II) has formed. The SED is marked by strong stellar emission, the disc appears to be optically thick in the infrared and mostly optically thin in the millimetre-regime (Class II). After $\sim 10^6 - 10^7\,\mathrm{yr}$, accretion ceases and the disc material has grown into planets and smaller bodies or dissipated due to processes such as disc winds. In this Stage III, the star is surrounded by a gas-poor debris disc containing dust created by collisions of larger bodies. The SED is dominated by the black body radiation of the pre-main-sequence star (Class III). Finally, the disc vanishes, the star enters the main sequence and a fully developed stellar system is born. This

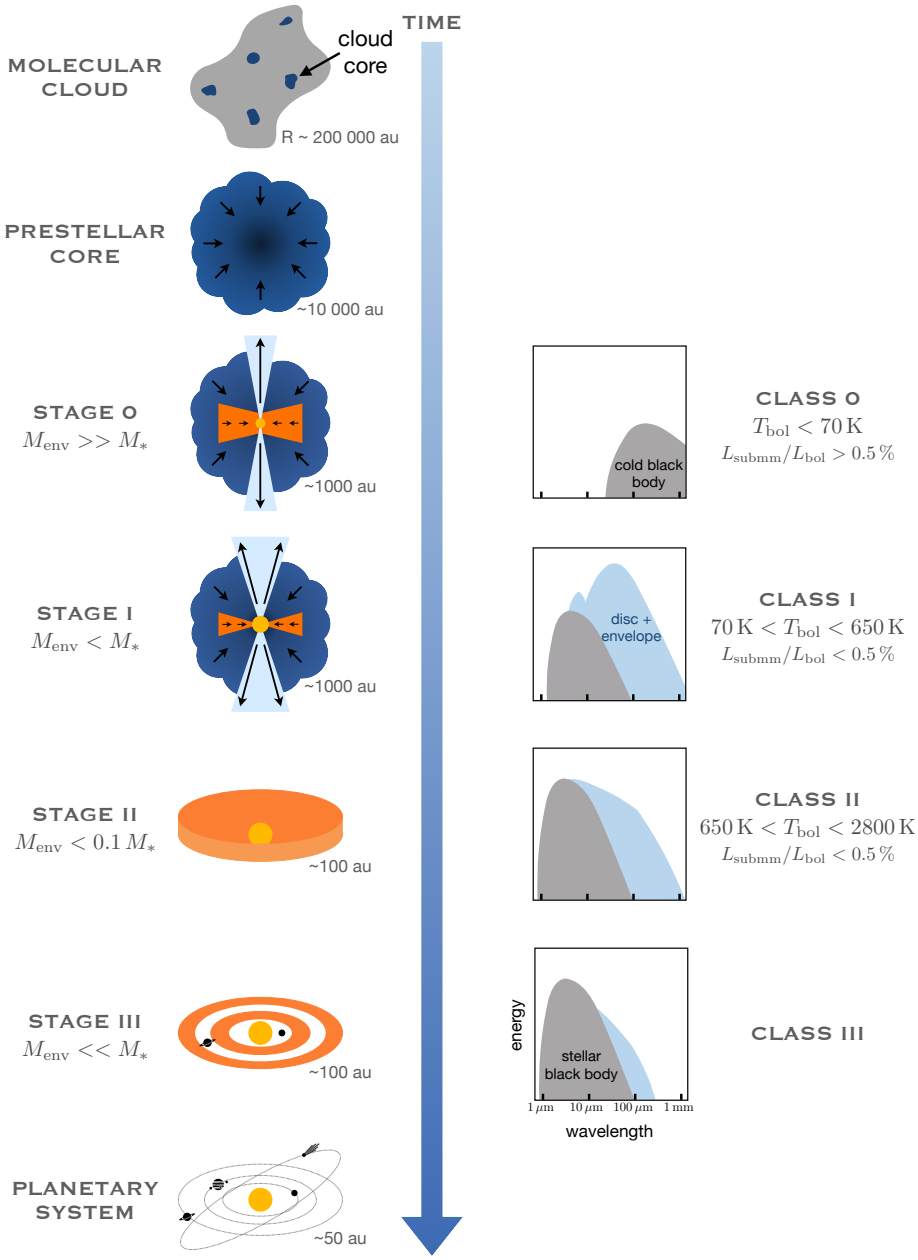

Figure 1.1: Schematic overview of the different theoretical stages (left) and observational classes based on the SED (right) of star formation. The focus of this thesis are Class II objects, which are also known as protoplanetary discs.

thesis focuses on the second evolutionary stage where substructures in the gas disc can be observed with the Atacama Large Millimeter/submillimeter Array (ALMA; ALMA Partnership et al. 2015) and analysed in the context of their (possibly dynamical) origins.

1.2 Protoplanetary discs

Circumstellar discs are a natural outcome of the planet-formation process. During the gravitational collapse of a rotating cloud core, the lowest angular momentum material falls towards the centre, forming a protostar as density and temperature rise (e.g., Terebey et al. 1984; Yorke et al. 1993), while the highest angular momentum material distributes into a rotating accretion disc from which the protostar is feeding during the first few million years of its lifetime. As a consequence, the protoplanetary disc contains only a small mass fraction ($10^{-1} - 10^{-4}\,M_*$; Manara et al. 2022) compared to the total mass of the system, but most of the angular momentum is deposited therein. Such a Keplerian disc is hydrodynamically stable (Drazin & Reid 1981; Ruden 1993) and without a mechanism to decrease angular momentum, the particles would just continue to orbit the central star at the same radius instead of spiralling inwards to be accreted. Thus, for a protoplanetary disc to evolve, angular momentum needs to be either lost from the system entirely or redistributed within the disc. Such processes, described further in the following section, occur on timescales much larger than the orbital or dynamical timescale, hence protoplanetary discs represent dynamically long-lived structures which evolve and eventually disperse slowly over a timescale of a few million years.

1.2.1 Disc evolution

Two, not mutually exclusive, processes have been proposed to be the main drivers of global disc evolution: Magnetically-driven disc winds (MHD disc winds) and viscous stresses. The latter are believed to play an especially important role during the earlier stages of a still massive circumstellar disc, while disc winds start to dominate at later phases when the viscous accretion rates drop below the wind mass-loss rates. In the classical picture, the disc is described as a vertically thin and axisymmetric sheet of viscous fluid. A shear between two adjacent gas annuli causes the redistribution of angular momentum, meaning that the inner disc loses angular momentum to the outer disc (e.g., Shakura & Sunyaev 1973; Lynden-Bell & Pringle 1974; Pringle 1981; Hartmann et al. 1998). As a consequence of angular momentum conservation, the outermost disc regions expand to larger radii, a process known as viscous spreading, while the innermost regions move towards the star where they can be accreted.

The source of viscosity remains a matter of active debate, but it is known that molecular viscosity caused by random motions of gas particles is too low to account for the observed lifetimes of protoplanetary discs (Armitage 2019). Instead, a viscously evolving disc is proposed to be turbulent (Shakura & Sunyaev 1973). One mechanism commonly invoked to be the dominant driver of turbulence

in discs is the magneto-rotational instability (MRI; Balbus & Hawley 1991), which can occur in weakly magnetized but sufficiently ionized discs. Other mechanisms include the vertical shear instability (VSI; Richard & Zahn 1999; Nelson et al. 2013; Stoll & Kley 2014) or gravitational instabilities (Lin & Pringle 1987), where spiral density waves redistribute angular momentum. For simplicity, it is usually assumed that the viscosity is constant across the disc, however, this is unlikely physical. The MRI for example is expected to be suppressed in the so-called dead zones (e.g., Blaes & Balbus 1994; Sano & Stone 2002; Turner et al. 2010; Flock et al. 2015), disc regions of low ionization, which stand in contrast to a uniform viscosity. Regardless of the exact origin, assuming a constant viscosity brings the advantage that the disc evolution can be described by a single dimensionless parameter α in the so-called α-prescription

$$\nu \equiv \alpha \frac{c_\mathrm{s}^2}{\Omega_\mathrm{K}} = \alpha c_\mathrm{s} H, \tag{1.1}$$

which was introduced by Shakura & Sunyaev (1973). Here, c_s is the isothermal sound speed, Ω_K the Keplerian orbital frequency, $H = c_\mathrm{s}/\Omega_\mathrm{K}$ the vertical pressure scale height, and α describes the efficiency of angular momentum transport due to turbulence.

In contrast to viscous evolution, a disc-wind-driven evolution represents an external way to remove angular momentum (and mass) and does not require turbulence. In the presence of a magnetic field, a magnetic disc wind can be launched from the disc surface by the magneto-centrifugal force if the poloidal field lines are inclined at a sufficiently large angle from the rotation axis (e.g., Blandford & Payne 1982; Pascucci et al. 2022). The accelerated material consequently carries away angular momentum, causing the remaining material to lose angular momentum and move inwards. Models have indeed shown that such magnetic disc winds can efficiently remove the angular momentum required to drive the stellar accretion (e.g., Ferreira et al. 2006; Béthune et al. 2017; Zhu & Stone 2018; Tabone et al. 2022a,b).

Despite being nearly ubiquitously invoked in the context of disc evolution, observational evidence for both (strong) turbulence in discs and magnetic disc winds is scarce. Understanding what modulates angular momentum transport in discs, influencing their lifetime and thus the time planetary systems have to form, represents one of the major missing pieces of the planet-formation puzzle.

1.2.2 Disc dispersal

While the simple theory of viscous evolution described in the previous section can roughly account for the observed morphology and physical properties of protoplanetary discs, it however predicts a decelerated dispersal where the disc becomes steadily fainter at all wavelengths, resulting in a long final phase of homogeneous fading. Since evidence for such slowly draining discs is lacking, other mechanisms which rapidly deplete the disc at advanced stages must be at play and result in a much shorter dispersal time, which (according to observations) makes up only

about 10 % of the total disc lifetime. Among these mechanisms is photoevaporation, which is believed to play a significant role and is detailed in the following.

1.2.2.1 Photoevaporation

Photoevaporation describes the phenomenon when high-energy stellar photons (either internal or external) irradiate, and consequently heat, the upper protoplanetary disc layers until the thermal energy exceeds the gravitational binding energy and a thermal wind is centrifugally launched from the surface at a given radius (see reviews of Hollenbach et al. 2000; Clarke 2011; Alexander et al. 2014; Gorti et al. 2016; Ercolano & Pascucci 2017; Pascucci et al. 2022). YSOs typically show vigorous accretion and thus photoevaporation is thought to take over the disc's evolution at later stages when the accretion rate has considerably dropped, then initialising a fast inside-out clearing. In a simplified picture, schematically shown in Fig. 1.2 (adapted from Ercolano & Pascucci 2017), the disc evolves through three main stages: As previously mentioned, for most of the disc's lifetime, the evolution is governed by viscosity (Stage 1). Even though photoevaporation may already be responsible for a small amount of mass loss, the latter is dominated by viscous accretion, meaning that the surface density is only marginally influenced by photoevaporation during the first few million years. Both the surface density and mass accretion rate gradually decrease over time, resulting in a lower opacity which enables the radiation to penetrate into deeper disc layers. At some point, the accretion rate drops below the wind mass-loss rate ($\dot{M}_{\rm acc} < \dot{M}_{\rm w}$) and photoevaporation begins to dominate the mass loss. Beyond the so-called gravitational radius

$$R_{\rm g} = \frac{GM_*}{c_{\rm s}^2}, \tag{1.2}$$

inwards flowing parcels are blown away with the wind rather than reaching the inner disc regions to be accreted. As a result, the replenishment of mass inside of $R_{\rm g}$ is prevented and an annular gap or cavity is formed, that fully detaches the inner and outer disc regions from each other (Stage 2). Now isolated from matter resupply, the inner disc is rapidly accreted onto the central star within 10^5 years. The outer disc on the other hand is being illuminated directly (Alexander et al. 2006a,b) and quickly erodes in an outwards direction (Stage 3). This final phase of disc dispersal appears within a few 10^5 years (Clarke 2011; Gorti & Hollenbach 2009) and thus the evolution of protoplanetary discs is also called a two-timescale behaviour.

The exact location and time of gap opening depends on the spectrum of the irradiating photons and there is an ongoing debated in the literature about what type of radiation may be the main driver of photoevaporative winds: Far-ultraviolet radiation (FUV; $6\,\mathrm{eV} < h\nu < 13.6\,\mathrm{eV}$), extreme-ultraviolet radiation (EUV, $13.6\,\mathrm{eV} < h\nu < 100\,\mathrm{eV}$) or (soft) X-rays ($0.1\,\mathrm{keV} < h\nu < 10\,\mathrm{keV}$). EUV photons can ionize hydrogen atoms in the surface disc layers, creating a nearly isothermal ($\sim 10^4\,\mathrm{K}$) atmosphere which is sharply separated from the neutral gas. The EUV heating rate is rather insensitive to the incident spectrum and thus the integrated mass-loss rate depends mostly on the EUV photon rate, typically resulting in mass-loss

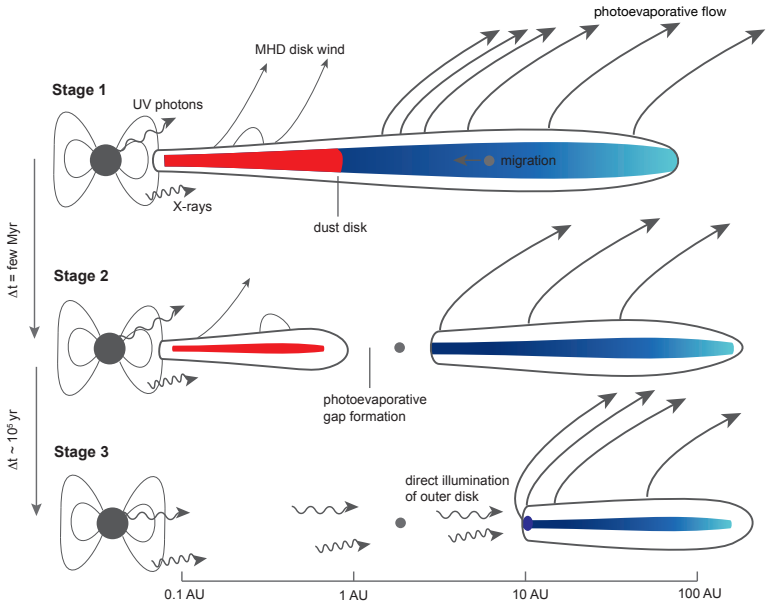

Figure 1.2: Schematic view of the three main stages of disc evolution and dispersal, adapted from Ercolano & Pascucci (2017), which is based on Alexander et al. (2014).

rates of the order of $10^{-10}\,M_\odot\,\mathrm{yr}^{-1}$. EUV photons are fully absorbed within a relatively small neutral hydrogen column $N_\mathrm{H} \approx 10^{20}\,\mathrm{cm}^{-2}$ (Hollenbach & Gorti 2009; Gorti & Hollenbach 2009), making it difficult to constrain the ionizing photon fluxes. Nevertheless, data suggest the rates to be generally low, with the mass loss being concentrated around R_g. EUV photoevaporation is thus ineffective in removing outer disc material and seems to be less important as a driver of disc dispersal until the later stages when the inner disc has already drained. FUV radiation is capable of dissociating H_2 molecules and creates a neutral atomic layer (the energies are too low to ionize the hydrogen atoms). FUV photons show larger penetration depths ($N_\mathrm{H} \approx 10^{21} - 10^{23}\,\mathrm{cm}^{-2}$) than EUV photons, which is however strongly influenced by the abundance of small dust grains and polycyclic aromatic hydrocarbons (PAHs; Alexander et al. 2014; Ercolano & Pascucci 2017). As a consequence, they can drive stronger winds with the mass-loss rates increasing to $10^{-8}\,M_\odot\,\mathrm{yr}^{-1}$ (Gorti & Hollenbach 2009). Also, the mass-loss profile is qualitatively different: While it still peaks around R_g, significant mass loss is also established at large radii beyond 100 au. This opens the possibility for secondary gaps and FUV photoevaporation models sometimes even predict a reversed outside-in clearing (Gorti et al. 2015). Stellar X-rays arise from the magnetically confined hot plasma in the stellar corona and are predominantly absorbed by the K-shells of heavy elements such as oxygen or carbon, releasing photoelectrons that can ionize and heat the gas disc (Alexander et al. 2014). Similar to FUV, X-rays can efficiently deposit energy up to columns of $N_\mathrm{H} \approx 10^{21} - 10^{22}\,\mathrm{cm}^{-2}$. They show a broad wind profile and drive mass-loss rates of the order of $10^{-8}\,M_\odot\,\mathrm{yr}^{-1}$,

depending on the spectral shape and total X-ray luminosity L_X (Owen et al. 2010, 2011, 2012). For young stars, high X-ray luminosities around $10^{30}\,\mathrm{erg\,s^{-1}}$ are typically observed (e.g., Preibisch & Feigelson 2005; Preibisch et al. 2014).

1.2.3 Transition discs

One particularly interesting subgroup of YSOs is represented by the so-called transition discs. They are characterized by inner regions depleted in dust (and possibly gas) and were first identified observationally through a lack of infrared excess in the SED of some YSOs. The launch of the *Spitzer* Space Telescope (*Spitzer*) in 2003 opened up the possibility to observe a large sample of discs with a broad coverage of infrared wavelengths. *Spitzer* studies targeting Class II and Class III objects revealed that a fraction of discs ($\sim 10\,\%$; e.g., Skrutskie et al. 1990) are marked by a lack of near-infrared (NIR) and mid-infrared (MIR) excess while still showing an excess of emission at longer wavelengths, indicating that optically thick emission is coming from an outer disc. Besides these classical transition discs with a hole reaching all the way to the central star, also sources labelled as 'pre-transitional' were detected (Espaillat et al. 2007). The latter are characterized by a NIR excess, but a lack of emission in the MIR. This suggests that an optically thick disc is still present in both the inner and outer disc, which are separated by an annular gap. In Fig. 1.3, examples of the SED of a pre-transitional and transition disc, compared to the median SED (representing a continuous disc) in the Taurus star-forming region, are shown alongside a schematic view of the different groups.

Observations have shown that transition discs appear to be a diverse group of objects, making it difficult to settle on a single definition, and further suggesting different formation routes. Initially classified solely based on their SED, they were thought to be on the verge of dispersal, with their low occurrence pointing towards a short dispersal timescale. Photoevaporation naturally accounts for the formation of transition discs, but models have failed to explain those discs with large holes and simultaneously vigorous accretion (e.g., Owen et al. 2011; Ercolano & Pascucci 2017; Picogna et al. 2019). Detailed observations of transition discs became especially available with the arrival of ALMA and showed that they come with a variety of substructures such as rings, gaps, and spiral or azimuthal asymmetries. While some of the transition discs may represent an intermediate (transitioning) state between an optically thick (full) disc and disc dispersal, dynamical clearing by a massive companion represents an alternative explanation: At least some of the cavities – and in particular the very deep ones – are expected to be the result of such processes rather than representing an evolutionary state. Transition discs, therefore, represent ideal laboratories to probe disc evolution as well as planet-formation models and may enable us to catch planet formation in action.

1.2.4 Planet formation

Planets are built from the dust and gas in protoplanetary discs, starting from the micron-sized grains that are inherited from the interstellar medium (ISM). Thus,

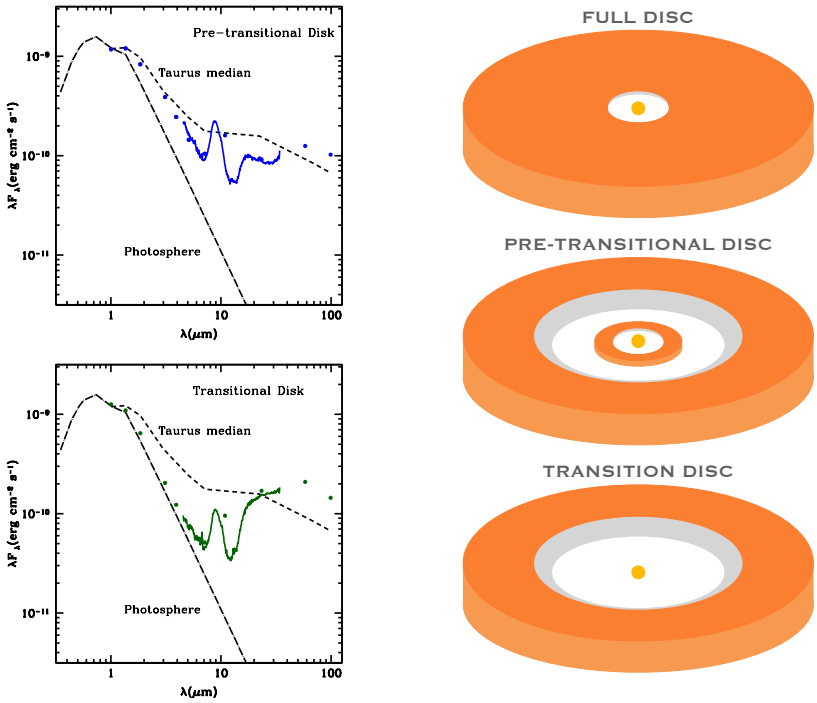

Figure 1.3: Left: SED of a pre-transitional disc (Espaillat et al. 2007) and a transitional disc (Calvet et al. 2005) relative to the Taurus median SED (D'Alessio et al. 1999), as shown in Espaillat et al. (2014). Right: Schematic view of a full, pre-transitional, and transition disc.

planet-formation models must account for the grains to grow by at least 13 orders of magnitude (for recent reviews, see e.g., Johansen & Lambrechts 2017; Izidoro & Raymond 2018; Drazkowska et al. 2022). Both theoretical research (e.g., Wada et al. 2008; Paszun & Dominik 2009; Birnstiel et al. 2010, 2012; Krijt & Kama 2014; Krijt et al. 2015) and laboratory experiments (e.g., Blum & Wurm 2008; Güttler et al. 2010; Kothe et al. 2010; Weidling et al. 2012; Blum et al. 2014) have shown that in the beginning, the dense disc environment allows grains to efficiently stick together in collisions and form millimetre- or even centimetre-sized particles, also called pebbles. This is supported by observations of the different dust size distributions with e.g., ALMA, which further indicate that grain growth already happens on a relatively short timescale of $\sim 10^5$ yr (Harsono et al. 2018).

One limiting factor of grain growth is fragmentation. As the particles grow, the relative velocities at which they impact increase (e.g., Brauer et al. 2008) and at values great than $\sim$1–10 m s^{-1} (e.g., Dominik & Tielens 1997; Blum & Wurm 2008; Wada et al. 2008; Gundlach et al. 2011) the grains tend to fragment or bounce instead of sticking together upon collision. The exact threshold between growth and fragmentation, also called fragmentation velocity, depends on numerous factors, including disc properties such as turbulent mixing or vertical settling, and

grain properties such as grain composition, shape, and surface. For example, the presence of an icy mantel on the grain surface increases the fragmentation velocity and allows for a more efficient grain growth (e.g., Wada et al. 2008; Gundlach et al. 2011).

Another obstacle to the formation of larger bodies beyond the centimetre-sized pebbles is the radial drift barrier. In the beginning, the dust grains are small enough to be well coupled to the gas, which is supported by a pressure gradient and thus rotates at a slightly sub-Keplerian speed. As the grains grow, they decouple from the gas more and more and since they are not supported by pressure they move at Keplerian velocities. Consequently, the particles constantly experience a 'headwind' from the slower-moving gas, which causes them to lose angular momentum and drift inwards. This process can be very fast, causing particles to drift towards the host star within a few 100 years without having the time to grow planets (Whipple 1972; Weidenschilling 1977). The timescale on which the drifting occurs strongly depends on the grain size, mass, and also the density of the surrounding gas and can be quantified with the Stokes number or dimensionless stopping time. The Stokes number is given by the ratio of the stopping and the dynamical timescale. While very small particles, which are dragged with the gas, have Stokes numbers much smaller than one, large metre-sized bodies have Stokes numbers much bigger than one and their transfer of angular momentum to the gas is negligible, thus both of these regimes are not strongly affected by radial drift. The grains with sizes in between ($0.1\,\mathrm{mm} - 1\,\mathrm{m}$) show Stokes numbers around one and experience the strongest gas drag, causing them to quickly spiral towards the star.

A mechanism to overcome the radial drift barrier is the trapping of pebbles in so-called pressure bumps, regions of enhanced density that create a local pressure maximum (Pinilla et al. 2012a,b). Different, not mutually exclusive, mechanisms can account for the presence of such dust traps, including vortices, MRI, spirals in self-gravitating discs, dead zones, and snowlines, but also the outer edge of a gap created by a massive planet. Inside the pressure bumps, particles have the time to grow into metre- or kilometre-sized planetesimals (for a review, see e.g., Pinilla & Youdin 2017). Dust traps are an explanation for the commonly observed ring-like structures in protoplanetary discs, e.g., with ALMA (Andrews 2020).

Following the growth of km-sized planetesimals, gravity starts to dominate the planet-formation process. In this context, planetesimals can either grow through collisions, which can also result in fragmentation (Kokubo & Ida 1996; Tanaka & Ida 1999), or through the accretion of the remaining pebbles (Ormel & Klahr 2010; Lambrechts & Johansen 2012). During a phase of runaway accretion, planetary embryos are formed, with the largest bodies growing the fastest. These planetary embryos later form rocky planets or, if a planetary core has sufficiently grown ($\sim 10\,M_{\mathrm{Earth}}$), accrete the surrounding gas from the disc to form giant planets (e.g., Pollack et al. 1996). Forming such massive cores within the disc's lifetime through planetesimal collisions has been shown to be difficult, especially in the outer disc regions (e.g., Thommes et al. 2003). Pebble accretion on the other hand represents a much faster route to grow these cores once enough planetesimals are formed. Besides the core accretion scenario, an alternative mechanism to form gas

giants is gravitational instability: Similar to the formation of stars, a sufficiently massive and cold disc can become unstable and undergo a gravitational collapse (Boley 2009). This process tends to form very massive planets, or even companion stars rather than planets (e.g., Kratter et al. 2010), at large orbital distances. Through migration processes, these planets can however end up closer to the star.

The onset of planet formation remains an active topic of research, but more and more studies suggest that it starts already in the embedded phase. Evidence of grain growth has been found in protostellar envelopes (Kwon et al. 2009; Miotello et al. 2014; Harsono et al. 2018) and the majority of protoplanetary discs are observed to not have sufficient material to form planetary systems (Ansdell et al. 2016; Manara et al. 2018), even though the disc mass may be underestimated. Young systems on the other hand appear to be massive enough (Tychoniec et al. 2018).

1.3 Disc observations

While evidence for circumstellar material was found already in early times, for example in optical emission spectra (Herbig 1950) or as an excess of emission in the infrared (Ney et al. 1973), it was not until the early 1990s that protoplanetary discs were observed with the *Hubble* Space Telescope (HST) in the Orion Nebula Cluster at optical wavelengths (O'dell & Wen 1994; O'dell & Wong 1996). In the following, discs were also studied in the millimetre-regime with instruments such as the IRAM Plateau de Bure observatory (now NOEMA) or the Submillimeter Array (SMA). Altogether, these observations revealed flat structures around newborn stars, and only with the recent advancement of ALMA and the Spectro-Polarimetric High-contrast Exoplanet REsearch (SPHERE) on ESO's Very Large Telescope(VLT), the door was opened to resolve circumstellar discs at high spatial and spectral resolution. In Fig. 1.4, an HST image of a protoplanetary disc in the Orion Nebula is shown alongside the first ALMA image of the HL Tau disc, highlighting how ALMA has revolutionized the field.

1.3.1 ALMA

The cold ($20 - 50\,\mathrm{K}$) molecular gas of protoplanetary discs emits predominantly at millimetre wavelengths through rotational lines, which can easily be excited at such temperatures, and millimetre-sized grains make up an important contributor in the dust distribution. To study discs in the millimetre-regime, the Atacama Large Millimeter/submillimeter Array (ALMA), an interferometer located in the Atacama desert of the Chilean Andes at a height of about 5000 m, represents the most suited facility. With 66 ($54\times12\,\mathrm{m}$ and $12\times7\,\mathrm{m}$) antennas, operating in 10 Bands that cover wavelengths between 0.3 and 3.6 mm, and possible configurations with baselines ranging from 160 m up to 16 km, ALMA provides both the sensitivity and high resolution to detect faint molecular emission and resolve substructures in the gas as well as the dust, which are further described in the following. Aside from detailed studies of individual sources, ALMA has also allowed for large sur-

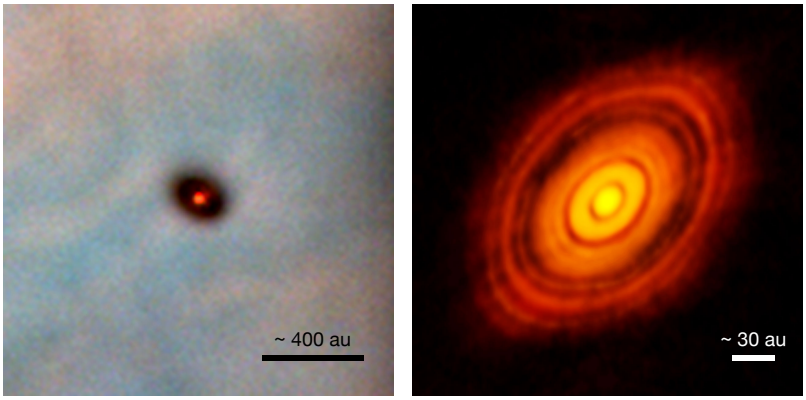

Figure 1.4: Left: Optical HST image of a protoplanetary disc in the Orion Nebula Cluster. Credit: Mark McCaughrean (MPIA), C. Robert O'Dell (Rice University), and NASA/ESA. Right: ALMA image of the HL Tau disc at millimetre wavelengths. Credit: ALMA (ESO/NAOJ/NRAO).

veys, including comprehensive observations of different star-forming regions (e.g., Pascucci et al. 2016; Barenfeld et al. 2016, 2017; Ansdell et al. 2016, 2017; Cox et al. 2017; Long et al. 2017, 2018, 2019; Ward-Duong et al. 2018; Cazzoletti et al. 2019; Cieza et al. 2019; Williams et al. 2019). These population studies have enabled scientists to link important disc properties such as the disc size or mass to the properties of the host star (e.g., Manara et al. 2022; Miotello et al. 2022), which has important implications on the disc evolution and planet-formation processes. They have further shown that the average protoplanetary disc is very different from the largest and brightest discs, which are usually targeted in individual observations.

1.3.2 Dust substructures

Emission from the dust in protoplanetary discs is expected to be brightest at millimetre wavelengths, as millimetre-sized grains dominate the dust population for Class II sources. In this context, the thermal radiation coming from cold dust particles is determined by the particle size, which is comparable to the observed wavelength (Draine 2006). Furthermore, the emission in the millimetre-regime is mostly optically thin and traces dust grains close to the midplane of the disc, where planet formation takes place. Thus, ALMA represents the ideal facility to probe the bulk of the dust content, study dust substructures in the planet-formation region, and search for signposts of planet–disc interactions.

In contrast to the smooth and symmetric structures observed prior to ALMA, high-resolution ALMA observations over the past decade have revealed that a variety of substructures such as gaps or cavities, rings, spiral arms, and azimuthal asymmetries are ubiquitous in the dust component (e.g., van der Marel et al. 2013; Andrews et al. 2018; Cazzoletti et al. 2018; Long et al. 2018; Andrews 2020; Öberg

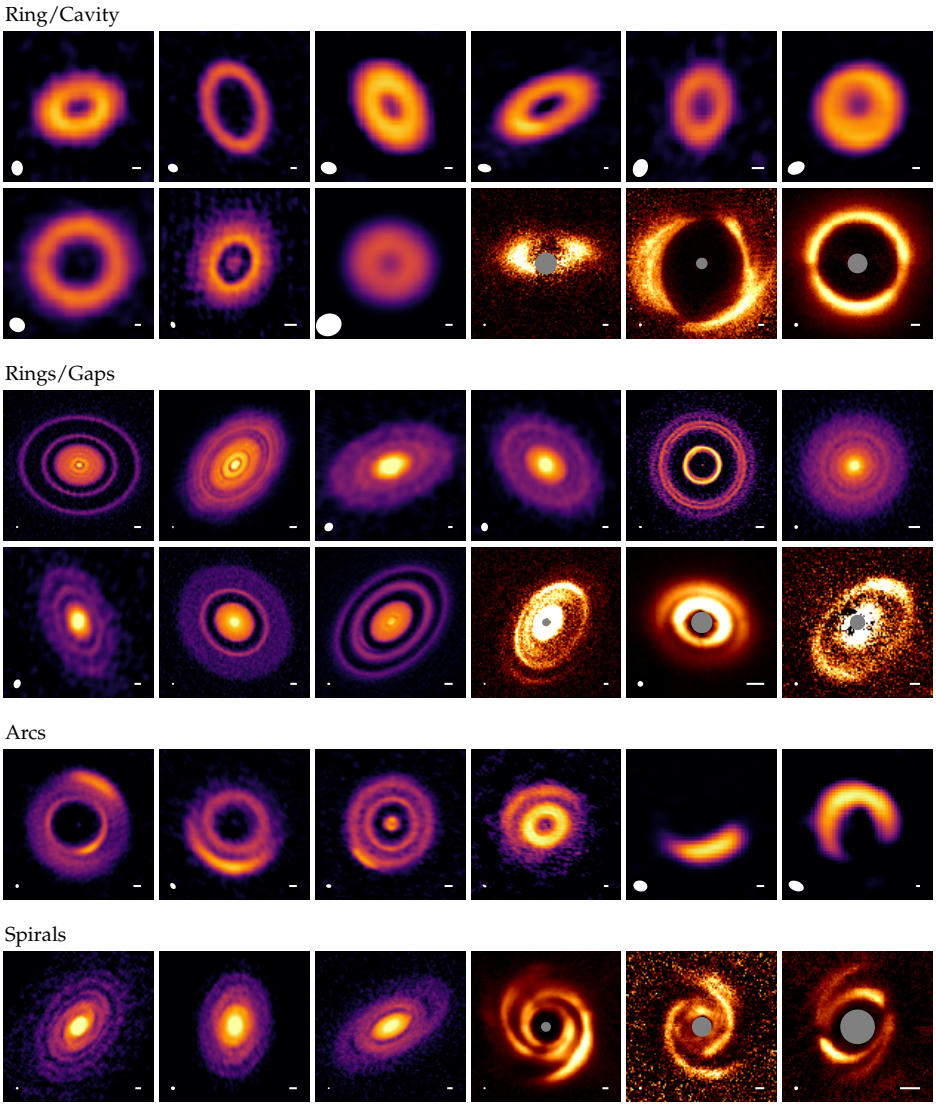

Figure 1.5: Overview of the dust substructures observed at high resolution with ALMA and VLT/SPHERE (indicated by different colormaps), as presented in Andrews (2020).

et al. 2021; Bae et al. 2022; Benisty et al. 2022). Examples of such structures are shown in Fig. 1.5. Also included here are near-infrared scattered light images, which trace the μm-sized grains in the surface disc layers, where spiral structures are particularly well pronounced.

While an interplay of various mechanisms such as photoevaporation (e.g., Owen et al. 2011; Picogna et al. 2019), gravitational instabilities (e.g., Kratter & Lodato 2016), magnetorotational instabilities (e.g., Flock et al. 2015, 2017; Riols & Lesur

2019), zonal flows (e.g., Uribe et al. 2015), or compositional baroclinic instabilities (e.g., Klahr & Bodenheimer 2004) may be responsible for the observed substructures, at least some of them are expected to be the result of dynamical interactions with (massive) planets. Planets are capable of carving gaps in the gas (as the tidal forces will result in a redistribution of angular momentum), producing local pressure maxima which, as previously mentioned, can efficiently trap the dust particles into rings (Lin & Papaloizou 1979). For very massive planetary or binary companions, an entire cavity may be cleared. Planets are further capable of triggering the Rossby-Wave instability (Lovelace et al. 1999; Li et al. 2000, 2001) which creates so-called vortices, i.e., high-pressure dust trapping regions, that can explain the observed azimuthal asymmetries. Theoretical work and simulations have shown that planets can also generate spiral arms (e.g., Ogilvie & Lubow 2002; Rafikov 2002; Dong et al. 2015, 2016; Bae & Zhu 2018a,b).

1.3.3 Gas substructures

In terms of mass, the bulk of the disc material is made up of molecular gas rather than dust, which is not only more difficult to observe due to lower intensities but also not as straightforward to interpret: Molecular emission does not only depend on the gas density but also on its abundance, which is strongly affected by the physical properties of the disc and the chemical reactions taking place therein. Moreover, the most abundant molecule in the gas phase is molecular hydrogen (H_2) which lacks a permanent electric dipole moment, making the detection of H_2 emission extremely challenging. Instead, ALMA observations of the gas content often focus on the second most abundant molecule carbon monoxide (CO), which is marked by a relatively simple and stable chemistry.

Lines from the main isotopologue ^{12}CO are optically thick in most disc regions and thus they trace material emitting from the upper layers of the disc. These are close to the layers probed by the small dust grains in NIR scattered light and are therefore more likely to show spiral substructures. Observations of the latter have for example been observed by Teague et al. (2019b) and are further investigated in Chapters 3, 4, and 5. In the context of planets, spiral features can be explained as follows: The spiral wakes excited by a companion result in an increased surface density and thus higher opacity which moves the $\tau = 1$ layer to a higher altitude where the temperature is generally higher (Phuong et al. 2020a,b). To trace disc layers which are closer to the midplane, less abundant isotopologues such as ^{13}CO, C^{18}O, or also C^{17}O, ^{13}C^{17}O (Booth et al. 2019), and ^{13}C^{18}O are needed. While these molecules are even more difficult to observe with sufficient sensitivity, they are more likely to provide information about annular substructures such as gaps or cavities. The latter have indeed been confirmed by several observations (e.g., Perez et al. 2015a; van der Marel et al. 2016; Dong et al. 2017; Ubeira Gabellini et al. 2019).

Besides CO, which is marked by a relatively easy and well-understood chemistry, also other molecules, such as CN, CS, C_2H, HCO^+, DCO^+, N_2H^+ just to name a few, are interesting to study both through modelling and observations, as each molecule provides unique information about the physical properties of the

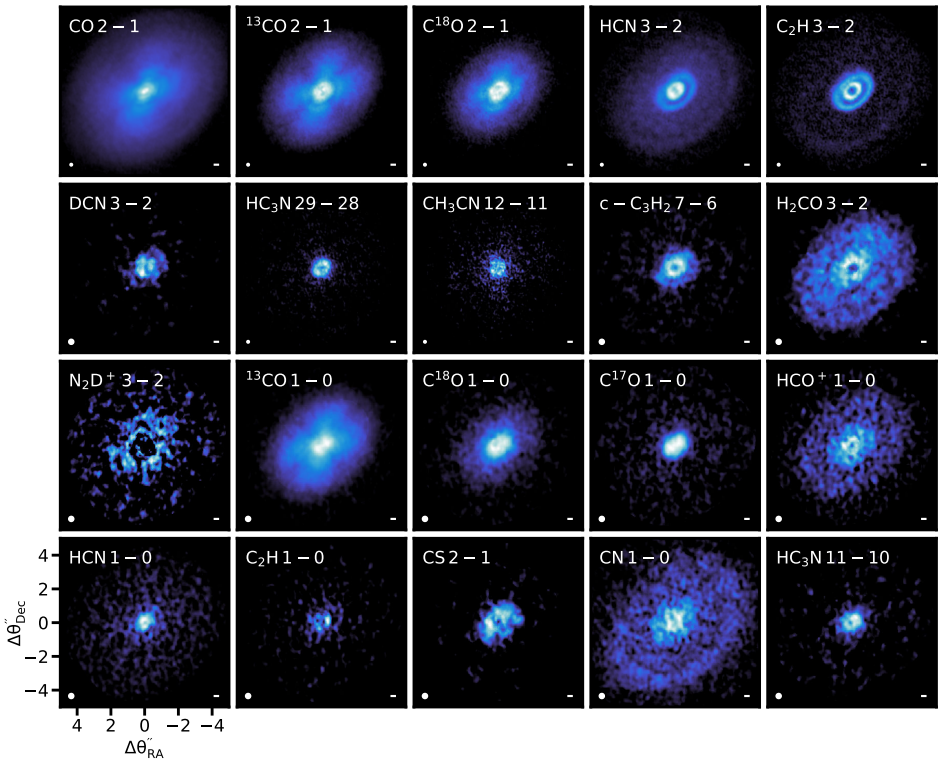

Figure 1.6: Gallery of the MAPS observations of the HD 163296 disc. Shown are the Moment 0 maps of 20 lines targeted with ALMA. Adapted from Öberg et al. (2021).

disc and the underlying chemistry. A comprehensive ALMA study of the chemical inventory of protoplanetary discs was recently performed within the MAPS program (Molecules with ALMA at Planet-forming Scales; Öberg et al. 2021), showing an impressive diversity in the abundances, distributions, and substructures of the molecules. A gallery of the MAPS observations is shown in Fig. 1.6 for the HD 163296 disc.

In contrast to the dust, gas emission includes information on the dynamics – or kinematics – in protoplanetary discs, as the lines emitted by rotating gas are red- and blueshifted depending on whether the material is moving towards or away from the observer. This opens up a unique new window to study the mechanisms being at play in discs. Disc kinematics represent a key topic of this thesis and are therefore described in more detail in the following section.

1.4 Kinematics

Ultimately, only a direct detection of a young planet can confirm the link between the observed gas and dust substructures and planet formation. However, the

dense and opaque environment surrounding young planets makes such a task very challenging and feasible only for the most massive and bright planets that are less affected by dust extinction (Sanchis et al. 2020). To date, the only robust detection of embedded (several $M_{\rm J}$-sized) planets and their circumplanetary discs are those of the PDS 70 system (Keppler et al. 2018; Haffert et al. 2019; Benisty et al. 2021). This has triggered the development of other more indirect detection techniques.

Among these methods, a particularly promising one is to study the velocity field of the rotating gas, observed through molecular line emission. Deviations from purely Keplerian rotation (as expected of unperturbed gas) yield information about the processes shaping the disc (see Pinte et al. 2022 for a review). For detailed studies of kinematical substructures, a high spectral resolution is essential ($\sim 50\,\mathrm{m\,s^{-1}}$), and a relatively high spatial resolution is preferred ($< 0\farcs1$). While such observations are accessible with ALMA they come at high observational costs, thus this field remains in its infancy and the number of sources for which the kinematics have been thoroughly observed and analysed is limited.

Under the assumption that the disc is in both radial and vertical hydrostatic equilibrium and that the gravity is dominated by the central star, the rotation velocity can be written as

$$\frac{v_\phi^2(r,z)}{r} = \frac{GM_* r}{(r^2+z^2)^{3/2}} + \frac{1}{\rho_{\rm gas}}\frac{\partial P_{\rm gas}}{\partial r}, \tag{1.3}$$

where $\partial P_{\rm gas}/\partial r$ is the radial pressure gradient (Rosenfeld et al. 2013). Self-gravity is neglected in Eq. 1.3. Quantifying deviations from the rotation velocity can thus be used to trace perturbations in the pressure gradient, for example induced by a planet, which causes a negative gradient inside and a positive one outside of its orbit (Kanagawa et al. 2015; Teague et al. 2018a).

For a given frequency, line emission is concentrated in a region of constant projected velocity, also called isovelocity curve. Due to the Keplerian rotation of the disc, these channels follow a 'butterfly' pattern (Horne & Marsh 1986; Beckwith & Sargent 1993). The nature of the velocity field was shown through earlier observations (e.g., Dutrey et al. 2014b), however, ALMA's high spatial resolution opened the possibility to resolve and separate emission from both the upper (above the midplane) and the lower (below the midplane) disc surfaces. Channel maps, which are relatively noisy, can be collapsed into a map displaying the full rotation field. In this context, different methods have been used such as the integration over the spectral axis to obtain the intensity weighted average velocity or Moment 1 map, fitting of a Gaussian profile (Casassus & Pérez 2019) or double Gaussian profile (Casassus et al. 2021; Izquierdo et al. 2022), or the quadratic method introduced by Teague & Foreman-Mackey (2018). While collapsing a cube into a rotation map brings the advantage of an increased signal-to-noise ratio (SNR), it washes out the distinction between the upper and lower disc surfaces.

Both the velocity channels and rotation maps directly reflect the underlying gas velocity and for a non-perturbed Keplerian disc they are expected to be smooth. Perturbations to the velocity on the other hand result in visible features that can be analysed by modelling the rotation velocity. Two methods are used in this

thesis to study disc kinematics, one modelling the rotation map (Chapters 3 and 4) and the other modelling the channel maps (Chapter 5). The former approach is relatively straightforward: The projected line-of-sight velocity is given by

$$v_{\phi,\mathrm{proj}}(r,\phi) = v_\phi(r)\cos\phi\sin i, \tag{1.4}$$

where ϕ is the polar angle and i the inclination of the disc. To deproject the sky-plane coordinates (x, y) into the disk-frame coordinates (r, ϕ), information of the disc geometry, namely the source centre, inclination, position angle, and height $z(r)$ of the emission surface, can be used based on the assumption of axisymmetry (Rosenfeld et al. 2013). These parameters can then be left free to find the best-fitting parameters for a given model of v_ϕ (e.g., as in Eq. 1.4). To fit the rotation map, this thesis uses the EDDY package, presented in Teague (2019). In the second approach, the channel maps are fitted individually. This method was recently introduced by Izquierdo et al. (2021) as the DISCMINER tool. In the DISCMINER, parametric prescriptions are adopted to reproduce the line profiles in each channel, with the intensity being described by a generalized bell kernel. This approach has the advantage that the upper and lower emission surfaces can be modelled simultaneously. It further retrieves information on the line width, which is not accessible through the first method. With the DISCMINER, localized velocity perturbations can be identified both in radius and azimuth.

While the different mechanisms taking place in the disc will all leave their individual fingerprints in the kinematics, with their exact contribution and morphology yet to be disentangled, kinematical features of planet–disc interactions are particularly exciting and outlined in the following.

1.4.1 Kinematical signatures of planets

Planets have been found to excite spiral density waves at Lindblad resonances just outside their orbit (Goldreich & Tremaine 1979, 1980; Papaloizou & Lin 1984), which can manifest in a one-armed spiral structure, called the planet wake (Ogilvie & Lubow 2002). This disturbs the density structure of the disc but also the velocity field and can result in significant azimuthal deviations from Keplerian rotation (up to a few 10 %) and radial motions (e.g., Bollati et al. 2021), with the azimuthal deviations being largest near the planet location and the radial motions dominating at large distances from the wake (Rafikov 2002). The planetary wake also triggers vertical motions in the form of meridional eddies (Fung & Chiang 2016). The exact amplitude of the perturbation strongly depends on the planetary mass, but also the disc structure. In addition to the Lindblad spirals, planets can launch buoyancy spirals under certain thermal conditions (e.g., Zhu et al. 2012, 2015; Lubow & Zhu 2014; McNally et al. 2020). These spirals appear to be much more tightly wound, especially close to the location of the planet, and predominantly trigger vertical motions, thus both types of spirals produce distinctive kinematical features. Non-Keplerian spirals have been observed in the gas disc of several sources: TW Hya (Teague et al. 2019b), HD 100453 (Rosotti et al. 2020a), HD 135344B (Casassus et al. 2021), HD 163296 and MWC 480 (Teague et al. 2021), HD 142527 (Garg et al. 2021), and J 1604 (Stadler et al. 2023) are all marked by spiral substructures.

Chapters 3, 4, and 5 further explore the kinematical spirals in a number of sources. Another signature of a spiral wake, the so-called Doppler-flip, a sign reversal in the non-Keplerian velocity component, has been reported in the HD 100546 disc by Casassus & Pérez (2019); Casassus et al. (2022), with its planetary origin, however being debated (Norfolk et al. 2022). A detailed kinematical analysis of the protoplanetary disc around HD 100546 is conducted in Chapter 5.

As previously mentioned, planets are capable of carving an annular gap in the disc, resulting in steep pressure gradients at the edges and a sub-Keplerian flow at the inner and super-Keplerian flow at the outer edge. It is however important to note that, depending on the planetary mass, a gap may be visible in the dust while the gas profile is only slightly affected (Dipierro et al. 2016) and deviations from Keplerian rotation may not be observed around a dust gap. Furthermore, a gas density gradient may be hidden in deep cavities, where the opacity is reduced and consequently the temperature gradient becomes the dominating factor (Rab et al. 2020). Deviations in the rotation profile, likely tracing pressure gradients in gas gaps, have been measured by Teague et al. (2018a) in HD 163296. From the edges of a gas gap, material (viscously) moves towards the gap centre and the midplane, creating significant motions also known as meridional flows (Kley et al. 2001; Tanigawa et al. 2012; Szulágyi et al. 2014; Morbidelli et al. 2014), which have been observed in the kinematics (Teague et al. 2019a; Yu et al. 2021). These ordered flows are not exclusive to planet-induced gaps and studying their azimuthal variations provides insights into the underlying mechanisms that formed the gap. In addition, planets can trigger turbulent motions, which result in a local enhancement of line width (Dong et al. 2019). These motions, even though hard to detect, can further help to distinguish between a planet and other gap-opening processes.

An embedded planet perturbs the gas flow in such a way that an additional Doppler shift is induced in the molecular emission, which manifests in the channel maps as a distortion of the iso-velocity curve, also referred to as 'kinks' or 'wiggles'. Kink-features that are in agreement with planets of several $M_{\rm J}$ have been observed in HD 163296 and HD 97048 (Pinte et al. 2018b, 2019), tentative detections were identified by Pinte et al. (2020) in eight of the DSHARP sources (Andrews et al. 2018), as well as in CI Tau (Rosotti et al. 2021). Modelling of the channel maps of HD 163296 with the DISCMINER yielded strong indications for two embedded planets (Izquierdo et al. 2022). A localized kinematic structure was detected in atomic carbon of the same disc (Alarcón et al. 2022). On top of that, the presence of a circumplanetary disc (CPD) – an accretion disc which channels material onto a sufficiently massive planet – can cause a spot in the channels which is detached from the iso-velocity curve of the parent disc: The gas flow onto the planet adds a significant velocity distortion and under certain conditions (e.g., certain respective disc orientations), the CPD emission can decouple from the emission of the background disc (e.g., Perez et al. 2015b). A summary of the expected kinematic signatures in a planet-forming disc is presented in Fig. 1.7.

Altogether, kinematical observations open the opportunity to find embedded planets which escape the classical detection techniques and yield important implications on the planet-formation processes. Knowledge of the planetary location

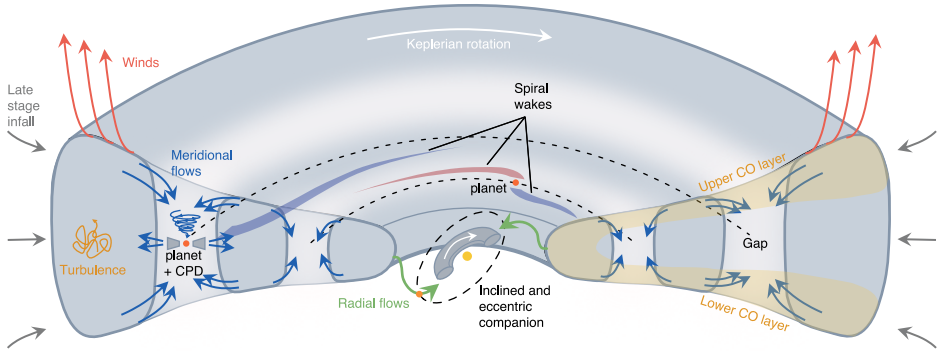

Figure 1.7: Schematic view of the possible kinematic signatures, exhibited by a planet-forming disc. Adapted from Pinte et al. (2022)

and mass is crucial to put constraints on the current planet-formation models (such as gravitational instability or pebble accretion). Linking kinematical signatures with the location of dust gaps provides information about the onset of planet formation, as planet-carved gaps indicate that the planet formation has already reached an advanced stage. This suggests that the timescales in which planets are formed are even shorter than previously thought or that some migration processes have already taken place. By increasing the database of detected young planets, kinematical studies bring the potential of population studies to understand possible patterns and link them to the properties of mature exoplanet populations.

1.5 This thesis

In the last decade, ground-breaking facilities such as ALMA and SPHERE have revolutionized the field of planet formation: With high angular resolution observations of the circumstellar material, it is now possible to uncover numerous and diverse substructures that are exhibited by discs. The interpretation of these substructures is however not straightforward, as different mechanisms, often being at play simultaneously, are shaping the disc. Three key questions have been triggered:

1. Are these substructures the result of planet–disc interactions or other mechanisms?

2. If planets are the cause, what can we learn about these planets, for example in terms of location or mass, and if not planet-driven, what can we learn about the disc?

3. What modulates angular momentum transport in the disc as well as disc dispersal, influencing the disc lifetime and thus the time to build planets?

This dissertation focuses on interpreting disc substructures in the context of disc winds as well as planet–disc interactions by using different modelling and obser-

vational techniques. It contributes to the understanding of how common they are, if they follow certain patterns and if differences or similarities can be identified for different disc populations. A special focus is set on transition discs, which represent ideal laboratories to observe planet formation in action and test disc evolution models. The individual chapters and their conclusions are summarized as follows:

Chapter II: Photoevaporative disc winds in carbon-depleted discs
One mechanism able to explain the formation of gaps and cavities in discs is photoevaporation, however, it can not account for the observed diversity of transition discs and especially fails at explaining discs with large cavities and simultaneous strong gas accretion. This chapter investigates photoevaporative winds acting in discs in which, as commonly observed, volatile carbon is depleted, and how they affect the formation of cavities. For this purpose, radiative transfer and hydrodynamical models are combined. The results show that (X-ray) photoevaporative winds are, with respect to solar metallicity discs, stronger in such carbon-depleted discs, resulting in enhanced mass-loss rates and mass-loss profiles extending to larger radii. These results may explain a larger number of the observed transition discs. Additionally, very high carbon depletion may represent a mechanism of very fast disc dispersal towards the end of the disc's lifetime.

Chapter III: Spiral structures in the gas disc of CQ Tau
In the last decade, high-angular-resolution observations have shown that circumstellar discs are marked by a variety of substructures, triggering the question of whether they are caused by planet–disc interactions. In this chapter, both the kinematics and brightness temperatures of the disc around CQ Tau are analysed using high-resolution CO observations taken with ALMA. To search for deviations from Keplerian rotation and variations in the temperature structure, a Keplerian disc model is fitted to the velocity field. The results yield significant spiral features in both the gas velocity and brightness temperature residuals, which together with spirals observed in the near-infrared and a detected deep gas and dust cavity point towards ongoing giant planet formation in the disc.

Chapter IV: A survey of the kinematics and brightness temperatures of transition discs
To interpret the origin of the various substructures exhibited by protoplanetary discs, it is crucial to understand how common they are and if they follow certain patterns. In this chapter, the analysis conducted in Chapter III is expanded to a sample of 36 large cavity transition discs, pushing the available ALMA observations to their limits. For the analysis, archival CO data are used, taken in Band 6 and Band 7. For the first time, the substructures found in the kinematics and brightness temperature are compared to other indicators for the presence of planets for a large sample of sources. The results yield strong features such as arcs or spirals, possibly associated with the presence of planets or companions, in about 20 % of discs, while the

majority of the sources do not present as clear signatures. Almost all discs that exhibit spirals in near-infrared scattered light show at least tentative features in the CO data.

Chapter V: Spirals and meridional flows in the planet-forming disc around HD 100546
The disc surrounding the Herbig star HD 100546 represents a particularly interesting target to search for planet–disc interactions, as numerous direct and indirect evidence for ongoing planet formation has been observed in both the dust and gas emission. In this chapter, a multi-line analysis of the gas kinematics is conducted, using several CO lines observed in Band 6, 7, and 10 with ALMA. To model the line emission for each intensity cube, the DISCMINER package is used. The analysis reveals extended spiral structures in the kinematics of all lines, whose overall morphology is well reproduced by linear and logarithmic functions. They are consistent with spirals driven by an embedded companion – either planetary or binary – inside of 50 au. The pitch angles of the spirals decrease towards the midplane, which is in agreement with theoretical predictions for a dynamical interaction scenario. Indications of a second companion located further out between 90-150 au are seen in the form of meridional flows towards the midplane and pressure minima, as well as a tentative gap in the more optically thin tracers. An asymmetry in the emission heights of the blue- and redshifted sides may indicate infalling material on the redshifted side of the disc or an inner warped disc, casting a shadow over the outer disc.

1.5.1 Future outlook

ALMA has transformed our view of planet-forming discs and this thesis provides some first steps in the direction of interpreting their substructures. It further helps to understand which of the sources are the most promising to target with other instruments, dedicated at the search and direct imaging of exoplanets. At the same time, it stresses the importance of even better observations, both in terms of resolution and sensitivity, to really disentangle the different mechanisms being at play in discs and the origin of the substructures remains a burning open question. We have now reached a time where new and exciting opportunities are opening up both with ALMA (e.g., exoALMA large program; PI: R.Teague) and the James Webb Space Telescope (JWST).

While ALMA observations of molecular line emission may not reach the same spatial resolution as achieved for the continuum, they can be used to analyse the gas flow throughout the disc, opening a unique new window to detect embedded planets and probe physical processes in the disc. The field of disc kinematics has just started to emerge and very deep line observations taken at high spectral and spatial resolutions are essential and will allow us to also detect smaller mass planets at shorter periods. Furthermore, a systematic and comprehensive survey of a large number of planet-forming discs, covering a wide range of disc-star system morphologies, will be needed to link the properties of discs and their young planets to the mature exoplanet populations that are observed with an enormous variety.

In this context, it is important to also analyse the smaller discs, generally thought to be less structured, in addition to the massive and bright discs that are typically studied in detail. This is an essential step to understand if there are systematic differences between these groups and if in particular Herbig Ae/Be or T Tauri discs follow different patterns.

So far, mostly the brighter CO lines have been used to map out the disc kinematics. However, to really understand the mechanisms behind the observed substructures it is crucial to trace them throughout the full radial and vertical extent of the disc. This requires deep high-resolution observations of a range of molecular tracers aside from CO, which further brings the opportunity to understand the chemical signatures of planets. To interpret the observations, fundamental work is also required on the theoretical side. Dedicated modelling of both planet–disc interactions and other disc-shaping mechanisms such as disc winds or gravitation instabilities and their imprints on the kinematics and temperature structure is crucial to understand the role that individual processes play in the planet-formation puzzle. Exciting opportunities will also open up with JWST and the Extremely Large Telescope (ELT) to directly image young (proto-)planets, that are responsible for the deviations in the velocity field. In combination with ALMA, these facilities will pave the way for a comprehensive characterization of the youngest exoplanets. Coupling ALMA observations of the overall disc structure with JWST spectroscopy projects, tackling the inner disc structure, will further enable us to access the connection of inner and outer disc structures, which is so far not fully understood.

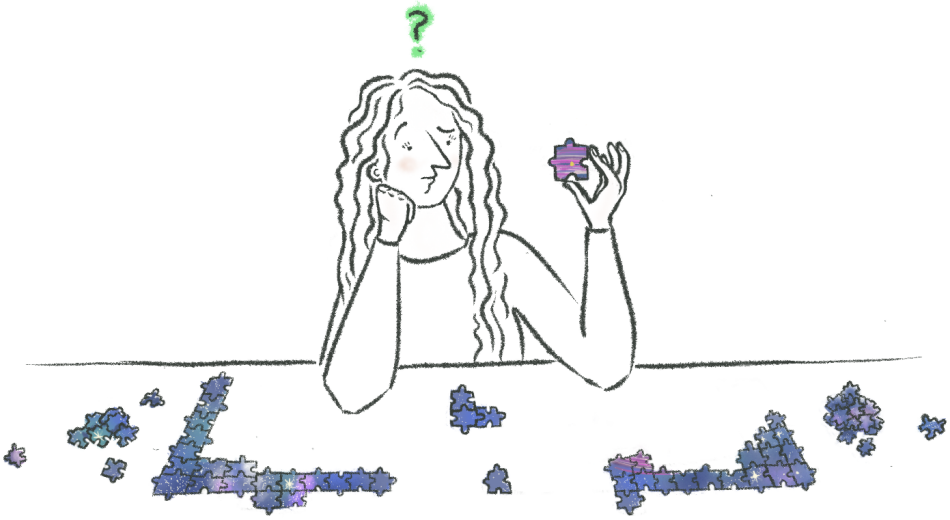

PART I

Models of photoevaporative disc winds

Captain, the most elementary
and valuable statement in science,
the beginning of wisdom, is,
"I do not know".

Data, Star Trek: The Next Generation

Chapter 2

Radiation-hydrodynamical models of X-ray photoevaporation in carbon-depleted circumstellar discs

L. Wölfer, G. Picogna, B. Ercolano, E. F. van Dishoeck

MNRAS, 490, 5596 (2019)

ABSTRACT

The so-called transition discs provide an important tool to probe various mechanisms that might influence the evolution of protoplanetary discs and therefore the formation of planetary systems. One of these mechanisms is photoevaporation due to energetic radiation from the central star, which can in principle explain the occurrence of discs with inner cavities like transition discs. Current models, however, fail to reproduce a subset of the observed transition discs, namely objects with large measured cavities and vigorous accretion. For these objects, the presence of (multiple) giant planets is often invoked to explain the observations. In our work, we explore the possibility of X-ray photoevaporation operating in discs with different gas-phase depletion of carbon and show that the influence of photoevaporation can be extended in such low-metallicity discs. As carbon is one of the main contributors to the X-ray opacity, its depletion leads to larger penetration depths of X-rays in the disc and results in higher gas temperatures and stronger photoevaporative winds. We present radiation-hydrodynamical models of discs irradiated by internal X-ray+EUV radiation assuming carbon gas-phase depletions by factors of three, 10, and 100 and derive realistic mass-loss rates and profiles. Our analysis yields robust temperature prescriptions as well as photoevaporative mass-loss rates and profiles which may be able to explain a larger fraction of the observed diversity of transition discs.

2.1 Introduction

The nurseries of planets, circumstellar discs, are dense remnants of the star formation process, enclosing all the gas and dust material crucial for the formation of planetary systems. Far from being static, they evolve and ultimately disperse while they give birth to planets, moons, and minor bodies. As the disc dispersal proceeds on timescales which are of the same order as the planet formation timescales (e.g., Helled et al. 2014), the disc evolution and planet formation processes are directly linked and occur as a highly coupled and complex problem.

In this regard, the so-called transition discs are of particular interest, as they show evidence for inner dust (and possibly gas) depleted regions (e.g., Strom et al. 1989) and are therefore often treated as being on the verge of dispersal. These cavities can reach various sizes from sub-au to several tens of au, with many transition discs simultaneously showing evidence of gas accretion onto the central star. Understanding the occurrence and underlying physics of transition discs may enable us to probe various mechanisms that could play a role during disc evolution and influence the planet-formation and migration processes.

Many different mechanisms have been proposed so far to explain the observed diversity of transition discs (e.g., photoevaporation, planet–disc interactions, magnetohydrodynamic processes), none of which however can explain the whole database of observations (e.g., Alexander et al. 2014; Espaillat et al. 2014). One promising mechanism is internal photoevaporation, which describes the formation of inner holes or gaps as a result of the interaction of high-energy stellar radiation with the disc material, naturally producing transition discs. It was however assumed for a long time that photoevaporation can only account for very few of the observed objects. Especially those discs which were found to have cavities at large disc radii and simultaneously vigorous gas accretion onto the central star (of order $10^{-8}\,\mathrm{M}_{\odot}\,\mathrm{yr}^{-1}$) are not explained by current photoevaporation models (Owen et al. 2011; Ercolano & Pascucci 2017; Picogna et al. 2019). These discs are therefore often suggested as being an indicator of the presence of (multiple) giant planets, which are in principle able to dynamically carve significant gaps into a disc.

Recent studies have however shown that the range of photoevaporative influence can be extended in discs of reduced metallicity compared to the solar elemental abundances (Ercolano et al. 2018). Indeed, several observations of gas-phase depletion of volatile carbon and oxygen in outer disc regions have been reported in the last years (Hogerheijde et al. 2011; Favre et al. 2013; Ansdell et al. 2016; Kama et al. 2016; Du et al. 2017; Miotello et al. 2017). Carbon and oxygen represent the main contributors to the X-ray opacity, thus a disc depleted in these elements experiences stronger (X-ray) photoevaporative winds and enhanced mass-loss rates, as the X-ray radiation can penetrate further into the disc and heat the gas in deeper disc layers.

In this paper, we investigate the effects of X-ray photoevaporation in such metal-depleted discs, adopting different degrees of carbon depletion, and perform detailed radiation-hydrodynamical simulations following the approach of Picogna et al. (2019). FUV photoevaporation is not included in this work, yet it can play

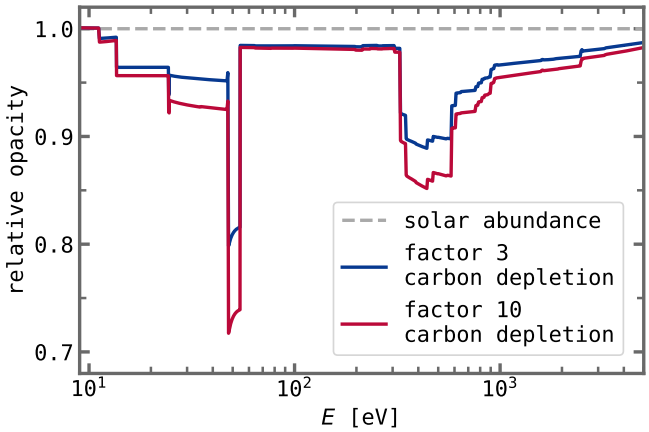

Figure 2.1: Relative opacity, shown for a carbon depletion by a factor of three (blue) and 10 (red) with respect to the undepleted case.

a role at larger disc radii (e.g., Gorti et al. 2009). Thus, the presented mass-loss rates are a lower limit to the actual mass-loss rates. We describe the numerical methods and setups we used in Sect. 2.2 whereas our main results are presented in Sect. 2.3. A conclusion of our analysis and an outlook for future research are given in Sect. 2.4.

2.2 Methods

2.2.1 Thermal Calculations

We used the gas and dust radiative transfer code MOCASSIN (Ercolano et al. 2003, 2005, 2008b) to model gas temperatures of circumstellar discs with different carbon abundances that are irradiated by an X-ray+EUV spectrum (presented in Ercolano et al. 2008a, 2009, unscreened spectrum of Fig. 3 in Ercolano et al. 2009) of a $0.7\,\mathrm{M}_\odot$ star. In total, we set up three simulations with mostly standard solar abundances but varying degrees of carbon depletion. Our standard interstellar gas-phase abundances are taken from Savage & Sembach (1996) (C: 1.4×10^{-4}; O: 3.2×10^{-4}). These values take into account that some fraction of the solar abundances (Asplund et al. 2005) are locked up in refractory material. Subsequently, we depleted the gas-phase carbon abundance relative to the interstellar value by factors of three, 10, and 100. This has a strong impact on the opacity as visible in Fig. 2.1 where the relative opacity of the carbon depletion by a factor of three and 10 to the undepleted case is shown, respectively. The curves are presented for a column density of $\approx 5 \times 10^{20}\,\mathrm{pp\,cm^{-2}}$ and an ionization parameter $\xi = \frac{L_\mathrm{X}}{nr^2}$ (Tarter et al. 1969) of $\log(\xi) = -2$, where L_X is the X-ray luminosity, r the distance from the star, and n the electron number density.

The adopted synthetic thermal spectrum was created with the plasma code PINTofALE (Kashyap & Drake 2000) in order to match *Chandra* spectra of T Tauri stars observed by Maggio et al. (2007). All simulations were run for column densities up to $2.5 \times 10^{22}\,\mathrm{pp\,cm^{-2}}$ and for in total 20 ionization parame-

ters between $\log(\xi) = -8$ and $\log(\xi) = -2$. From the output of the simulations, we obtained the equilibrium gas temperature at the upper disc layers as a function of the ionization parameter. We furthermore divided the disc into 10 sections of size $2.5 \times 10^{21}\,\mathrm{pp\,cm^{-2}}$ and retrieved a temperature prescription for each column density bin. For higher column densities than $2.5 \times 10^{22}\,\mathrm{pp\,cm^{-2}}$ we assumed that the gas and dust are thermally coupled and used the dust temperatures from the models of D'Alessio et al. (2001), mapped to our models.[1]

In order to fit the modelled data, we adopted the following ad-hoc relation

$$\log_{10}\left(T(\xi)\right) = d + \frac{1.5 - d}{\left[1.0 + (\log_{10}(\xi)/c)^b\right]^m} \tag{2.1}$$

with the resulting curves being shown in Fig. 2.2 and the corresponding coefficients being listed in Table 2.1.

In Fig. 2.2, we also include the parameterization for a solar metallicity disc as a reference (the underlying data were taken from Picogna et al. 2019). The lowest, medium, and highest column densities are highlighted with colour. Figure 2.2 shows that the three different carbon depletion sets clearly vary from each other and from the solar metallicity set and that the temperatures increase as expected with increasing degree of depletion. In addition, the curves become flatter and are distributed more narrowly over the whole column density range for a higher depletion. This results from a lower gas opacity in the X-ray regime in case of a stronger depletion.

Our parameterization schemes include the column density independent curve for solar metallicity used by Owen et al. (2010, 2011, 2012). We note that the inclusion of a column density parameter helps to model the temperatures more accurately at different disc locations. Similar to Picogna et al. (2019), we find the temperature error to be reduced to less than 1 % for all simulations (compare Appendix 2.A). Furthermore, our calculations extend to lower ξ values ($\log(\xi) = -8$ instead of $\log(\xi) = -6$), which allows us to simulate the outer disc regions that are important for studying the evolution of transition discs more extensively. The prescription of Owen et al. (2010) reaches a higher maximum temperature due to an integration over a finer grid. This in principle allows to resolve a region of low density that is heated by EUV radiation, however, this region does not contribute to the total mass-loss rate and is therefore not relevant for the purpose of this work. A detailed description and discussion of the new temperature prescriptions for solar abundance discs and their impact on photoevaporative mass-loss rates and profiles can be found in Picogna et al. (2019).

To test the reliability of our temperature prescriptions we performed additional Monte Carlo simulations with higher resolution and furthermore applied different

[1] The radiation-hydrodynamical calculations were actually performed using temperature parameterizations which extended to columns of $5 \times 10^{22}\,\mathrm{pp\,cm^{-2}}$. We however found a posteriori that the high column density curves ($> 2.5 \times 10^{22}\,\mathrm{pp\,cm^{-2}}$) are severely affected by Monte Carlo noise and as a consequence carry large errors on the temperatures. We have thus decided not to include these high-column parameterizations in this work. We further note that the errors on the high-column parameterization do not affect the hydrodynamical simulations presented here, since the region of parameter space affected represents only a very small percentage of our simulation domain, well below the wind launching region.

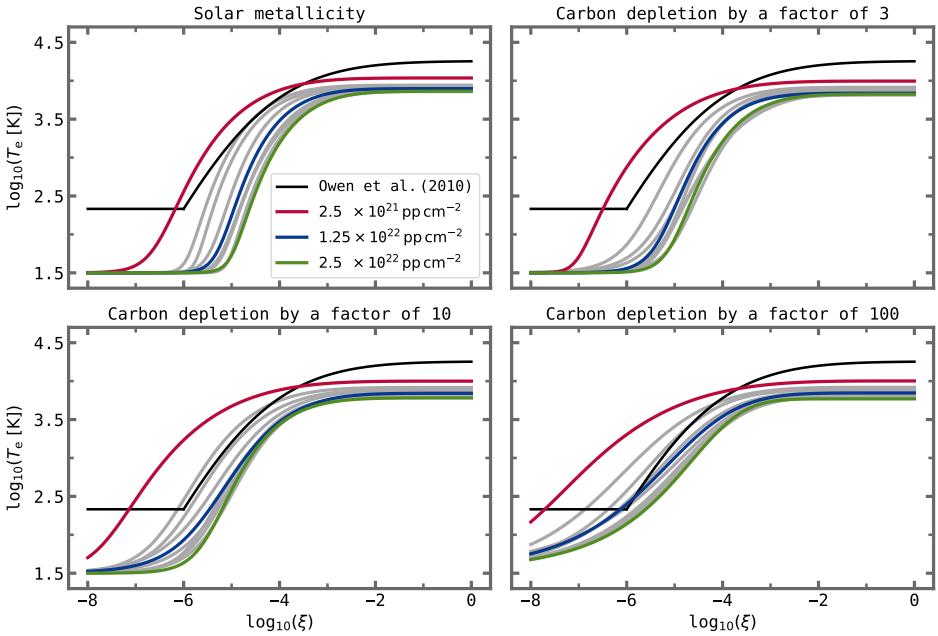

Figure 2.2: Temperature parameterization for the different carbon depletions by a factor of three (top right), 10 (bottom left), and 100 (bottom right). The temperatures for solar metallicity are included as a reference in the top left panel (Picogna et al. 2019). In each panel, the lowest column density curves are highlighted in red, the medium ones in blue, and the highest ones in green while the black curve represents the parameterization by Owen et al. (2010). The four different carbon abundance sets clearly differ from each other, showing higher gas temperatures for stronger depletion.

binnings, with both tests yielding the same results as presented in Fig. 2.2. In terms of the microphysics, which are relatively well known, the MOCASSIN code has been thoroughly benchmarked (see Ercolano et al. 2003, 2005, 2008b), which together with the small temperature error confirms the robustness of our parameterization.

2.2.2 Hydrodynamics

We used the open source hydro-code PLUTO (Mignone et al. 2007) to model different carbon-depleted as well as solar metallicity protoplanetary discs until a 'steady state' was reached, in order to find reliable photoevaporative mass-loss rates $\dot{M}$ and $\dot{\Sigma}$ profiles. We performed several simulations with PLUTO, adopting a two-dimensional spherical coordinate system centred around a $0.7\,\mathrm{M}_\odot$ star in the $r-\theta$ plane, since the problem we address is symmetric along the ϕ dimension. We furthermore implemented the temperature prescriptions described in Sect. 2.2.1 and interpolated from the curves for the whole column density range directly in PLUTO. Outside of this range, we set the lowest column density of $2.5 \times 10^{21}\,\mathrm{pp\,cm^{-2}}$ as

Table 2.1: Coefficients of the temperature parameterization for the different carbon depletions by factors of three, 10, and 100 and all 10 column density bins up to $2.5 \times 10^{22}\,\mathrm{pp\,cm^{-2}}$.

N_{H} $1 \times 10^{20}\,\mathrm{pp\,cm^{-2}}$	b	c	d	m
Carbon depletion by a factor of 3				
0–25	−49.6442	−7.0423	3.9952	0.1008
25–50	−15.6516	−5.7592	3.9144	0.3904
50–75	−13.5273	−5.2914	3.8841	0.5038
75–100	−13.8039	−5.1523	3.8620	0.4904
100–125	−20.0278	−5.2913	3.8378	0.3184
125–150	−18.2243	−5.1041	3.8208	0.4003
150–175	−19.2923	−5.3050	3.8429	0.2354
175–200	−23.5695	−5.3299	3.8464	0.1839
200–225	−16.7558	−4.9177	3.8138	0.3483
225–250	−22.9758	−5.0689	3.8247	0.2440
Carbon depletion by a factor of 10				
0–25	−21.1849	−7.7162	4.0001	0.2214
25–50	−15.1575	−6.4422	3.9176	0.3672
50–75	−14.1757	−6.2253	3.8915	0.3679
75–100	−10.8864	−5.8325	3.8743	0.4958
100–125	−11.1109	−5.6791	3.8418	0.4705
125–150	−11.2723	−5.5136	3.8344	0.4798
150–175	−17.3954	−5.7711	3.8030	0.2998
175–200	−13.5226	−5.3788	3.8126	0.4469
200–225	−13.9993	−5.4703	3.7953	0.4657
225–250	−19.0899	−5.5465	3.7807	0.3046
Carbon depletion by a factor of 100				
0–25	−11.3726	−8.2547	4.0024	0.3494
25–50	−7.3249	−6.7159	3.9200	0.6860
50–75	−6.9106	−5.9662	3.8872	0.8848
75–100	−6.3211	−5.6836	3.8557	0.9324
100–125	−5.6213	−5.3946	3.8461	1.1009
125–150	−4.7809	−4.7992	3.8218	1.5653
150–175	−5.5289	−5.0542	3.8155	1.1728
175–200	−5.1865	−4.5065	3.7945	1.7157
200–225	−5.5705	5.0308	3.7948	1.1407
225–250	−5.0972	−4.1973	3.7693	2.2123

a limit and used the assumption described in the previous subsection for higher column densities than $2.5 \times 10^{22}\,\mathrm{pp\,cm^{-2}}$. In terms of the $\log(\xi)$ range, we assumed $T = T_{\mathrm{dust}}$ for values smaller than $\log(\xi) = -8$ and applied the maximum temperature we found in our temperature parameterization for values larger than $\log(\xi) = -2$. As an initial density and temperature structure of the discs, we took the results of Ercolano et al. (2008a, 2009), which were obtained from hydrostatic equilibrium models.

To avoid numerical issues in the low-density regions near the pole and at larger radii, we defined a logarithmic grid scaling in both directions. Being positive in the radial and negative in the polar direction, this leads to a finer grid close to the star. Another issue that needs to be considered is the outer boundary of the domain. Here, unwanted oscillations can occur (observed also in Picogna et al. 2019 and Nakatani et al. 2018a) and affect the inner disc regions and therefore the final results. To deal with this, we adopted an outer boundary inside the computational domain at 980 au, after which the gas was not evolved in time. Due to this sort of damping region, unrealistic oscillations and reflections could successfully be prevented.

All simulations described in the upcoming sections were run for 300–500 orbits at 10 au. In this context, a good compromise needs to be found for the total number of orbits: if too few orbits are performed, a steady-state value of $\dot{M}$ cannot be reached. As the disc is however continuously losing mass, a real equilibrium cannot be found and the mass-loss rate will change over time due to the disc's evolution. We therefore have to find a time span in which first of all, the change of the total disc mass M_{disc} is stable and not too rapid and secondly, the disc has not evolved significantly yet. Above a certain number of orbits, depending on the disc's properties (e.g., the mass), no steady state is established and M_{disc} will decrease rapidly due to the wind, resulting in a rapid change in the mass-loss rates.

2.2.2.1 Primordial Discs

With the purpose of investigating the effects of carbon abundance in various protoplanetary discs, we set up six types of primordial disc (i.e., full disc without a hole) simulations for four disc masses in a range between $M_{\mathrm{disc}} = 0.005\,M_*$ and $M_{\mathrm{disc}} = 0.1\,M_*$. Besides a solar metallicity simulation, these simulation types included three with a homogeneous carbon depletion by a factor of three, 10, and 100 throughout the whole disc and two additional inhomogeneous simulations where we assumed solar abundances within 15 au distance from the star and carbon depletion factors of three and 10, respectively, outside of this radius. No self-gravity was included in our models, but may play a role for the highest mass disc of our sample ($M_{\mathrm{disc}} = 0.1\,M_*$). The parameter space of all primordial disc simulations is shown in Table 2.2.

2.2.2.2 Transition Discs

Alongside the primordial discs, we also modelled several transition discs for different initial hole radii and corresponding to all primordial disc simulations. In

Table 2.2: Parameter space for the primordial disc simulations with PLUTO.

Variable	Value
Disc extent	
Radial (au)	0.33–1000, log spaced
Polar (rad)	0.005–$\pi/2$, log spaced
Grid resolution	
Radial	412
Polar	160
Physical properties	
$M_{\rm disc}$ (M_*)	$0.005, 0.01, 0.05, 0.1$
Luminosity $L_{\rm X}$ (erg s^{-1})	2×10^{30}
Luminosity $L_{\rm EUV}$	1.26 $L_{\rm X}$
Viscosity parameter α	0.001
Mean molecular weight μ	1.37125

this context, we chose a similar setup as before, increasing however the inner radial boundary, depending on the hole radius, and adjusted the number of radial grid cells in order to have the same resolution in the modelled region as for the primordial disc simulations. To set up a realistic cavity without an abrupt density change, we added an exponential decay of the density close to the defined gap radius. Again, we used the hydrostatic models of Ercolano et al. (2008a, 2009) as initial conditions.

Similar to Picogna et al. (2019) and Owen et al. (2010), we find that adiabatic cooling can be neglected in our calculations. We thus conclude that the gas should be in thermal equilibrium, which we prove in Appendix 2.C by directly comparing the advection and recombination timescales throughout the computational domain. Here we find that the advection timescale is significantly exceeding the timescale for the recombination processes. This result stands in contrast to Wang & Goodman (2017) who find adiabatic cooling to play an important role in the thermal balance of their models. There are however a number of important differences in the model setup and assumptions which may contribute to these discrepancies. This is discussed in more detail in Picogna et al. (2019).

2.2.3 Calculation of the mass-loss rates and $\dot{\Sigma}$ profiles

In order to derive the mass-loss rates and profiles $\dot{\Sigma}$, we adopted the approach used by Picogna et al. (2019), which is similar to the methods followed by Owen et al. (2010). In this context, we first remapped the grid onto a Cartesian grid of 4000×4000 and defined a radius in the disc from which we followed the streamlines of the gas to the base of the flow. Here, the location of the flow base is characterized by the local maximum of the derivative of the temperature profile at each cylindrical radius. We checked that this definition is consistent with the Bernoulli parameter.

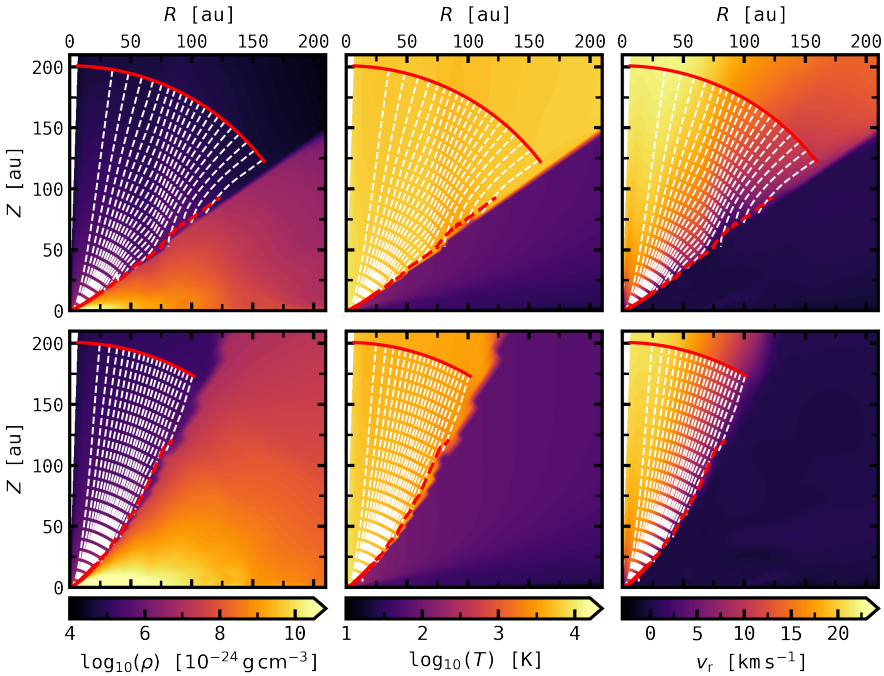

Figure 2.3: Disc structure for the lowest mass ($0.005\,M_*$, top panels) and highest mass ($0.1\,M_*$, bottom panels) primordial discs at the end of a simulation with carbon depletion by a factor of three. Depicted are the mass density (left panels), temperature (middle panels), and radial velocity (right panels). The wind streamlines are overlaid as white dashed lines at 5 % intervals of the integrated mass-loss rate. The radius of the streamlines calculation and sonic surface are plotted with solid and dashed red lines, respectively.

While the domain of our calculations extends to 1000 au, we chose to calculate mass-loss rates out to 200 au. The reasons for this choice are discussed in detail in Appendix 2.B. From the streamline calculations, we derived the mass loss as a function of the cylindrical radius and a value for the total mass-loss rate. We furthermore applied a fit

$$\dot{M}(R) = 10^{a\,\lg^6(R)+b\,\lg^5(R)+c\,\lg^4(R)+d\,\lg^3(R)+e\,\lg^2(R)+f\,\lg(R)+g} \tag{2.2}$$

for the mass-loss rates from which we were able to calculate the $\dot{\Sigma}$ profiles via

$$\dot{\Sigma} = \ln(10)\left(\frac{6a\ln^5(R)}{R\ln^6(10)} + \frac{5b\ln^4(R)}{R\ln^5(10)} + \frac{4c\ln^3(R)}{R\ln^4(10)} + \frac{3d\ln^2(R)}{R\ln^3(10)} + \frac{2e\ln(R)}{R\ln^2(10)} + \frac{f}{R\ln(10)}\right)\frac{\dot{M}(a,b,c,d,e,f,g,R)}{2\pi R}\,. \tag{2.3}$$

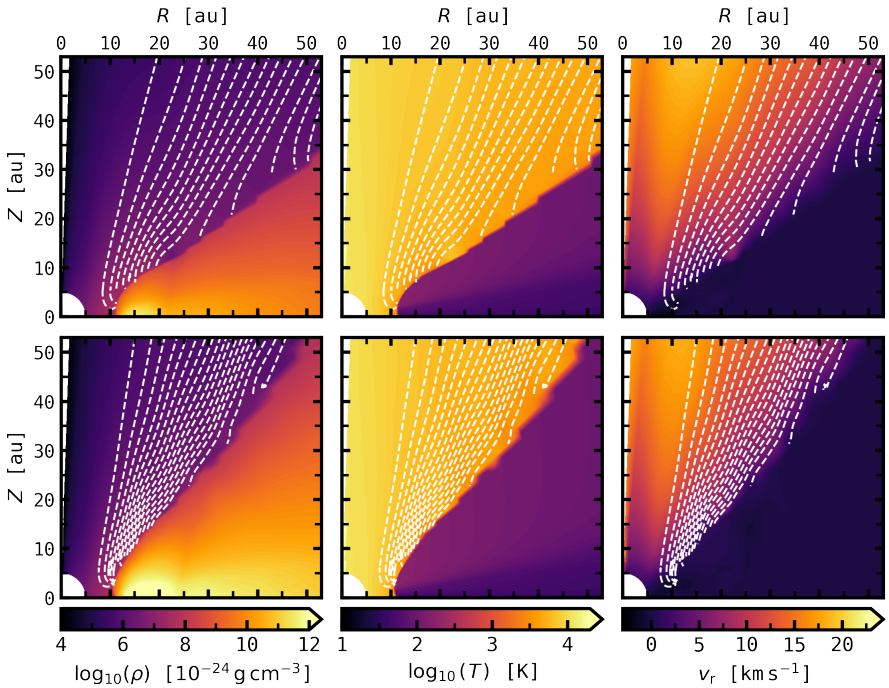

Figure 2.4: Disc structure for the lowest mass ($0.005\,M_*$, top panels) and highest mass ($0.1\,M_*$, bottom panels) transition discs (factor three depletion), displayed for a hole radius of $R_{\rm H} \approx 11\,$au. Depicted are the mass density (left panels), temperature (middle panels), and radial velocity (right panels). The wind streamlines are overlaid as white dashed lines at 5 % intervals of the integrated mass-loss rate.

2.3 Results

Figures 2.3 and 2.4 display examples of the density, temperature, and radial velocity structure of the primordial and transition discs, respectively. In each case, an example for the lowest mass disc of $0.005\,M_*$ (top panels) and the highest mass disc of $0.1\,M_*$ (bottom panels) is shown at the end of a simulation with carbon depletion by a factor of three. The transition discs in Fig. 2.4 have cavities with radius $R_{\rm H} \approx 11\,$au. Furthermore, we overlay the disc structure with the streamlines of the photoevaporative wind flow (white dashed lines), plotting a streamline for every interval of 5 % of the integrated mass loss. The radius of 200 au, from which the streamline calculation starts, is marked by a solid red line while the dashed red line indicates the sonic surface. For the primordial discs, we find that the streamlines mostly originate from a radius inside of 50 au, whereas the percentage of these lines drops with decreasing carbon abundance. In general, the fraction is comparable for the various disc masses but we still notice a slight drop in the percentage of streamlines inside of 50 au with decreasing mass as well.

In total, all primordial disc simulations behaved in a stable manner over the

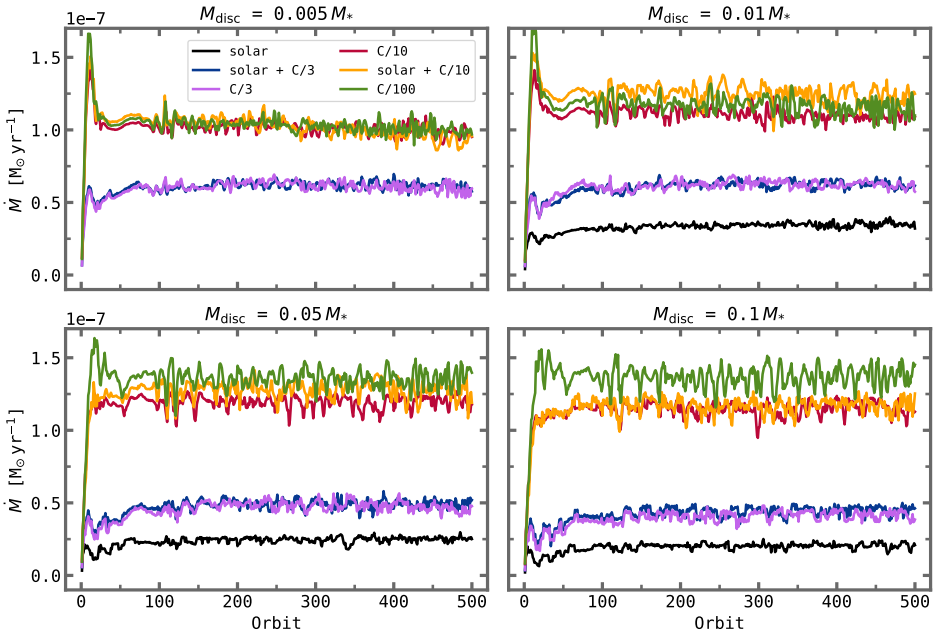

Figure 2.5: Mass-loss rate as a function of orbits for the different carbon depletion setups and disc masses. Shown are the results of the primordial disc simulations. Aside from a small scatter, the mass-loss rates behave stable after ≈ 100 orbits.

whole range of orbits after a small adjustment time. Quite in contrast to that, the transition disc simulations evolved relatively fast within a few hundred orbits, showing two sorts of behaviour: first, the inner hole radius moved outwards about $1-5$ au within 100 orbits (~ 3800 yr), depending on the disc mass, degree of depletion and initial hole radius, which indicates some sort of inside-out clearing. Secondly, for a disc mass of $0.005\,M_*$ (and partly $0.01\,M_*$), the disc quickly starts to thin out for depletion factors above three, whereby this effect is more pronounced for a larger initial cavity. Such a behaviour indicates some kind of rapid clearing of (lower mass) transition discs that are harbouring a very extended hole (see Sect. 2.3.4).

2.3.1 Mass-loss rates for the primordial disc simulations

The evolution of the mass-loss rate of the primordial disc models is presented in Fig. 2.5 for all five (six) simulations of each disc mass. First, it becomes clear that the mass-loss rate is, apart from a small scatter, relatively stable beyond 100 orbits. Moreover, the mass-loss rates of the homogeneously and the inhomogeneously depleted discs lie relatively close to each other, implying that the overall mass-loss is mostly dominated by the outer disc regions, with the solar abundances inside of 15 au causing no significant effect. We note however that despite the small mass-loss rate variation, the $\dot{\Sigma}$ profiles can be noticeably influenced by the different

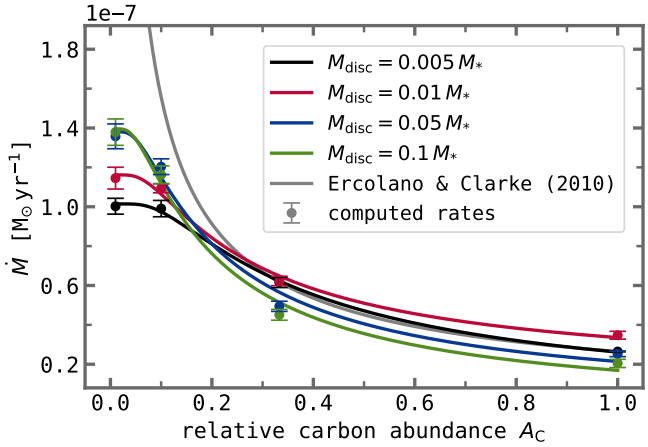

Figure 2.6: Mass-loss rate as a function of the relative carbon abundance A_C. Shown are the data and fits according to Eq. 2.4 for the four disc masses. The metallicity relation found by Ercolano & Clarke (2010) is included as a reference. In contrast, our relations predict a less extreme increase of the mass-loss rate with decreasing carbon abundance (metallicity).

depletion architectures and differ from each other significantly (see Sect. 2.3.3). As expected, the mass-loss rates increase with carbon depletion, the difference between the carbon depletion by a factor of 10 and 100 becomes more pronounced with higher disc mass.

In Fig. 2.6, we show the mass-loss rate as a function of the relative carbon abundance A_C (compared to the solar carbon abundance value) for all four disc masses. Here, the average mass-loss rates were calculated from the last 100 orbits, the solar abundance value for the lowest mass disc was adopted from Picogna et al. (2019). To fit the data, we applied the following relation

$$\dot{M}(A_C) = a \cdot e^{-\frac{b}{A_C}} + c, \tag{2.4}$$

finding

$$\dot{M}(A_C) = (-9.33 \times 10^{-8})\,\mathrm{M_\odot\,yr^{-1}} \cdot e^{-\frac{0.29}{A_C}} + (1.02 \times 10^{-7})\,\mathrm{M_\odot\,yr^{-1}} \tag{2.5}$$

for the $0.005\,M_*$ disc,

$$\dot{M}(A_C) = (-1.05 \times 10^{-7})\,\mathrm{M_\odot\,yr^{-1}} \cdot e^{-\frac{0.24}{A_C}} + (1.16 \times 10^{-7})\,\mathrm{M_\odot\,yr^{-1}} \tag{2.6}$$

for the $0.01\,M_*$ disc,

$$\dot{M}(A_C) = (-1.4 \times 10^{-7})\,\mathrm{M_\odot\,yr^{-1}} \cdot e^{-\frac{0.18}{A_C}} + (1.38 \times 10^{-7})\,\mathrm{M_\odot\,yr^{-1}} \tag{2.7}$$

for the $0.05\,M_*$ disc, and

$$\dot{M}(A_C) = (-1.45 \times 10^{-7})\,\mathrm{M_\odot\,yr^{-1}} \cdot e^{-\frac{0.17}{A_C}} + (1.4 \times 10^{-7})\,\mathrm{M_\odot\,yr^{-1}} \tag{2.8}$$

for the $0.1\,M_*$ disc. Besides these four relations, we also include the metallicity relation

$$\dot{M}_w \propto Z^{-0.77} \tag{2.9}$$

found by Ercolano & Clarke (2010) as a reference in Fig. 2.6. While there are fundamental differences between the approach used here and that of Ercolano & Clarke (2010), as also discussed below, a comparison is still interesting as previous work used this relation to investigate the effect of carbon depletion on transition disc populations (Ercolano et al. 2018). We show here that there are important differences, particularly at low values of carbon abundance, highlighting the need for further work on population syntheses of transition discs using our current results. In contrast to the relation by Ercolano & Clarke (2010), our simulations predict a flatter and somewhat saturating increase of the mass-loss rate with decreasing carbon abundance (metallicity). In Fig. 2.6, we only show the relation of Ercolano & Clarke (2010) for the lowest mass disc, using the mass-loss rate for solar metallicity found by Picogna et al. (2019) as $\dot{M}_0$. Comparing our new and the old relation for each disc mass individually, we find that the two curves follow (except for the disc mass of $0.01\,M_*$) a very similar slope down to a carbon abundance of 0.2–0.3 but differ significantly for smaller carbon abundances. The comparison of our model to the model of Ercolano & Clarke (2010) is mostly for illustrative purposes, as the two models have substantial differences. Rather than performing hydrodynamical calculations to extract mass-loss rates, Ercolano & Clarke (2010) performed thermal calculations and looked for a hydrostatic solution. The mass-loss rates were then calculated assuming that at each radius the surface mass-loss rate $\dot{\Sigma}$ is the product of the density and the sound speed at the base of the flow. The base of the flow at each radius was identified as the first height starting from the midplane, where the temperature of the gas becomes equal to the local escape temperature. This simplified method carries large uncertainties (see discussion in Owen et al. 2010). In contrast, this work performs detailed hydrodynamical calculations to extract the wind mass-loss rates and profiles. Furthermore, Ercolano & Clarke (2010) lowered the abundance of all elements by the same amount to investigate the metallicity dependency, since their work aimed at studying disc lifetimes in regions of lower metallicity (e.g., the extreme outer Galaxy) and their effect on planet formation. The goal of this work is different as we want to investigate the effects of the observationally determined gas-phase depletion of carbon in discs. Therefore, we only lower the abundance of carbon. It is thus not surprising that the resulting effect on the mass-loss rate is lower since the opacity suppression is not as high as in Ercolano & Clarke (2010).

Comparing the four disc masses, we notice a reversed behaviour, as the mass-loss rates are decreasing with disc mass for larger carbon abundances, but increasing with disc mass for smaller carbon abundances. Being comparable for the lower mass discs, a significant rise in the mass-loss rate from factor 10 to factor 100 carbon depletion can be distinguished for the higher mass discs. The reason behind the various effects connected to the disc mass is that depending on the carbon abundance, photoevaporation is efficient in distinct regions of the disc. While for high carbon abundances ($A_{\rm C} \gtrsim 0.3$) the total mass loss is mainly dominated by the inner disc, the disc becomes more transparent to X-ray radiation for lower carbon abundances, which can then drive a significant flow from the outer disc regions. Now two effects have to be considered: one is that radiation can penetrate radially further into a lower mass disc, whereas more mass can in principle be removed if

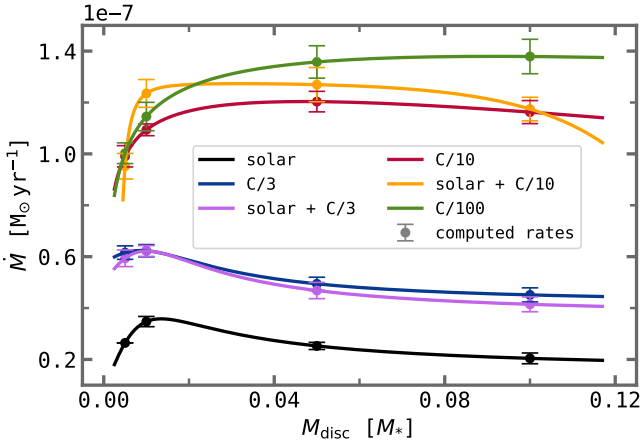

Figure 2.7: Mass-loss rate as a function of disc mass, shown for the six different carbon abundance cases. While for higher carbon abundances the mass loss is overall going down with disc mass, it increases when the carbon abundance is low.

a larger reservoir is hit. In this context, the low-mass disc experiences stronger winds when the depletion is moderate because the effect of reaching larger radii dominates over the effect of the larger mass content, which is anyway small near the star. For strong depletion however, the radiation can heat the large amount of mass present in the outer disc, which is why the radius of the layers reached by the radiation becomes less important. To conclude, we would like to note that even though clear variations can be distinguished between the four disc masses, these differences are in fact remarkably small, keeping in mind that the discs span a wide realistic mass range.

In Fig. 2.7, we display the dependency of the total mass-loss rate on the disc mass for each carbon abundance, applying the following ad-hoc functions

$$\dot{M}(M_{\rm disc}) = \frac{a + M_{\rm disc}}{b + c \cdot M_{\rm disc}^2} + d \tag{2.10}$$

for the higher carbon abundance and

$$\dot{M}(M_{\rm disc}) = a \cdot M_{\rm disc}^{(b \cdot M_{\rm disc}^c)} + d \tag{2.11}$$

for the lower carbon abundance cases. For no or moderate depletion (black, purple, and blue curve), the mass-loss rate is overall decreasing with increasing disc mass due to the fact that the radiation cannot reach the radially further disc layers. As the radiation can however hit a larger mass reservoir if more material is present, the mass-loss rate does not follow a steep, but rather flat slope after a short increase. If on the other hand, the carbon abundance is low (red, orange, and green curve), the mass-loss rate is in general increasing with disc mass. Similar to the high carbon abundance cases these curves are marked by a flat rise and are then slightly decreasing when the disc mass becomes too high for the radiation to penetrate far enough into the disc layers.

All average mass-loss rates for the primordial disc simulations, calculated from the last 100 orbits, are listed in Table 2.3. The corresponding uncertainties are calculated from the standard deviation.

Table 2.3: Average mass-loss rates of the primordial disc simulations calculated from the last 100 orbits.

Simulation	$\dot{M}$ ($M_\odot yr^{-1}$)
Disc mass 0.005 M_*	
Solar (Picogna et al. 2019)	2.644×10^{-8}
C/3	$(6.16 \pm 0.26) \times 10^{-8}$
Solar + C/3	$(5.94 \pm 0.32) \times 10^{-8}$
C/10	$(9.91 \pm 0.41) \times 10^{-8}$
Solar + C/10	$(9.52 \pm 0.50) \times 10^{-8}$
C/100	$(1.00 \pm 0.04) \times 10^{-7}$
Disc mass 0.01 M_*	
Solar	$(3.47 \pm 0.20) \times 10^{-8}$
C/3	$(6.23 \pm 0.24) \times 10^{-8}$
Solar + C/3	$(6.22 \pm 0.21) \times 10^{-8}$
C/10	$(1.09 \pm 0.02) \times 10^{-7}$
Solar + C/10	$(1.24 \pm 0.05) \times 10^{-7}$
C/100	$(1.14 \pm 0.06) \times 10^{-7}$
Disc mass 0.05 M_*	
Solar	$(2.53 \pm 0.14) \times 10^{-8}$
C/3	$(4.94 \pm 0.26) \times 10^{-8}$
Solar + C/3	$(4.68 \pm 0.32) \times 10^{-8}$
C/10	$(1.20 \pm 0.04) \times 10^{-7}$
Solar + C/10	$(1.27 \pm 0.07) \times 10^{-7}$
C/100	$(1.36 \pm 0.06) \times 10^{-7}$
Disc mass 0.1 M_*	
Solar	$(2.04 \pm 0.21) \times 10^{-8}$
C/3	$(4.51 \pm 0.28) \times 10^{-8}$
Solar + C/3	$(4.15 \pm 0.29) \times 10^{-8}$
C/10	$(1.16 \pm 0.04) \times 10^{-7}$
Solar + C/10	$(1.17 \pm 0.05) \times 10^{-7}$
C/100	$(1.38 \pm 0.07) \times 10^{-7}$

2.3.2 Hole radius dependency

As mentioned before, the transition discs evolved relatively fast during our simulations. It was therefore more challenging to find stable mass-loss rates, and thus profiles, because the full range of orbits could not be taken into account. We therefore decided to use a suitable range of 100 orbits (and not necessarily the last orbits), for which we calculated the average hole radius and mass-loss rate. In this context, we considered several factors in order to find the best possible time span. First, we tried to find a range for which the mass-loss rate was relatively stable. Furthermore, we checked if the evolution of the disc mass was moderate and not

too rapid in this range. In addition, we only chose orbits for which significant thinning of the disc had not begun yet. In general, it was easier to match these three conditions (simultaneously) for the higher mass disc simulations. In case of the larger depletions (factor 10 and 100) no stable mass-loss rates for hole radii above $R_{\rm H} \approx 25\,{\rm au}$ could be found for the $0.005\,M_*$ disc. Similarly, no stable mass-loss rates were established at these depletion factors for the $0.01\,M_*$ disc simulations above $R_{\rm H} \approx 35\,{\rm au}$. These discs evolved extremely fast and were (almost) completely dispersed during the simulation. We discuss the implications of this rapid disc dispersal in Sect. 2.3.4.

The transition disc simulations can be used to test the dependency of the photoevaporative mass-loss rate on the inner hole radius. The results of this parameter study are presented in Fig. 2.8 and Table 2.D.1 (see Appendix 2.D). In Fig. 2.8, we plot the mass-loss rate as a function of the hole radius (black dots) which we fit with the following relation

$$\dot{M}(R_{\rm H}) = \frac{a}{1 + \left(\frac{\dot{M}-b}{c}\right)^2} + d \tag{2.12}$$

(red solid lines). The primordial mass-loss rates (blue dots) are excluded from this fit but included in a second one (red dashed lines) for which we applied different functions. It is difficult to determine which curve would better match the mass-loss rate for small hole radii ($R_{\rm H} < 5\,{\rm au}$), as we do not have any hydrodynamical models for these transition discs. When a gap opens at very small disc radii, an inner disc is in general still present, shielding the outer disc from the star's direct radiation. By the time this inner disc is accreted, the hole will however have developed to larger radii. It is therefore not realistic to model a transition disc with a very small hole radius, as such a disc would still behave like a primordial one. Thus, it is probably more appropriate to treat transition discs and primordial discs independently from each other and use the fit for which the primordial mass-loss rate is excluded. In a follow-up paper, we will present a population synthesis model for which we will switch between our primordial and transition disc models, applying the fit for the hole radius dependency (red solid lines) down to $2-3\,{\rm au}$.

From Fig. 2.8, we notice a reversed (overall) trend similar to the one described in Sect. 2.3.1, as the mass-loss rate decreases with hole radius for no or moderate depletion and increases with hole radius for strong depletion. With increasing hole radius, the initial mass of the disc decreases as larger parts are cut compared to the primordial disc. For no or moderate depletion this means that more and more mass is removed from the disc regions where photoevaporation is effective, leading to weaker photoevaporative winds. For strong depletion on the other hand, the radiation can penetrate into disc regions that are not affected by the cut in the inner disc. Even though the disc mass is still lower for a larger hole radius in this case, the mass-loss rates increase with hole radius, as more disc layers and especially the midplane are irradiated directly. In principle, this effect of directly irradiated layers occurs as well for the moderate depletion, being however dominated by the opposite effect caused by the cut of the inner regions if the inner hole radius is large enough. Even though we can clearly identify the behaviour of

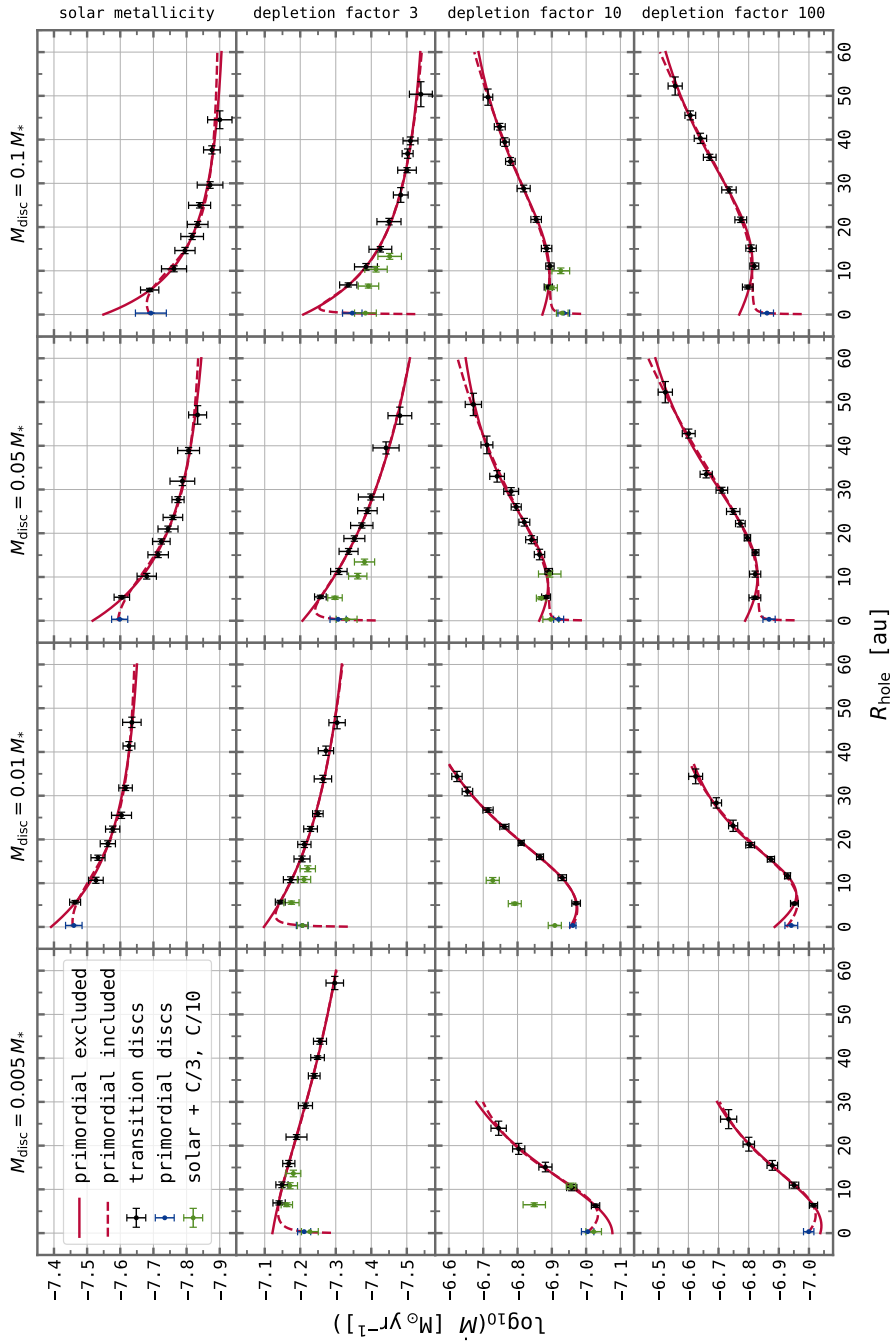

Figure 2.8: Mass-loss rate as a function of hole radius, shown for the different disc masses and carbon abundances. The black and blue dots are the mass-loss rates of the transition and primordial discs. The solid red lines display a fit for the transition discs only, the primordial disc simulations are taken into account in the fit shown by the red dashed lines. The green dots represent the inhomogeneously depleted discs.

the different curves, the absolute difference in the mass-loss rates for various hole radii is minimal.

The behaviour explained above and in Sect. 2.3.1 can indeed be seen when comparing the four disc masses for each carbon abundance case individually (along the rows). Again, we find that the mass-loss rate is decreasing with disc mass if the depletion is low. For higher depletions on the other hand, the mass-loss rate is smaller for the lower mass discs below a hole radius of $R_{\rm H} \approx 15\,$au, while it is higher for larger radii. Moreover, the slope of the curves becomes steeper with increasing disc mass when the depletion is low and flatter when the depletion is high.

Besides the data for the homogeneously depleted discs, we also include the mass-loss rates of the inhomogeneously depleted transition discs in Fig. 2.8 (green dots). For the carbon depletion by a factor of three, these values lie slightly below the ones for the homogeneously depleted discs but suggest a similar slope. In case of the carbon depletion by factor 10, the values lie very close to the ones for the homogeneously depleted discs for the two higher disc masses, but quite far off for the lower mass discs.

2.3.3 Mass-loss profiles $\dot{\Sigma}$

The resulting mass-loss profiles from our primordial disc models are displayed in Figs. 2.9, 2.10, and 2.E.1. In Fig. 2.9, we present the profiles of the four different (homogeneous) carbon abundance setups for all disc masses. It strikes out that the profiles in general extend further with increasing depletion, with the difference between the high and the low carbon abundances becoming more pronounced with increasing disc mass. Carbon-depleted discs are thus experiencing a significant mass loss at larger disc radii, which enables the formation of transition discs with large cavities that could still show an accretion signature. We will test the effect of our profiles on disc evolution in a follow-up population synthesis model.

As mentioned before, the total mass-loss rates of the homogeneously and inhomogeneously depleted discs are very similar, the corresponding profiles however show some substantial differences (compare examples in Fig. 2.10). While the inhomogeneously depleted discs experience a slightly enhanced mass loss in the inner and outer part of the disc compared to the homogeneously depleted disc, the mass loss is lower in the mid regions. In both cases, the profiles extend to a similarly large disc radius.

Figure 2.E.1 displays a comparison of the profiles of the four different disc masses for each carbon abundance individually. Here it becomes evident that for solar metallicity and moderate carbon depletion the profiles are clearly different: while the mass loss is similar for radii up to $\approx 50\,$au, the profiles extend to larger radii if the disc mass is low. In contrast to that, these differences disappear with decreasing carbon abundance, as the X-ray opacity becomes low, resulting in very similar, disc mass independent profiles.

Alongside the primordial mass-loss profiles, we show some examples of transition disc profiles in Fig. 2.E.2 for the lowest mass disc and in Fig. 2.E.3 for the highest mass disc. Regarding the solar metallicity, factor three depletion, and

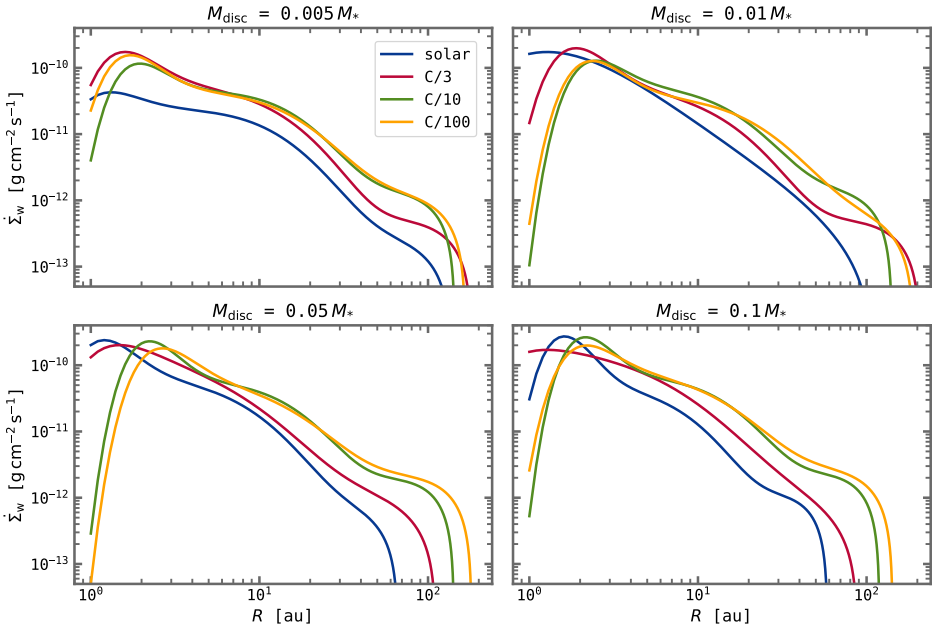

Figure 2.9: Mass-loss profiles $\dot{\Sigma}$ of the primordial discs, shown for the four different disc masses and homogeneous carbon abundances. With increasing depletion, the profiles extend to larger disc radii. The solar metallicity profile for the lowest mass disc is taken from Picogna et al. (2019).

inhomogeneously depleted discs, the overall shape of the profiles does not change for the transition discs compared to the primordial discs, with the peak however decreasing with increasing hole radius. Furthermore, some of the features are becoming more pronounced for the transition disc profiles. In principle, all profiles extend to a similar disc radius, which is however slightly below that for the primordial disc and increases slightly with hole radius, partly exceeding the profile for the primordial disc when the hole radius becomes very large. For the higher depletions (factor 10 and 100) on the other hand, the profiles extend to smaller radii when the hole radius increases (but increase again for very large hole radii), with this effect being more pronounced for a lower mass disc. One possible reason for this behaviour might be that the strong wind in the inner part of the disc, which occurs for large carbon depletion, shields the very outer part of the disc from the star's radiation. Therefore, the photoevaporative wind significantly drops in these disc regions. With increasing hole radius, the effect becomes stronger, and thus the profiles shallower, as the wind intensifies with more layers being hit directly by high-energy stellar radiation. Being marked by a weaker disc wind, the higher carbon abundance simulations do not show this behaviour.

Concerning the transition disc profiles, we note that the inner edge of the profiles should in principle be very sharp at the location of the hole radius, only beyond which the disc is present. As we applied a fit to our simulated data, which could

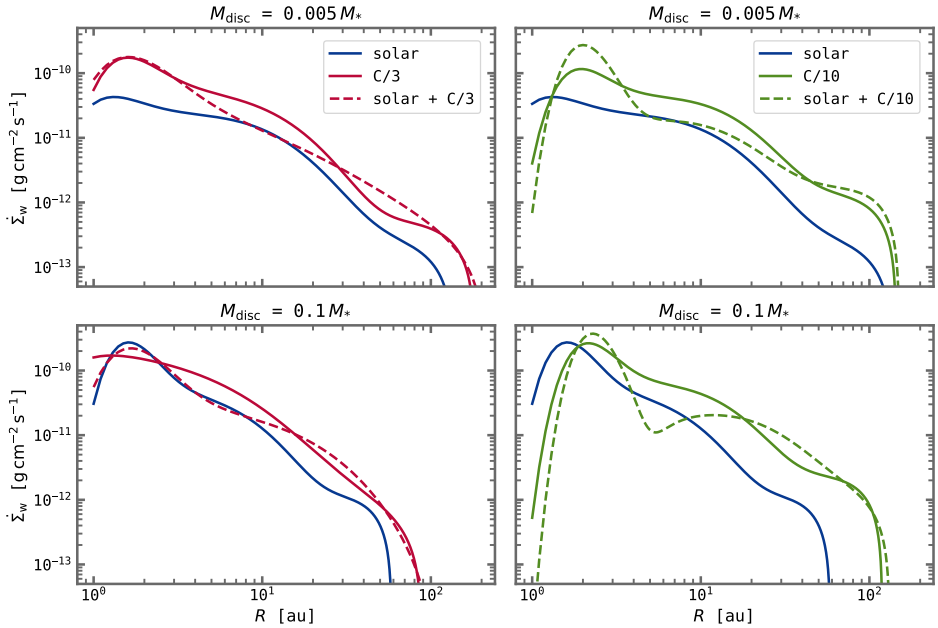

Figure 2.10: Mass-loss profiles $\dot{\Sigma}$ for the inhomogeneously depleted discs, shown for the lowest mass disc of 0.005 M_* (top plots) and the highest mass disc of 0.1 M_* (bottom plots). Compared to the homogeneously depleted discs, the mass loss is slightly higher close to and far from the star and lower in the mid disc regions. The solar metallicity profile for the lowest mass disc is taken from Picogna et al. (2019).

not account for such an abrupt cut, this feature is not represented in the depicted profiles. For the purpose of this work and the following population synthesis this treatment is sufficient and does not influence the results. If however applied to other problems, a cut of the profile at the hole radius should be considered.

2.3.4 Rapid disc dispersal of carbon-depleted discs

As mentioned in Sect. 2.3.2, some of the lower mass transition discs are evolving extremely fast in the course of our simulations if the depletion is high and the hole radius is relatively large. In Fig. 2.11, we show an example for such a low-mass disc (0.005 M_*), depleted in carbon by a factor of 10 and harbouring a cavity with an initial hole radius of $R_{\rm H} \approx 30$ au. Here, the disc is quickly moving outwards, thinning out rapidly, and completely dispersed after about 500 orbits ($\approx 19\,000$ yr). This represents the final stages of photoevaporation that can be observed directly in the course of the simulations for carbon-depleted lower mass discs. Due to deeply penetrating X-rays (causing strong mass-loss rates), a metal-depleted disc can thus experience a very rapid clearing of the order of 10^4 yr, which inhibits any further planet formation in the disc and could furthermore prevent the formation of so-called relic discs. Relic discs are non-accreting transition discs, harbouring

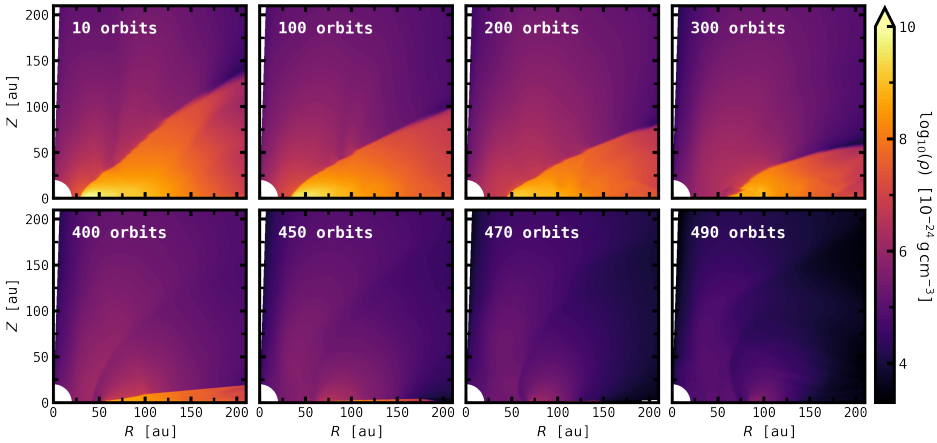

Figure 2.11: Rapid disc clearing of a low-mass transition disc (0.005 M_*) with an initial hole radius of $R_{\rm H} \approx 30$ au and a carbon depletion by a factor of 10. The disc is fully dispersed within 500 orbits, corresponding to $\approx 19\,000$ yr.

large holes, that are frequently predicted by current photoevaporation models, but not generally observed, thus representing one of the main open questions for these models. A full investigation of the impact of this rapid dispersal of (low-mass) carbon-depleted discs is beyond the scope of this paper but will be part of a forthcoming work on the demographics of transition discs.

2.4 Conclusions

For this work, we performed radiation-hydrodynamical simulations of X-EUV-driven photoevaporation in different solar metallicity and carbon-depleted primordial and transition discs. We probed different carbon depletion factors (three, 10, and 100), disc masses between 0.005 and 0.1 M_* as well as varying inner holes between 5 and 60 au. Our models significantly improve on the previous hydrostatic models of Ercolano et al. (2018) by performing hydrodynamical calculations with new temperature prescriptions, based on tailored photoionization and thermal calculations. The main results of our analysis are summarized in the following.

Our new approach yields that carbon depletion results in higher gas temperatures compared to solar abundances, with the temperature increasing with the degree of depletion (see Fig. 2.2). From the hydrodynamical simulations, we determined new reliable total mass-loss rates of order 10^{-8} to $10^{-7}\,{\rm M}_\odot\,{\rm yr}^{-1}$ (compare Tables 2.3 and 2.D.1) and find that the total mass-loss rate is about two to six times higher for carbon-depleted discs compared to solar metallicity discs (depending on the depletion and the disc mass). The mass loss in our calculations is dominated by the X-ray radiation. Even though we also included EUV in the irradiating spectrum, its contribution is negligible, as the EUV is already absorbed in small column densities and does not reach the high-density regions. FUV radiation is not

included in our analysis. As FUV could in principle drive a significant mass loss in the outer parts of the disc, our results for the mass-loss rates represent a lower limit. Other authors like Gorti & Hollenbach (2009) or Nakatani et al. (2018b) suggest that the effects of X-ray photoevaporation are minimal compared to FUV photoevaporation, thus a quantitative comparison of X-ray and FUV heating in low-metallicity discs is needed but outside the scope of this paper.

For each disc mass, we find improved relations for the dependency of the total mass-loss rate on the carbon abundance, which predict a less extreme increase of the photoevaporative mass loss with decreasing carbon abundance than the relation found by Ercolano & Clarke (2010) (see Fig. 2.6) for the dependency of the mass loss on the metallicity. These relations turn out to be weakly dependent on the disc mass. Moreover, we obtain scalings for the dependency of the total mass-loss rate on the disc mass for each carbon abundance setup, showing a reversed behaviour depending on the degree of depletion (see Fig. 2.7). In this context, we identify different effects to be responsible for the opposite trends.

Similar to the reversed behaviour of the disc mass dependencies we find opposing trends for the dependency of the total mass-loss rate on the hole radius, resulting from the fact that photoevaporation is effective in different disc regions for different carbon abundances and that a cut in the inner part of the disc is either affecting these regions or not (see Fig. 2.8). Comparing the mass-loss rates for the homogeneously and inhomogeneously depleted discs, we find that the values are in principle very similar, including however some outliers in the case of the carbon depletion by a factor of 10 and the two lower disc masses. The according inhomogeneously depleted disc simulations behaved less stable than the other simulations. Further tests (e.g., with higher resolution) could show if the mass-loss rates are resulting from numerical effects or if transition discs with solar abundances inside of 15 au and strong carbon depletion outside of 15 au are indeed experiencing an enhanced photoevaporative mass-loss due to the disc being less stable.

In our analysis, we derived reasonable mass-loss profiles $\dot{\Sigma}$ for all simulated primordial and transition discs (compare Figs. 2.9 to 2.E.3). From the primordial disc profiles, we can indeed conclude that the influence of X-ray photoevaporation is extended in carbon-depleted discs, as the profiles extend to larger disc radii with increasing degree of depletion (Fig. 2.9). In this context, the differences of the curves become more pronounced for higher disc masses, with the profiles for no or moderate depletion being clearly disc mass dependant while the profiles for higher depletions turn out to be very similar (Fig. 2.E.1). Interestingly, even though the total mass loss is comparable for the homogenously and inhomogeneously depleted discs, it is generated from different regions in the disc (Fig. 2.10). While the corresponding $\dot{\Sigma}$ profiles extend to similar radii in both cases, the mass loss is slightly enhanced close to the star and at larger disc radii and significantly lower for mid disc regions if the disc is depleted inhomogeneously.

Some of our lower mass transition discs are marked by a rapid disc dispersal, proceeding on a timescale of the order of 10^4 yrs (compare Fig. 2.11). This potentially helps to prevent the formation of relic discs in a population synthesis model and will be studied in more detail in a follow-up paper.

The models presented here represent a detailed study of X-ray-driven pho-

toevaporation in carbon-depleted discs and lay the foundation for a number of future investigations. Implementing the mass-loss profiles together with the total mass-loss rates into a population synthesis code could reveal the demographics of transition discs and show if carbon depletion can account for the majority of the observed diversity of transition discs and especially those discs that appear with large cavities and simultaneously strong accretion onto the central star. As we find a significant mass-loss at larger disc radii (up to $\approx 200\,\mathrm{au}$), we expect the formation of large cavities and even multiple holes, which we will test in a follow-up work.

Acknowledgements

We thank the anonymous referee for his/her detailed review, which significantly helped to improve this paper. We acknowledge the support from the DFG Research Unit 'Planet Formation Witnesses and Probes: Transition Discs' (FOR 2634/1, ER 685/8-1, and ER 685/11-1). This work was performed partly on the computing facilities of the Computational Center for Particle and Astrophysics (C2PAP) and partly on the HPC system DRACO of the Max Planck Computing and & Data Facility (MPCDF).

Appendix

2.A Temperature error

Using only a single-slab parameterization for the column density, the models of Owen et al. (2010, 2011, 2012) can result in errors for the temperature of the order of 30 %. As shown in Fig. 2.A.1 for carbon depletion by a factor of three and 100, respectively, this error is significantly reduced within our models. Even though the relative error slightly increases with the degree of depletion, it is always less than 1 % for the whole computational domain in all simulations. The error was calculated by comparing the temperature coming directly from PLUTO to the temperature that is found from post-processing the steady-state from the PLUTO simulations in MOCASSIN.

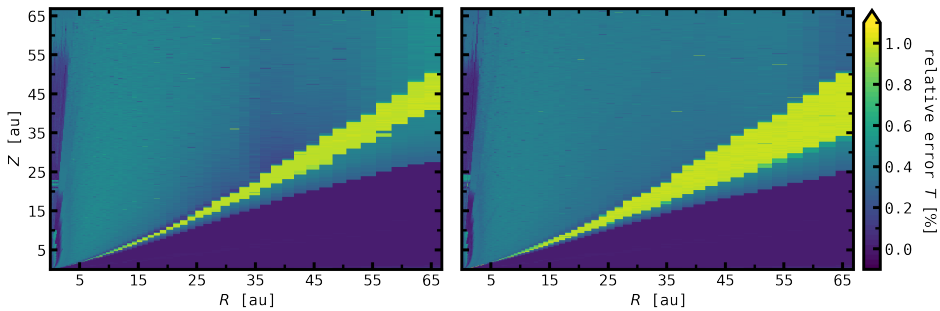

Figure 2.A.1: Relative error of the temperature determined in PLUTO with respect to the one post-processed with MOCASSIN after a steady-state was reached in PLUTO. Shown are examples for the carbon depletion by a factor of three (top panel) and 100 (bottom panel) for the lowest mass disc of $M_{\rm disc} = 0.005\,M_*$.

2.B Choice of the (internal) disc radius of the streamlines calculation

While the outer radius of the computational domain is fixed at 1000 au, the choice of the disc radius from which the streamlines are calculated is crucial for the distinction between the material that is actually removed from the disc and the material that is just redistributed within the disc. In this context, we tested different (internal) radii ranging from 100 to 800 au for the primordial, low-mass disc simulations ($M_{\rm disc} \approx 0.005\,M_*$). The result of this test is shown in Fig. 2.B.1 for carbon depletion by a factor of three with the overall behaviour being representative for all simulations. From the plot, we note that the lowest mass-loss rate is adjusted for the smallest radius of 100 au, while the value is in general decreasing with increasing internal disc radius. The small value of the 100 au radius, contradicting the overall trend, indicates that in this case important regions where

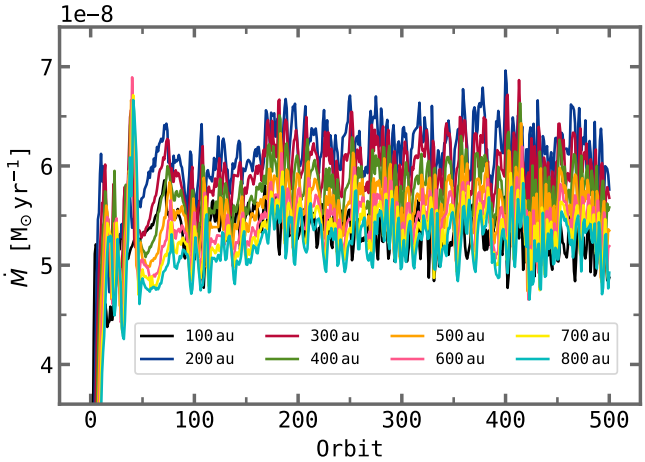

Figure 2.B.1: Mass-loss rate as a function of orbits, shown for internal disc radii between 100 and 800 au and the carbon depletion by a factor of three simulation of the 0.005 M_* disc. The mass-loss rate is overall decreasing with increasing radius.

photoevaporation was effective were cut out. The decrease in the mass-loss rate for larger radii is caused by the effect that some of the gas streamlines fall back below the sonic surface at larger disc radii. However, we cannot fully trust those streamlines at large radii ($r > 200$ au) because the number of orbits they went through is limited and possibly they have not yet reached a stable state. Despite the variations, the mass-loss rate is comparable for all (internal) disc radii, possibly making them all suitable for the further calculations. Nevertheless, we decided to choose a radius of 200 au, which yields the highest mass-loss rate. By doing so, we maximize the number of orbits at the given location, which is important for the streamlines stability, avoiding at the same time cutting too much of the outer disc regions. Moreover, we thus exclude the outermost regions that are possibly affected by the numerical oscillations and reflections from the outer boundary, which we described in Sect. 2.2.2.

Even though a radius of 200 au provides a good compromise for the purpose of this work, it would in principle be favourable to extend the hydrodynamical simulations in order to increase the number of orbits also for larger disc radii. As mentioned above, we found that some streamlines in the beginning leave the disc but later fall back onto it. If the chosen radius is too small in these cases, streamlines, which are truly not contributing to the photoevaporative wind flow that leaves the disc, could be included in the mass-loss calculations. Performing additional hydrodynamical simulations could help to test the significance of this effect and yield detailed information about the influence of the different disc radii on the mass-loss rates and $\dot{\Sigma}$ profiles.

2.C Test for radiative equilibrium

The approach we followed in this analysis is based on the assumption that the disc is in radiative equilibrium. This means that microphyiscal processes, which affect the temperature equilibrium, occur on timescales shorter than the hydrodynamical

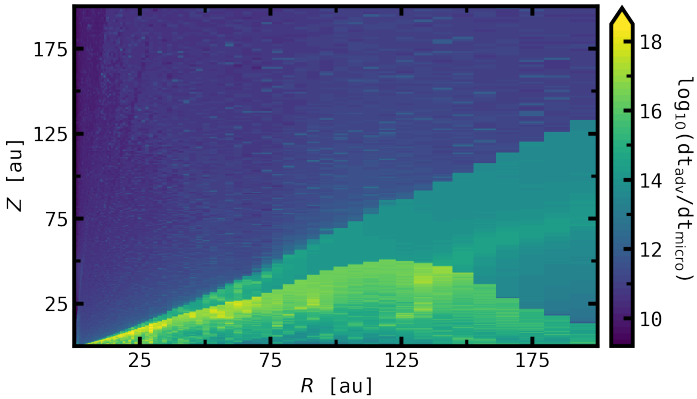

Figure 2.C.1: Advection timescale $\tau_{\rm adv}$ divided by the microphysical recombination timescale $\tau_{\rm rec}$ in order to test for radiative equilibrium. Displayed is the test for the carbon depletion by a factor of three setup. The fraction is significantly larger than one for the whole computational domain.

timescale. The most important microphysical process is hydrogen recombination, which proceeds on the longest timescale (Ferland 1979; Salz et al. 2015)

$$\tau_{\rm rec} = \frac{1}{\alpha_{\rm A}(T_{\rm e})n_{\rm e}} \simeq 1.5 \times 10^9\,{\rm s} \cdot \left(\frac{T_{\rm e}}{1\,{\rm K}}\right)^{0.8} \cdot \left(\frac{n_{\rm e}}{{\rm ptcls/cm^3}}\right)^{-1}, \tag{2.13}$$

with $T_{\rm e}$ as the electron temperature, $n_{\rm e}$ as the electron density, and $\alpha_{\rm A}(T_{\rm e})$ as the temperature-dependent recombination rate. In order to check whether the hydrodynamical timescale is greater than this recombination timescale, we compared $\tau_{\rm rec}$ to the advection timescale $\tau_{\rm adv}$ for the regions that are important for the wind dynamics. The result of this test is presented in Fig. 2.C.1, where we plot the ratio of the advection and radiation timescale for the carbon depletion by a factor of three setup. In order to compute the advection timescale, we have used the expression $\mathrm{d}x/v_{\rm gas}$ for each grid cell, which corresponds to the time a gas parcel takes to cross a grid cell. Figure 2.C.1 shows that our assumption of radiative equilibrium is valid in the whole computational domain, as the hydrodynamical advection timescale is several orders of magnitude larger than the microphysical recombination timescale. Only very close to the Z-axis there is a region that shows a smaller value of the fraction, although still considerably above one. We performed this test for all carbon depletion setups, which yielded similar results as shown in Fig. 2.C.1.

2.D Mass-loss rates of the transition disc simulations

Table 2.D.1: Average mass-loss rates and hole radii of the transition disc simulations.

	Disc mass 0.005 M_*		Disc mass 0.01 M_*		Disc mass 0.05 M_*		Disc mass 0.1 M_*	
	$R_{\rm H}$ (au)	$\dot{M}$ ($M_\odot\ yr^{-1}$)	$R_{\rm H}$ (au)	$\dot{M}$ ($M_\odot\ yr^{-1}$)	$R_{\rm H}$ (au)	$\dot{M}$ ($M_\odot\ yr^{-1}$)	$R_{\rm H}$ (au)	$\dot{M}$ ($M_\odot\ yr^{-1}$)
Solar			5.7 ± 0.4	$(3.44 \pm 0.13) \times 10^{-8}$	5.4 ± 0.4	$(2.49 \pm 0.17) \times 10^{-8}$	5.6 ± 0.4	$(2.05 \pm 0.13) \times 10^{-8}$
	/	/	10.7 ± 0.7	$(2.98 \pm 0.15) \times 10^{-8}$	10.2 ± 0.7	$(2.10 \pm 0.14) \times 10^{-8}$	10.5 ± 0.7	$(1.74 \pm 0.15) \times 10^{-8}$
	/	/	15.8 ± 0.6	$(2.94 \pm 0.14) \times 10^{-8}$	15.1 ± 0.6	$(1.94 \pm 0.14) \times 10^{-8}$	14.6 ± 0.7	$(1.61 \pm 0.11) \times 10^{-8}$
	/	/	19.0 ± 0.7	$(2.74 \pm 0.14) \times 10^{-8}$	18.1 ± 0.6	$(1.89 \pm 0.11) \times 10^{-8}$	17.8 ± 0.7	$(1.53 \pm 0.11) \times 10^{-8}$
	/	/	22.4 ± 0.7	$(2.65 \pm 0.13) \times 10^{-8}$	21.0 ± 0.7	$(1.81 \pm 0.12) \times 10^{-8}$	20.6 ± 0.7	$(1.47 \pm 0.10) \times 10^{-8}$
	/	/	25.5 ± 0.7	$(2.50 \pm 0.17) \times 10^{-8}$	23.6 ± 0.5	$(1.75 \pm 0.12) \times 10^{-8}$	25.0 ± 0.6	$(1.45 \pm 0.11) \times 10^{-8}$
	/	/	/	/	27.7 ± 0.7	$(1.68 \pm 0.07) \times 10^{-8}$	/	/
	/	/	31.8 ± 0.6	$(2.42 \pm 0.11) \times 10^{-8}$	31.9 ± 0.6	$(1.64 \pm 0.14) \times 10^{-8}$	29.6 ± 0.8	$(1.35 \pm 0.12) \times 10^{-8}$
	/	/	41.4 ± 1.0	$(2.37 \pm 0.10) \times 10^{-8}$	38.9 ± 0.7	$(1.57 \pm 0.12) \times 10^{-8}$	37.7 ± 0.9	$(1.33 \pm 0.07) \times 10^{-8}$
	/	/	46.8 ± 1.2	$(2.32 \pm 0.15) \times 10^{-8}$	47.1 ± 2.1	$(1.47 \pm 0.09) \times 10^{-8}$	44.5 ± 2.0	$(1.26 \pm 0.11) \times 10^{-8}$
C/3	6.9 ± 0.5	$(7.24 \pm 0.28) \times 10^{-8}$	5.7 ± 0.4	$(7.19 \pm 0.23) \times 10^{-8}$	5.5 ± 0.4	$(5.54 \pm 0.21) \times 10^{-8}$	6.8 ± 0.5	$(4.63 \pm 0.26) \times 10^{-8}$
	11.0 ± 0.7	$(7.11 \pm 0.29) \times 10^{-8}$	10.8 ± 0.7	$(6.72 \pm 0.32) \times 10^{-8}$	11.3 ± 0.7	$(4.92 \pm 0.26) \times 10^{-8}$	10.9 ± 0.8	$(4.13 \pm 0.30) \times 10^{-8}$
	15.9 ± 0.7	$(6.80 \pm 0.27) \times 10^{-8}$	15.5 ± 0.7	$(6.25 \pm 0.33) \times 10^{-8}$	15.9 ± 0.7	$(4.62 \pm 0.28) \times 10^{-8}$	14.9 ± 0.6	$(3.76 \pm 0.27) \times 10^{-8}$
	/	/	18.9 ± 0.7	$(6.15 \pm 0.26) \times 10^{-8}$	18.8 ± 0.6	$(4.45 \pm 0.30) \times 10^{-8}$	/	/
	22.0 ± 0.6	$(6.48 \pm 0.44) \times 10^{-8}$	22.4 ± 0.6	$(5.91 \pm 0.27) \times 10^{-8}$	21.8 ± 0.6	$(4.25 \pm 0.30) \times 10^{-8}$	21.2 ± 0.8	$(3.56 \pm 0.27) \times 10^{-8}$
	/	/	25.9 ± 0.6	$(5.63 \pm 0.19) \times 10^{-8}$	25.2 ± 0.6	$(4.09 \pm 0.25) \times 10^{-8}$	/	/
	29.1 ± 0.6	$(6.11 \pm 0.28) \times 10^{-8}$	/	/	28.3 ± 0.7	$(4.00 \pm 0.32) \times 10^{-8}$	27.3 ± 1.7	$(3.29 \pm 0.15) \times 10^{-8}$
	35.9 ± 0.5	$(5.77 \pm 0.18) \times 10^{-8}$	33.8 ± 0.8	$(5.46 \pm 0.31) \times 10^{-8}$	/	/	33.0 ± 0.6	$(3.16 \pm 0.18) \times 10^{-8}$
	/	/	/	/	/	/	36.8 ± 1.1	$(3.15 \pm 0.11) \times 10^{-8}$
	40.1 ± 0.4	$(5.65 \pm 0.25) \times 10^{-8}$	40.3 ± 1.1	$(5.35 \pm 0.26) \times 10^{-8}$	39.5 ± 1.4	$(3.63 \pm 0.31) \times 10^{-8}$	39.7 ± 1.1	$(3.09 \pm 0.15) \times 10^{-8}$
	43.9 ± 0.7	$(5.56 \pm 0.23) \times 10^{-8}$	46.7 ± 1.4	$(4.98 \pm 0.26) \times 10^{-8}$	46.9 ± 2.0	$(3.32 \pm 0.27) \times 10^{-8}$	50.4 ± 2.9	$(2.89 \pm 0.21) \times 10^{-8}$
	57.2 ± 1.5	$(5.05 \pm 0.29) \times 10^{-8}$	/	/	/	/	/	/
Solar + C/3	6.5 ± 0.4	$(6.89 \pm 0.25) \times 10^{-8}$	5.5 ± 0.4	$(6.69 \pm 0.33) \times 10^{-8}$	5.2 ± 0.4	$(5.04 \pm 0.23) \times 10^{-8}$	6.5 ± 0.5	$(4.06 \pm 0.27) \times 10^{-8}$
	10.8 ± 0.7	$(6.75 \pm 0.33) \times 10^{-8}$	10.8 ± 0.7	$(6.16 \pm 0.27) \times 10^{-8}$	10.2 ± 0.6	$(4.35 \pm 0.26) \times 10^{-8}$	10.4 ± 0.6	$(3.87 \pm 0.28) \times 10^{-8}$
	13.6 ± 0.8	$(6.61 \pm 0.33) \times 10^{-8}$	13.3 ± 0.7	$(6.02 \pm 0.30) \times 10^{-8}$	13.4 ± 0.7	$(4.17 \pm 0.27) \times 10^{-8}$	13.3 ± 0.7	$(3.54 \pm 0.27) \times 10^{-8}$

Table 2.D.1 continued.

	Disc mass 0.005 M_*		Disc mass 0.01 M_*		Disc mass 0.05 M_*		Disc mass 0.1 M_*	
	$R_{\rm H}$ (au)	$\dot{M}$ ($M_\odot\, yr^{-1}$)	$R_{\rm H}$ (au)	$\dot{M}$ ($M_\odot\, yr^{-1}$)	$R_{\rm H}$ (au)	$\dot{M}$ ($M_\odot\, yr^{-1}$)	$R_{\rm H}$ (au)	$\dot{M}$ ($M_\odot\, yr^{-1}$)
C/10	6.3 ± 0.4	$(9.39 \pm 0.26) \times 10^{-8}$	5.4 ± 0.3	$(1.07 \pm 0.03) \times 10^{-7}$	5.4 ± 0.3	$(1.31 \pm 0.04) \times 10^{-7}$	6.3 ± 0.4	$(1.29 \pm 0.04) \times 10^{-7}$
	10.4 ± 0.7	$(1.10 \pm 0.04) \times 10^{-7}$	11.3 ± 0.7	$(1.17 \pm 0.03) \times 10^{-7}$	11.3 ± 0.7	$(1.29 \pm 0.03) \times 10^{-7}$	11.1 ± 0.7	$(1.28 \pm 0.04) \times 10^{-7}$
	15.1 ± 1.1	$(1.32 \pm 0.06) \times 10^{-7}$	16.0 ± 0.6	$(1.36 \pm 0.03) \times 10^{-7}$	15.1 ± 0.7	$(1.37 \pm 0.05) \times 10^{-7}$	15.1 ± 0.7	$(1.30 \pm 0.04) \times 10^{-7}$
	19.3 ± 1.3	$(1.57 \pm 0.07) \times 10^{-7}$	19.2 ± 0.5	$(1.55 \pm 0.03) \times 10^{-7}$	18.5 ± 0.6	$(1.44 \pm 0.06) \times 10^{-7}$	/	/
	/	/	22.9 ± 0.5	$(1.73 \pm 0.05) \times 10^{-7}$	22.5 ± 0.5	$(1.52 \pm 0.05) \times 10^{-7}$	21.7 ± 0.6	$(1.40 \pm 0.05) \times 10^{-7}$
	24.0 ± 1.6	$(1.80 \pm 0.09) \times 10^{-7}$	26.7 ± 0.5	$(1.93 \pm 0.07) \times 10^{-7}$	26.0 ± 0.6	$(1.60 \pm 0.05) \times 10^{-7}$	/	/
	/	/	31.0 ± 1.0	$(2.22 \pm 0.08) \times 10^{-7}$	29.6 ± 0.5	$(1.66 \pm 0.08) \times 10^{-7}$	28.8 ± 0.8	$(1.52 \pm 0.07) \times 10^{-7}$
	/	/	34.4 ± 1.2	$(2.38 \pm 0.08) \times 10^{-7}$	33.0 ± 0.8	$(1.82 \pm 0.09) \times 10^{-7}$	35.0 ± 0.9	$(1.67 \pm 0.05) \times 10^{-7}$
	/	/	/	/	40.2 ± 0.7	$(1.95 \pm 0.08) \times 10^{-7}$	39.4 ± 1.0	$(1.73 \pm 0.05) \times 10^{-7}$
	/	/	/	/	/	/	42.9 ± 0.8	$(1.79 \pm 0.07) \times 10^{-7}$
	/	/	/	/	49.5 ± 2.3	$(2.14 \pm 0.22) \times 10^{-7}$	49.7 ± 1.9	$(1.93 \pm 0.06) \times 10^{-7}$
Solar	6.5 ± 0.4	$(1.42 \pm 0.10) \times 10^{-7}$	5.3 ± 0.3	$(1.62 \pm 0.07) \times 10^{-7}$	5.2 ± 0.3	$(1.35 \pm 0.04) \times 10^{-7}$	6.1 ± 0.4	$(1.26 \pm 0.05) \times 10^{-7}$
+ C/10	10.7 ± 0.7	$(1.11 \pm 0.03) \times 10^{-7}$	10.6 ± 0.7	$(1.87 \pm 0.08) \times 10^{-7}$	10.7 ± 0.7	$(1.28 \pm 0.10) \times 10^{-7}$	10.0 ± 0.6	$(1.19 \pm 0.07) \times 10^{-7}$
C/100	6.4 ± 0.4	$(9.66 \pm 0.30) \times 10^{-8}$	5.3 ± 0.3	$(1.12 \pm 0.03) \times 10^{-7}$	5.2 ± 0.4	$(1.51 \pm 0.07) \times 10^{-7}$	6.3 ± 0.4	$(1.60 \pm 0.06) \times 10^{-7}$
	11.0 ± 0.7	$(1.12 \pm 0.04) \times 10^{-7}$	11.7 ± 0.7	$(1.18 \pm 0.03) \times 10^{-7}$	10.7 ± 0.7	$(1.51 \pm 0.06) \times 10^{-7}$	11.1 ± 0.7	$(1.52 \pm 0.05) \times 10^{-7}$
	15.5 ± 1.1	$(1.32 \pm 0.05) \times 10^{-7}$	15.5 ± 0.6	$(1.34 \pm 0.04) \times 10^{-7}$	15.6 ± 0.6	$(1.50 \pm 0.04) \times 10^{-7}$	15.2 ± 0.8	$(1.56 \pm 0.06) \times 10^{-7}$
	20.3 ± 1.6	$(1.59 \pm 0.07) \times 10^{-7}$	18.7 ± 0.6	$(1.57 \pm 0.05) \times 10^{-7}$	19.0 ± 0.7	$(1.60 \pm 0.04) \times 10^{-7}$	21.7 ± 0.6	$(1.69 \pm 0.07) \times 10^{-7}$
	/	/	23.1 ± 1.3	$(1.79 \pm 0.06) \times 10^{-7}$	22.2 ± 0.8	$(1.69 \pm 0.06) \times 10^{-7}$	/	/
	26.1 ± 2.2	$(1.85 \pm 0.12) \times 10^{-7}$	/	/	25.0 ± 0.7	$(1.79 \pm 0.09) \times 10^{-7}$	/	/
	/	/	28.4 ± 1.2	$(2.03 \pm 0.08) \times 10^{-7}$	29.8 ± 0.7	$(1.95 \pm 0.09) \times 10^{-7}$	28.5 ± 0.7	$(1.85 \pm 0.10) \times 10^{-7}$
	/	/	34.4 ± 1.7	$(2.38 \pm 0.13) \times 10^{-7}$	33.5 ± 0.8	$(2.19 \pm 0.10) \times 10^{-7}$	35.9 ± 0.7	$(2.14 \pm 0.10) \times 10^{-7}$
	/	/	/	/	42.8 ± 1.0	$(2.51 \pm 0.12) \times 10^{-7}$	40.3 ± 1.2	$(2.29 \pm 0.11) \times 10^{-7}$
	/	/	/	/	/	/	45.5 ± 1.0	$(2.48 \pm 0.10) \times 10^{-7}$
	/	/	/	/	52.3 ± 2.4	$(3.00 \pm 0.16) \times 10^{-7}$	52.2 ± 2.1	$(2.78 \pm 0.15) \times 10^{-7}$

2.E Additional $\dot{\Sigma}$ profiles

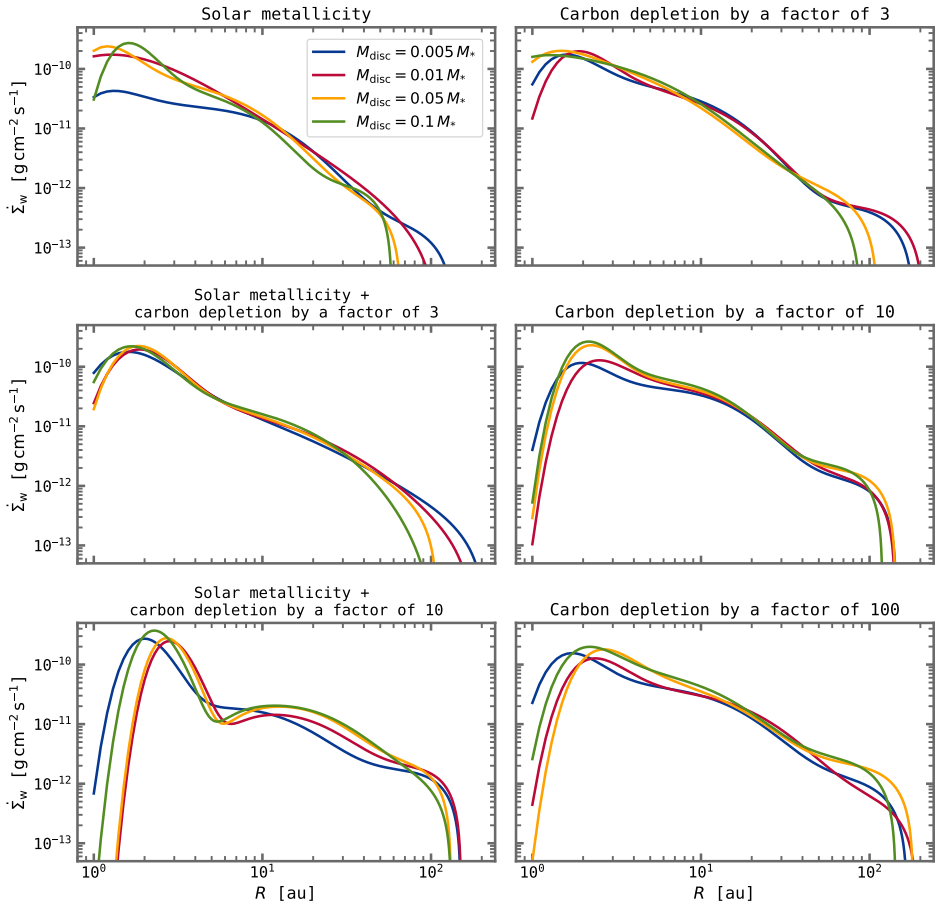

Figure 2.E.1: Comparison of the mass-loss profiles $\dot{\Sigma}$ of the four disc masses for each carbon abundance setup. With increasing depletion, the profiles become more similar.

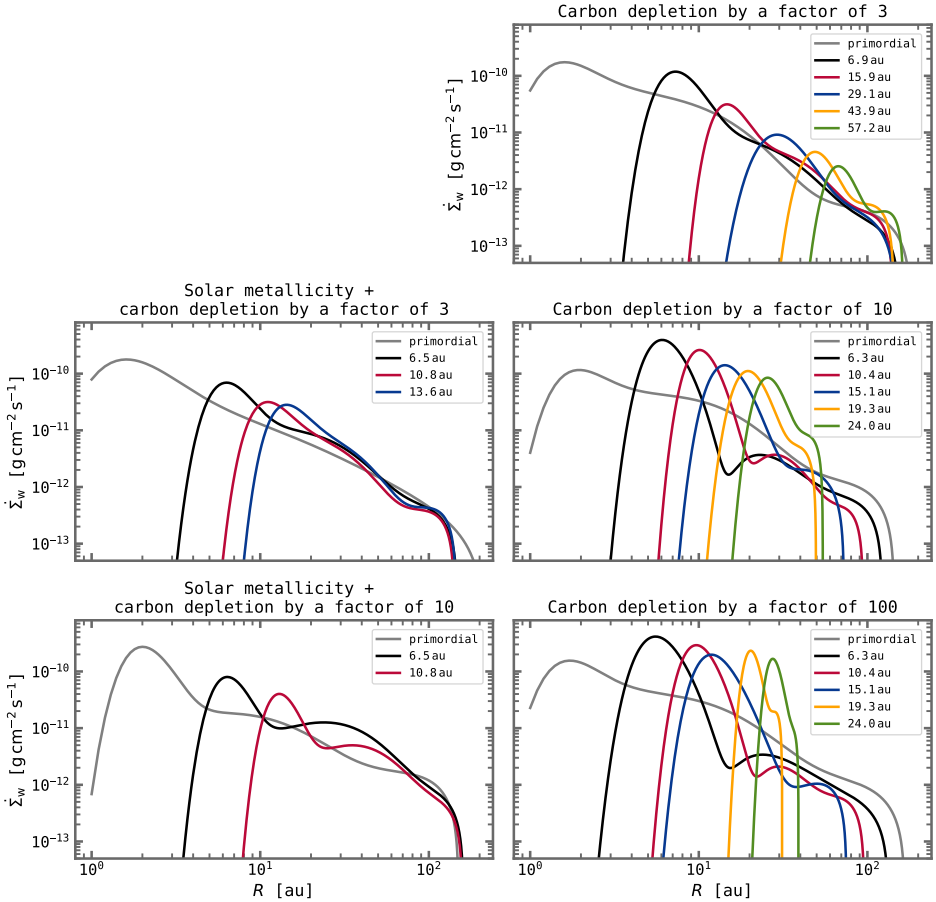

Figure 2.E.2: Examples of mass-loss profiles $\dot{\Sigma}$ for low-mass transition discs ($0.005\,M_*$) with various hole radii, shown for the different carbon abundance setups.

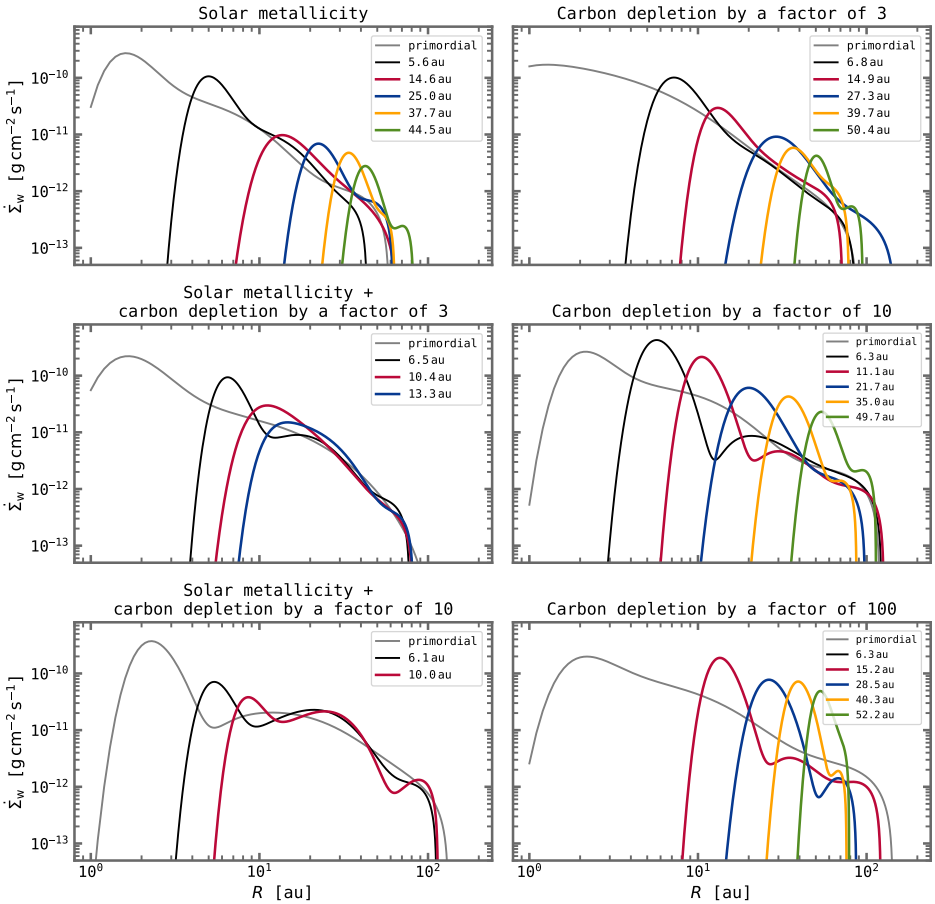

Figure 2.E.3: Examples of mass-loss profiles $\dot{\Sigma}$ for high-mass transition discs ($0.1\,M_*$) with various hole radii, shown for the different carbon abundance setups.

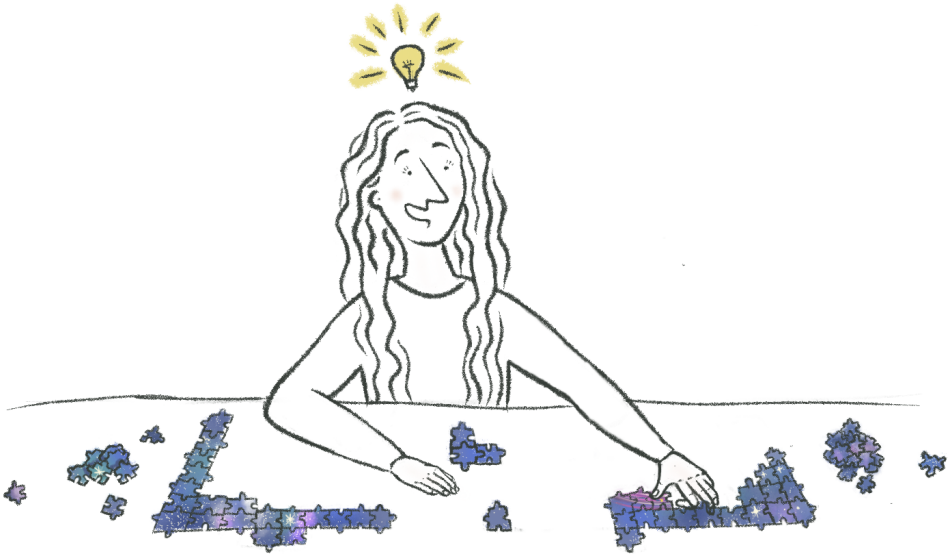

PART II

Gas substructures observed with ALMA

Zwei Dinge erfüllen das Gemüt mit immer neuer und zunehmender Bewunderung und Ehrfurcht, je öfter und anhaltender sich das Nachdenken damit beschäftigt: Der bestirnte Himmel über mir und das moralische Gesetz in mir.

Immanuel Kant

Chapter 3

A highly non-Keplerian protoplanetary disc

Spiral structure in the gas disc of CQ Tau

L. Wölfer, S. Facchini, N. T. Kurtovic, R. Teague,
E. F. van Dishoeck, M. Benisty, B. Ercolano, G. Lodato,
A. Miotello, G. Rosotti, L. Testi, M. G. Ubeira Gabellini

A&A, 648, A19 (2021)

ABSTRACT

Context. In recent years, high-angular-resolution observations have revealed that circumstellar discs appear in a variety of shapes with diverse substructures being ubiquitous. This has given rise to the question of whether these substructures are triggered by planet–disc interactions. Besides direct imaging, one of the most promising methods to distinguish between different disc-shaping mechanisms is to study the kinematics of the gas disc. In particular, the deviations of the rotation profile from Keplerian velocity can be used to probe perturbations in the gas pressure profile that may be caused by embedded (proto-) planets.

Aims. In this paper, we aim to analyse the gas brightness temperature and kinematics of the transitional disc around the intermediate-mass star CQ Tau in order to resolve and characterize substructure in the gas caused by possible perturbers.

Methods. For our analysis, we used spatially resolved ALMA observations of the three CO isotopologues ^{12}CO, ^{13}CO, and C^{18}O ($J = 2 - 1$) from the disc around CQ Tau. We further extracted robust line centroids for each channel map and fitted a number of Keplerian disc models to the velocity field.

Results. The gas kinematics of the CQ Tau disc present non-Keplerian features, showing bent and twisted iso-velocity curves in ^{12}CO and ^{13}CO. Significant spiral structures are detected between ~ 10 and 180 au in both the brightness temperature and the rotation velocity of ^{12}CO after subtraction of an azimuthally symmetric model, which may be tracing planet–disc interactions with an embedded planet or low-mass companion. We identify three spirals, two in the brightness temperature and one in the velocity residuals, spanning a large azimuth and radial extent. The brightness temperature spirals are morphologically connected to spirals observed in near-infrared (NIR) scattered light in the same disc, indicating a common origin. Together with the observed large dust and gas cavity, these spiral structures support the hypothesis of a massive embedded companion in the CQ Tau disc.

3.1 Introduction

Due to angular momentum conservation, circumstellar discs are the natural outcome of the star formation process when infalling material from a molecular cloud core is channelled towards the newly formed central star. These accretion discs composed of gas and dust represent the nurseries of planetary systems. They evolve and ultimately disperse while giving birth to various objects, with the evolutionary processes significantly influencing the ongoing planet formation. At the same time, the forming planets backreact on the disc and affect its evolution and structure, resulting in a highly coupled and complex problem.

High-angular-resolution observations indeed show that circumstellar discs are commonly marked by a variety of substructures in the gas and especially the dust, such as gaps, rings, or even cavities, as well as spiral arms and azimuthal asymmetries (e.g., van der Marel et al. 2013; Casassus 2016; Andrews et al. 2018; Cazzoletti et al. 2018; Long et al. 2018; Andrews 2020). Such substructures might be caused by embedded (proto-) planets (e.g., Lin & Papaloizou 1986; Zhang et al. 2018; Lodato et al. 2019), suggesting that planet formation occurs already in early evolutionary stages. However, there exist other mechanisms that could also account for the observations, such as the magnetorotational instability (MRI; e.g., Flock et al. 2015, 2017; Riols & Lesur 2019), zonal flows (e.g., Uribe et al. 2015), the compositional baroclinic instability (Klahr & Bodenheimer 2004), and gravitational instability (Kratter & Lodato 2016).

One way to distinguish between the different scenarios and to understand possible planet–disc interactions is to directly image a young planet in its environment (e.g., Keppler et al. 2018; Wagner et al. 2018). As this technique is only feasible for very few, massive objects that are not affected by dust extinction (Sanchis et al. 2020), another promising method is to look for perturbations that are induced in the velocity field of the rotating gas. In this context, studying the gas component can help to access the different dynamical processes that are shaping the disc and reveal a number of previously undetected substructures. The density structure of dust grains that are typically probed by ALMA observations is determined by the gas dynamics. It is therefore of paramount importance to directly access and characterize the gas kinematics to distinguish between various scenarios.

Different and complementary image analysis techniques to probe disc kinematics are being developed. For a geometrically thick disc around a single star that is both in radial and vertical hydrostatic equilibrium, the gas rotation velocity $v_{\rm rot}$ is given by

$$\frac{v_{\rm rot}^2}{r} = \frac{GM_* r}{\left(r^2+z^2\right)^{3/2}} + \frac{1}{\rho_{\rm gas}}\frac{\partial P}{\partial r}, \tag{3.1}$$

with r being the cylindrical radius, M_* the mass of the star, $\rho_{\rm gas}$ the gas density, and $\partial P/\partial r$ representing the radial pressure gradient. Identifying deviations from Keplerian rotation can therefore be used to probe the local pressure gradient and to characterize the shape of the perturbation. Additional deviations may arise for a massive disc due to its gravitational field.

This technique has recently been used by Teague et al. (2018a, 2019a) to con-

strain the gas surface density profile of the HD 163296 disc, leading to the kinematical detection of two embedded Jupiter-mass planets as well as significant meridional flows. In addition, Teague et al. (2018b) report a vertical dependence on the pressure maxima, studying the gas kinematics of AS 209. The deviations from Keplerian rotation are further used by Rosotti et al. (2020b) to measure the gas-dust coupling as well as the width of gas pressure bumps. Pinte et al. (2018b, 2019) detect 'kink' features in the iso-velocity contours of HD 163296 and HD 97048 data, respectively, consistent with a Jupiter-mass planet ($\sim 2\,M_{\rm J}$). Tentative detections of such azimuthally located features have also been reported in a few discs of the ALMA DSHARP large program (Andrews et al. 2018; Pinte et al. 2020), but more data are needed to confirm the robustness of such claims. Similarly, a possible signature for an embedded planet in the HD 100546 disc is presented by Casassus & Pérez (2019) who reveal a Doppler-flip in the residual kinematical structure after subtracting a Keplerian best-fit model, as expected from a planet–disc interaction model (e.g., Perez et al. 2015b; Pérez et al. 2018).

One type of disc, the so-called transition disc, is of particular interest because examples show evidence for dust (and gas)-depleted inner regions (e.g., Strom et al. 1989; Ercolano & Pascucci 2017). Sometimes treated as being in a transition phase from an optically thick disc to disc dispersal, transition discs may enable us to probe various mechanisms that play a role during disc evolution and represent excellent candidates to catch planet formation in action. Detecting a planet in discs with cavities may link planet formation with fully formed planetary systems and put constraints on the formation processes and timescales.

In this work, we study the transitional disc around CQ Tau. Following Ubeira Gabellini et al. (2019), who focused on the radial profiles, characterization of the present dust and gas cavity, and possible formation mechanisms, we analyse the gas component of the CQ Tau disc both in terms of its velocity and temperature structure, finding significant spiral structures. The paper is organized as follows: In Sect. 3.2 we describe the observations and data reduction, whereas the observational results are presented in Sect. 3.3. A description and analysis of the spiral structure are shown in Sect. 3.4 alongside the method used to extract and model the gas kinematics. Our results are discussed in Sect. 3.5 and summarized in Sect. 3.6.

3.2 Observations

3.2.1 Target

The variable star CQ Tau (UX Ori class) is a YSO of spectral type F2 located in the Taurus star-forming region at a distance of ~ 162 pc (Gaia Collaboration et al. 2018) (RA = $05^{\rm h}35^{\rm m}58.47^{\rm s}$, Dec = $+24^\circ44'54.09''$; J2000). The intermediate-mass star ($1.67\,{\rm M}_\odot$; Garcia Lopez et al. 2006; Ubeira Gabellini et al. 2019) has an estimated age of ~ 10 Myr and is surrounded by a massive circumstellar disc (Natta et al. 2000), which is found to have a high accretion rate of the order of $10^{-8} - 10^{-7}\,{\rm M}_\odot\,{\rm yr}^{-1}$ (Donehew & Brittain 2011; Mendigutía et al. 2012).

The disc around CQ Tau represents one of the first discs whose millimetre (mm) continuum was observed with different instruments (e.g., OVRO interferometer, Mannings & Sargent 1997; PdBI, Natta et al. 2000; VLA, Testi et al. 2001) in order to constrain its dust properties. An analysis of the spectral slope at mm-wavelengths revealed that dust grains have grown to larger sizes than the typical ISM size (Testi et al. 2001, 2003; Chapillon et al. 2008). The average dust opacity coefficient was constrained by Banzatti et al. (2011) using VLA (1.3-3.6 cm), PdBI (2.7-1.3 mm), and SMA (0.87 mm) observations, probing significant grain growth in the disc with up to centimetre (cm)-sized grains. Trotta et al. (2013) further find that larger grains are present in the inner disc with respect to the outer disc, indicating a variation of grain growth with radius.

Subsequent high-resolution gas and dust observations revealed the CQ Tau disc to be a transition disc with an inner cavity. Tripathi et al. (2017) detect a gap in the 880 μm continuum emission of new and archival SMA data and Pinilla et al. (2018) report a dust cavity of ~ 46 au in ALMA observations of the mm continuum, fitting the intensity profile in the visibility plane. Ubeira Gabellini et al. (2019) present recent ALMA observations, confirming a large cavity of 53 au radius (peak of the Gaussian dust ring) in the 1.3 mm continuum as well as a smaller gas cavity of 20 au in the ^{13}CO and C^{18}O emission, fitting the surface density profiles. The authors performed 3D hydrodynamical simulations which suggest a hidden planet of several $M_{\rm J}$ located at ~ 20 au as a possible cause for the observed gas and dust-depleted regions. Even though such a planet could not be detected in combined Keck/NIRC2 and Subaru/AO188+HiCIAO observations of CQ Tau (Uyama et al. 2020), due to a lack of contrast (compare their Fig. 3), the data reveal the presence of a small spiral seen in small dust grains on scales of $30 - 60$ au that might be induced by a companion candidate.

3.2.2 Data reduction

We present 1.3 mm ALMA observations of the CQ Tau system in band 6, combining datasets from cycles 2, 4, and 5 (2013.1.00498.S, PI: L. Pérez; 2016.A.00026.S; 2017.1.01404.S., PI: L. Testi), previously presented at a lower angular resolution in Ubeira Gabellini et al. (2019), and detailed in Table 3.A.1. These three projects have different antenna configurations, but they share a similar spectral setup. The longest baseline from the first project extended to 1091 m, while for the latest two it was increased to 3700 m and 8500 m respectively, thus enhancing the spatial resolution. In all three observations the ALMA correlator was configured to observe the 1.3 mm dust continuum emission, as well as the molecular lines ^{12}CO, ^{13}CO, and C^{18}O $J = 2 - 1$.

After applying ALMA standard pipeline calibration, we followed a similar processing as for the DSHARP data calibration (Andrews et al. 2018), using `CASA 5.4.1`. We started by flagging the channels located at $\pm 25\,{\rm km\,s^{-1}}$ from each spectral line, and averaged the remaining channels to 125 MHz width channels, which were combined with the data from the continuum spectral windows. As a next step, we aligned the dust continuum emission and checked by comparison the flux calibration of each individual execution, to ensure they all have the same flux.

Table 3.1: Characteristics of the data for the three lines ^{12}CO, ^{13}CO, and C^{18}O $J = 2-1$.

line	intrinsic resolution (kHz)	spectral resolution ($\mathrm{m\,s^{-1}}$)	b_{maj} ($''$)	b_{min} ($''$)	b_{PA} ($^\circ$)	rms channels ($\mathrm{Jy\,beam^{-1}}$)
^{12}CO	244	500	0.121	0.098	8.004	1.2e-3
^{13}CO	488	700	0.128	0.103	7.676	1.0e-3
C^{18}O	488	1000	0.129	0.103	8.814	0.7e-3

To enhance the signal-to-noise ratio (S/N), self-calibration was performed in two stages. First, we self-calibrated the shorter baseline dataset, corresponding to the Cycle 2 observations (dataset 1 in Table 3.A.1), by applying three steps of phase-only calibration using solution intervals of 300, 120, and 30 s, and one step of amplitude calibration using the whole observation time range as a solution interval. This self-calibrated short baseline dataset was then combined with the extended baseline datasets from the observations obtained in Cycles 4 and 5 (datasets 2 and 3), and four phase calibrations with solution intervals of 900, 360, 150, and 90 s, as well as one amplitude calibration with a solution interval of 360 s.

All the dust continuum emission calibration steps, including the centroid shifting and self-calibration tables, were then applied to the molecular line emission channels. The continuum emission was subtracted using the `uvcontsub` task, and image cubes were generated for each isotopologue (compare channel maps in Appendix 3.B) using a robust parameter of 0.6 and Keplerian masking. This value was found to give the best trade-off between spatial resolution and sensitivity. The Keplerian mask was calculated with the package `keplerian_mask`[1], using an inclination of 35 °, position angle of 235 °, distance of 162 pc, stellar mass of 1.54 $M_\odot$, and systemic velocity of 6.17 $\mathrm{km\,s^{-1}}$. These values were chosen after some initial fits for the gas kinematics, explained later in Sect. 3.4.2. We further chose an inner and outer radius of 0 and 2$''$,respectively, and convolved with the beam rescaled by 1.5 times its size. Some important characteristics of the data are given in Table 3.1.

3.3 Observational results

3.3.1 Integrated intensity and brightness temperature maps

In Fig. 3.1 we show the velocity-integrated intensity maps (left panels) along with the peak brightness temperature maps (right panels) for the three different CO isotopologues. The underlying channel maps are presented in Appendix 3.B. The ^{12}CO integrated intensity is overlaid by the contours of the 1.3 mm continuum. To compute the integrated as well as the peak intensity maps we used the

[1] `https://github.com/richteague/keplerian_mask`

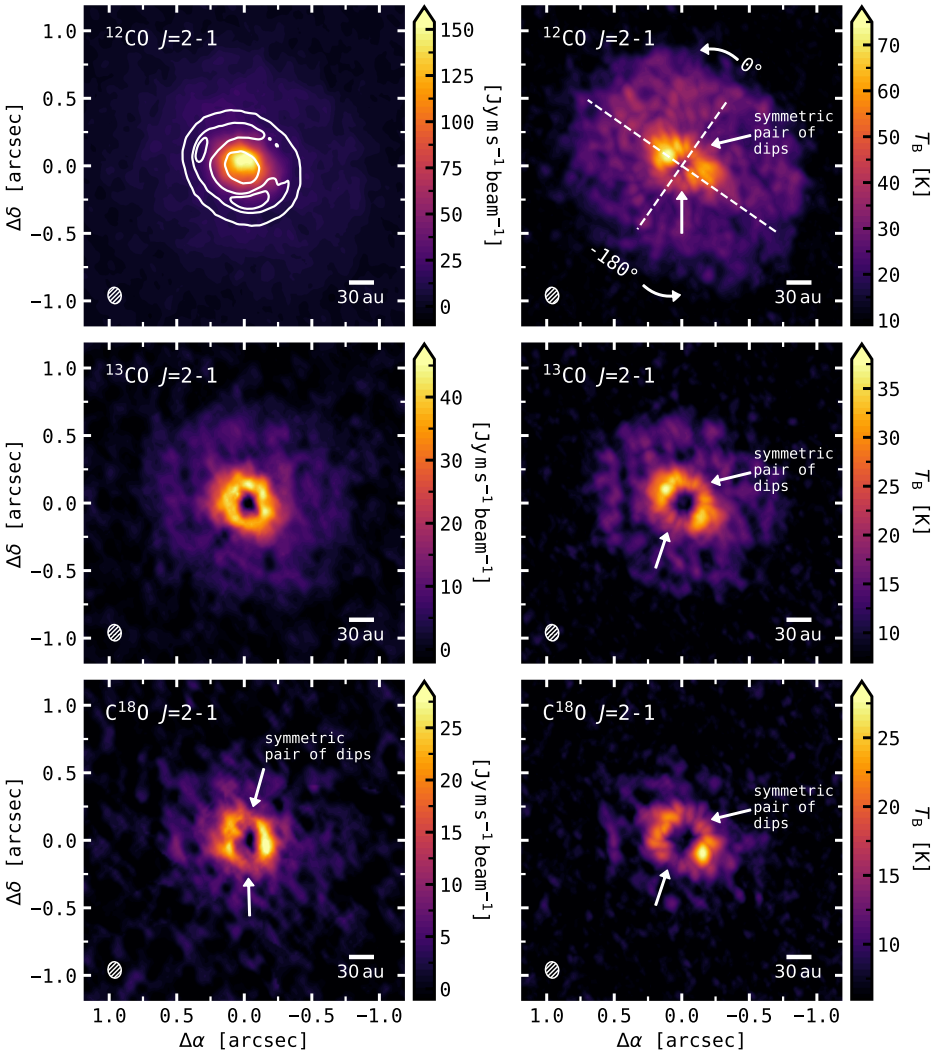

Figure 3.1: ALMA observations of the velocity-integrated intensity (left panels) and peak brightness temperature (right panels) of the ^{12}CO (top panels), ^{13}CO (middle panels), and C^{18}O (bottom panels) $J = 2 - 1$ transition. The conversion from flux to brightness temperature was performed with the Planck law. The contours of the continuum are overplotted on top of the ^{12}CO integrated intensity at 20, 100, and 130 σ (1 σ = 11 μJy beam^{-1}). The synthesized beam is shown in the bottom left corner of each panel.

`bettermoments` code described in Teague & Foreman-Mackey (2018) and then converted from flux density units to units of Kelvin with the Planck law. In addition, the Keplerian mask described in Sect. 3.2.2 is applied in the velocity-integrated intensity maps to enhance the S/N. This results in a peak S/N of 40 for the ^{12}CO, 20 for the ^{13}CO, and 14 for the C^{18}O velocity-integrated intensity as well as 29 for the ^{12}CO, 19 for the ^{13}CO, and 18 for the C^{18}O peak intensity.

While the optically thick ^{12}CO data do not trace any cavities in the gas distribution, a significant gas cavity is observed in the inner disc region as seen in the optically thinner ^{13}CO and C^{18}O emission, shown also by Ubeira Gabellini et al. (2019) at a lower angular resolution. In addition to Ubeira Gabellini et al. (2019), we clearly note a drop in the peak intensity of all isotopologues and integrated intensity of C^{18}O by roughly 35–60 % (with respect to the peak) in the northwest and southeast parts of the disc along the minor axis (symmetric pair of dips). It becomes especially prominent in the C^{18}O data and co-locates with a possible under-brightness in near-infrared (NIR) scattered light (see Fig. 4 of Uyama et al. 2020). Similar to the NIR under-brightness, the drop in peak intensity appears to be more pronounced (relative to the peak $\sim$ 7–12 % deeper dip) on the southeast side of the disc (compare also Sect. 3.3.2).

Such symmetric features are often linked to the presence of a misaligned inner disc, casting a shadow over the outer disc (e.g., Marino et al. 2015; Facchini et al. 2018; Casassus & Pérez 2019). However, the co-location of this under-brightness with the minor axis of the disc suggests that caution should be exercised because beam dilution can lead to artificial azimuthal features due to the low compact emission of the line central channels.

To test for this effect, we used the DALI (Dust And LInes Bruderer et al. 2012; Bruderer 2013) model presented by Ubeira Gabellini et al. (2019) and convolved the spectral image cubes with the beam of our observation. The resulting peak intensity map is shown in the left panel of Fig. 3.C.1 of Appendix 3.C for ^{12}CO. Two clear dips appear along the minor axis, with the results being similar for the more optically thin lines. Thus, beam dilution can mostly account for the strong under-brightness seen in the data. Similar to the data, the upper side of the disc (including the northwest dip) appears slightly brighter in the model map. The disc vertical structure is likely playing a role here with the northwest side being the far side of the disc, thus associated with a larger projected emission area and a less severe beam dilution. In agreement with that, the upper side of the disc is also found to be brighter in some of the channels (compare Appendix 3.B).

The brightness temperature map of ^{12}CO shows that the disc is also brighter, and thus likely warmer, on the northeastern side. While ^{13}CO does not show any strong east–west asymmetry, the disc is clearly brighter on the southwestern side of C^{18}O, which instead of a higher temperature may trace a small over-density due to the lower optical depth of the line.

3.3.2 Radial and azimuthal cuts

Figure 3.2 presents the normalized azimuthal variations of the peak intensity (before $T_{\rm B}$ conversion) for the three CO isotopologues. Each profile is shown for the

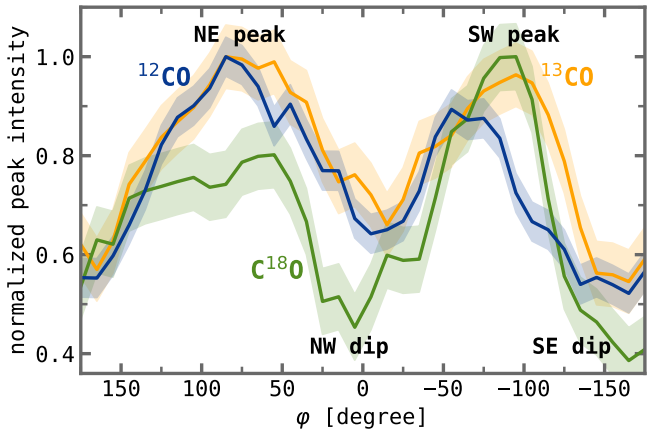

Figure 3.2: Azimuthal variation of the peak intensity for an annulus of 20–40 au (0.″12–0.″25), normalized to the peak value and shown for the three CO isotopologues. The uncertainties are given as 1 σ.

ring of strongest intensity between 0.″12–0.″25 ($\sim$ 20–40 au) with the uncertainty being the rms computed on the peak intensity map. To rotate and deproject the maps, a position angle of 235 ° and inclination of 35 ° (compare results of subsubsection 3.4.2.2) were used.

As discussed above, we indeed find an opposite east–west asymmetry in the curves for ^{12}CO and C^{18}O, while the intensity of ^{13}CO is relatively symmetric about the y-(minor) axis. The intensity of the left (east) peak compared to the right (west) peak is roughly 10 % higher for the ^{12}CO and 25 % lower for the C^{18}O peak intensity. This matches the brightness and temperature differences seen in the maps of Fig. 3.1, where the east side of the disc is brighter in ^{12}CO but fainter in C^{18}O.

In addition, the profiles underline that the under-brightness appears stronger on the southeast side of the disc. For comparison, the azimuthal profiles derived from the DALI model are shown in the right panel of Fig. 3.C.1 for all three isotopologues. In contrast to the data, no strong east–west asymmetry is seen in the peaks. The peak intensity further drops by roughly 35–45 % at the dips with the southeast dip being (relative to the peak) about 2–6 % deeper compared to the northwest dip. The asymmetry found in the under-brightness is thus more pronounced in the data. Together with the under-brightness seen in NIR, where beam dilution cannot be invoked to explain the latter, this supports the assumption that an additional shadowing may occur on the south side of the disc. While the continuum shows two clumps (top left panel of Fig. 3.1), they are present at a different location from the brightness asymmetries and from the symmetric pair of dips and are therefore unlikely to account for the variations.

Figure 3.3 displays the normalized radial intensity profiles for the three CO isotopologues as well as the 1.3 mm continuum. The curves are obtained from the azimuthally averaged intensity per annuli of size 0.″02 ($\sim$ 3.2 au) from the peak intensity maps (before $T_{\rm B}$ conversion), again using an inclination and position angle of 35 ° and 235 °, respectively. The error bars are calculated as the standard deviation per annulus divided by the square root of the number of independent

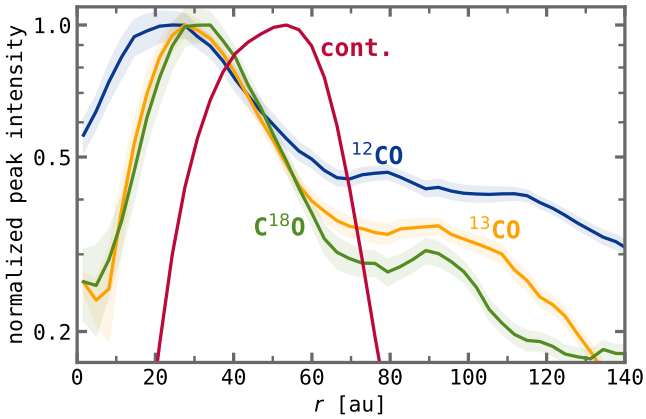

Figure 3.3: Azimuthally averaged radial intensity profiles of the continuum (red), ^{12}CO (blue), ^{13}CO (orange), and C^{18}O (green) data. The profiles are derived from the corresponding peak intensity maps and normalized to the peak value.

beams in the annulus. Compared with the profiles shown by Ubeira Gabellini et al. (2019) for the integrated intensity, we notice a drop of the peak intensity in the radial profile of C^{18}O between $\sim$ 65 and 85 au of about 3 % (relative to the peak value) in addition to the intensity drop at the $\sim$ 20 au cavity in ^{13}CO and C^{18}O. A corresponding slight dip is present in the ^{13}CO peak intensity profile. Being more optically thin, C^{18}O is mostly tracing the column density. Therefore, the observed feature may be indicative of a depleted region around 75 au, possibly carved by an unseen companion. Continuum absorption is unlikely to account for the dip because the peak of the continuum flux lies around 52 au rather than 75 au. Another explanation may be the enhancement of emission around $\sim$ 90 au at the edge of the continuum, rather than a dip, potentially caused by an enhanced desorption of CO ices by increased UV or a temperature inversion (e.g., Cleeves et al. 2016; Facchini et al. 2017).

3.4 Analysis

3.4.1 Temperature structure

As the ^{12}CO emission is optically thick and in local thermodynamic equilibrium (LTE) at these low rotational transitions, the brightness temperature (top right panel of Fig. 3.1) can be used as a probe of the gas kinetic temperature. In this context, the gas temperatures up to 75 K that we observe are as they would be expected in the upper disc layers (Bruderer et al. 2014). To uncover small perturbations in this temperature structure, similar to Teague et al. (2019b), we subtract an azimuthally averaged radial $T_{\rm B}$ profile similar to the one shown in Fig. 3.3. This leaves significant spiral structure in the resulting residuals as shown in Fig. 3.4. Two clear spirals are observed, a smaller one (Sp$_{\rm T1}$) spanning an azimuth of $\sim 100\,^{\circ}$ between $\sim$ 10 and 180 au and a larger spiral (Sp$_{\rm T2}$) covering more than half an azimuth at a similar radial extent. Both spirals have the same orientation. The small spiral seen in the NIR by Uyama et al. (2020) at radii of

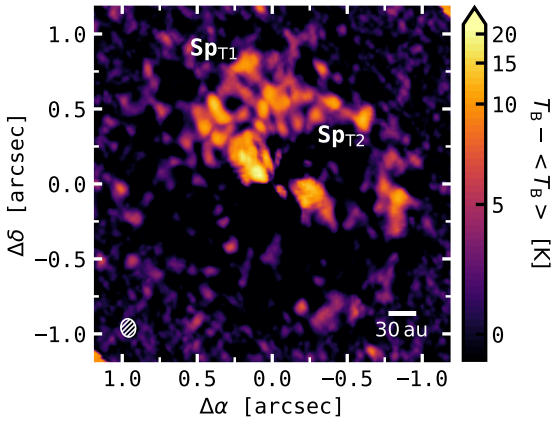

Figure 3.4: Residuals of the ^{12}CO brightness temperature after subtraction of an azimuthally averaged radial profile. Two spirals Sp$_{T1}$ and Sp$_{T2}$ are spanning an azimuth of $\sim$100 ° and $>$180 °, respectively, between $\sim$10 and 180 au.

$\sim$ 30–60 au co-locates with the anchoring point of the large spiral observed here (compare Fig. 3.7 in Sect. 3.4.3).

3.4.2 Velocity structure

The BETTERMOMENTS package can also be used to generate the observed rotation velocity of the gas (similar to a moment 1 map). The code fits a quadratic model to the brightest pixel as well as the two neighbouring pixels to find the centroid of the line in pixel coordinates. Compared to other methods, this approach is more robust to noise or errors in the line shape, allowing a precision that is greater than the velocity resolution. The resulting velocity structure of the disc, masking regions below $4\,\sigma$ for ^{12}CO and $3.5\,\sigma$ for ^{13}CO and C^{18}O, is shown in Fig. 3.5. Besides the velocity field of all three isotopologues, the corresponding error map of ^{12}CO is included in the top right panel. These statistical uncertainties are calculated by linearising and propagating the uncertainty from the fluxes to the centroid estimate. For most regions, the achieved precision is well below the channel width of $500\,\mathrm{m\,s^{-1}}$. In the central regions, the uncertainties increase due to beam smearing.

The isovelocities of the outer disc in the ^{12}CO velocity map match those of a Keplerian flat disc model (e.g., Rosenfeld et al. 2013), whereas significant distortions can be seen in the inner disc (up to $\sim 0\farcs5$), with the kinematics in the centre being slightly twisted and the blue- and redshifted parts bending in opposite directions. In the top left panel of Fig. 3.5, the maximum and minimum velocities along the red- and blueshifted major axes are overlaid, emphasising the non-Keplerian term present in the inner disc. For the case of a razor-thin Keplerian disc, a dipole morphology would be expected that is symmetric about the semi-major axis. The isovelocities further hint towards a rather non- or slightly elevated or flared emission surface because the lobes of the rotation pattern are overall not distinctively bent away (in one direction) from the disc major axis, although this may be resulting from the perturbing spiral structure. We still attempted to fit for the emission surface, however, none of the fits converged. In the

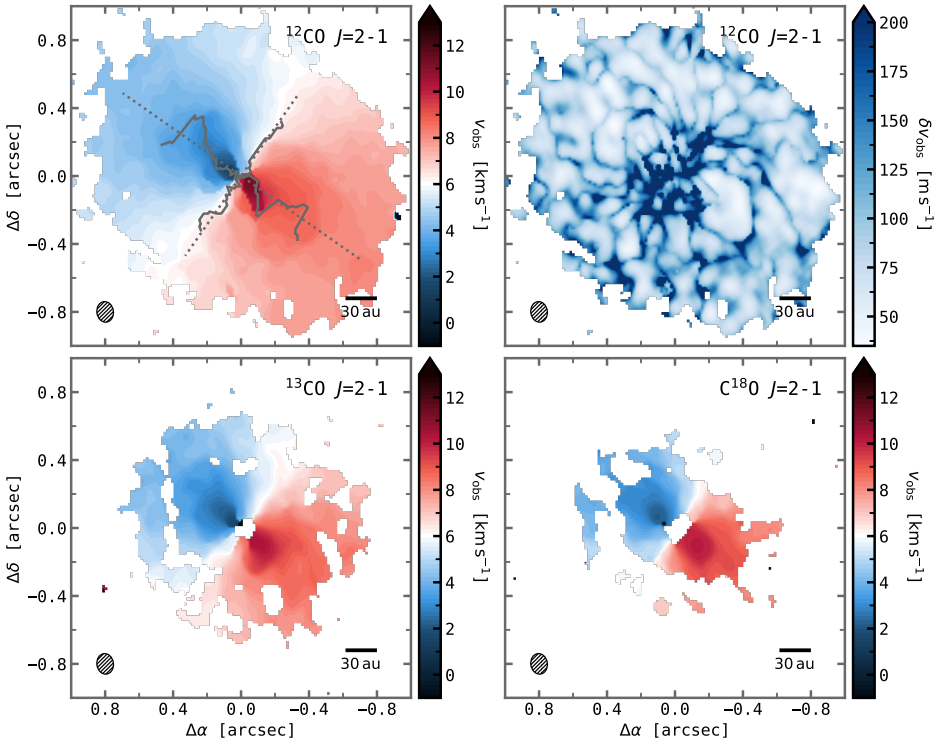

Figure 3.5: Rotation map of the three CO isotopologues and the corresponding uncertainties of ^{12}CO (top right panel), calculated with BETTERMOMENTS. Regions below $4\,\sigma$ (^{12}CO) and $3.5\,\sigma$ (^{13}CO, C^{18}O) are masked out. The maximum and minimum velocities along the red- and blueshifted major axes are overlaid with grey lines on the ^{12}CO rotation pattern.

following, we therefore focus on a razor-thin disc Keplerian model. The rotation pattern of ^{13}CO shows a similar twisting and bending to the ^{12}CO emission while no substructure can be discerned in the less bright C^{18}O.

3.4.2.1 Analysis of the gas rotation velocity

To analyse the gas kinematics of the disc around CQ Tau and characterize the apparent deviations from Keplerian velocity, we fitted a Keplerian profile

$$v_{\rm rot}(r,\phi) = \sqrt{\frac{GM_*}{r}} \cdot \cos\phi \cdot \sin i + v_{\rm LSR}, \tag{3.2}$$

with (r,ϕ) being the deprojected cylindical coordinates, i the inclination of the disc, and $v_{\rm LSR}$ the systemic velocity, to the rotation map of ^{12}CO shown in Fig. 3.5 using the EDDY code (Teague 2019). The associated uncertainties were included in the fit. In order to deproject the sky-plane coordinates (x,y) into the midplane

cylindrical coordinates (r, ϕ), the disc centre (x_0, y_0), i, and the disc position angle PA were used. The latter is measured between the north and the redshifted semi-major axis in an easterly direction. As a first step, the starting positions of the free fit parameters were optimized with `scipy.optimize`, with their posterior distributions estimated using the MCMC sampler. In this context, we used 200 walkers, 5000 steps to burn in, and 5000 additional steps to sample the posterior distribution function. For all of our models we assumed flat priors that were allowed to vary over a wide range. The uncertainties of the posterior distributions represent the 16th to 84th percentiles about the median value.

In addition to the razor-thin disc model, a parameterization for the emission surface as well as a warped structure can be included in the model. The results of our modelling are reported in the following and summarized in Table 3.D.1 of Appendix 3.D.

3.4.2.2 Razor-thin disc model

For the razor-thin disc models we fixed the object's distance and inclination to 162 pc and 35 ° (Ubeira Gabellini et al. 2019), respectively, and fitted for the disc centre ($x_0, y_0 \in \{-0\farcs5, 0\farcs5\}$), systemic velocity ($v_{\rm LSR} \in \{-5\,{\rm km\,s^{-1}}, 20\,{\rm km\,s^{-1}}\}$), stellar mass ($M_* \in \{0.1\,M_\odot, 5\,M_\odot\}$), and disc position angle (PA $\in \{-360\,°, 360\,°\}$).

In the first two runs (run 1, 2 in Table 3.D.1), we attempted to fit the entire disc, choosing an outer radius of $1''$(162 au) to exclude possible noise at the disc's edge. For the second run, we further set an inner boundary of $0\farcs25$ (40 au), which corresponds to the inner edge of the Gaussian ring of the dust continuum, as obtained by Ubeira Gabellini et al. (2019). Both setups result in very similar fit parameters, yet returning a slightly smaller stellar mass when the disc centre is excluded. In addition, we tried to fit specific regions of the disc, including only the inner disc (run 3, 4), outer disc (run 5, 6), or annuli of size $0\farcs2$ (runs 7-10). Overall we find that $v_{\rm LSR}$ slightly increases towards the outer disc, while PA is relatively constant. The largest scatter is found for the stellar mass M_*, which ranges from 1.47 to 1.65 $\rm M_\odot$, driven by the model trying to account for the non-Keplerian structure in the rotation map.

All thin disc models rapidly converged with a Gaussian posterior distribution function (PDF), resulting in similar residuals when the model is subtracted from the velocity data. We tried both convolving the models with the beam of the observation and not using the convolution, with both approaches returning comparable results. In this context, we note that convolving channel maps prior to collapsing them into the rotation map would be a better approach than convolving the model map as it is done in EDDY. However, generating channel maps, as opposed to a simple rotation map, requires far more model assumptions which is why we choose not to do it. The effects are negligible outside the disc centre (i.e. outside approximately two times the beam FWHM) and thus do not significantly affect our results.

The posterior distributions presented in Table 3.D.1 show very small and likely underestimated uncertainties, especially in the context of the scatter that is found in the stellar mass. One possibility is that the uncertainties in the velocity centroids

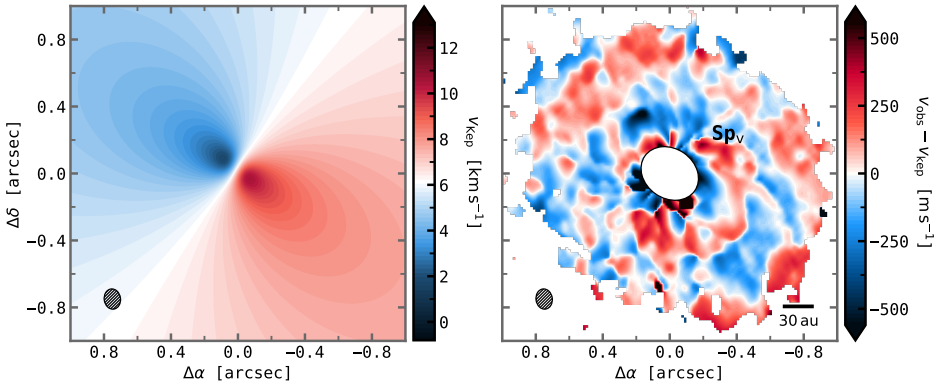

Figure 3.6: Best-fit Keplerian rotation model (left panel) and the residuals calculated by subtracting the model from the observed rotation velocity (right panel), shown for ^{12}CO. The residuals inside a radius of 1.5 times the FWHM of the beam are masked out. In the residuals, a spiral Sp$_{\rm v}$ is spanning more than one azimuth between $\sim$ 40 and 180 au.

are underestimated. We therefore performed an additional run of model 2 with the velocity errors increased by a factor of ten. This returns very similar fit parameters with the uncertainties also being a factor of ten larger, albeit still too small to account for the observed scatter. Therefore, the small uncertainties cannot only be explained by underestimated velocity errors but result from systematic uncertainties in our model.

Figure 3.6 shows the results from run 2, including the best-fit model (left panel) and the corresponding residuals (right panel) after subtraction from the data. The model corresponds to a position angle PA $= 235\,^{\circ}$, systemic velocity $v_{\rm LSR} = 6173\,{\rm m\,s^{-1}}$, and a stellar mass of $M_* = 1.57\,{\rm M_\odot}$. While the residuals are less than about 5 % of the velocity data outside of $\sim 0\farcs2$, they (partly) grow to more than 50 % in the very inner disc ($< 0\farcs1$) which suffers strongly from beam smearing effects (Teague et al. 2018c, 2016). We therefore masked out the residuals inside a radius of 1.5 times the FWHM of the beam. The residuals clearly reveal the non-Keplerian structure of the rotation velocity, showing significant spiral features (Sp$_{\rm v}$) that cover more than one azimuth at radii of 40–180 au, with the same orientation and a similar location as the spirals observed in the gas temperature.

As twisted kinematics are sometimes linked to the presence of a misaligned inner disc, we performed several runs adding the parameterization of a potential warp in the (flat disc) model. However, none of these models converged. Besides being limited by the spatial resolution of the data ($0\farcs121 \times 0\farcs098$), the kinematics are strongly dominated by the large spiral structure in the outer disc. Thus, a small feature such as a warp in the very inner disc regions cannot be fitted by our simple model. For the same reason, we were not able to obtain any constraints on the emission surface.

Table 3.2: Parameters for the by-eye parameterization with a linear and logarithmic spiral.

	Linear spiral		**Logarithmic spiral**		
Spiral	a ($''$)	b ($''$ rad^{-1})	a ($''$)	b ($''$)	k (rad^{-1})
Brightness temperature					
$\mathrm{Sp_{T1}}$	1.284	-0.559	1.451	-0.309	0.831
$\mathrm{Sp_{T2}}$	0.710	-0.141	1.130	-0.383	0.642
Rotation velocity					
$\mathrm{Sp_{v}}$	0.815	-0.078	1.123	-0.309	0.166

3.4.3 Analysis of the spiral structure

Three significant spirals are observed in the residuals presented in Sects. 3.4.1 and 3.4.2: two in the brightness temperature and one in the rotation velocity of ^{12}CO. All spirals show the same orientation, suggesting a counter-clockwise rotation of the disc if the spirals are trailing, and they cover a large azimuth and radial extent. A counter-clockwise rotation implies that the southeast side of the disc is closer to the observer, which should be visible in the rotation map as a bending of the high-velocity components towards the north. While this is true for the blueshifted side, the spiral may be driving such a large velocity perturbation that the redshifted side is bending the other way, therefore resembling a warp. The geometry of the disc agrees with the southeast dip in the peak brightness temperature map being dimmer due to beam dilution (see Sect. 3.3.1).

We reproduce the spiral morphology with different functional forms, in particular an Archimedean (linear) spiral

$$r = a + b\phi, \tag{3.3}$$

as well as a spiral,

$$r = a + b\mathrm{e}^{k\phi}, \tag{3.4}$$

where r represents the radius and ϕ the polar angle of the spiral. As Eq. 3.4 is similar to the equation of a logarithmic spiral, we refer to it as such in the following. The resulting parameters are presented in Table 3.2 and the corresponding spirals are shown in Fig. 3.7 for the brightness temperature and in Fig. 3.8 for the rotation velocity. In both cases, we plot the deprojected and rotated maps, using the inclination and position angle found in Sect. 3.4.2.2 (top panels). Again, the inner disc regions are masked out inside a radius of 1.5 times the FWHM of the beam for the velocity residuals. Additionally, the polar-deprojected maps are shown (bottom panels). The spiral fits are overlaid as $\mathrm{Sp_{T1}}$ and $\mathrm{Sp_{T2}}$ in the temperature and as $\mathrm{Sp_{v}}$ in the velocity residuals with white and black dashed lines.

Both functions provide a good and very similar parameterization for the small temperature spiral $\mathrm{Sp_{T1}}$, with the overall linear nature becoming clear when looking at the polar-deprojected map. For the second, large temperature spiral $\mathrm{Sp_{T2}}$,

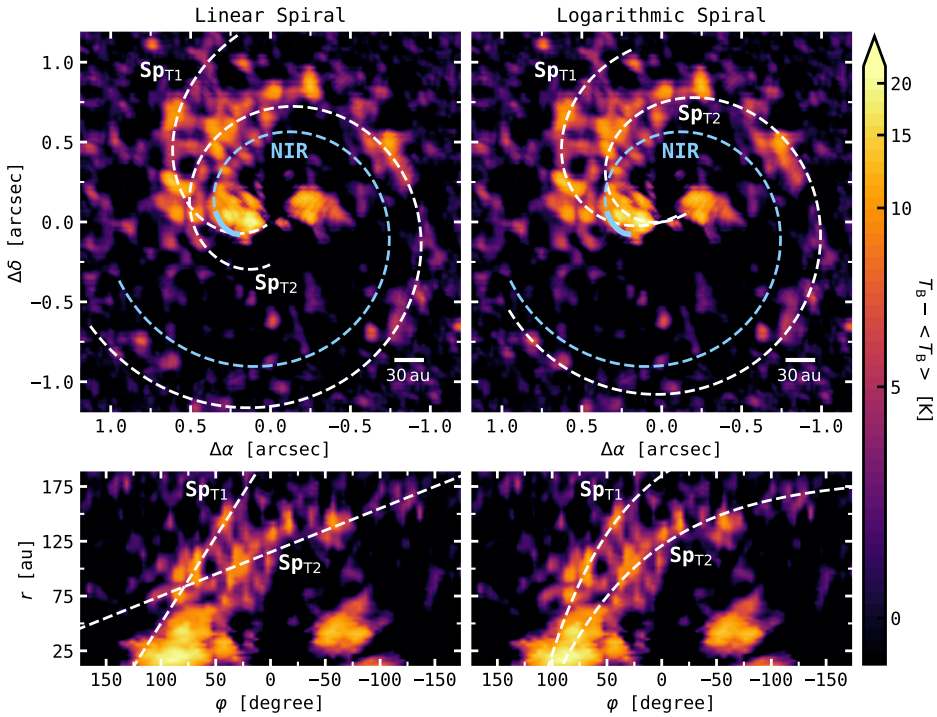

Figure 3.7: Deprojected and rotated (top panels) as well as polar-deprojected (bottom panels) T_B residuals of ^{12}CO with overlaid Archimedean and logarithmic spirals. The blue dashed lines show the fit of the spiral observed in the NIR by Uyama et al. (2020), extrapolated to large azimuthal angles. The solid blue line highlights the spiral region used by Uyama et al. (2020) to obtain the fit.

the linear spiral is not able to account for the curvature that is obvious in the polar-deprojected plot and is thus missing the inner part of the spiral. The logarithmic parameterization on the other hand is able to better represent the anchoring point of the spiral. The velocity spiral $\mathrm{Sp_v}$ is again well represented by both functions. No large differences can be seen between the two parameterizations, with the overall nature being very close to linear. As a comparison, the $\mathrm{Sp_{T2}}$ spiral is also included in the velocity residuals. While the two spirals are co-located in the outer regions, they deviate from each other towards the inner disc for both spiral functions.

The spiral found in the NIR is overlaid on the brightness temperature residuals in Fig. 3.7. Here, the solid line represents the location of the NIR spiral, while the dashed line shows the extrapolation of the fit performed by Uyama et al. (2020) for this spiral with a function $r = a + b\phi^n$. The NIR spiral matches the anchoring point of the temperature spirals and follows the course of $\mathrm{Sp_{T2}}$ at the inner edge, suggesting they are connected.

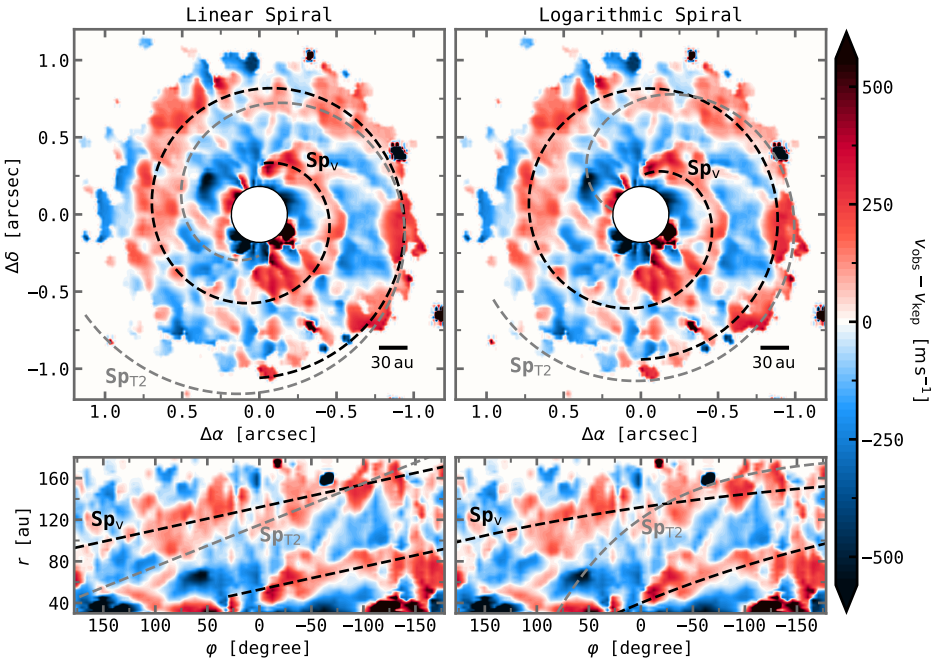

Figure 3.8: Deprojected and rotated (top panels) as well as polar-deprojected (bottom panels) velocity residuals of ^{12}CO with overlaid Archimedean and logarithmic spirals. The spiral $\mathrm{Sp_{T2}}$ observed in T_B is overlaid as a grey dashed line. The residuals inside a radius of 1.5 times the FWHM of the beam are masked out.

In addition to the ^{12}CO data, we search for features in the residuals of ^{13}CO and C^{18}O, presented in Fig. 3.9 for T_B (top panels) and the velocity (bottom panels). The residuals are calculated again by subtracting an azimuthally symmetric model, using the best-fit model from run 2 for the velocity. The logarithmic spirals $\mathrm{Sp_{T2}}$ and $\mathrm{Sp_v}$ observed in ^{12}CO are overlaid for comparison. Even though no clear spiral structure can be found in the brightness temperature of either ^{13}CO or C^{18}O, the launching point of the spiral is clearly visible in the ^{13}CO residuals and some indication of a spiral matching the logarithmic parameterization of $\mathrm{Sp_{T2}}$ is present. Similarly, the velocity residuals of ^{13}CO also show signs of a spiral similar to that observed in ^{12}CO, yet slightly more tightly wound, while no substructures can be distinguished in C^{18}O.

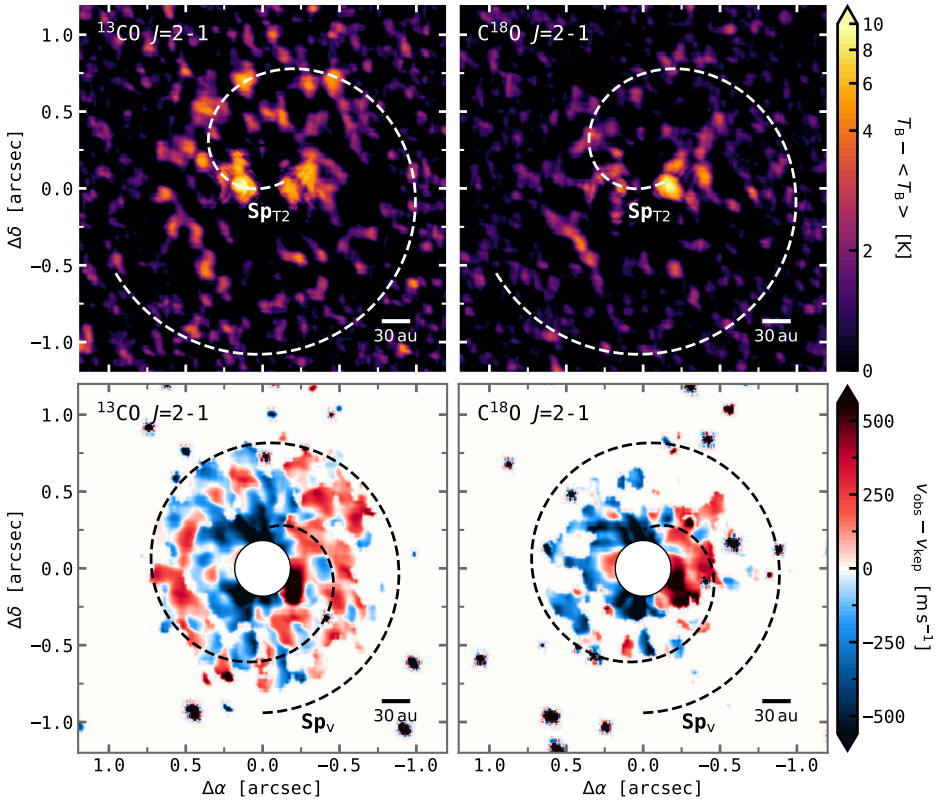

Figure 3.9: Deprojected and rotated T_B (top) and velocity (bottom) residuals of ^{13}CO (left) and C^{18}O (right). The logarithmic spirals Sp_{T2} and Sp_v observed in ^{12}CO are overlaid. The residuals inside a radius of 1.5 times the FWHM of the beam are masked out in the velocity residuals.

Using

$$\tan\beta = \left|\frac{dr}{d\phi}\right| \cdot \frac{1}{r}, \tag{3.5}$$

we calculate the pitch angle β for all three spirals. The resulting angles are shown in Fig. 3.10 for the linear and logarithmic fit. Here, the solid lines are shown at the location where the spirals are present, while the dashed lines represent the extrapolation towards smaller radii. We further included the constant pitch angle found by Uyama et al. (2020), who fitted a logarithmic spiral of $r = be^{k\phi}$ to the spiral feature observed in the NIR. As mentioned above, this spiral is located at the anchoring point of spiral Sp_{T2}, yet spanning a smaller radial extent of $\sim$ 30–60 au and azimuth of roughly 50 °. The pitch angle of the NIR spiral, which is given as $\sim$ 34 °, seems consistent with the pitch angle found from the linear parameterization for spiral Sp_{T2}, however, in these radial regions the linear fit failed to reproduce the spiral morphology (shaded region in Fig. 3.10). Here the

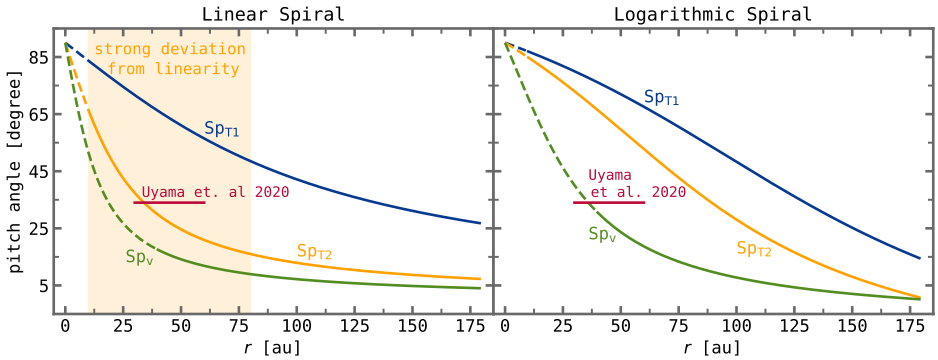

Figure 3.10: Pitch angle of the three spirals observed in the T_B and rotation velocity residuals of ^{12}CO, shown for the linear and logarithmic spiral. The constant pitch angle of the NIR spiral found by Uyama et al. (2020) is included as a reference. The shaded region represents the disc regions where the linear fit fails to reproduce the morphology of spiral Sp$_{T2}$.

logarithmic spiral provided a better approximation with the resulting pitch angles lying 20–40 ° above that of the NIR spiral. The pitch angle decreases faster with radius for the logarithmic spirals, with the angles being larger until $\sim$ 126 au (Sp$_{T1}$), 147 au (Sp$_{T1}$), and 106 au (Sp$_v$) compared to the linear spiral, yet overall comparable for Sp$_{T1}$ and Sp$_v$ (keeping in mind an uncertainty due to the by-eye parameterization). This is expected because both functions provide a similar parameterization for these spirals. The largest difference is seen for Sp$_{T2}$, where the Archimedean spiral was not able to sufficiently reproduce the inner parts of the spiral.

3.5 Discussion

Both the gas temperature and the rotation velocity of ^{12}CO show significant spiral structures over the bulk of the disc when an azimuthally symmetric model is subtracted from the observations (Figs. 3.7, 3.8). Together with a similar feature found in the NIR (Uyama et al. 2020), the extent of the structures over a large azimuth (>180 ° temperature, >360 ° velocity) and radius (10–180 au temperature, 40–180 au velocity) with a S/N of 2–6 suggests they are real features. Both the large temperature spiral SP$_{T2}$ and the NIR spiral appear to follow a similar course, strongly suggesting a link between the two. The location of the spirals matches those of the prominent distortions and bendings occurring in the velocity field and are possibly the cause of the latter. Higher spatial and spectral resolution will be necessary to resolve the very inner disc regions and confirm the presence of the spirals at a higher S/N.

Although no significant spiral structure is observed in the ^{13}CO and C^{18}O lines, indications for such features are present in both the brightness temperature and rotation velocity residuals of ^{13}CO and may be made accessible with deeper

high-resolution observations.

All three spirals observed in ^{12}CO are well described by a modified logarithmic spiral, and two (i.e. not SP_{T2}) are well described by an Archimedian (linear) spiral with radially decreasing pitch angles (Fig. 3.10). The angles found for the logarithmic parameterization mostly lie above those of the linear one. Overall, all three spirals are loosely wound and consequently show relatively large pitch angles. These characteristics may be explained through Lindblad-resonance-driven spiral wakes of a massive embedded companion (e.g., Ogilvie & Lubow 2002; Rafikov 2002; Bae & Zhu 2018a,b).

As the optically thick ^{12}CO is tracing higher disc layers, significantly smaller pitch angles, and thus more tightly wound spirals, are expected at the midplane if the disc is passively heated with a positive vertical temperature gradient (compare Juhász & Rosotti 2018). In this context, to distinguish between different spiral-launching scenarios it is crucial to use observations spanning the full vertical extent. If the spirals were for example caused by gravitational instability, similar pitch angles would be expected for the midplane and the surface layers because the midplane would be heated by shocks in that case. Given the small number of spirals, gravitational instability however seems a rather unlikely cause for the spiral structures we observe (e.g., Cossins et al. 2009; Hall et al. 2020). It is worth considering, nevertheless, that several spiral arms could possibly appear as only two or three arms due to resolution effects (Dipierro et al. 2014) and the disc around CQ Tau happens to be relatively massive, therefore gravitational instability cannot be ruled out at this point.

So far, no clear spiral structures have been found in the dust continuum (or optically thin lines) of CQ Tau that could be used to further distinguish possible launching scenarios, but these could be made accessible with higher spatial resolution data. Spiral arms have been observed with ALMA in the continuum of several discs, including for example Elias 2-27 (Pérez et al. 2016), IM Lup and WaOph 6 (Huang et al. 2018), G17.64+0.16 (Maud et al. 2019), MWC 758 (Boehler et al. 2018; Dong et al. 2018), and HD 100453 (Rosotti et al. 2020a). For the latter, counterparts to the observed NIR spirals (Wagner et al. 2015; Benisty et al. 2017) were not only found in the dust continuum but also the CO emission, enabling the authors to study the thermal structure of the disc and link the spirals to a known binary companion. The velocity residuals of ^{13}CO possibly suggest a spiral slightly more tightly wound than the corresponding spiral in ^{12}CO. A more tightly wound spiral would show smaller pitch angles, which would support the findings of Juhász & Rosotti (2018).

It is difficult to determine whether the spirals observed in the temperature and the velocity trace the same underlying perturbation. Even though the spirals Sp_{T2} and Sp_v do not fully overlap, they appear to align in the outer parts of the disc between $\sim$ 130 and 180 au and from 0 to -180 °, hinting towards the same formation mechanism. On the other hand, the calculated pitch angles for the according spirals differ by several degrees. However, we note that the pitch angles are only a rough estimate because no actual fit was performed and that the actual pitch angles may lie much closer for Sp_{T2} and Sp_v.

Similarly, Teague et al. (2019b) observe temperature and velocity spirals in

TW Hydra that appear to align but do not fully overlap, and therefore there may be a physical mechanism behind these differences. The authors suggest that layers with different thermal properties are traced, arguing that close to the disc's surface spirals in the velocity should be more pronounced due to efficient cooling, while the heat produced by spirals would be more efficiently trapped closer to the midplane. In the case of a companion, the spiral density waves created by either a planet or binary companion will lead to an increase in surface density and thus in a higher CO opacity. This will move the $\tau = 1$ layer to a higher altitude, where the temperature is generally higher, resulting in the observed spiral substructure in the gas temperature (Phuong et al. 2020a,b).

Even though it is impossible to fully disentangle all three velocity components (v_r, v_z, v_ϕ), the same orientation in the residuals coupled with the full azimuthal coverage hint towards a vertical perturbation (compare Appendix B in Teague et al. 2019b). This is consistent with the (potentially) companion-launched spirals in HD 100453 (Rosotti et al. 2020a). As shown by Pinte et al. (2019), an embedded planet will cause perturbations in all three velocity directions, with their strength decreasing with height above the midplane for radial and rotational motions, whereas they increase with height for vertical motions. Gas flowing towards the midplane and falling into the observed cavity could be another explanation for the vertical motions. As the vertically moving material will receive more stellar light it may appear brighter regardless of the underlying surface density.

In case the spirals are indeed launched by an embedded planet outside of its orbit, they are expected to converge towards the planet location (Juhász et al. 2015; Bae & Zhu 2018a,b). As this results in a rapid increase in the pitch angle towards the planet, a possible companion is expected to be located inside of $\sim$ 25 au in our case. This is consistent with the findings of Ubeira Gabellini et al. (2019), who propose an unseen planet of $6 - 9\,M_\mathrm{J}$ to explain the deep dust and gas cavity. Given such a location and mass, a companion is not expected to be noticeably affected by extinction in any band (Sanchis et al. 2020). We note that dynamically launched spirals tend to open up only close to the planet, and consequently become more tightly wound at larger distances, resulting in small pitch angles. It is therefore puzzling, that the spirals we observe are still very open far from the possible companion.

In the channel maps presented in Figs. 3.B.1, 3.B.2, and 3.B.3, no clear kinks similar to Pinte et al. (2018b, 2019) are detected and the two sides of the disc cannot be resolved due to spectral and spatial resolution limitations. As several studies (Uyama et al. 2020; Ubeira Gabellini et al. 2019), including ours, on the other hand indicate the presence of a massive companion of CQ Tau at < 25 au, imprints on the iso-velocities are expected and may be made accessible with higher resolution or sensitivity.

3.6 Summary

In this work, we present high-angular-resolution ALMA observations of ^{12}CO, ^{13}CO, and C^{18}O $J = 2-1$ data of the disc around CQ Tau and use the ^{12}CO data

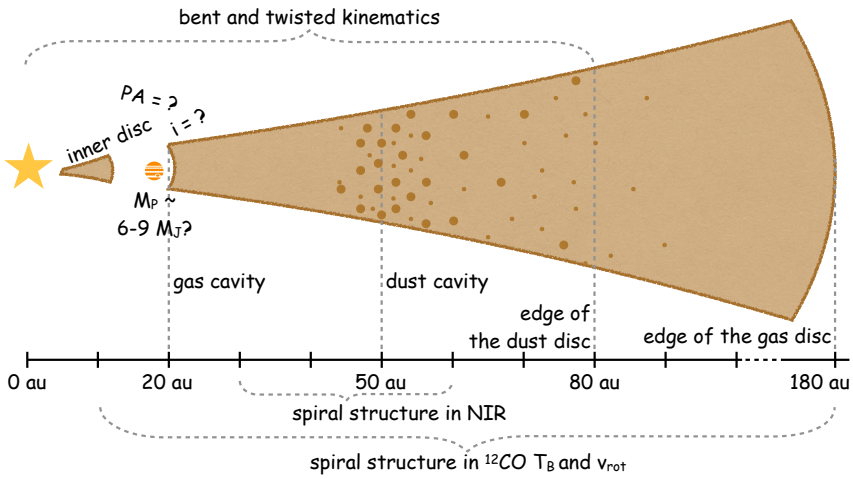

Figure 3.11: Illustration of the possible morphology of the disc around CQ Tau.

to analyse the gas temperature and kinematics of the disc. The main results of this analysis are summarized as follows.

The morphology of the significant spiral structure observed in the brightness temperature and rotation velocity of ^{12}CO together with the number of spirals and large pitch angles supports a dynamical launching scenario, for example an embedded planet or binary, rather than gravitational instabilities. Such a companion is expected to be relatively massive and to be located inside of ~ 25 au, which is in agreement with Ubeira Gabellini et al. (2019). Further multi-line observations at a higher velocity resolution and 3D modelling are required to further distinguish the different mechanisms.

In addition to the gas cavity, an intensity drop can be seen on the northwest and southeast sides of the disc in all three isotopologues. Postprocessing the DALI model presented by Ubeira Gabellini et al. (2019) revealed the under-brightness to be caused by beam dilution rather than by a temperature or line width effect. As the dip in the southeast appears to be more pronounced and is co-located with the under-brightness in scattered light, some additional shadowing may still occur, potentially caused by the spiral itself or misaligned regions in the disc.

Figure 3.11 presents an illustration of the possible morphology of the disc around CQ Tau, taking into account the results from Ubeira Gabellini et al. (2019), Uyama et al. (2020), and this work: a dust and gas cavity are present in the disc at ~ 50 and ~ 20 au, respectively, which could be explained by a massive companion inside of 20 au. Spiral structures are found in $T_{\rm B}$, $v_{\rm rot}$, and NIR, further supporting the hypothesis of an unseen companion. The inner disc regions, including their position angle and inclination, remain unresolved.

Altogether it appears that the disc around CQ Tau is far from a Keplerian disc. Therefore, a more detailed non-Keplerian model is required to describe the

gas rotation and could be addressed in future work. The possibility of a massive companion in particular, either a binary star or very massive planet, needs to be further explored. To construct such a model, higher angular and spectral resolution ALMA data are essential. Furthermore, NIR interferometry observations at milliarcsec resolution with VLTI-Gravity (Gravity Collaboration et al. 2017) could help to constrain the inclination and position angle of the innermost disc, providing information on the presence of misaligned regions. Combining dust and gas observations of different molecular lines with high S/N is needed to constrain the vertical temperature profile and to further analyse the clearly observed spiral structure of the gas disc.

Acknowledgements

We thank the referee Simon Casassus for his constructive comments and suggestions that helped to improve our work. This paper makes use of the following ALMA data: 2013.1.00498.S, 2016.A.000026.S, and 2017.1.01404.S. ALMA is a partnership of ESO (representing its member states), NSF (USA) and NINS (Japan), together with NRC (Canada) and NSC and ASIAA (Taiwan) and KASI (Republic of Korea), in cooperation with the Republic of Chile. The Joint ALMA Observatory is operated by ESO, auI/NRAO and NAOJ. We acknowledge the support from the DFG Research Unit 'Planet Formation Witnesses and Probes: Transition Discs' (FOR 2634/1, ER 685/8-1 & ER 685/11-1). N. K. acknowledges support provided by the Alexander von Humboldt Foundation in the framework of the Sofja Kovalevskaja Award endowed by the Federal Ministry of Education and Research. G. R. acknowledges support from the Netherlands Organisation for Scientific Research (NWO, program number 016.Veni.192.233). This work was partly supported by the Italian Ministero dell'Istruzione, Università e Ricerca (MIUR) through the grant Progetti Premiali 2012 iALMA (CUP C52I13000140001), by the Deutsche Forschungsgemeinschaft (DFG, German Research Foundation) ref. No. FOR 2634/1 TE 1024/1-1, and by the DFG cluster of excellence Origin and Structure of the Universe (www.universe-cluster.de), and by the EC Horizon 2020 research and innovation programme, Marie Sklodowska-Curie grant agreement NO 823823 (Dustbusters RISE project).

Appendix

3.A ALMA observing log

Table 3.A.1: Observational characteristics of the ALMA data sets used in this work.

Set	Pjoject ID	Date	Config.	Baselines (m)	N_{ant}	Exp. time (min)
1	2013.1.00498.S	30 Aug 2015	C34-6	20–1091	35	15.12
2	2016.A.00026.S	07 Aug 2017	C40-7	81–3700	40	19.66
3	2017.1.01404.S	20 Nov 2017	C43-8	92–8500	44	28.73
		23 Nov 2017	C43-8	92–8500	48	28.73

3.B Channel maps

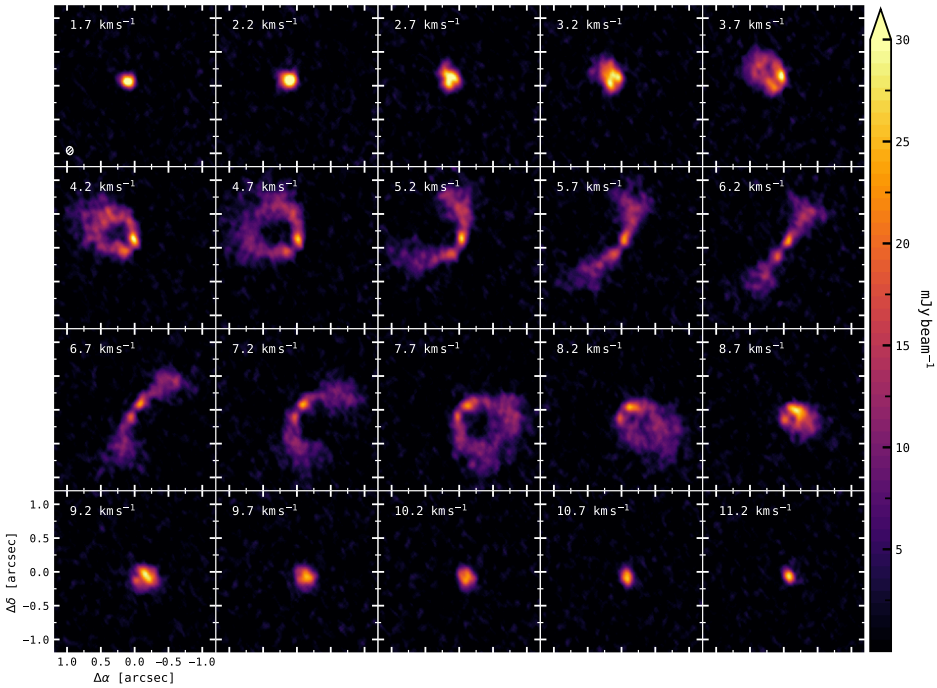

Figure 3.B.1: The ^{12}CO $J = 2-1$ line imaged with a channel width of $\Delta v = 0.5\,\mathrm{km\,s^{-1}}$ and a beam of $0\farcs121$x$0\farcs098$.

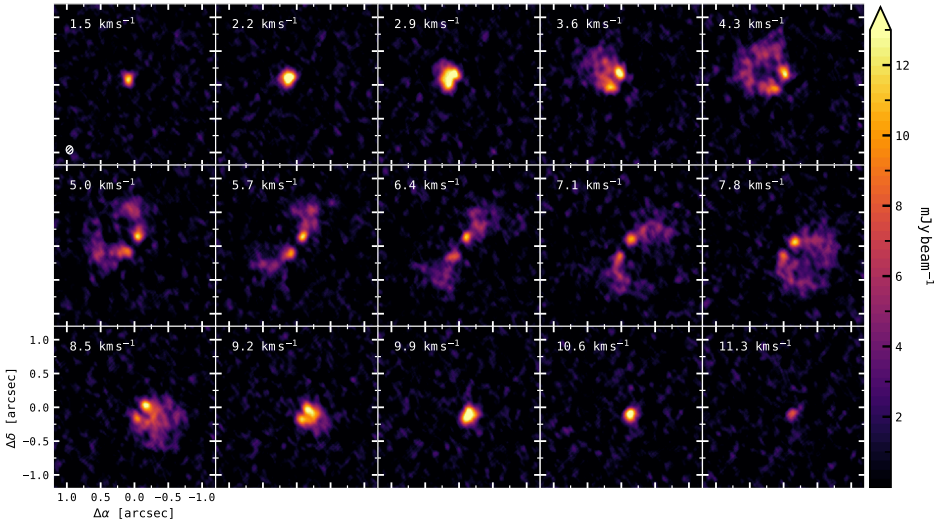

Figure 3.B.2: The ^{13}CO $J = 2-1$ line imaged with a channel width of $\Delta v = 0.7\,\mathrm{km\,s^{-1}}$ and a beam of 0.″128x0.″103.

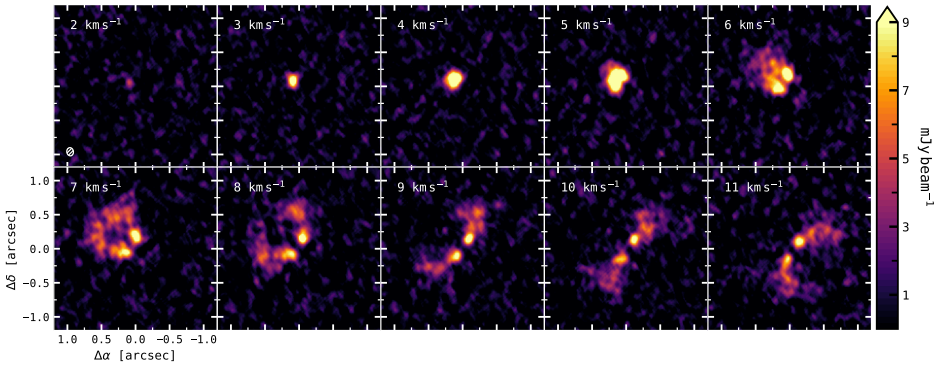

Figure 3.B.3: The C^{18}O $J = 2-1$ line imaged with a channel width of $\Delta v = 1.0\,\mathrm{km\,s^{-1}}$ and a beam of 0.″129x0.″103.

3.C Beam dilution

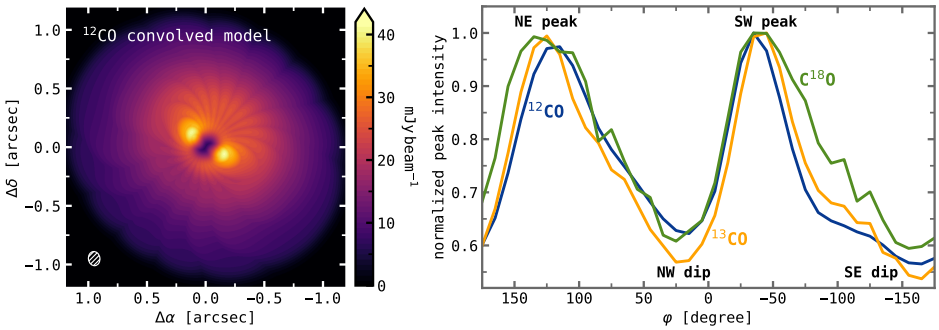

Figure 3.C.1: Left: Peak intensity map from postprocessing the DALI model presented by Ubeira Gabellini et al. (2019), shown for ^{12}CO. Right: Azimuthal variations of the peak intensity of ^{12}CO, ^{13}CO, and C^{18}O for an annulus of 20–40 au (0.″12–0.″25), derived from the DALI model and normalized to the peak value.

3.D Posterior distributions of the modelling

Table 3.D.1: Posterior distributions of the razor-thin disc models. The uncertainties represent the 16th to 84th percentiles about the median value.

Run	$r_{\rm in}$ ($''$)	$r_{\rm out}$ ($''$)	x_0 ($''$)	y_0 ($''$)	PA ($^\circ$)	$v_{\rm LSR}$ ($\rm m\,s^{-1}$)	M_* ($\rm M_\odot$)
$n_{walkers}$ = *200*, n_{burnin} = *5000*, n_{steps} = *5000*							
Full disc							
1	0.0	1.0	0.0089 ± 0.0002	0.0064 ± 0.0001	234.22 ± 0.03	6177.1 ± 0.8	1.582 ± 0.002
2	0.25	1.0	0.0072 ± 0.0003	0.0243 ± 0.0003	234.58 ± 0.03	6172.9 ± 0.8	1.570 ± 0.002
Inner disc							
3	0.0	0.4	0.0116 ± 0.0002	0.0051 ± 0.0002	232.98 ± 0.07	6124.1 ± 2.3	1.626 ± 0.003
4	0.0	0.5	0.0106 ± 0.0002	0.0058 ± 0.0002	233.11 ± 0.05	6145.8 ± 1.6	1.642 ± 0.002
Outer disc							
5	0.4	1.0	0.0066 ± 0.0004	0.0130 ± 0.0004	234.69 ± 0.04	6183.7 ± 0.9	1.570 ± 0.002
6	0.5	1.0	0.0061 ± 0.0005	0.0114 ± 0.0006	234.87 ± 0.04	6185.6 ± 1.0	1.541 ± 0.002
Annuli							
7	0.2	0.4	0.0124 ± 0.0004	0.0282 ± 0.0005	233.57 ± 0.08	6095.8 ± 2.5	1.580 ± 0.003
8	0.4	0.6	0.0033 ± 0.0006	0.0141 ± 0.0006	233.67 ± 0.06	6179.9 ± 1.7	1.636 ± 0.003
9	0.6	0.8	0.0031 ± 0.0008	0.0245 ± 0.0008	235.60 ± 0.06	6169.4 ± 1.4	1.473 ± 0.003
10	0.8	1.0	0.0242 ± 0.0013	0.0020 ± 0.0012	235.33 ± 0.07	6194.9 ± 1.7	1.650 ± 0.004

McCoy: So what's your problem?
Spock: Acceleration is no longer a constant.
McCoy: Well, then you're just gonna have to take your best shot.
Spock: Best shot?
McCoy: Guess, Spock. Your best guess.
Spock: Guessing is not in my nature, Doctor.
McCoy: Well, nobody's perfect.

Star Trek IV: The Voyage Home

Chapter 4

Kinematics and brightness temperatures of transition discs

A survey of gas substructures as seen with ALMA

L. Wölfer, S. Facchini, N. van der Marel, E. F. van Dishoeck,
M. Benisty, A. J. Bohn, L. Francis, A. F. Izquierdo, R. Teague

A&A, 670, A154 (2023)

ABSTRACT

Context. In recent years, high-angular-resolution observations of the dust and gas content in circumstellar discs have revealed a variety of morphologies, naturally triggering the question of whether these substructures are driven by forming planets interacting with their environment or other mechanisms. While it remains difficult to directly image embedded planets, one of the most promising methods to distinguish disc-shaping mechanisms is to study the kinematics of the gas disc. Characterizing deviations from Keplerian rotation can then be used to probe underlying perturbations such as planet–disc interactions. Creating spiral structures, the latter can also be traced in the brightness temperature.

Aims. In this paper we aim to analyse the gas brightness temperatures and kinematics of a sample of 36 transition discs observed with the Atacama Large Millimeter/submillimeter Array (ALMA) to resolve and characterize possible substructures that may be tracing embedded companions.

Methods. For our analysis, we use archival Band 6 and Band 7 ALMA observations of different CO isotopologues (^{12}CO, ^{13}CO, and C^{18}O) and fit different Keplerian disc models (thin and thick disc geometry) to the retrieved velocity field of each disc.

Results. After the subtraction of an azimuthally averaged brightness temperature profile and Keplerian rotation model from the peak brightness temperature and velocity maps, we find significant substructures in eight sources of our sample (CQ Tau, GG Tau, HD 100453, HD 142527, HD 169142, HP Cha, TW Hya, and UX Tau A) in both the brightness temperature and velocity residuals. Other sources show tentative features, while about half of our sample does not show any substructures in the temperature and kinematics that may be indicative of planet–disc interactions.

Conclusions. For the first time, we compare the substructures from our analysis with various other indicators for the presence of planets. About 20 % of discs show strong features such as arcs or spirals, possibly associated with the presence of planets, while the majority of discs do not present as clear planet-driven signatures. Almost all discs that exhibit spirals in near-infrared scattered light show at least tentative features in the CO data. The present data are able to reveal only very massive bodies and a lack of features may suggest that, if there are planets at all, they are of lower mass ($<$ 1-3 $M_{\rm J}$) or may be located closer to the star within deep cavities. Deeper and higher resolution observations and modelling efforts are needed to confirm such scenarios.

4.1 Introduction

Circumstellar discs are formed as a consequence of angular momentum conservation during the process of star formation when material from a molecular cloud core is channeled towards the newborn star in the centre. Also called protoplanetary or planet-forming discs, they provide the gas and dust needed for the formation of planetary systems such as our Solar System. Far from being static, they evolve and eventually disperse while birthing planets, with different mechanisms shaping their appearance and the planet formation processes. At the same time, planets interact with their environment and are expected to alter their host disc's structure, leaving observable marks depending on their mass and location in the disc.

In the last decade, high-angular-resolution dust and gas observations with the Atacama Large Millimeter/submillimeter Array (ALMA; ALMA Partnership et al. 2015) as well as near-infrared (NIR) scattered light observations with, for example, the Spectro-Polarimetric High-contrast Exoplanet REsearch (SPHERE; Beuzit et al. 2019), the Gemini Planet Imager (GPI; Macintosh et al. 2014), or the Subaru telescope's High-Contrast Coronographic Imager for Adaptive Optics (HiCIAO), equipped with the Extreme Adaptive Optics System (SCExAO; Jovanovic et al. 2015) have indeed shown that a variety of substructures, such as gaps or even cavities, rings, spiral arms, and azimuthal asymmetries, are ubiquitous in both the dust and the gas component of planet-forming discs (e.g., van der Marel et al. 2013; Benisty et al. 2015, 2017, 2018; Casassus 2016; Andrews et al. 2018; Cazzoletti et al. 2018; Long et al. 2018; Andrews 2020; Uyama et al. 2020).

Even though there exist several mechanisms that may explain these observations, such as gravitational instabilities (e.g., Kratter & Lodato 2016), photoevaporation (e.g., Owen et al. 2011; Picogna et al. 2019), magnetorotational instabilities (e.g., Flock et al. 2015, 2017; Riols & Lesur 2019), zonal flows (e.g., Uribe et al. 2015), or compositional baroclinic instabilities (e.g., Klahr & Bodenheimer 2004), at least some of the substructures are expected to be linked to the presence of (massive) planets (Lin & Papaloizou 1979; Zhang et al. 2018). To interpret the origin of the various substructures, it is crucial to understand how common they are, if they follow certain patterns, and if differences or similarities can be identified for different star-disc system morphologies.

One particularly interesting subgroup of young stellar objects (YSOs) is represented by the so-called transition discs. Originally identified through a lack of infrared (IR) excess in their spectral energy distribution (SED; Strom et al. 1989), they are characterized by dust (and gas) depleted inner regions (e.g., Espaillat et al. 2014; Ercolano & Pascucci 2017). While they are sometimes classified as an intermediate state between a full optically thick disc and disc dispersal, planet–disc interactions provide an alternative explanation for the observed cavities. At least some transition discs – especially those with very deep dust and gas cavities (e.g., van der Marel et al. 2016) – are expected to be the result of the dynamical clearing of a massive companion that is either planetary or binary. This may imply that transition discs are not an evolutionary state that every disc goes through, since massive planets (or binary companions) are not found around every star (e.g., Johnson et al. 2010; Nielsen et al. 2019; van der Marel & Mulders 2021). Tran-

sition discs, therefore, represent excellent candidates to catch planet formation in action, test planet formation models, and probe disc evolution mechanisms.

To unambiguously link the observed substructures to the presence of a planet, the latter needs to be directly imaged in its environment. However, this method is only feasible for very bright and massive planets that are not severely affected by dust extinction (Sanchis et al. 2020). To date, the only system in which a robust direct detection of proto-planets has been obtained is PDS 70, hosting two planets with masses of several $M_{\rm J}$ (Keppler et al. 2018; Haffert et al. 2019; Benisty et al. 2021).

Alternatively we can study the indirect effects that planets may have on the dust and gas distributions. In this context, one promising method is to investigate the kinematics to look for perturbations that are induced in the velocity field of the rotating gas. Identifying deviations from Keplerian rotation can then be used to probe the local pressure gradient and to characterize the shape of the perturbation. Teague et al. (2018a) used this technique to constrain the rotation profile of HD 163296 and its deviation from a Keplerian profile. In addition, Teague et al. (2019a) report significant meridional flows in that disc. Evidence of similar meridional flows was found in HD 169142 by Yu et al. (2021). The kinematics of AS 209 were studied by Teague et al. (2018b) and Rosotti et al. (2020b) who measured the gas-dust coupling as well as the width of gas pressure bumps and report a vertical dependence on the pressure maxima. So-called kink features were detected by Pinte et al. (2018b, 2019) in the iso-velocity curves of HD 163296 and HD 97048 that are consistent with a Jupiter-mass planet. A possible signature of an embedded planet was also found by Casassus & Pérez (2019) in the HD 100546 disc in the form of a Doppler flip in the residual kinematics. In TW Hya (Teague et al. 2019b), HD 100453 (Rosotti et al. 2020a), HD 135344B (Casassus et al. 2021), CQ Tau (Wölfer et al. 2021), and HD 163296 and MWC 480 (Teague et al. 2021), spiral structures are seen in the kinematics after subtraction of a Keplerian model, which is possibly connected to a companion. Non-Keplerian gas spirals are further detected in HD 142527 by Garg et al. (2021). Calcino et al. (2022) show that the outer kink in HD 163296 is possibly associated with a planetary spiral wake. Izquierdo et al. (2021) developed a new, channel-map-fitting package to robustly identify localized velocity perturbations in both radius and azimuth and thus infer the position of an embedded planet. Applied to HD 163296 data, they are able to find indications for two embedded planets with this method (Izquierdo et al. 2022).

In addition to the kinematics, it can also be useful to look for substructures or asymmetries in the peak intensity (brightness temperature) residuals in the search for evidence of companions. The density waves created by a companion result in an increase in surface density and thus in a higher opacity. This moves the $\tau = 1$ layer to a higher altitude where the temperature is generally higher, resulting in spiral substructures in the gas brightness temperature (Phuong et al. 2020a,b). In addition, planets can generate tightly wound spirals in the brightness temperature through buoyancy resonances (Bae et al. 2021). The temperature structure in planet-driven spiral arms was investigated by Muley et al. (2021) and their models may explain the observed thermal features in discs such as TW Hya

and CQ Tau: Teague et al. (2019b) and Wölfer et al. (2021) report the detection of spiral structures in the ^{12}CO brightness temperature of TW Hya and CQ Tau, respectively, after the subtraction of an azimuthally averaged model. These spirals are (at least partly) linked to the spirals observed in the velocity residuals (for TW Hya, see also Sturm et al. 2020), and in the case of CQ Tau they are connected to a small spiral in the NIR (Uyama et al. 2020).

Studying the gas component in discs may enable one to assess the different dynamical processes described above that are shaping the disc and reveal previously undetected substructures. In this context, probing different disc layers with various molecules may help distinguish between the formation mechanisms of the observed substructures (e.g., Pinte et al. 2018a; Law et al. 2021a). For example, in a passively heated disc with a positive vertical temperature gradient, more tightly wound spirals are expected towards the midplane in the planetary scenario, while similar spiral pitch angles would be established between the surface and midplane layers if resulting from gravitational instabilities (Juhász & Rosotti 2018). Furthermore, an embedded planet induces perturbations in all three velocity components, which vary as a function of height: The magnitude of radial and rotational perturbations ($v_{\rm r}$, v_{φ}) decreases and that of vertical perturbations ($v_{\rm z}$) increases towards the disc surface (Pinte et al. 2019).

To this point, the connection between inner and outer disc structures in protoplanetary discs is not fully understood, but it represents an important piece in the planet-formation puzzle. Several observations of transition discs in NIR scattered light have revealed dark regions (e.g., Stolker et al. 2016; Casassus et al. 2018), which are commonly interpreted as shadows resulting from a misalignment between the inner and the outer disc (e.g., Marino et al. 2015; Facchini et al. 2018). One particularly exciting explanation for this is the presence of (a) massive misaligned companion(s) inducing a misalignment in specific disc regions around them (Francis & van der Marel 2020; Perraut & Gravity Collaboration 2021; Bohn et al. 2022).

In this work, we investigate archival CO data of a sample of 36 transition discs in terms of both their velocity and brightness temperature structure to search for possible perturbations and features that may be linked to the presence of embedded companions. The paper is structured as follows: In Sect. 4.2, we give an overview of the selected targets. The observational results, including brightness temperature and velocity maps as well as radial intensity profiles, are presented in Sect. 4.3. In Sect. 4.4, we describe our analysis, showing the resulting velocity and brightness temperature residuals. These results are discussed in Sect. 4.5 where a comparison with other indicators of planets is done. A summary of our work is presented in Sect. 4.6.

4.2 Observations

Our selected sample consists of 36 transition discs, chosen from the sample of Francis & van der Marel (2020) where sufficient CO data are available. Except for TW Hya, these discs show large ($>$ 25 au) inner dust cavities and therefore

represent the ideal candidates to search for planet–disc interactions. It comprises different star-disc system architectures, including a range of spectral types (M2 to A0; primary) and stellar masses ($0.4\,M_\odot$ to $2.6\,M_\odot$, primary), counting 23 TTauri and 13 Herbig stars. Some stellar and disc properties of our targets are listed in Table 4.1.

For our analysis, we collected either Band 6 or Band 7 archival CO line data, observed with ALMA. For most sources (two-thirds), we used re-imaged (and self-calibrated) data cubes that are either public or were obtained via private communication; for the remaining sources, we used archival data products. This is indicated in Table 4.2, where some characteristics of the data cubes are listed for the main lines used in our study. Typical spectral resolutions of the data are a few 100 $\mathrm{m\,s^{-1}}$ and spatial resolutions lie between $\sim$ 6–135 au (median: 31 au). RMS values lie between $\sim$0.5–47 K (median: 3.4 K) when scaled for a channel width of $100\,\mathrm{m\,s^{-1}}$.

To assess if combining re-imaged and archival products affects our results, we compared the re-imaged data sets with the archival products for the same data set. We find that the Keplerian fit (see Sect. 4.4.2) is not significantly affected. The detection of extended (over several beams) substructures, such as spirals or the non-detection of features, is also not affected. Only tentative features are sometimes only visible in the re-imaged data. Some examples for this test are shown in Fig. 4.D.1 in the Appendix: while clear spirals are found in both the re-imaged and archival product data of UX Tau A, a tentative spiral in the brightness temperature of HD 135344B and a tentative spiral (or arc) in the kinematics of J1604 are only visible in the re-imaged data. RXJ 1615, on the other hand, shows no clear spirals or arcs in both data products.

Several discs in our sample are affected by cloud absorption, namely AB Aur, HD 142527, HD 97048, HP Cha, IP Tau, IRS 48, PDS 99, SR 21, Sz 91, and SZ Cha. We masked the regions affected by this in the calculations of the radial profiles (Sect. 4.3.3) and brightness temperature residuals (Sect. 4.4.1). For some of the targets, we analysed additional CO isotopologues, which are listed with the data properties in the Appendix in Table 4.E.1. Our main lines for analysis (Table 4.2) are based on their brightness as well as the spatial and spectral resolution of the observation. A few of our targets have already been analysed with the same techniques, as explained in Sect. 4.4 (CQ Tau, Wölfer et al. 2021; HD 100453 Rosotti et al. 2020a; and TW Hya Teague et al. 2019b), but they are included in this work for comparison.

Table 4.1: Stellar properties, outer disc inclination, and dust cavity radius of the disc sample studied in this work.

Object	d (pc)	Spectral type	$T_{\rm eff}$ (K)	L ($L_\odot$)	M_* ($M_\odot$)	i (°)	Classification	Dust cavity (au)	Ref.[a]
AA Tau	137	K7	4350	1.1	0.68	59	TTS	44	1
AB Aur	163	A0	9520	65.1	2.56	23	Herbig	156	1
CQ Tau	163	F2	6890	10.0	1.63	35	Herbig	50	1
CS Cha	176	K2	4780	1.9	1.4	8	TTS	37	1
DM Tau	145	M2	3580	0.2	0.39	35	TTS	25	1
DoAr 44	146	K2	4780	1.9	1.4	20	TTS	40	1
GG Tau	140	K7+M0	4060	1.6	0.66	36	TTS	224	1
GM Aur	160	K5	4350	1.0	1.01	53	TTS	40	1
HD 100453	104	F0	7200	6.2	1.47	30	Herbig	30	1
HD 100546	110	A0	9520	25.0	2.13	42	Herbig	27	1
HD 135344B	136	F5	6440	6.7	1.51	12	Herbig	52	1
HD 139614	134	A9	7750	6.0	1.57	18	Herbig	-	2
HD 142527	157	F6+M5/M6	6360	9.9	1.69+0.26	27	Herbig	185	1,3
HD 169142	114	A5	8200	8.0	1.65	12	Herbig	26	1
HD 34282	312	A0	9520	10.8	2.11	59	Herbig	87	1
HD 97048	185	A0	9520	30.0	2.17	41	Herbig	63	1
HP Cha	160	K7	4060	2.4	0.95	37	TTS	50	1
IP Tau	131	M0	3850	0.6	0.54	45	TTS	25	1
IRS 48	134	A0	9520	17.8	1.96	50	Herbig	83	1
J1604.3-2130	150	K3	4780	0.7	1.1	6	TTS	87	1
LkCa 15	159	K2	4730	1.3	1.32	55	TTS	76	1
MWC 758	160	A7	7850	14.0	1.77	21	Herbig	62	1
PDS 70	113	K7	4060	0.3	0.8	52	TTS	74	1
PDS 99	155	K6	4205	1.1	0.88	55	TTS	56	1
RXJ1615.3-3255	156	K7	4100	0.6	0.73	47	TTS	-	2

Table 4.1 continued.

Object	d (pc)	Spectral type	$T_{\rm eff}$ (K)	L ($L_\odot$)	M_* ($M_\odot$)	i (°)	Classification	Dust cavity (au)	Ref.[a]
RXJ1852.3-3700	146	K2	4780	0.6	1.05	30	TTS	49	1
RY Lup	159	K2	4780	1.9	1.4	67	TTS	69	1
RY Tau	175	G2	5860	15.0	2.25	65	TTS	27	1
SR 21	138	G4	5770	11.0	2.12	16	TTS	56	1
Sz 91	159	M1	3850	0.2	0.54	45	TTS	86	1
SZ Cha	190	K2	5100	1.7	1.45	47	TTS	-	2
T Cha	107	G8	5570	1.3	1.12	73	TTS	34	1
TW Hya	60	K7	4205	0.3	0.81	7	TTS	2	1
UX Tau A	140	G8	5570	2.5	1.4	40	TTS	31	1
V1247 Ori	400	F0	7200	15.0	1.82	30	Herbig	64	1
V4046 Sgr	72	K7+K5	4060	0.5	0.9+0.85	34	TTS	31	1,4

Notes. [a] Unless indicated otherwise, data for spectral type, distance, effective temperature, stellar luminosity, stellar mass, and disc inclination are taken from (1) Francis & van der Marel (2020) where all original references for the spectral type can be found. The distances are according to Gaia Collaboration et al. (2018). (2) Bohn et al. (2022), (3) Claudi et al. (2019), (4) Rosenfeld et al. (2012). The radius of the dust cavity was determined by Francis & van der Marel (2020).

Table 4.2: Characteristics of the ALMA line data for the main lines of this analysis.

Object	Line	Project ID	Beam (″)	LAS (″)	Δv (km s^{-1})	RMS (mJy beam^{-1})	Cube source$^{(a)}$	Ref.
AA Tau	^{13}CO 3-2	2015.1.01017.S	0.28x0.22	8.0	0.11	13.5	A	
AB Aur	^{13}CO 3-2	2012.1.00303.S	0.37x0.23	7.2	0.2	6.2	P/PC	1
CQ Tau	^{12}CO 2-1	2013.1.00498.S	0.12x0.1	5.3	0.5	1.2	P/PC	2
		2016.A.00026.S		2.9				
		2017.1.01404.S		2.7				
CS Cha	^{12}CO 3-2	2017.1.00969.S	0.1x0.07	2.4	0.11	4.2	A	
DM Tau	^{12}CO 2-1	2016.1.00724.S	0.86x0.8	10.5	0.08	17.6	A	
DoAr 44	^{13}CO 3-2	2012.1.00158.S	0.25x0.19	3.2	0.5	13.7	P/PC	3
GG Tau	^{12}CO 2-1	2018.1.00532.S	0.34x0.27	9.7	0.08	2.6	A	
GM Aur	^{12}CO 2-1	2018.1.01055.L	0.15x0.15	3.6–44.1	0.2	2.8	P/PC	4, 5
HD 100453	^{12}CO 3-2	2017.1.01424.S	0.05x0.05	1.3	0.42	1.0	P/PC	6
HD 100546	^{12}CO 2-1	2016.1.00344.S	0.08x0.06	1.1/2.7	0.5	1.2	P/PC	7
HD 135344B	^{13}CO 3-2	2012.1.00158.S	0.26x0.21	3.1	0.24	19.1	P/PC	3
HD 139614	^{13}CO 2-1	2015.1.01600.S	0.77x0.55	8.4	0.4	26.5	P/PC	8
HD 142527	^{12}CO 2-1	2015.1.01353.S	0.28x0.26	3.9	0.09	2.5	A	
HD 169142	^{12}CO 2-1	2015.1.00490.S	0.18x0.13	4.2	0.05	1.2	P/PC	9
HD 34282	^{12}CO 3-2	2013.1.00658.S	0.26x0.2	5.1/9.7	0.2	8.2	P/PC	10
HD 97048	^{13}CO 3-2	2016.1.00826.S	0.11x0.07	1.8/4.4	0.12	3.8	P/PC	11
HP Cha	^{12}CO 2-1	2016.1.00583.S	0.3x0.21	6.2	0.63	3.7	A	
IP Tau	^{12}CO 2-1	2013.1.00163.S	0.24x0.21	3.2	1.0	5.5	P/PC	12
IRS 48	^{12}CO 3-2	2013.1.00100.S	0.19x0.13	1.4-3.5	0.24	8.3	P/PC	13
J1604	^{12}CO 3-2	2015.1.00888.S	0.23x0.19	3.3/6.7	0.21	7.1	P/PC	14
LkCa 15	^{12}CO 2-1	2018.1.01255.S	0.41x0.29	7.6	0.04	6.0	P/PC	15
MWC 758	^{13}CO 3-2	2012.1.00725.S	0.19x0.16	5.0	0.11	8.9	P/PC	16
PDS 70	^{12}CO 3-2	2017.A.00006.S	0.11x0.1	2.3	0.42	1.1	P/PC	17

Table 4.2 continued.

Object	Line	Project ID	Beam (″)	LAS (″)	Δv (km s^{-1})	RMS (mJy beam^{-1})	Cube source$^{(a)}$	Ref.
PDS 99	^{12}CO 2-1	2015.1.01301.S	0.3x0.22	4.9	0.16	8.3	A	
RXJ1615	^{12}CO 3-2	2012.1.00870.S	0.3x0.23	3.2/6.5	0.21	14.1	P/PC	18
RXJ1852	^{12}CO 2-1	2018.1.00689.S	0.16x0.12	1.8	0.63	4.3	A	
RY Lup	^{12}CO 3-2	2017.1.00449.S	0.22x0.17	2.71	0.85	4.0	P/PC	19
RY Tau	^{12}CO 2-1	2013.1.00498.S	0.28x0.16	1.67	0.5	9.1	A	
SR 21	^{12}CO 2-1	2018.1.00689.S	0.14x0.12	1.71	0.64	4.8	A	
Sz 91	^{12}CO 3-2	2012.1.00761.S	0.17x0.13	1.36	0.2	11.8	A	
SZ Cha	^{12}CO 3-2	2013.1.01075.S	0.82x0.43	3.70	0.5	26.2	P/PC	12
T Cha	^{12}CO 2-1	2017.1.01419.S	0.24x0.17	2.55	0.32	9.0	A	
TW Hya	^{12}CO 3-2	2015.1.00686.S	0.14x0.13	0.37	0.25	3.5	P/PC	20
		2016.1.00629.S		1.3/6.0				
UX Tau A	^{12}CO 3-2	2015.1.00888.S	0.2x0.16	2.41	0.21	3.4	P/PC	21
V1247 Ori	^{12}CO 3-2	2016.1.01344.S	0.05x0.03	0.86	1.0	2.0	P/PC	22
V4046 Sgr	^{12}CO 2-1	2016.1.00724.S	0.41x0.29	4.48	0.08	9.9	A	

Notes. $^{(a)}$ P/PC: re-imaged data cube. Public data or obtained via private communication, A: archival data product.

References. (1) van der Marel et al. (2021); (2) Wölfer et al. (2021); (3) van der Marel et al. (2016); (4) Öberg et al. (2021); (5) Huang et al. (2021); (6) Rosotti et al. (2020a); (7) Pérez et al. (2020); (8) Stapper et al. in prep.; (9) Yu et al. (2021); (10) van der Plas et al. in prep. ; (12) Pinte et al. (2019); (12) Bohn et al. (2022); (13) van der Marel et al. in prep.; (14) Mayama et al. (2018); (15) Leemker et al. (2022); (16) Boehler et al. (2018); (17) Keppler et al. (2019); (18) Perez et al. in prep.; (19) Qian et al. in prep.; (20) Huang et al. (2018); (21) Ménard et al. (2020); (22) Kraus et al. (2017).

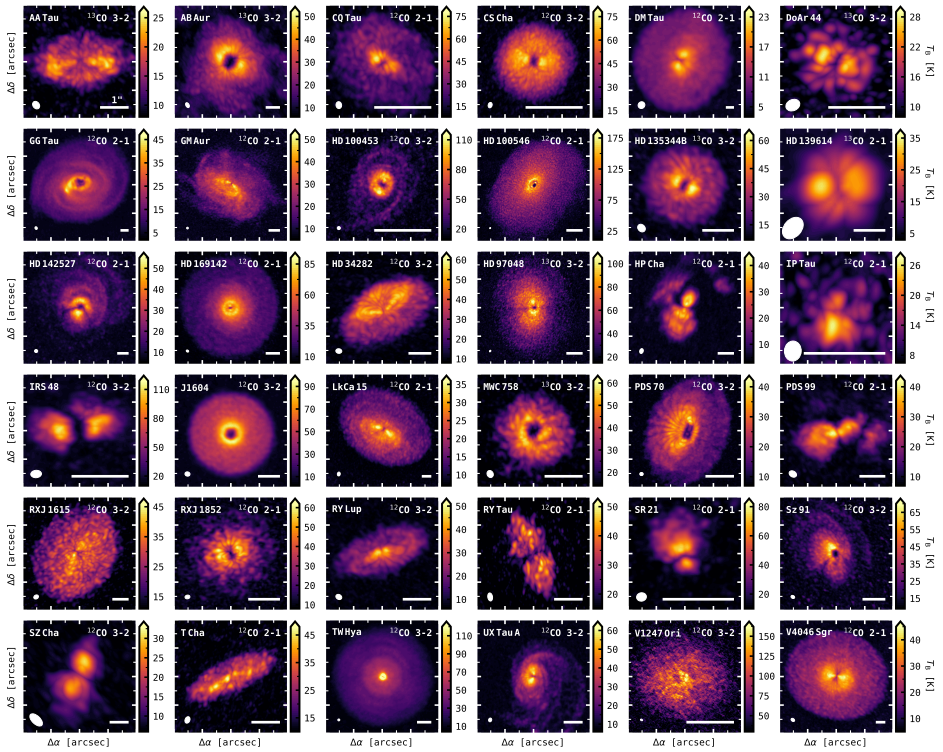

Figure 4.1: Peak brightness temperature maps of the gas emission in our targets, shown for the main CO lines used in this analysis. The conversion from peak intensity to units of Kelvin was done with the Planck law. The circle and bar in the bottom left and bottom right corner of each panel indicate the beam and a 1″ scale, respectively.

4.3 Observational results

4.3.1 Brightness temperature

In Fig. 4.1 we present the peak brightness temperature maps (continuum subtracted) for the main CO lines (mostly ^{12}CO and some ^{13}CO). Maps for the additional lines can be found in Figs. 4.E.1 and 4.E.2 in the Appendix. The maps presented in Fig. 4.1 are shown again in Fig. 4.A.1 with overlaid continuum images, illustrating that for most targets the dust disc (millimetre-sized grains, B6 and B7) is substantially smaller than the gas disc. This can readily be explained by radial drift processes and/or by the difference between dust and gas opacities (Facchini et al. 2017; Trapman et al. 2019).

To compute the peak intensity maps, we used the standard moment eight implementation in the BETTERMOMENTS code (Teague & Foreman-Mackey 2018) and then converted from flux density units to units of Kelvin with the Planck

law. No masking was applied in the computation of the maps. The brightness temperature traces a combination of kinetic gas temperature and column density, with the optically thick lines mostly measuring the temperature while the more optically thin lines mostly trace the column density. In this context, the observed gas temperatures of $\sim 30\,\mathrm{K}$ up to $\sim 200\,\mathrm{K}$ are as expected in the upper disc layers (see e.g., Bruderer 2013; Bruderer et al. 2014; Leemker et al. 2022). As discussed below, some of the discs show interesting features in their peak brightness temperature. Very massive companions are clearly observable from the peak brightness temperature due to their ability to induce spirals which are prominent enough to be observed with this data quality. Clear spiral structures can be discerned in GG Tau, HD 100453, HP Cha, and UX Tau A. GG Tau is (at least) a quadruple star system surrounded by a massive disc, with the substructures likely tracing star-disc or planet-disc interactions (Leinert et al. 1991; Dutrey et al. 2014a; Phuong et al. 2020a). HD 100453 and UX Tau A are also known to have stellar companions that are responsible for the observed spirals (Rosotti et al. 2020a; Ménard et al. 2020). HP Cha is affected by cloud absorption on the blueshifted side, but the extended (redshifted) structure suggests interactions with the environment such as infalling material from a streamer or a fly-by. Even though the disc around V4046 Sgr is also known to be circumbinary, no clear substructures can be seen. The reason for this is that the two stars in the system are orbiting each other at a small distance ($< 1\,\mathrm{au}$, $2.4\,\mathrm{d}$, Stempels & Gahm 2004), acting similar to a single gravitational point source on much larger scales.

Indications of spirals are visible in CQ Tau, where one side of the disc is substantially brighter, representing the anchoring point of the spiral (see Wölfer et al. 2021) as well as in HD 135344B and TW Hya. For HD 135344B, similar spiral features have been found by Casassus et al. (2021) in ^{12}CO 2-1 data. Other discs such as HD 142527 (in all CO isotopologues, Casassus et al. 2015; Garg et al. 2021; Yen & Gu 2020) or Sz 91 show arc-like azimuthal asymmetries. Tsukagoshi et al. (2019) explain the arc-like structure in Sz 91 with a flared disc, showing emission from the front and the back side, in combination with a dust ring.

In a couple of maps – for example of AB Aur, CQ Tau, or MWC 758 – symmetric dimmed regions are visible. Such features are commonly linked to the presence of a misaligned inner disc, casting a shadow over the outer disc (e.g., Marino et al. 2015; Facchini et al. 2018). Beam dilution effects can, however, cause artificial features along the minor axis (see example of CQ Tau in Wölfer et al. 2021), thus caution should be taken when interpreting these under-brightnesses. The misalignment hypothesis has recently been tested by Bohn et al. (2022) for a sub-sample of our discs by comparing the position angle and inclination of the inner disc measured with VLTI/GRAVITY and the outer disc measured with ALMA. Significant misalignments are found for CQ Tau, HD 100453, HD 142527, HD 34282, RY Lup, and V1247 Ori. Francis & van der Marel (2020) also find misalignments from ALMA inner disc images, which are significant for eight sources in either position angle or inclination (AB Aur, GG Tau, HP Cha, MWC 758, PDS 70, SR 24 S, TW Hya, and V4046 Sgr). In Fig. 4.2, some examples are given for the different features that can be observed in the brightness temperature. We note that arcs can also be seen as part of a spiral. In this work we identify spirals as structures covering a larger

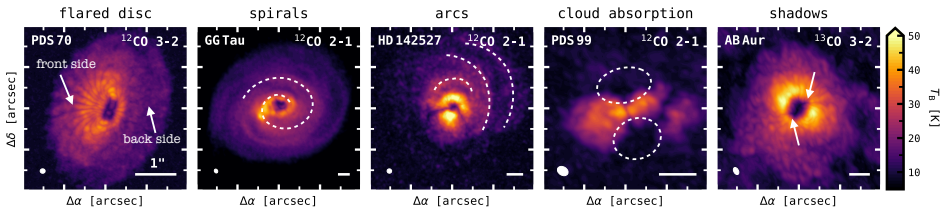

Figure 4.2: Examples of the different features seen in the brightness temperature of our sources. The circle and bar in the bottom left and bottom right corner of each panel indicate the beam and a 1″ scale, respectively.

range of radii, while arcs are mostly observed at one radius.

To uncover small substructures in the brightness temperature structure, we further analyse these maps in Sect. 4.4.1 by subtracting azimuthally symmetric brightness temperature profiles from the data.

4.3.2 Rotation velocity

In Fig. 4.3 we present the kinematics of our targets, again showing the main lines, while the additional lines can be found in the Appendix in Figs. 4.E.3 and 4.E.4. To compute the line-of-sight velocity of the gas, we used the quadratic method implemented in the BETTERMOMENTS package: a quadratic function is fitted to the brightest pixel in the spectrum as well as the two neighbouring pixels to find the centroid of the line in pixel coordinates. To reduce the noise at the disc edge, we applied a masking for regions below a certain signal-to-noise ratio (S/N). The magnitude of this clipping was obtained via inspection of each individual map, ranging between $2\,\sigma$ to $5\,\sigma$.

Even though the spiral features are not as prominent in the kinematics as in brightness temperature maps, they are still observable in GG Tau, HD 100453, HP Cha, and UX Tau A. CQ Tau, HD 135344B, and TW Hya show indications of spirals in the brightness temperature, in the kinematics these indications are only present for TW Hya. CQ Tau, however, shows twisted kinematics in the centre that resemble a warp, but are likely caused by the spiral structure (Wölfer et al. 2021). Clearly twisted kinematics can also be seen in the centre of HD 142527, for which several indications of a warped disc have been found (Marino et al. 2015; Casassus et al. 2015; Bohn et al. 2022).

For several discs with higher inclinations, the vertical structure becomes visible in the isovelocity curves bending away from the semi-major axis in one direction (e.g., AA Tau, GM Aur, HD 97048, LkCa 15, PDS 70, RY Lup, T Cha, and V1366 Ori). Fitting for this structure can be used to determine the flaring and scale height of the disc (e.g., Casassus & Pérez 2019; Teague et al. 2019a). Other more face-on or inclined, yet less elevated discs show a dipole morphology that is symmetric about the semi-major axis (e.g., AB Aur, CS Cha, HD 135344B, HD 139614, TW Hya, and V4046 Sgr).

To reveal possible deviations from Keplerian rotation that may be indicative of

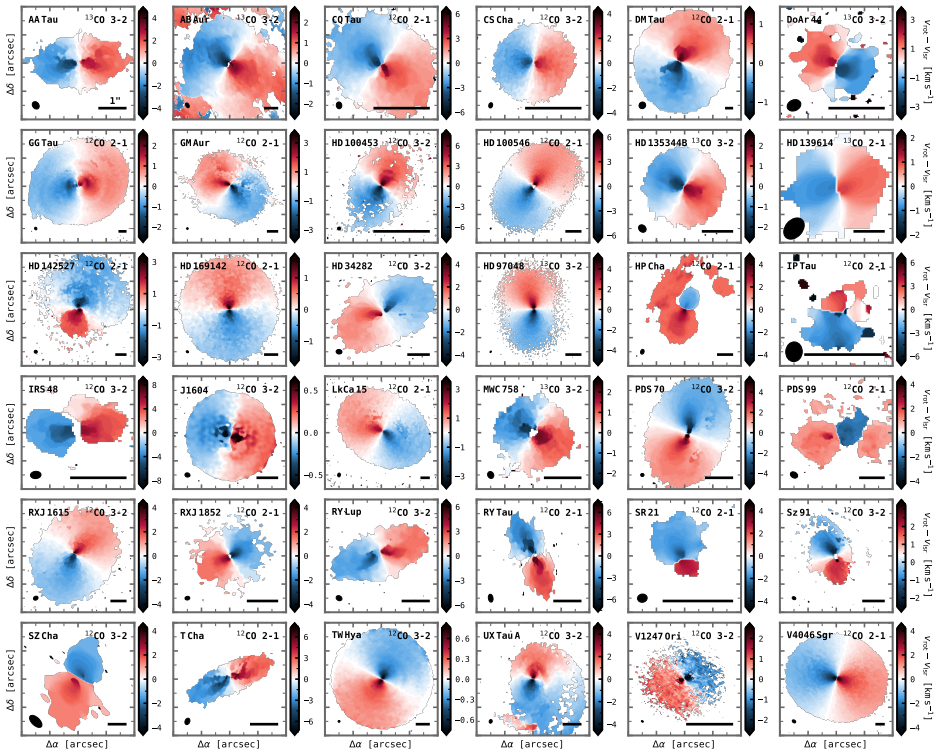

Figure 4.3: Rotation velocity maps of the gas emission in our targets, shown for the main CO lines used in this analysis. The maps were computed with BETTERMOMENTS. The circle and bar in the bottom left and bottom right corner of each panel indicate the beam and a 1″ scale, respectively.

the presence of companions, we attempt to fit a Keplerian model to the rotation velocity of the discs in Sect. 4.4.2 assuming thin and thick disc geometries.

4.3.3 Radial profiles

In Fig. 4.4, the radial peak intensities are displayed for the different CO lines (coloured lines) as well as the millimetre continuum (black lines). These curves were calculated by azimuthally averaging the peak intensities for radial annuli of an equal width, using the GOFISH package (Teague 2019). By default, the widths of the annuli in this package are given as one-fourth of the beam major axis. For the computation we assumed the geometries (thin or thick disc) obtained from the fitting of the rotation maps (see Sect. 4.4.2). For both geometries we recovered similar radial profiles (due to similar fits, see discussion in Sect. 4.4.2) and thus the curves are only shown for the thin disc geometry in Fig. 4.4. All profiles are plotted normalized to the peak value. The uncertainties, shown as shaded regions, correspond to the standard deviation per annulus divided by the square root of

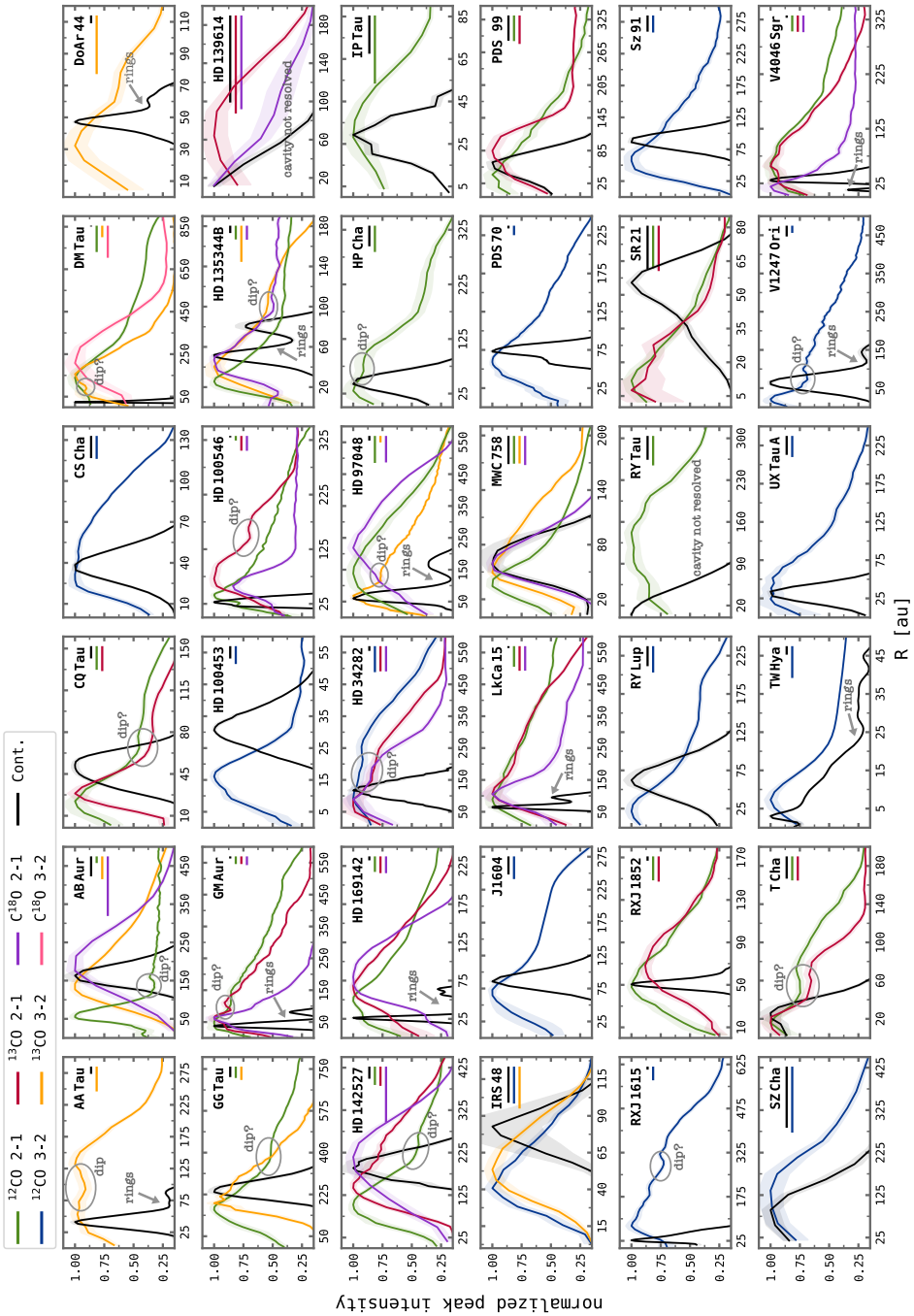

Figure 4.4: Azimuthally averaged and normalized radial peak intensity profiles for the different CO lines (coloured lines) and continuum emission (black lines). The major beam of each observation is indicated by the bars in the top right corner. Some features of the profiles are annotated in the individual panels.

the number of independent beams in the annulus. Some discs in our sample are affected by cloud absorption, which can result in an artificially lower brightness temperature and a larger azimuthal scatter. We therefore excluded the affected azimuthal angles from our calculation. The beam size of the continuum and lines is indicated by a coloured bar in each panel. The interpretation of radial profiles depends on the resolution. Given the inhomogeneity of our sample in that regard, the trends reported below may be subject to change with higher and comparable resolutions. The main features of the profiles are annotated in the individual panels of Fig. 4.4.

The radial profiles can be used to estimate the size of the cavity (steep emission drop). In this context, it is important to note that artificial cavities can be created in the peak intensity, depending on the beam size. Near the star the emission is less extended than the beam size and during the beam convolution the intensity gets diluted over the full extent of the beam, hence the peak intensity decreases. When studying the inner disc, it is therefore important to look at the velocity-integrated intensity, which is less affected by this issue. However, for the integrated intensity, there may be contributions from the back side of the disc (Rab et al. 2019). The radial profiles for the integrated intensity are shown in the Appendix in Fig. 4.F.1.

The measured brightness temperature is also affected by the subtraction of the continuum (except for HD 97048, all data are continuum subtracted). For optically thick lines, which absorb part of the underlying continuum, line emission may be removed when subtracting the continuum, leading to artificial temperature drops (e.g., Weaver et al. 2018; Rosotti et al. 2021; Bosman et al. 2021). Since in this work we are mostly interested in substructures rather than obtaining a robust measurement of the temperature, we do not expect this effect to significantly affect our results.

As is visible in Fig. 4.4 (and Fig. 4.F.1), the CO emission peaks inside the dust cavity for most discs, which is as expected from previous work (Bruderer 2013; van der Marel et al. 2016). For a few discs, such as HD 139614, the inner dust cavity is not resolved due to limited resolution. The radial profiles can further show dips or wiggles, especially in the dust indicating ring structures and depleted regions. It is important to note that it is also possible that instead of a dip, an enhanced desorption of CO ices by increased UV or a temperature inversion in the outer disc (more optically thin) at the edge of the continuum can result in an enhancement of gas emission (e.g., Cleeves et al. 2016; Facchini et al. 2017).

4.4 Analysis

4.4.1 Brightness temperature structure

To uncover possible substructures in the brightness temperature, we constructed an azimuthally symmetric model with GOFISH and subtracted this model from the data. The package computes an azimuthally averaged radial profile for a given geometry (compare Sect. 4.3.3) and then projects it onto the sky to create an azimuthally symmetric model. For the disc geometry, we used the results for the thin and (if available) the vertically extended thick disc from the kinematics

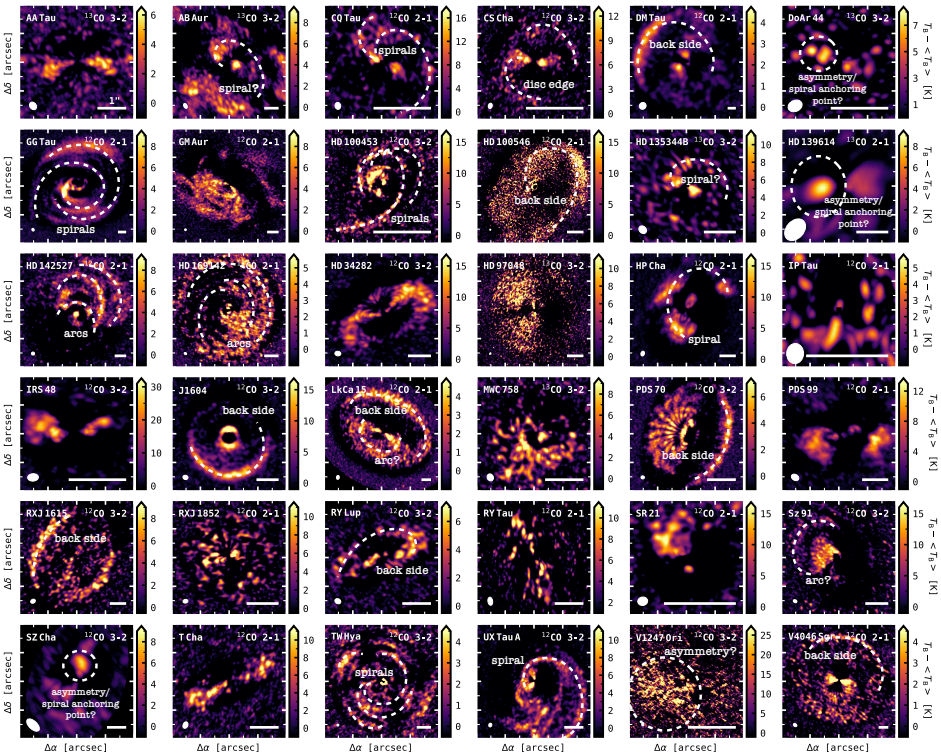

Figure 4.5: Brightness temperature residuals obtained with GOFISH, shown for the main CO lines used in this analysis and for a geometrically thin disc approximation. The circle and bar in the bottom left and bottom right corner of each panel indicate the beam and a 1″ scale, respectively. The main features are annotated.

modelling described in Sect. 4.4.2. The angles affected by cloud absorption were again excluded from the calculation. The resulting residuals are presented in Fig. 4.5 for the geometrically thin disc and in the Appendix for the geometrically thick disc models (Fig. 4.B.1). The colour scale has been adapted such that regions with hotter temperatures than the model are highlighted. In this work we are mostly interested in the general occurrence of features such as spirals and therefore this choice was made to help the readability of the plot. Residuals for the other CO lines can also be found in the Appendix. The main features are annotated in the individual panels and further discussed in Sect. 4.5.

4.4.2 Velocity structure

To analyse the gas kinematics of our sample, we used the EDDY code (Teague 2019) to fit a Keplerian profile

$$v_{\rm rot}(r,\phi) = \sqrt{\frac{GM_*}{r}} \cdot \cos\phi \cdot \sin i + v_{\rm LSR}, \tag{4.1}$$

with (r, ϕ) being the deprojected cylindical coordinates, i the inclination of the disc, and $v_{\rm LSR}$ the systemic velocity, to the rotation maps shown in Fig. 4.3. To deproject the sky-plane coordinates (x, y) into the midplane cylindrical coordinates (r, ϕ), the disc centre (x_0, y_0), i, and the disc position angle PA were used. The latter is measured between the north and the redshifted semi-major axis in an easterly direction. As a first step, the starting positions of the free fit parameters were optimized with `scipy.optimize` and their posterior distributions were estimated using the Markov chain Monte Carlo (MCMC) sampler.

In addition to the model for a geometrically thin disc, EDDY also includes the possibility to fit for the vertical structure of the disc. To parameterize the emission layer, we chose a simple model of a flared disc described by

$$z(r) = z_0 \cdot \left(\frac{r}{1''}\right) \cdot r^{\psi}, \tag{4.2}$$

where z_0 describes the elevation and ψ the flaring angle of the emission surface.

In the modelling process, we fixed the object's distance and stellar mass, taken from the literature, and fitted for the disc centre ($x_0, y_0 \in [-0\farcs5, 0\farcs5]$), systemic velocity ($v_{\rm LSR} \in [v_{\rm min}(\rm data), v_{\rm max}(\rm data)]$), inclination ($i \in [-90\,^\circ, 90\,^\circ]$), and disc position angle (PA $\in [-360\,^\circ, 360\,^\circ]$) as well as surface elevation ($z_0 \in [0, 5]$) and flaring angle ($\psi \in [0, 5]$) in the geometrically thick disc approximation. We also conducted runs where the inclination was fixed instead of the stellar mass and where both the inclination and the stellar mass were left as free parameters. Overall the results are very similar for these different cases and in the following we only show the results for the models where the stellar mass was fixed.

For most targets we downsampled the data by a factor of 2–4 before fitting. We fitted for the whole disc, choosing an outer radius depending on the disc size to exclude possible noise at the disc edge and an inner radius of twice the beam major axis to exclude regions that are strongly affected by beam smearing. For a few cases, where the beam is very large, we slightly reduced this inner radius to ensure a reasonable number of pixels to fit. For all models we used 100 walkers, 8000 steps to burn in, and 2000 additional steps to sample the posterior distribution function and assumed flat priors that were allowed to vary over a wide range. The uncertainties of the posterior distributions represent the 16th to 84th percentiles about the median value. The uncertainties on the kinematics, computed with BETTERMOMENTS, were included in the fit and are shown in Fig. 4.C.1. They mostly lie well below the channel width, but they increase in the central regions due to beam smearing.

While most models converged rapidly within a couple 100 steps, none of the models for HP Cha converged. Furthermore, the models considering the vertical structure of the disc – despite rapidly converging – often do not match the bending of the isovelocity curves clearly seen in the data of the higher-inclination discs and return substantially smaller values for the elevation and flaring than expected. We tried both orientations of the inclination (positive and negative) in this context. For highly inclined sources, the back side becomes prominently visible, resulting in a quadrupole morphology. However, this was fit with a dipole morphology and therefore the best fit lies between the two lobes of the quadrupole morphology,

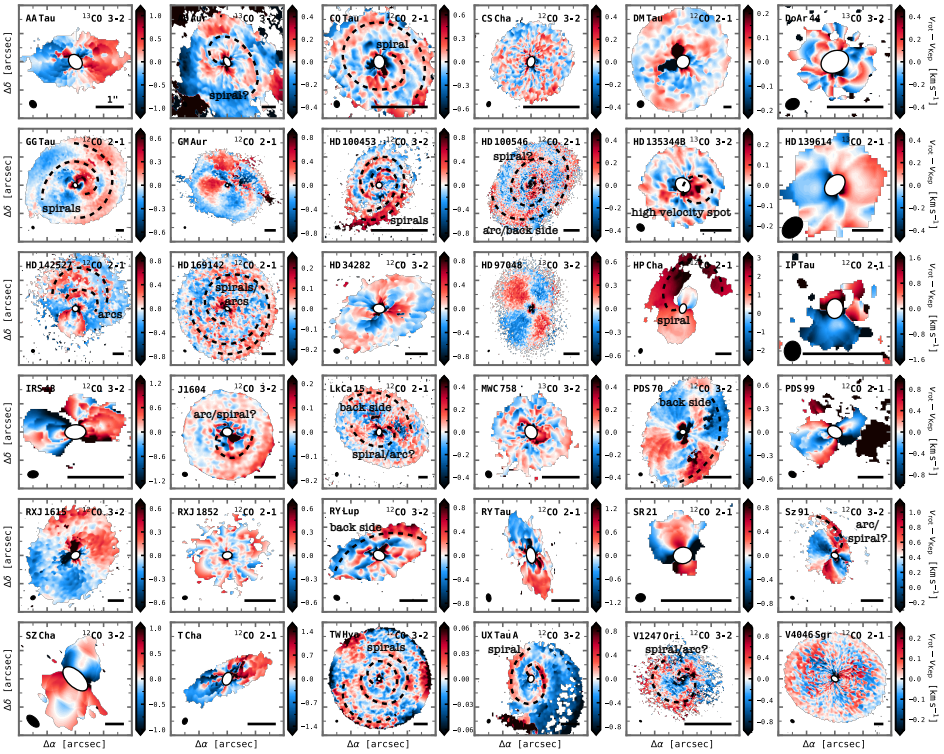

Figure 4.6: Rotation velocity residuals obtained with EDDY, shown for the main CO lines used in this analysis and for a geometrically thin disc approximation. The circle and bar in the bottom left and bottom right corner of each panel indicate the beam and a 1″ scale, respectively. The main features are annotated.

representing the average of the front and back side of the disc. The residuals of these models thus resemble those of the flat disc (see Figs. 4.6 and 4.B.1). Higher spectral and spatial resolution data and individual modelling of the two disc sides (front and back) may be required to find a better fit for the vertical structure (e.g., directly from the channel maps).

In Fig. 4.6, the residuals after subtraction of the Keplerian model from the data are shown for the geometrically thin disc approximation. The residuals of the vertically extended disc approximation of the main CO lines are presented in Fig. 4.B.1. Again, the residuals for the other CO lines can be found in the Appendix. In the plots we have masked out disc regions inside of twice the beam, since these are strongly affected by beam smearing and not included in the fit. The main features are again annotated in the individual panels and further discussed in the following section. Same as for the brightness temperature residuals, we have marked the substructures found in the positive residuals. While it is interesting to study both the positive and negative residuals, the interpretation of these structures is not straightforward and a lot of effort is currently put into

understanding the different patterns, which will be part of upcoming works. In contrast to that, this work aims to compare the different substructures found in the gas of circumstellar discs that may be indicative of embedded planets.

4.5 Discussion

The residuals presented in Figs. 4.5 and 4.6 show various features that are annotated in the different panels. For the discs that show very clear substructures (see Sect. 4.5.1), the different maps and radial profiles are collected again in Fig. 4.7.

For several higher-inclination discs, the vertical structure is still clearly visible in the residuals in form of a butterfly-like pattern even after subtraction of a geometrically thick disc model (e.g., AA Tau, HD 34282). As previously mentioned, most of these fits returned only slightly elevated emission surfaces and are not able to reproduce the actual vertical structure of the disc. For these geometrically thick disc models, still only a single side of the disc has been modelled; whereas, for the highly inclined discs, both the front and back sides are visible. An approach modelling both sides independently (such as used in the Discminer, Izquierdo et al. 2021) would be needed to avoid this problem. Connected to that, in a few cases, arc features can be seen at the disc edge, which result from looking into the back side of the disc (e.g., J1604, LkCa 15, and PDS 70).

In Table 4.3 we list some features that may be indicative of interactions between the disc and planets and/or stellar companions. Here, a green check mark stands for the detection of a feature, a red cross identifies a non-detection, and brackets indicate a tentative detection. Especially if several features are observed in the same disc, this is a strong indication that we are tracing embedded planets or companions. As a deep gas cavity, we have marked cases where a clear drop is seen in the radial profile of the peak and integrated intensity for at least the more optically thin lines that tend to trace the column density. In a few cases, such as LkCa 15 or HD 34282, no steep drop is discerned, but the gas cavity is very extended and better data are needed to confirm if a deep cavity is present (Leemker et al. 2022). In this work we do not investigate the presence of kink features and thus these are missing as a possible planet signpost in Table 4.3. While Pinte et al. (2020) report the detection of such azimuthally located features in about half of the discs in the DSHARP programme (Andrews et al. 2018), more data are needed to confirm the robustness of such claims and it is difficult to draw conclusions on the presence of kinks in our sample, given the inhomogeneity of spatial and spectral resolutions. Furthermore, the interpretation of kink features is not straightforward as they can be caused by a gap or density substructure rather than a planet (Izquierdo et al. 2021). More detailed studies (beyond the scope of our work) of a homogenous data set at high resolution are needed to test for such scenarios. In the following, we describe the observed structures in more detail.

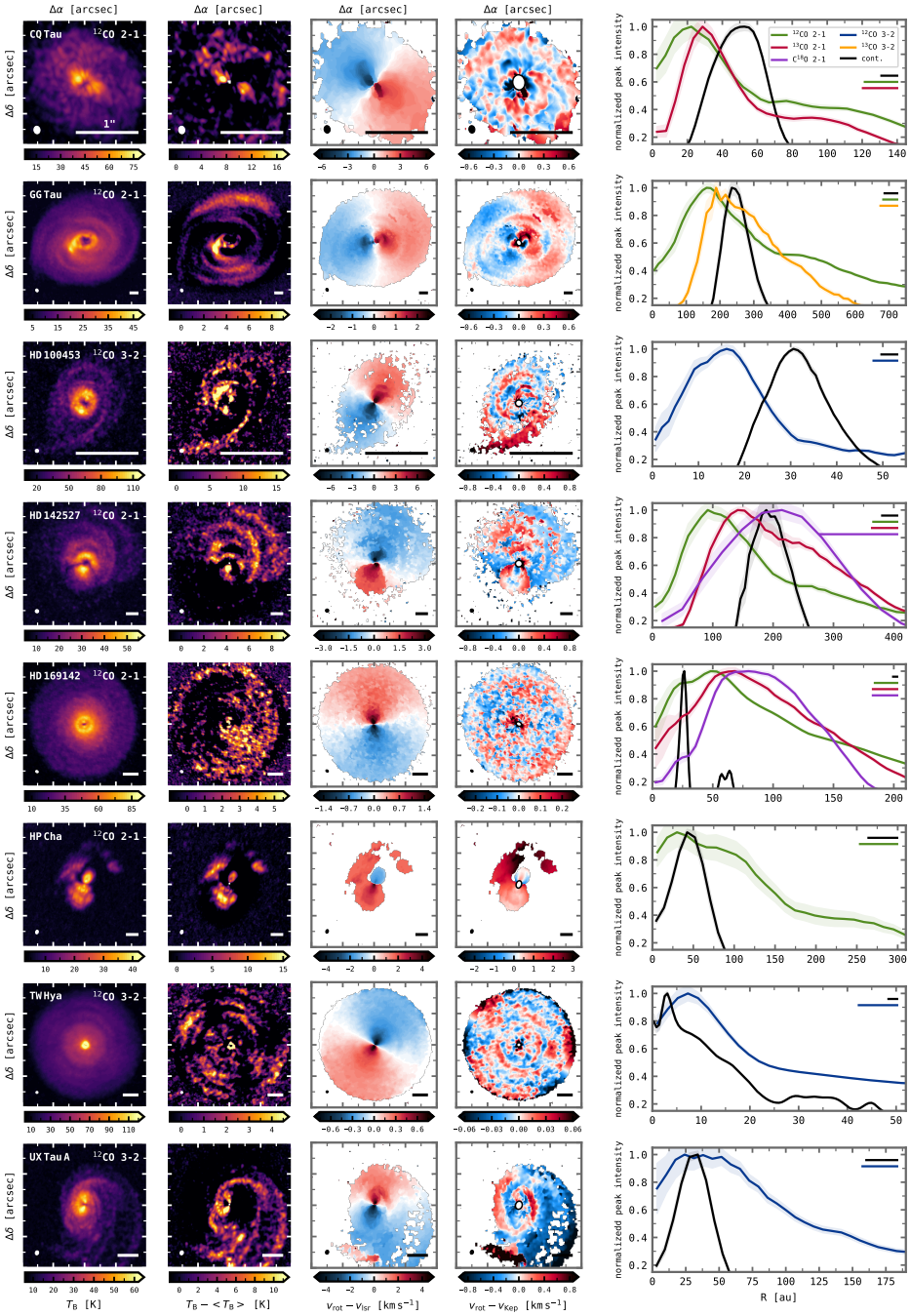

Figure 4.7: Brightness temperature and velocity maps as well as their corresponding residuals and radial profiles, shown for the eight targets with the clearest substructures. The circle and bar in the bottom left and bottom right corner of the maps indicate the beam and a 1″ scale, respectively. For the radial profiles, the major beam of each observations is indicated by the bars in the top right corner.

Table 4.3: Summary of the various features which are exhibited by our targets and may be indicative of embedded planets.[a]

Source	Deep gas cavity	T_B spirals/arcs	v_{rot} spirals/arcs	NIR spirals	NIR shadows	Misalignment[b] inner/outer	Comments	Ref.
AA Tau	✗	✗	✗	-	-	-		
AB Aur	✓	(✓)	(✓)	✓	✗	✓ (A)		1
CQ Tau	✓	✓	✓	✓	✓	✓ (A+G)		2
CS Cha	✓	✗	✗	✗	✗	-		3
DM Tau	✗	✗	✗	-	-	-	low res.	
DoAr 44	✓	(✓)	✗	✗	✓	-		2
GG Tau	✓	✓	✓	✓	✓	✓ (A)	multiple	4
GM Aur	✓	✗	✗	✗	✗	✗ (A+G)		2
HD 100453	✓	✓	✓	✓	✓	✓ (A+G)	binary	2
HD 100546	✓	✗	(✓)	✓	✗	-		2,5
HD 135344B	✓	(✓)	(✓)	✓	✓	-		2
HD 139614	✗	(✓)	✗	✗	✓	-	low res.	2
HD 142527	✓	✓	✓	✓	✓	✓ (A+G)	binary, warp cloud absorption	2
HD 169142	✓	✓	✓	✗	(✓)	-		2,6
HD 34282	(✓)	✗	✗	✗	✗	✓ (A+G)		2
HD 97048	✓	✗	✗	✗	✗	-	cloud absorption	2
HP Cha	✗	✓	✓	-	-	✓ (A)	cloud absorption	
IP Tau	✗	✗	✗	✗	✗	✗ (A+G)	cloud absorption	2
IRS 48	✓	✗	✗	-	-	-	cloud absorption	
J1604	✓	✗	(✓)	✗	✓	-		7
LkCa 15	(✓)	(✓)	(✓)	✗	(✓)	-		2,8
MWC 758	✓	✗	✗	✓	✗	✓ (A)		9
PDS 70	✓	✗	✗	✗	✗	✗ (A+G) , ✓ (A)	imaged planets	2

Table 4.3 continued.

Source	Deep gas cavity	T_B spirals/arcs	v_{rot} spirals/arcs	NIR spirals	NIR shadows	Misalignment[b] inner/outer	Comments	Ref.
PDS 99	✓	✗	✗	-	-	-	cloud absorption	
RXJ 1615	✗	✗	✗	✗	✗	✗ (A+G)		2
RXJ 1852	✓	✗	✗	✗	✗	-		10
RY Lup	✗	✗	✗	(✓)	✗	✓ (A+G)		2,11
RY Tau	✗	✗	✗	✗	✗	-		12
SR 21	✗	✗	✗	✓	✗	-	cloud absorption	13
Sz 91	✓	(✓)	(✓)	✗	✗	-	cloud absorption	14
SZ Cha	✗	(✓)	✗	✗	✓	✗ (A+G)	low resolution cloud absorption	2
T Cha	✗	✗	✗	✗	✗	-		6
TW Hya	✗	✓	✓	✗	✗	✓ (A)		16
UX Tau A	✗	✓	✓	✓	✗	-	binary	2
V1247 Ori	✗	(✓)	(✓)	✓	✓	✓ (A+G)		2
V4046 Sgr	✗	✗	✗	✗	✗	✓ (A)	binary	17

Notes. [a] Green checkmarks point out a detection, red crosses a non-detection, and brackets indicate if a detection is tentative. The absence of substructures does not necessarily imply the absence of a companion/planet but may be a resolution/sensitivity effect. [b] A: Obtained from ALMA continuum data in Francis & van der Marel (2020), A+G: Obtained from ALMA CO and GRAVITY data in Bohn et al. (2022).

References. For spirals and shadows observed in the NIR scattered light. (1) Boccaletti et al. (2020); (2) Bohn et al. (2022) (original reference can be found in this paper); (3) Ginski et al. (2018); (4) Keppler et al. (2020); (5) Garufi et al. (2016); (6) Pohl et al. (2017); (7) Pinilla et al. (2018); (8) Thalmann et al. (2016); (9) Benisty et al. (2015); (10) Villenave et al. (2019); (11) Langlois et al. (2018); (12) Takami et al. (2013); (13) Muro-Arena et al. (2020); (14) Tsukagoshi et al. (2014); (15) Pohl et al. (2017); (16) de Boer et al. (2020); (17) Avenhaus et al. (2018).

4.5.1 Clear spiral or arc-like features

A few discs show clear spiral or arc-like structures in both the brightness temperature and the velocity residuals (Fig. 4.7): CQ Tau (Wölfer et al. 2021), GG Tau, HD 100453 (Rosotti et al. 2020a), HD 142527 (Garg et al. 2021), HD 169142, HP Cha, TW Hya (Teague et al. 2019b), and UX Tau A (Ménard et al. 2020). Half of these discs (CQ Tau, GG Tau, HD 100453, and HD 142527) are also marked by a spiral in the NIR, deep gas cavities, shadows in the NIR, and a misalignment between the inner and outer disc (Francis & van der Marel 2020; Bohn et al. 2022). These four systems represent the best candidates for planet-disc or companion-disc interactions. In the cases of GG Tau, HD 100453, and HD 142527, binary components are indeed known, likely causing (at least part of) the observed spiral structures. Among these eight discs, HD 142527 and HP Cha are affected by cloud absorption on the redshifted and blueshifted sides, respectively; however, this is unlikely to explain the arc features on the blueshifted side of HD 142527 or the redshifted spiral in HP Cha.

4.5.2 Tentative spiral or arc-like features

Some of the discs show tentative features (spirals, arcs, or bright spots): for AB Aur, HD 135344B (see also Casassus et al. 2021), LkCa 15, Sz91, and V1247 Ori these are seen in both the brightness temperature and the velocity, with the ones in AB Aur and HD 135344B, which are also marked by most other features, being the most convincing. In addition to that, features are present in the brightness temperature residuals of DoAr 44, HD 139614, and SZ Cha and in the velocity residuals of HD 100546 and J1604. Most of these discs have deep gas cavities and are marked by shadows in the NIR; for the other cases (e.g., HD 139614 or SZ Cha), a deep cavity may be resolved with higher spatial resolution. Four of the ten sources with tentative features exhibit spirals in the NIR. It is important to note that some of the arc features may result from the misfit of the vertical structure (or other disc parameters) rather than dynamical interactions (see Fig. 12 in Yen & Gu 2020). Furthermore, some discs are strongly marked by cloud absorption. For example, the asymmetries seen in the brightness temperature of SZ Cha may result from this effect. For AB Aur, HD 100546, HD 139614, HD 135344B, and Sz 91, the residuals of the additional lines (shown in the Appendix) partly support the detection of the described features.

4.5.3 No spiral or arc-like features

Among the remaining sources that do not show any substructures in the kinematics or brightness temperature, most are in general marked by only a few of the indicators listed in Table 4.3 (except for a deep gas cavity). The only sources that have clearly observed NIR spirals are MWC 758 and SR 21. The lack of substructures in the brightness temperature and kinematics does not necessarily imply that there are no planet–disc interactions, but they may be unresolved instead. Besides simply being an effect of missing spatial or spectral resolution, the position and mass of an embedded planet can also result in the absence of detectable

substructures. For example, a planet closer to the star embedded in a deep cavity is more difficult to trace with the chosen methods, which are mostly able to reveal substructures on larger scales. To confirm the presence or absence of features and identify different trends, more homogeneous follow-up observations are needed.

4.5.4 Conclusive remarks

Within our sample, eight discs are marked by clear substructures. In all cases, features are seen in the gas temperature and the kinematics – indicating a connection – alongside other substructures in the gas and dust. Ten other discs show tentative features, of which half present signatures in the brightness temperature and kinematics simultaneously. Half of our sample is not showing any substructures in the ALMA data besides a deep gas cavity.

Except for MWC 758 and SR 21, all targets that exhibit clear spirals in NIR scattered light show at least tentative features in the brightness temperature and/or kinematics. Scattered light is tracing the hot upper disc layers, most likely to show spirals, and since ^{12}CO is also tracing the disc surface, we expect to observe these features there as well (Law et al. 2021b). However, many of the tentative features in our sample are not spirals, which is likely related to poor spatial resolutions as well as cloud absorption in some cases. To resolve the spirals expected from the NIR, high sensitivity and spectral and spatial resolution ALMA data are crucial. For the targets showing cloud absorption, deep observations of the less affected ^{13}CO may help to resolve clear substructures. Two targets (HP Cha and TW Hya) show clear spiral structures without a counterpart having been observed yet in the NIR.

It is expected that substructures such as spirals are more likely found in systems with high luminosity and a wide cavity, where the upper disc layers can reach higher temperatures, making it much easier to observe them (e.g., Garufi et al. 2018; van der Marel et al. 2021). We searched for such correlations in our data set: while we did not find any clear trends, most discs that show no spiral substructures indeed represent the less massive, cooler, and less luminous stars, and features tend to become more visible for the more luminous sources. Given, however, the inhomogeneity of our sample, we expect a large observational bias and, to draw clear conclusions on correlations, it is crucial to study a more uniform (in terms of resolution) data set that includes a wide range of spectral types and stellar masses. As shown for TW Hya, for which very high sensitivity data exist at high spatial resolution ($\sim$ 8 au), substructures can still be distinguished despite a sub-solar stellar mass and an almost face-on disc. To understand if there exist differences between the different stellar groups, comparable observations are essential.

Connected to that, the lack of features cannot be seen as an indication of missing embedded planets. PDS 70, for example, hosts two confirmed massive planets, which have been directly imaged, but it does not show any other features in our data despite a deep gas cavity. This is likely because the planets are located further inside the cavity in this system and higher sensitivity plus resolution observations are needed to reveal substructures, which are related to dynamical interactions, in the temperature and the kinematics.

Furthermore, as shown by Izquierdo et al. (2021), an embedded planet has to be rather massive to excite strong observable signatures in the kinematics: from simulations the authors find strong perturbations for planets more massive than $1\,M_{\rm J}$; however, to pick these up in ALMA data, very high spectral and spatial resolution is essential. Thus it is not surprising that in our sample the clearest features are seen in the multiple star systems.

4.6 Summary

In this work, we have analysed the brightness temperatures and kinematics of a sample of 36 large cavity transition discs, representing the best candidates to search for dynamical interactions. Our main results are summarized as follows.

- Eight discs out of our sample show significant perturbations in both the brightness temperature and velocity residuals, while no features are seen in half of the sample at the current (spatial and spectral) resolution and sensitivity.
- Several discs show tentative features that need to be confirmed with deep, high resolution ALMA observations in the upcoming years.
- Almost all targets that exhibit spirals in NIR scattered light show at least tentative features in the CO data.
- In most cases our method reveals deviations that are caused by sub-stellar companions.
- For about 60 % of the sources, a deep gas cavity is resolved in addition to the dust cavity at the current spatial resolution.

To detect planets in the Jupiter-mass range, the available observations are neither deep enough nor do they have the required spatial and spectral resolution, explaining the lack of features in many discs. Upcoming and future deep ALMA observations at high spectral and spatial resolution together with dedicated modelling efforts may reveal more of such features and help to disentangle different formation scenarios.

Acknowledgements

We greatly thank the referee Ruobing Dong for his helpful feedback that improved the quality of this work. We also would like thank all the people that kindly provided the re-imaged/self-calibrated data sets. This paper makes use of different ALMA data sets, detailed in Tables 4.2 and 4.E.1. ALMA is a partnership of ESO (representing its member states), NSF (USA) and NINS (Japan), together with NRC (Canada) and NSC and ASIAA (Taiwan) and KASI (Republic of Korea), in cooperation with the Republic of Chile. The Joint ALMA Observatory is operated by ESO, auI/NRAO and NAOJ.

Appendix

4.A Continuum

Figure 4.A.1 shows the peak brightness temperature maps of the main lines used for the analysis in this work with overlaid millimetre continuum (either ALMA B6 or B7). For most cases, the size of the dust disc is substantially smaller than that of the gas disc.

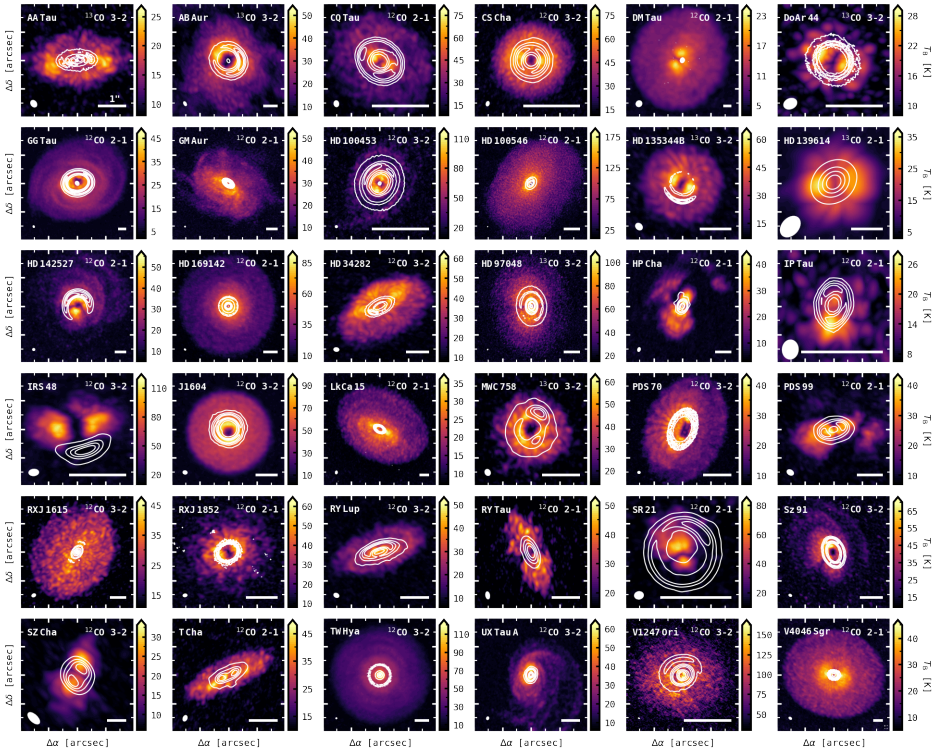

Figure 4.A.1: Peak brightness temperature maps of the gas emission in our targets, shown for the main CO lines with the continuum overlaid as white contours. Five contour levels are equally spaced between $3\,\sigma$ and the peak flux of the continuum. The circle and bar in the bottom left and bottom right corner of each panel indicate the beam and a $1''$ scale, respectively.

4.B Thick disc residuals of the main lines

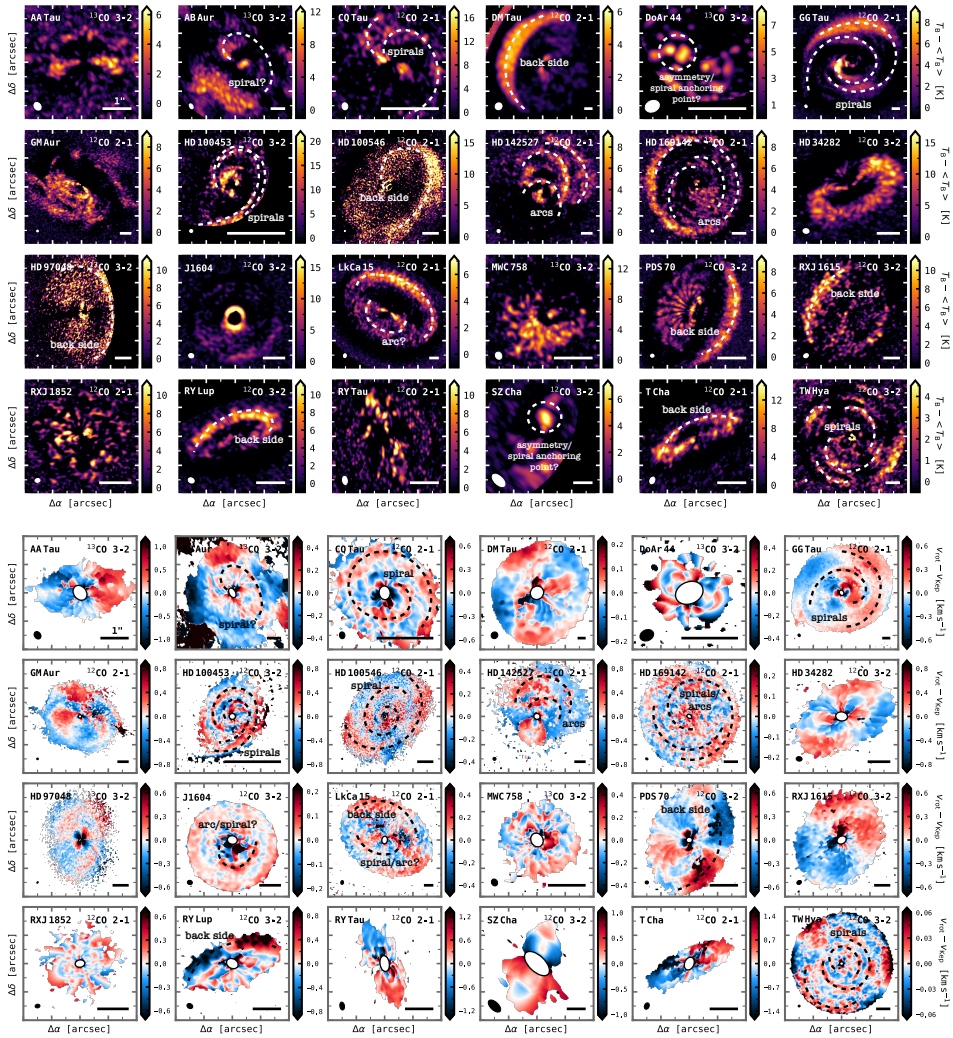

Figure 4.B.1: Brightness temperature (top) and rotation velocity (bottom) residuals, shown for the main lines used in this analysis and for a thick disc geometry. The circle and bar in the bottom left and bottom right corner of each panel indicate the beam and a 1″ scale, respectively. Some features are annotated.

4.C Uncertainties of the rotation velocity

In Fig. 4.C.1, we show the uncertainties of the kinematics for the main lines, computed with BETTERMOMENTS. These statistical uncertainties were calculated by linearising and propagating the uncertainty from the fluxes to the centroid estimate. The uncertainties mostly lie well below the channel width, but increase in the central regions due to beam smearing. For lower sensitivity observations, thermal broadening plays an important role, significantly increasing the uncertainties.

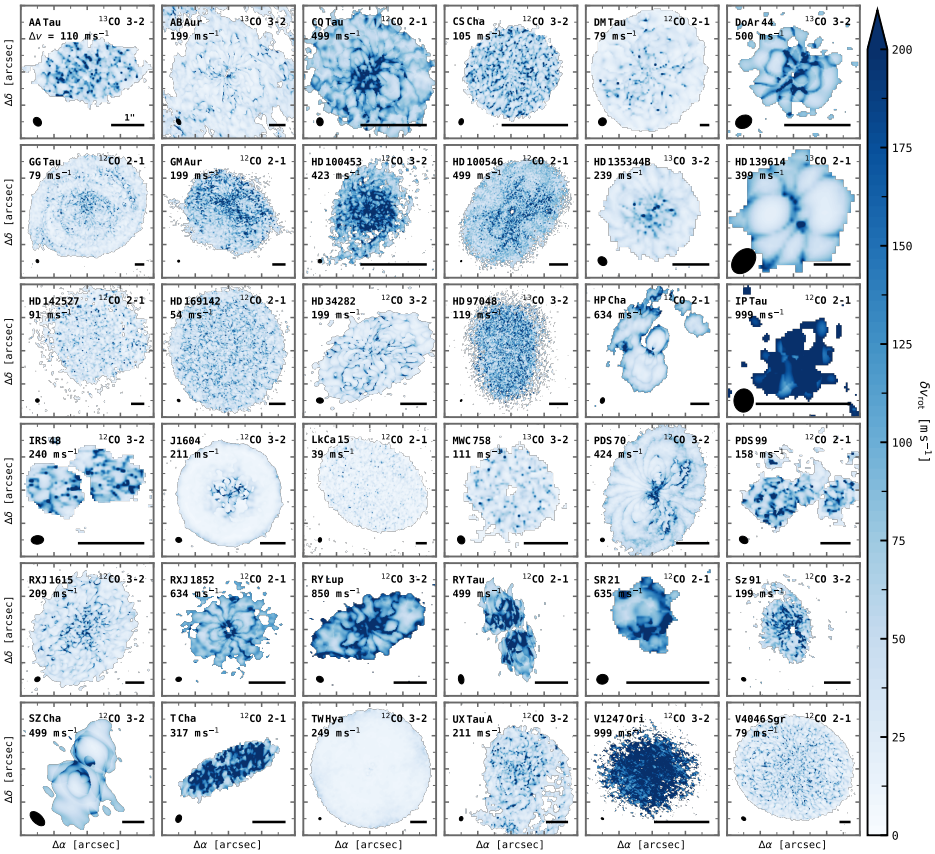

Figure 4.C.1: Kinematical uncertainties of the main lines of this analysis, computed with BETTERMOMENTS. The circle and bar in the bottom left and bottom right corner of each panel indicate the beam and a 1″ scale, respectively. The channel spacing is shown in the top left corner of each panel.

4.D Re-imaged and archival data products comparison

In this work, we have combined re-imaged with archival data products and it is important to understand what impact this has on the results. When re-imaged sets were available, we conducted our analysis for both the re-imaged and the according archival image cubes and compared the results. A few examples are shown in Fig. 4.D.1 for a disc with clear spirals, two discs with tentative spirals, and one without any observed features. We find that the fitting procedure is not significantly affected by the choice of cube: the detection of clear spirals as well as a non-detection do not depend on the data set. Due to an increased S/N, tentative features come out stronger (e.g., J1604) and in some cases only become visible (e.g., HD 135344B) in the re-imaged products, thus some tentative substructures may be hidden in the cases that we classify as non-detections, when the archival product data were used.

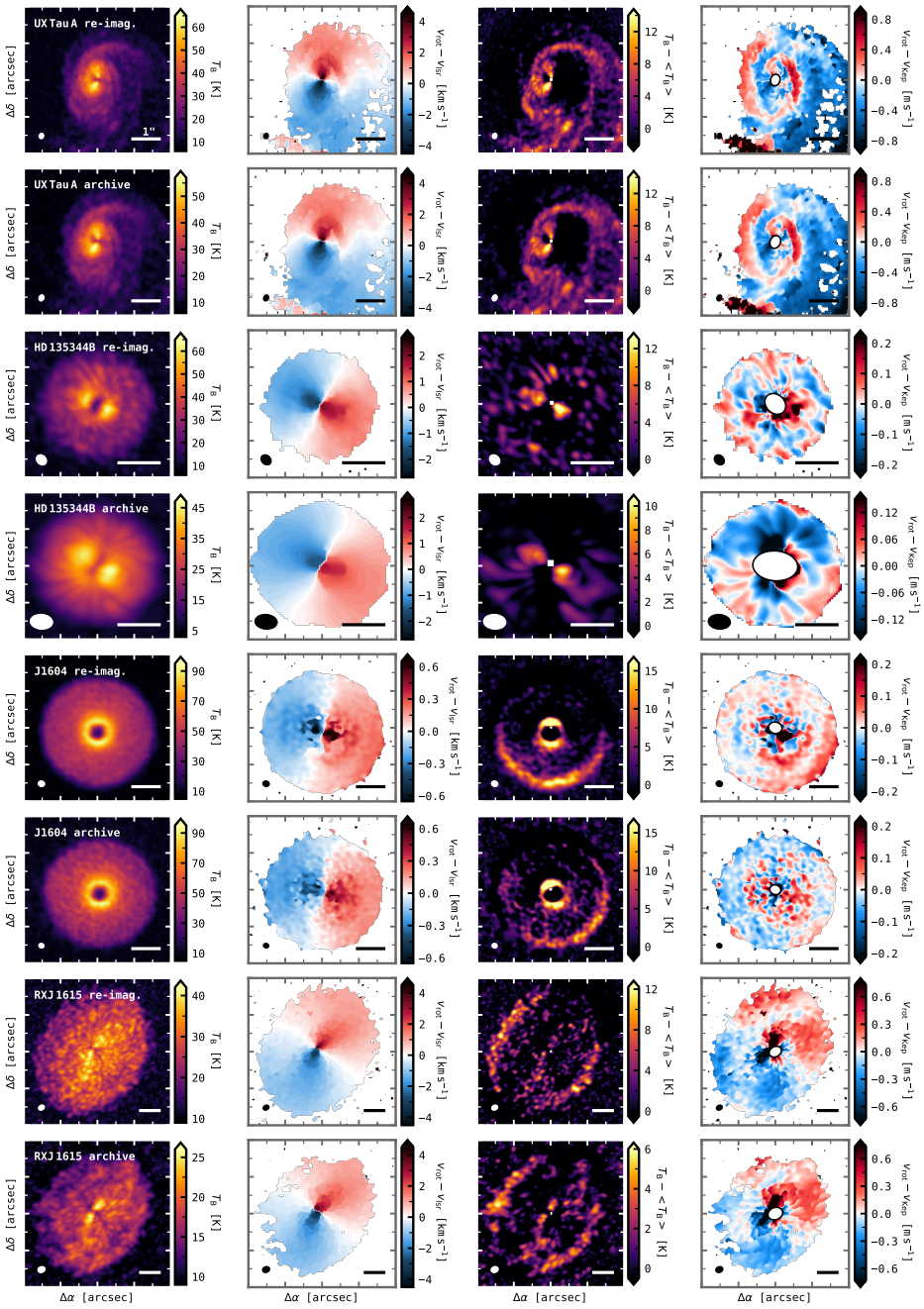

Figure 4.D.1: Comparison between the re-imaged and archival data for four sample sources, including one with clear spirals, two with tentative features, and one without any features. The circle and bar in the bottom left and bottom right corner of each panel indicate the beam and a 1″ scale, respectively.

4.E Additional lines

This appendix comprises the results for the additional lines used in this work. When studying substructures in discs, it is useful to look at various molecular tracers that probe different disc layers. Understanding if and how substructures vary vertically and radially can be used to assess the underlying perturbation. For example, in a passively heated disc with a vertical temperature gradient, the opening angle of a spiral is expected to decrease towards the midplane; whereas, for spirals launched by gravitational instability the midplane would be heated by shocks, resulting in similarly wound spirals throughout the disc (Juhász & Rosotti 2018).

4.E.1 Characteristics

Some characteristics of the data are listed below in Table 4.E.1. In most cases, the archival data products were used for the analysis, as indicated in the last column.

Table 4.E.1: Characteristics of the additional ALMA line data.

Object	Line	Project ID	Beam (″)	Δv (km s^{-1})	RMS (mJy beam^{-1})	source$^{(a)}$
ABAur	^{12}CO 3-2	2012.1.00303.S	0.31x0.19	0.05	11.4	P/PC
	^{12}CO 2-1	2015.1.00889.S	0.11x0.08	0.32	3.5	A
	^{13}CO, C^{18}O 2-1	2019.1.00579.S	0.95x0.57	0.17	9.5, 7.9	A
CQTau	^{13}CO 2-1	2013.1.00498.S	0.13x0.1	0.7	0.9	P/PC
		2016.A.00026.S				
		2017.1.01404.S				
DMTau	^{12}CO 3-2	2013.1.00647.S	1.0x0.75	0.2	55.9	A
	^{13}CO, C^{18}O 3-2	2016.1.00565.S	0.37x0.29, 1.04x0.81	0.11	16.8, 21.4	A
	^{13}CO, C^{18}O 2-1	2016.1.00724.S	0.9x0.84	0.08	19.2 , 14.1	A
GGTau	^{12}CO, ^{13}CO 3-2	2012.1.00129.S	0.4x0.3	0.25	5.7, 7.8	A
GMAur	^{13}CO 3-2	2016.1.00565.S	0.38x0.26	0.11	16.2	A
	^{13}CO, C^{18}O 2-1	2018.1.01055.L	0.15x0.15, 0.17x0.13	0.2	2.7, 1.1	P/PC
HD100546	^{12}CO 3-2	2011.0.00863.S	0.94x0.42	0.11	19.4	A
	^{13}CO, C^{18}O 2-1	2016.1.00344.S	0.25x0.14	0.17	6.8, 6.4	A
HD135344B	^{12}CO 3-2	2012.1.00870.S	0.36x0.29	0.11	38.9	A
	^{12}CO, ^{13}CO, C^{18}O 2-1	2018.1.01066.S	0.1x0.08	0.2	2.6, 2.8, 2.4	P/PC
HD139614	C^{18}O 2-1	2015.1.01600.S	0.73x0.53	0.33	11.9	A
HD142527	^{12}CO 3-2	2011.0.00465.S	0.57x0.35	0.5	11.1	P/PC
	^{13}CO, C^{18}O 3-2	2012.1.00725.S	0.31x0.27	0.11	8.0, 9.9	A
	^{13}CO, C^{18}O 2-1	2015.1.01353.S	0.29x0.26, 0.84x0.77	0.1	7.5, 19.3	A
HD169142	^{12}CO, ^{13}CO 3-2	2012.1.00799.S	0.18x0.13, 0.19x0.13	0.21, 0.22	17.9, 19.8	A
	^{13}CO, C^{18}O 2-1	2015.1.00490.S	0.19x0.14	0.08	5.4, 4.0	A
HD34282	^{12}CO, ^{13}CO, C^{18}CO 2-1	2015.1.00192.S	0.24x0.21, 0.25x0.23	0.08, 0.17	10.6, 7.9, 5.5	A
HD97048	^{12}CO 3-2	2013.1.00658.S	0.65x0.39	0.2	13.93	A
	^{12}CO, ^{13}CO, C^{18}O 2-1	2015.1.00192.S	0.46x0.22	0.3	6.9, 6.5, 6.30, 4.9	P/PC
HPCha	^{12}CO 3-2	2013.1.01075.S	0.77x0.4	0.2	35.7	A
IRS48	^{13}CO 3-2	2013.1.00100.S	0.21x0.16	0.26	14.4	A

Table 4.E.1 continued.

Object	Line	Project ID	Beam (″)	Δv (km s^{-1})	RMS (mJy beam^{-1})	Source$^{(a)}$
LkCa15	^{13}CO, C^{18}O 2-1	2018.1.00945.S	0.48x0.3	0.33	3.7, 4.8	P/PC
MWC758	^{12}CO 3-2	2011.0.00320.S	0.82x0.47	0.05	37.3	A
	C^{18}O 3-2	2012.1.00725.S	0.34x0.22	0.6	26.1	A
	^{12}CO, ^{13}CO, C^{18}O 2-1	2017.1.00940.S	0.2x0.15	1.26, 1.33	1.7, 1.6, 1.2	A
PDS99	^{13}CO 2-1	2015.1.01301.S	0.34x0.23	0.17	9.8	A
RXJ1852	^{13}CO 2-1	2018.1.00689.S	0.16x0.12	0.66	4.8	A
RYLup	^{12}CO 2-1	2017.1.00449.S	0.19x0.16	0.04	15.7	A
SR21	^{13}CO 3-2	2012.1.00158.S	0.27x0.23	0.24	11.5	A
	^{13}CO 2-1	2018.1.00689.S	0.15x0.12	0.66	5.1	A
Sz91	^{12}CO 2-1	2013.1.00663.S	0.62x0.59	0.5	27.6	A
TCha	^{12}CO, ^{13}CO 3-2	2012.1.00182.S	0.26x0.14, 0.27x0.14	0.85, 0.88	14.5, 17.4	A
	^{13}CO 2-1	2017.1.01419.S	0.24x0.16	1.33	5.0	A
UXTauA	^{12}CO 2-1	2013.1.00498.S	0.26x0.21	0.63	7.4	A
V4046Sgr	^{12}CO, ^{13}CO 3-2	2016.1.00315.S	0.28x0.17, 0.3x0.18	0.21, 0.44	25.4, 22.5	A
	^{13}CO, C^{18}CO 2-1	2016.1.00724.S	0.42x0.3	0.08	11.4, 7.8	A

Notes. $^{(a)}$ P/PC: re-imaged data cube. Public data or obtained via private communication, A: archival data product.

References. AB Aur: van der Marel et al. (2021); CQ Tau: Wölfer et al. (2021); GM Aur: Öberg et al. (2021); Huang et al. (2021); HD 135344B: Casassus et al. (2021); HD 142527: van der Marel et al. (2021); HD 97048: Stapper et al. in prep.; LkCa 15: Leemker et al. (2022).

4.E.2 Brightness temperature maps

Figures 4.E.1 and 4.E.2 show the brightness temperature maps for the additional CO lines in Band 6 and Band 7, respectively.

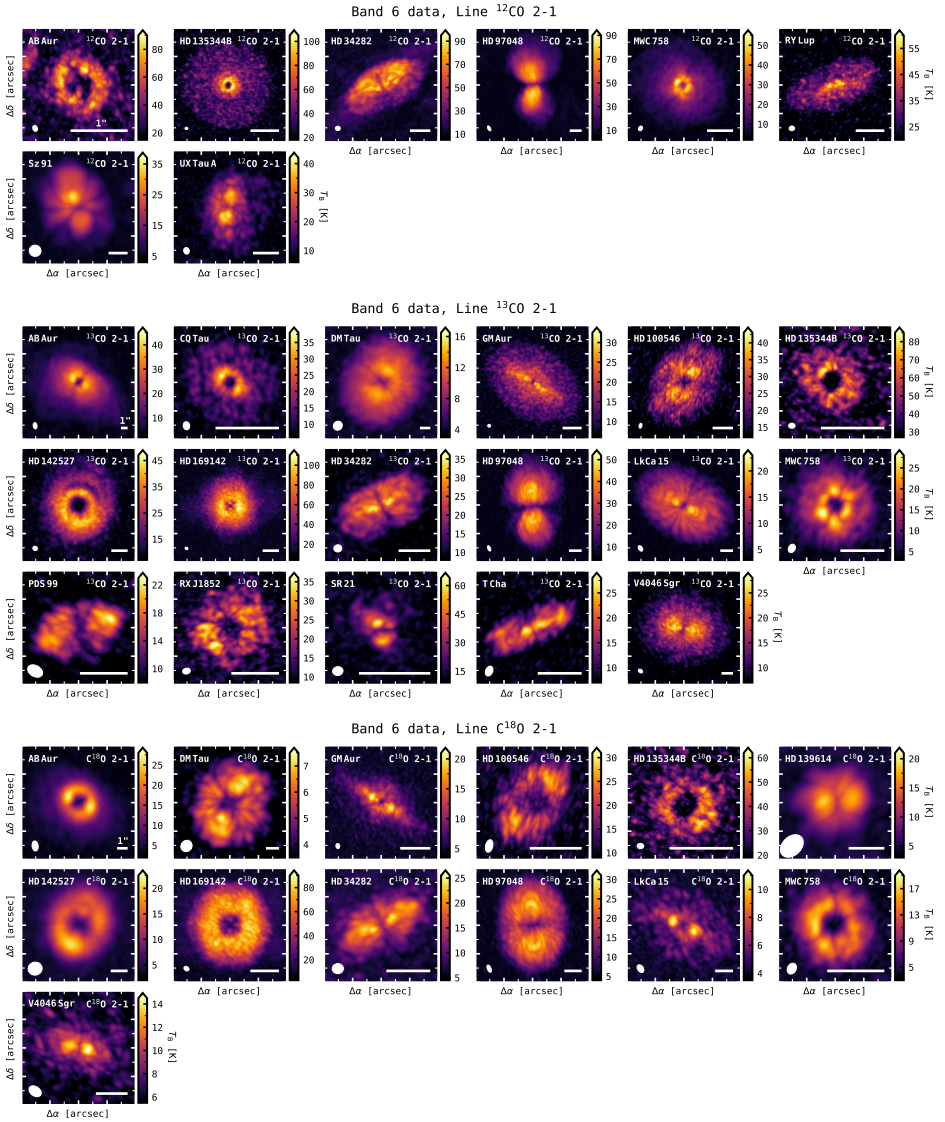

Figure 4.E.1: Peak brightness temperature maps of the gas emission in our targets, shown for the additional Band 6 CO lines used in this analysis. The conversion from peak intensity to units of Kelvin was done with the Planck law. The circle and bar in the bottom left and bottom right corner of each panel indicate the beam and a 1″ scale, respectively.

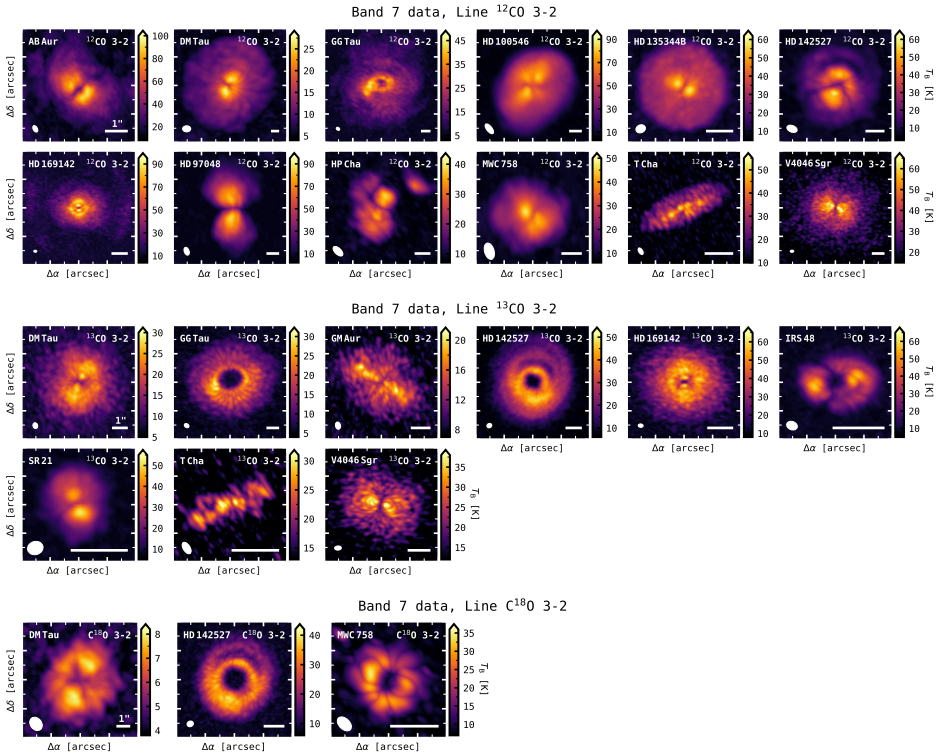

Figure 4.E.2: Peak brightness temperature maps of the gas emission in our targets, shown for the additional Band 7 CO lines used in this analysis. The conversion from peak intensity to units of Kelvin was done with the Planck law. The circle and bar in the bottom left and bottom right corner of each panel indicate the beam and a 1″ scale, respectively.

4.E.3 Rotation velocity maps

Figures 4.E.3 and 4.E.4 show the kinematical maps for the additional CO lines in Band 6 and Band 7, respectively.

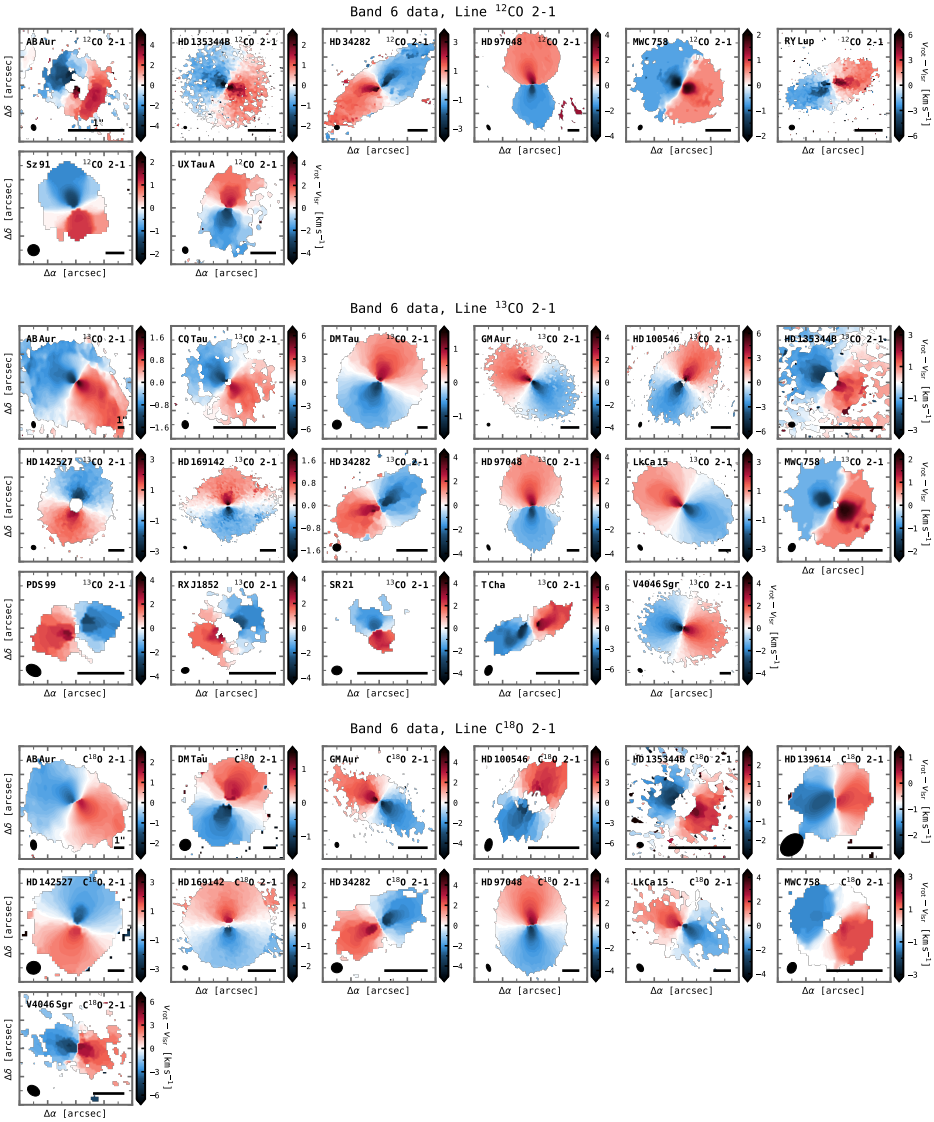

Figure 4.E.3: Rotation velocity maps of the gas emission in our targets, shown for the additional Band 6 lines used in this analysis. The maps were computed with BETTERMOMENTS. The circle and bar in the bottom left and bottom right corner of each panel indicate the beam and a 1″ scale, respectively.

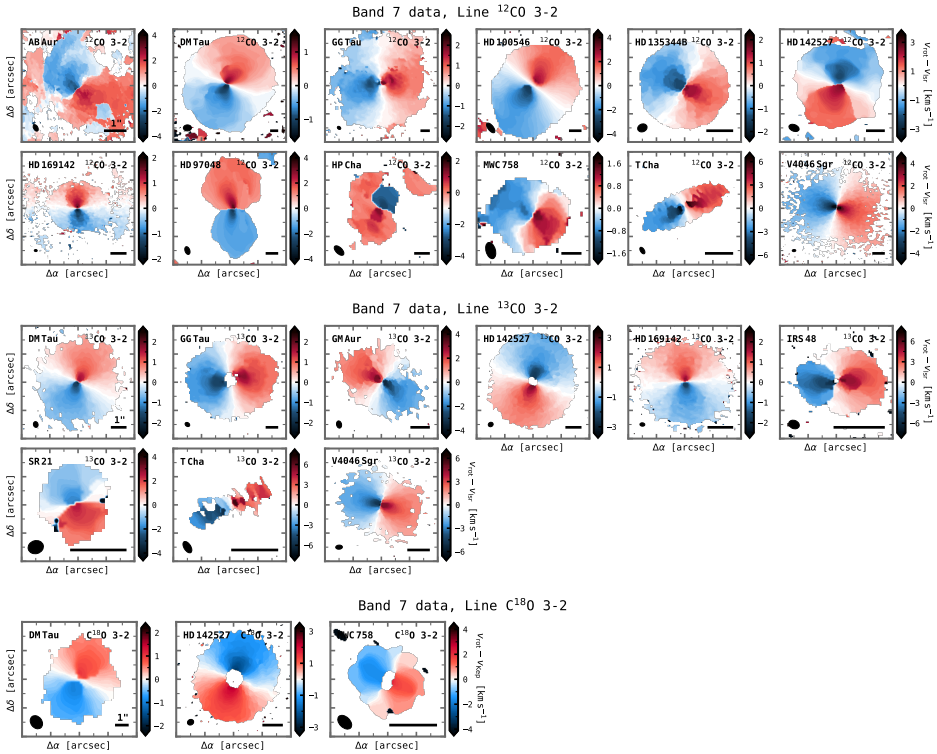

Figure 4.E.4: Rotation velocity maps of the gas emission in our targets, shown for the additional Band 7 lines used in this analysis. The maps were computed with BETTERMOMENTS. The circle and bar in the bottom left and bottom right corner of each panel indicate the beam and a 1″ scale, respectively.

4.E.4 Brightness temperature residuals

Figures 4.E.5, 4.E.6, and 4.E.7 show the brightness temperature residuals for the additional CO lines in Band 6 and Band 7 for both the thin and the thick disc geometry.

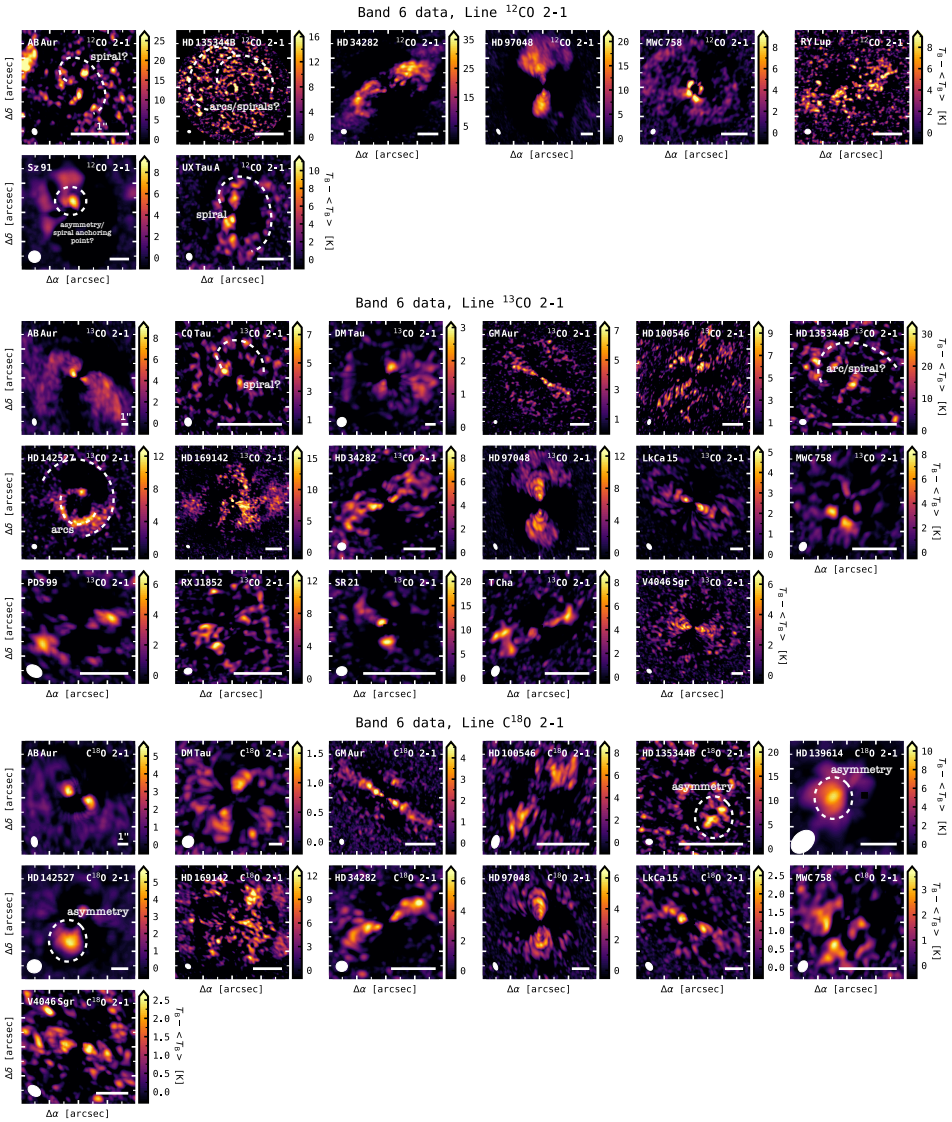

Figure 4.E.5: Brightness temperature residuals obtained with GOFISH, shown for the additional Band 6 lines used in this analysis and for a thin disc geometry. The circle and bar in the bottom left and bottom right corner of each panel indicate the beam and a 1″ scale, respectively. Some features are annotated.

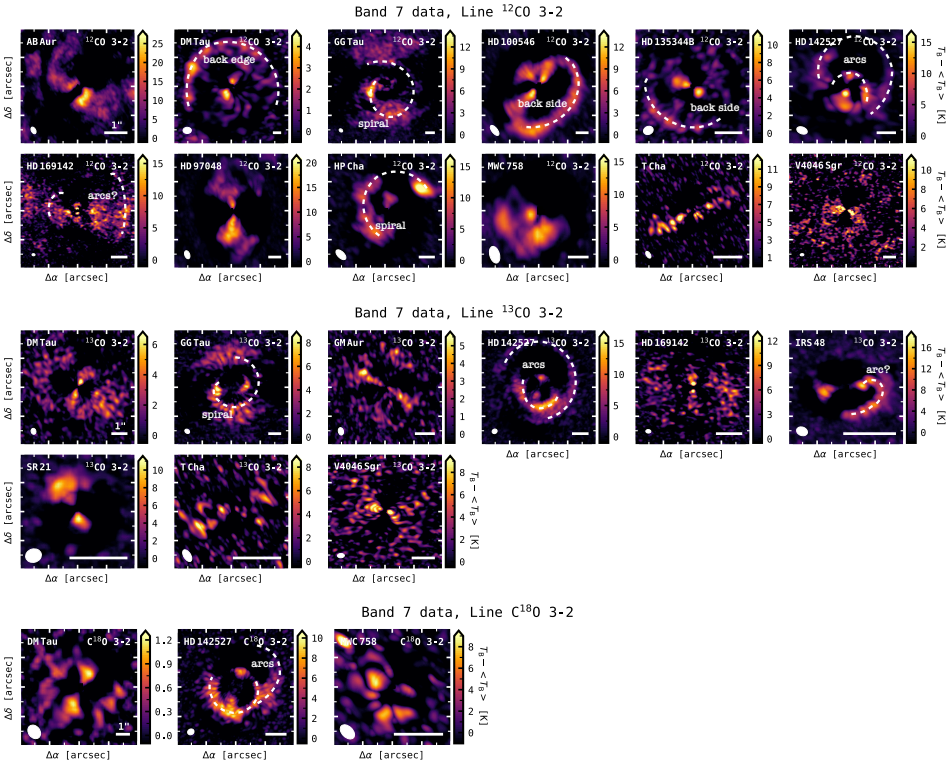

Figure 4.E.6: Brightness temperature residuals obtained with GOFISH, shown for the additional Band 7 lines used in this analysis and for a thin disc geometry. The circle and bar in the bottom left and bottom right corner of each panel indicate the beam and a 1″ scale, respectively. Some features are annotated.

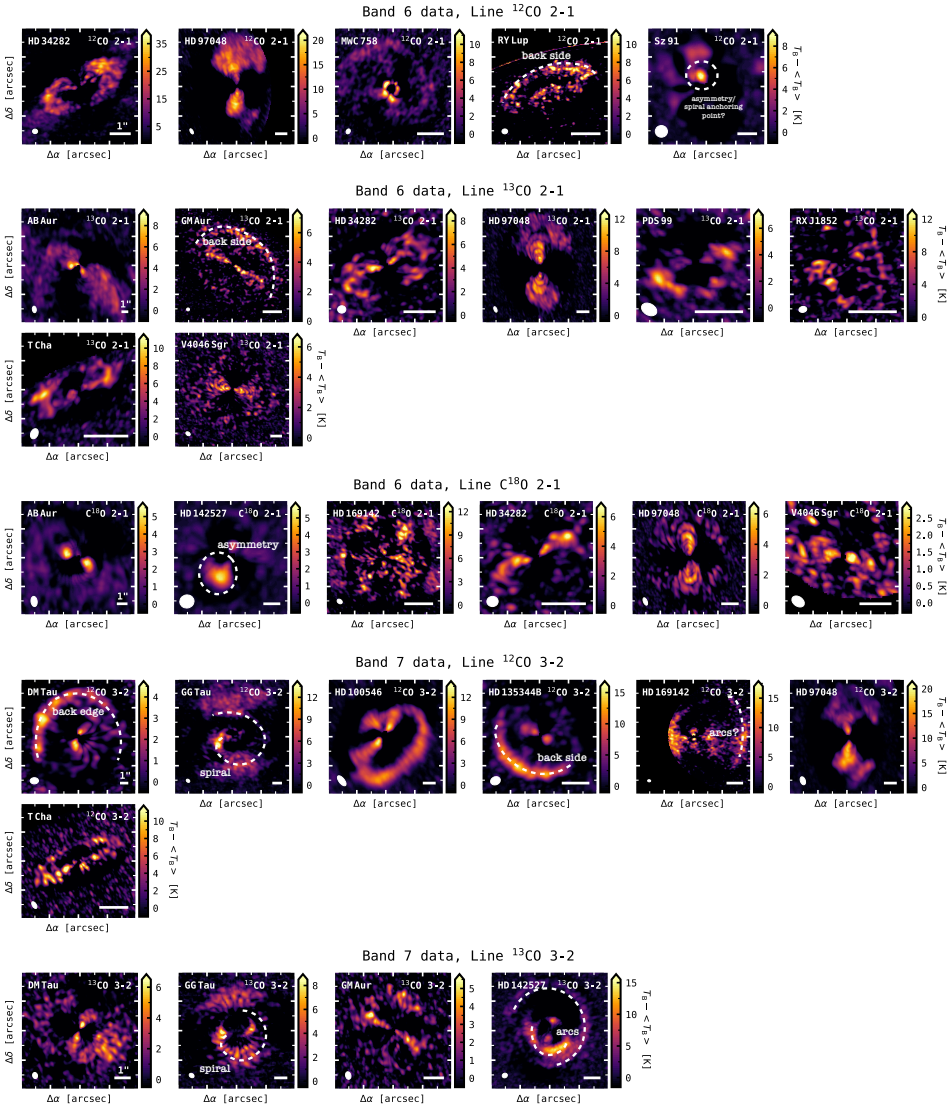

Figure 4.E.7: Brightness temperature residuals obtained with GOFISH, shown for the additional Band 6 and Band 7 lines used in this analysis and for a thick disc geometry. The circle and bar in the bottom left and bottom right corner of each panel indicate the beam and a 1″ scale, respectively. Some features are annotated.

4.E.5 Rotation velocity residuals

Figures 4.E.8, 4.E.9, and 4.E.10 show the rotation velocity residuals for the additional CO lines in Band 6 and Band 7 for both the thin and the thick disc geometry.

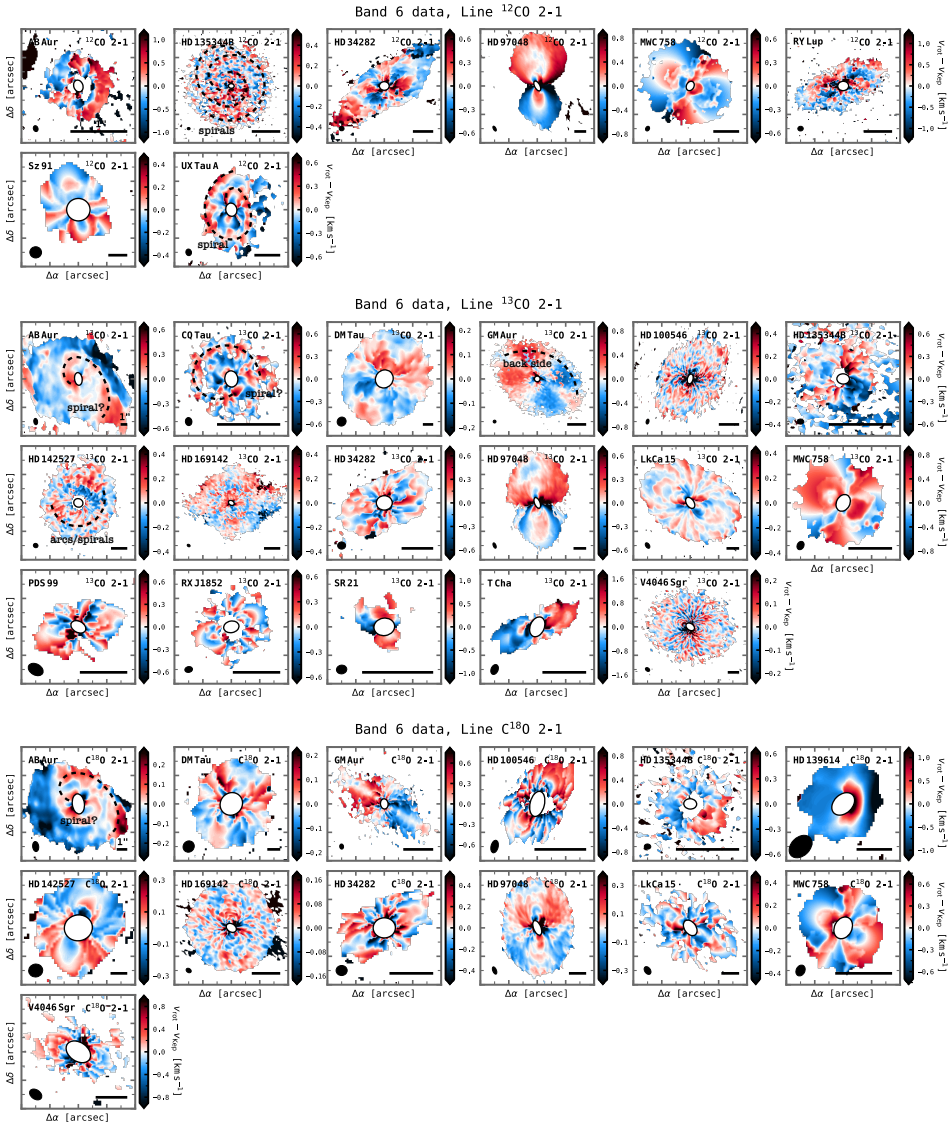

Figure 4.E.8: Rotation velocity residuals obtained with EDDY, shown for the additional Band 6 lines used in this analysis and for a thin disc geometry. The circle and bar in the bottom left and bottom right corner of each panel indicate the beam and a 1″ scale, respectively. Some features are annotated.

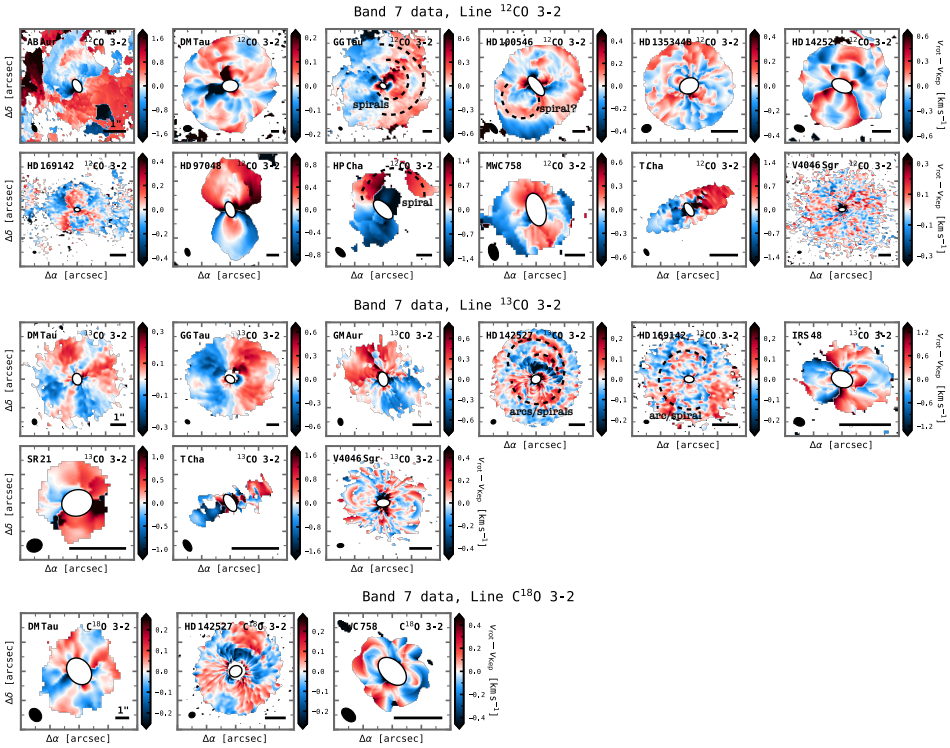

Figure 4.E.9: Rotation velocity residuals obtained with EDDY, shown for the additional Band 7 lines used in this analysis and for a thin disc geometry. The circle and bar in the bottom left and bottom right corner of each panel indicate the beam and a 1″ scale, respectively. Some features are annotated.

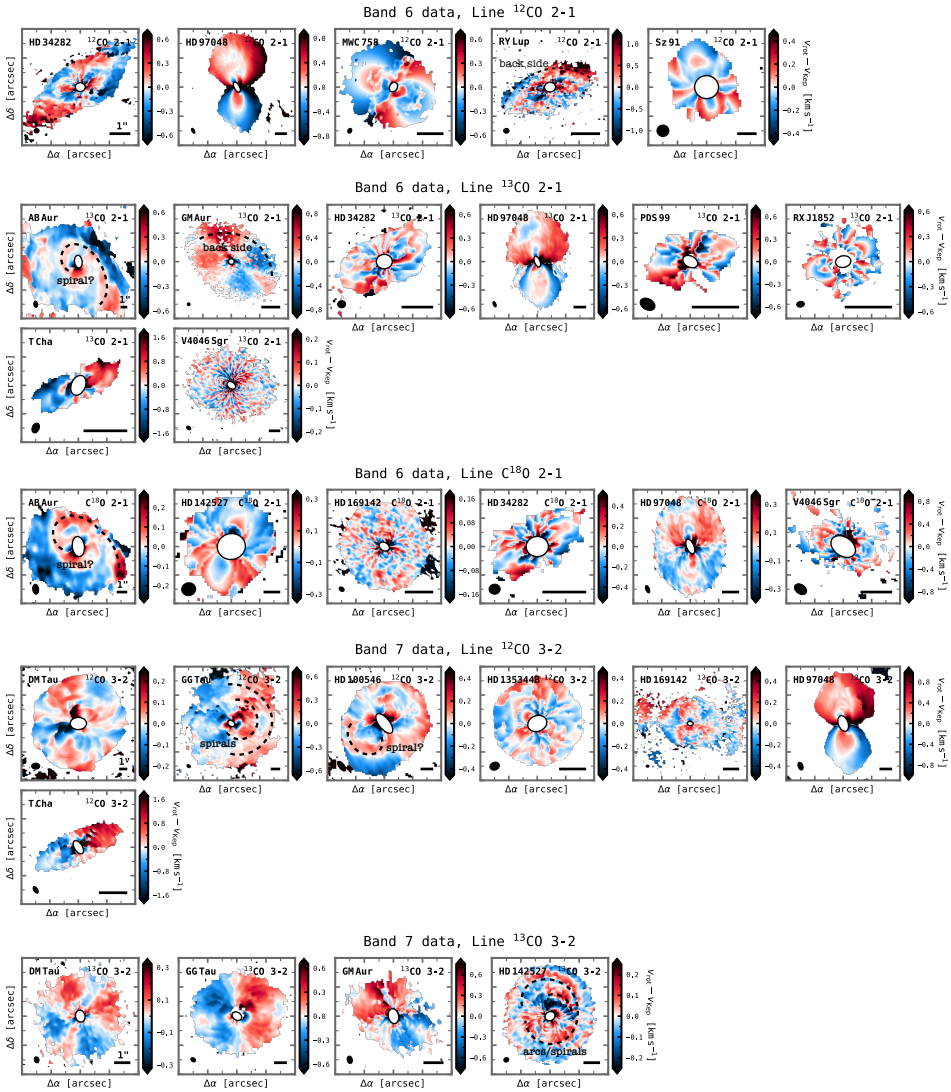

Figure 4.E.10: Rotation velocity residuals obtained with EDDY, shown for the additional Band 6 and Band 7 lines lines used in this analysis and for a thick disc geometry. The circle and bar in the bottom left and bottom right corner of each panel indicate the beam and a 1″ scale, respectively. Some features are annotated.

4.F Radial profiles of the integrated intensity

Figure 4.F.1 shows the radial profiles of the integrated CO intensity. Such profiles can be used to estimate the size of the cavity. As a deep cavity, we define those cases where a clear drop in emission can been seen in the inner regions for at least the more optically thin lines that tend to trace the column density.

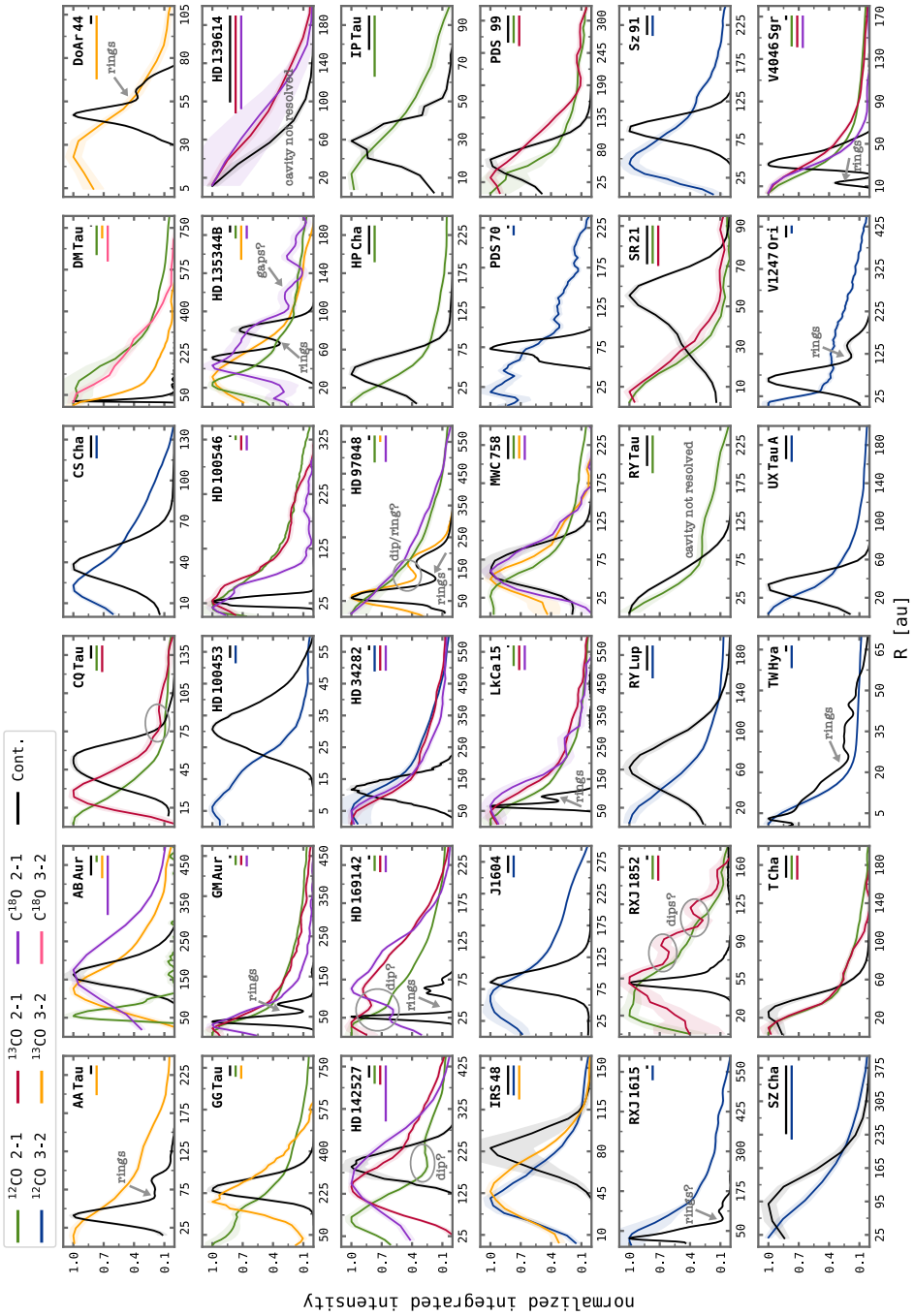

Figure 4.F.1: Azimuthally averaged and normalized radial integrated intensity profiles for the different CO lines (coloured lines) and continuum emission (black lines). The major beam of each observation is indicated by the bars in the top right corner. Some features of the profiles are annotated in the individual panels.

Once I get on a puzzle, I can't get off.

Richard P. Feynman

Chapter 5

Spirals and meridional flows in the planet-forming disc around HD 100546.

A multi-line study of its gas kinematics

L. Wölfer, A. F. Izquierdo, A. Booth, S. Facchini,
E. F. van Dishoeck, T. Paneque-Carreño, B. Dent

submitted to A&A

ABSTRACT

Context. The disc around the Herbig star HD 100546 represents a particularly interesting target to study dynamical planet–disc interactions as various features have been observed in both the dust and gas, that provide direct and indirect evidence for ongoing planet formation.

Aims. In this work, we aim to analyse the gas kinematics of five molecular CO emission lines (^{12}CO 7-6, ^{12}CO 3-2, ^{12}CO 2-1, ^{13}CO 2-1, C^{18}O 2-1), observed with ALMA in HD 100546, to reveal deviations from Keplerian rotation as well as substructures in the peak intensity and line width.

Methods. For our analysis, we fit the molecular intensity channels with the DISCMINER package to model the line profiles, and extract observables such as centroid velocity, peak intensity, and line width. Aside from fitting the full cube, we also conduct runs where the blue- and redshifted sides are modelled separately to search for possible asymmetries.

Results. Our analysis reveals prominent kinematical spiral features in all five lines on large scales of the disc and we reproduce their morphology with both a linear and logarithmic spiral. In ^{12}CO 2-1, spirals are also seen in the peak intensity residuals, the line width residuals exhibit a prominent ring of enhanced line widths around $125 - 330$ au. The models further show that the emission from the redshifted side originates from higher disc layers than that from the blueshifted side, with the asymmetry being especially pronounced for ^{12}CO 7-6 and ^{12}CO 3-2.

Conclusions. The pitch angles of the spirals are consistent with those driven by an embedded companion inside of 50 au and they suggest a dynamical mechanism rather than gravitational instabilities. They decrease closer to the midplane, which matches the predictions of Juhász & Rosotti (2018). We further find indications of a companion around 90–150 au, where tentative dips are present in the radial profiles of the integrated intensity of ^{13}CO and C^{18}O 2-1 and pressure minima are observed in the azimuthal velocities. For the first time, we also detect meridional flows in this region, which coincide with the dust gap found by Fedele et al. (2021). The asymmetry in the emission heights may be a result of infall from the disc's environment. Another explanation is provided by a warped inner disc, casting a shadow onto one side of the disc.

5.1 Introduction

In order to understand planet formation and the diversity of developed planetary systems such as our own, it is crucial to study the early stages when (proto-) planets are still embedded in their birthplaces – the so-called protoplanetary or planet-forming discs. These discs are not static objects but they evolve and eventually disperse over time with the evolutionary processes not only shaping the disc's appearance but also influencing (and putting a limit on) the planet-formation mechanisms. Conversely, planets interact with their environment, impact disc evolution, and are expected to alter their host disc's structure, for example in terms of density, temperature, or velocity. Even though such young embedded planets may be hidden from the direct eye of our telescopes, their planet–disc interactions still leave observable marks depending on the planet's mass and location.

In the last decade, high-angular-resolution observations of the dust and gas in protoplanetary discs with the Atacama Large Millimeter/submillimeter Array (ALMA; ALMA Partnership et al. 2015), the Spectro-Polarimetric High-contrast Exoplanet REsearch (SPHERE; Beuzit et al. 2019), or the Gemini Planet Imager (GPI; Macintosh et al. 2014) have enabled scientists to search for such signposts of planet–disc interactions. The observations revealed a variety of substructures such as gaps or even cavities, rings, spiral arms, and azimuthal asymmetries to be ubiquitous in both the dust and the gas component (e.g., Bae et al. 2022; Benisty et al. 2022). To interpret the origin of these substructures, it is necessary to understand how frequent they are, to discern possible patterns they follow, and to search for differences or similarities between different star-disc system morphologies.

While various mechanisms such as photoevaporation (e.g., Owen et al. 2011; Picogna et al. 2019), gravitational instabilities (e.g., Kratter & Lodato 2016), magnetorotational instabilities (e.g., Flock et al. 2015, 2017; Riols & Lesur 2019), zonal flows (e.g., Uribe et al. 2015) or compositional baroclinic instabilities (e.g., Klahr & Bodenheimer 2004) have been invoked to explain the observations, at least some of the substructures are expected to be linked to the presence of (massive) planets (Lin & Papaloizou 1979; Zhang et al. 2018). In this context, the so-called transition discs represent a particularly interesting subgroup of young stellar objects (YSOs). These discs are marked by inner regions depleted in dust (and gas) (e.g., Espaillat et al. 2014; Ercolano & Pascucci 2017) and were originally identified through a lack of infrared (IR) excess in their spectral energy distribution (SED; Strom et al. 1989). While they may represent an intermediate (transitioning) state between an optically thick (full) disc and disc dispersal, dynamical clearing by a massive companion represents an alternative explanation: at least some of the cavities – and especially the very deep ones (e.g., van der Marel et al. 2016) – are expected to be the result of such processes rather than representing an evolutionary state. Transition discs, therefore, represent ideal laboratories to probe disc evolution as well as planet formation models and may enable us to catch planet formation in action.

Ultimately, only a direct detection can confirm the link between the observed disc substructures and an embedded planet. However, the dense and opaque environment of these young planets makes such a task difficult and feasible only for

the very massive, bright planets that are less affected by dust extinction (Sanchis et al. 2020). To date, the only robust detections of forming planets (of several M_J) and their circumplanetary discs have been obtained for the PDS 70 system (Keppler et al. 2018; Haffert et al. 2019; Benisty et al. 2021).

The challenge of direct detections and our growing understanding of how planets interact with their host disc have triggered the development of other, indirect, detection techniques. One promising method is to study the velocity field of the rotating gas, observed through molecular line emission, to search for deviations from Keplerian rotation (Pinte et al. 2022). Identifying such variations in the kinematics can be used to probe the local pressure gradient and to characterize the shape of the perturbation. Indeed, several ALMA observations in recent years have reported both localized and extended kinematical deviations, which may be linked to the presence of planets: so-called kink-features are detected by Pinte et al. (2018b, 2019) in HD 163296 and HD 97048 and a Doppler flip is reported in the HD 100546 disc by Casassus & Pérez (2019). Teague et al. (2018a) and Teague et al. (2019a) study the rotation profile of HD 163296, finding perturbations and significant meridional flows that point towards embedded planets. Izquierdo et al. (2022) apply the DISCMINER tool (Izquierdo et al. 2021) – a new channel-map-fitting package able to model the upper and lower disc surfaces simultaneously and to identify localized velocity perturbations in both radius and azimuth – to the same disc and find strong indications for two embedded planets. Extended spiral structures are observed in the kinematical residuals of TW Hya (Teague et al. 2019b, 2022a), HD 100453 (Rosotti et al. 2020a), HD 135344B (Casassus et al. 2021), CQ Tau (Wölfer et al. 2021), HD 163296 and MWC 480 (Teague et al. 2021), and J1604 (Stadler et al. 2023). Non-Keplerian gas spirals are also found in HD 142527 by Garg et al. (2021).

Aside from the kinematics, it is also interesting to study the patterns in the peak intensity/brightness temperature as well as line widths, which are both shaped by the presence of companions and can be used to trace density substructures, vertical motions, or also turbulence. Planets can create density waves that result in an increased surface density and thus higher opacity, moving the $\tau = 1$ layer to a higher altitude where the temperature is generally higher (Phuong et al. 2020a,b). This leads to spiral substructures in the gas brightness temperature. Thermal spiral features are reported in TW Hya by Teague et al. (2019b) and in CQ Tau by Wölfer et al. (2021). These observations may be explained by the models of Muley et al. (2021), who investigate the temperature structure in planet-driven spiral arms. Wölfer et al. (2023) study the gas brightness temperature (and kinematics) of a sample of 36 transition discs, finding significant substructures such as spirals in eight sources. Around the orbit of a massive planet, turbulent motions are triggered which are expected to result in enhanced line widths. Izquierdo et al. (2022) indeed observe an enhancement of line widths around the gas gap at 88 au in HD 163296, which further supports their findings of a planet candidate at 94 au. Enhanced line widths are also found in HD 135344B by Casassus et al. (2021).

In this work, we present a multi-line study of CO gas emission in the transitional disc HD 100546, one particularly interesting target to study planet–disc interactions. The young Herbig Be star, located at ∼110 pc from the Earth (Gaia

Collaboration et al. 2018), is surrounded by a massive disc spanning several hundreds of au and showing various indications of ongoing planet formation, as described in the next section. For our analysis, we apply the DISCMINER package presented in Izquierdo et al. (2021) to archival B6 (^{12}CO 2-1, ^{13}CO 2-1, C^{18}O 2-1), B7 (^{12}CO 3-2), and B10 (^{12}CO 7-6) data to search for perturbations in the velocities, intensities, and line widths (possibly linked to embedded planets) and to obtain the vertical structure of the disc. Probing different layers of the disc with various isotopologues or transitions of the same molecule (as done in this study) or different molecules (e.g., Paneque-Carreño et al. 2023) is crucial to understand how the observed substructures vary and can help us to access their formation mechanism (e.g., Pinte et al. 2018a; Law et al. 2021b). We describe the source and observations in Sect. 5.2. Our modelling approach is detailed in Sect. 5.3 and the results are presented in Sect. 5.4. The latter are discussed in Sect. 5.5 and summarized in Sect. 5.6.

5.2 Observations

5.2.1 The HD 100546 system

In Fig. 5.1, we show the possible morphology of the HD 100546 system further described in the following. Observations of a compact source (in L'-Band) have been interpreted as direct evidence of an embedded companion in the outer disc at ~ 53 au (Quanz et al. 2013, 2015; Currie et al. 2015), also known as the giant planet candidate HD 100546 b. Subsequent Ks-Band observations, however, revealed a faint extended emission around the same location (Boccaletti et al. 2013) and thus the planetary origin of the observed feature yet needs to be confirmed. Another giant planet, HD 100546 c, may be located at $\sim$14 au, just inside the dust cavity. First postulated by Acke & van den Ancker (2006) and later identified as a point source in near-infrared scattered light data taken with GPI (Currie et al. 2015), the detection of HD 100546 c has been debated in the literature (e.g., Follette et al. 2017; Currie et al. 2017). The presence of the planet is supported by studies on the time variations of ro-vibrational CO emission lines (Brittain et al. 2009, 2013, 2014, 2019), tracing the inner edge of the disc. These observations showed an excess of CO P(26) line emission between 2003 and 2013 – consistent with an orbiting planet – that disappeared in 2017 as the possible planet moved behind the near side of the inner rim of the outer disc. Assuming a common origin, the feature observed in the scattered light is expected to disappear as well and recent observations with VLT/SPHERE indeed lack a detection (Sissa et al. 2018).

Alongside the direct measurements, the HD 100546 disc also exhibits a number of indirect evidence for planet–disc interactions. The scattered light images are marked by spiral structures (e.g., Garufi et al. 2016; Follette et al. 2017) and the millimetre continuum, well studied with ALMA, reveals a large inner cavity ($\lesssim$ 20 au) with the dust being concentrated into two prominent rings between 20–40 au and 150–250 au (e.g., Walsh et al. 2014; Pineda et al. 2019; Fedele et al. 2021). Models show that these substructures are consistent with two giant planets orbiting at locations of 10–15 au and 70–150 au (Pinilla et al. 2015; Fedele et al.

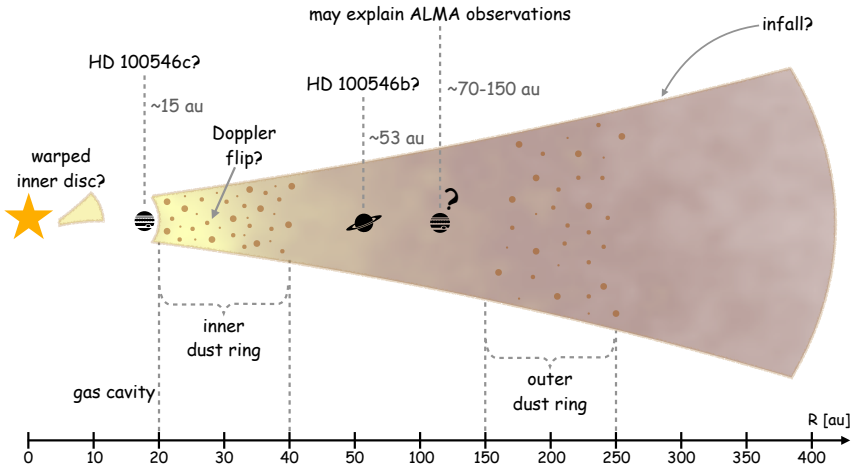

Figure 5.1: Possible morphology of the HD 100546 system. Substructures such as the dust rings have been observed, while the planet candidates have been proposed to explain the observations. The two planets suggested in the dust gap may refer to the same object for which the actual location is yet undetermined.

2021; Pyerin et al. 2021). In addition to the dust, the gas disc of HD 100546 has been studied through a range of molecular tracers. ALMA observations of the CO isotopologues are numerous and show that the disc is much more extended in the gas than in the dust (e.g., Walsh et al. 2014; Miley et al. 2019).

The ^{12}CO emission revealed non-Keplerian features in the kinematics that may be a signpost of ongoing planet formation: Walsh et al. (2017) find asymmetries that could be explained by a warped inner disc, which however stands in contrast to SPHERE observations of the disc by Garufi et al. (2016), who suggest radial flows mediated by planets as an alternative explanation. A warp has also been proposed by Panić et al. (2010) to account for asymmetric line observations (^{12}CO $J = 6-5$ and $J = 3-2$) from APEX. As mentioned before, Casassus & Pérez (2019) detect a Doppler flip at $\sim$28 au which is in agreement with the spiral wake created by a planet and coincides with a fine ridge in the millimetre continuum, suggesting a complex dynamical scenario. The Doppler flip is confirmed by Casassus et al. (2022), with the blueshifted side of the flip however disappearing when vertical and radial flows are taken into account. The authors propose an embedded outflow, launched by a companion of several $M_{\rm Earth}$, as a possible explanation. This could explain the observations by Booth et al. (2018), who detect non-Keplerian features in the blueshifted side of SO line emission that may be tracing a disk wind, a warped disc, or an accretion shock onto a CPD. Follow-up observations by Booth et al. (2023) support that the azimuthal SO asymmetry is indeed tracing an embedded planet. Another interpretation of the Doppler flip as being the kinematic counterpart of the NIR spiral is proposed by Norfolk et al. (2022). Pérez et al. (2020) analyse the wiggles seen in the velocity channels of ^{12}CO, ^{13}CO, and C^{18}O. They find that these substructures are in agreement with a massive planet,

with the strength of the wiggles decreasing for ^{13}CO and C^{18}O as expected from planet–disc interaction models. However, as shown by Izquierdo et al. (2021), such kink-like features can also be caused by a gap or density substructures rather than a planet and caution needs to be exercised in the interpretation of these perturbations.

HD 100546 is known to still be embedded in a faint envelope (Grady et al. 2001; Ardila et al. 2007), reaching out to about 1000 au. Such an envelope may be linked to secondary accretion events due to infalling material onto the disc, which is often accompanied by arc-shaped structures as observed in HD 100546 (Dullemond et al. 2019). Asymmetric accretion from an envelope can result in a tilt of the disc (Thies et al. 2011), the formation of vortices (Bae et al. 2015), or drive spirals due to accretion shocks, that propagate the disc (Lesur et al. 2015; Hennebelle et al. 2017). Spirals have been observed in HD 100546 in both the optical (Grady et al. 2001; Ardila et al. 2007) and the near-infrared (Avenhaus et al. 2014; Sissa et al. 2018).

In this paper, we aim to shed some additional light onto the observed kinematical deviations by analysing different CO tracers in data sets that cover both the inner and outer disc with the channel map fitting package DISCMINER.

5.2.2 ALMA observations

Molecular line emission of the disc around HD 100546 has been observed with ALMA in several frequency bands. In this paper, we make use of the data sets 2011.0.00863.S (PI: C. Walsh; Walsh et al. 2014), 2015.1.00806.S (PI: J. Pineda; Pineda et al. 2019), 2016.1.00344.S (PI: S. Pérez; Pérez et al. 2020), and 2018.1.00141.S (PI: B. Dent) that cover CO isotopologues in Bands 6, 7, and 10. Their properties are summarized in Table 5.1. For all of the data sets, we started with the archival pipeline-calibrated data and performed further reduction using CASA version 5.7.0 (McMullin et al. 2007).

The Band 6 data of the ^{12}CO, ^{13}CO, and C^{18}O $J = 2-1$ line were taken in two configurations during Cycle 4, an extended (C40-9) as well as a compact configuration (C40-6) with the same spectral setting. We self-calibrated and combined these data following the same procedure as described in Czekala et al. (2021): we self-calibrated the short-baseline data first and then combined it with the calibrated long-baseline data, after ensuring that the data sets share a common phase centre. Afterwards, we applied further iterations of self-calibration, both in phase and amplitude.

For the combination of the Band 7 data, we took a slightly different approach as the data sets do not share a significant overlap in the spectral settings (aside from both targeting the ^{12}CO $J = 3 - 2$ line). The long-baseline data taken during Cycle 3 have insufficient short baselines to properly recover spatial scales $> 1\farcs0$. To improve this, we combined the data with observations from Cycle 0. We note, that since these observations were taken in different cycles and taken with different settings, they are not optimal for data combination. Each data set was first self-calibrated (phase and amplitude) individually. The Cycle 0 data were initially pipeline calibrated in CASA version 3.4 and therefore we applied

Table 5.1: Observational properties of the ALMA data sets used in this work.

Project ID	Date	Baselines (m)	Int. time (min)	Central freq. (GHz)	Bandwidth (MHz)	Δv ($\mathrm{km\,s^{-1}}$)	Ang. res. ($''$)	LAS ($''$)
2011.0.00863.S Cycle 0	18 Nov 2012	21–375	12	345.798	469	0.211	0.57	6.66
2015.1.00806.S Cycle 3	02 Dec 2015	17–10800	30	345.796	469	0.212	0.035	0.471
2016.1.00344.S Cycle 4	Oct 2016 - Sep 2017	19–12200	35, 117	230.538 220.399 219.560	117	0.158	0.183, 0.037	1.983, 0.745
2018.1.00141.S Cycle 6	14 Apr 2019	15–780	28	807.499	1875	0.181	0.165	2.007

the CASA task *statwt* to these data to account for the change in the visibility weight initialization and calibration across different CASA versions < 4.3 [1]. The self-calibrated data sets were then combined after ensuring they share a common phase centre. For the Band 10 data, no self-calibration was performed due to a lack of signal-to-noise-ratio (SNR).

The continuum was subtracted using the `uvcontsub` task, flagging channels that contained line emission. We then imaged the lines with `tCLEAN` for both the continuum-subtracted and non-subtracted data sets. In the cleaning process, we used a Briggs robust weighting of +0.5, the 'multi-scale' deconvolver, and a Keplerian mask [2]. A slight `uv-taper` was applied in all Bands in order to improve the SNR in the images. The properties of the final images are summarized in Table 5.2. As high spectral resolution is essential to study kinematics, we imaged the lines with the best possible spectral resolution. However, to ease comparison between the lines, we also made images for the same velocity resolution, given by the lowest resolution among the data sets (B7, $210\,\mathrm{m\,s^{-1}}$). Since the Band 6 and 7 data are a combination of multiple configurations, we applied the JvM correction to the CLEAN images (Jorsater & van Moorsel 1995). This method aims to correct for imaging artefacts induced by the non-gaussianity of the dirty beam. The resulting epsilon values, the ratio of the CLEAN beam volume to the dirty beam volume, are given as 0.56 for Band 6 and 0.22 for Band 7.

In Figs. 5.A.1 and 5.A.2, we show a comparison between the final images of the individual and combined data sets for the Band 7 ^{12}CO $J = 3 - 2$ line, where it becomes very clear that the inclusion of the shorter baseline data significantly improves the recovery of flux and image fidelity in the outer disk.

Table 5.2: Characteristics of the data for the five lines analysed in this work.

Line	Δv ($\mathrm{km\,s^{-1}}$)	Beam ($''$)	RMS ($\mathrm{mJy\,beam^{-1}}$)	Line peak ($\mathrm{mJy\,beam^{-1}}$)
^{12}CO 2-1	0.17	0.10x0.08	0.6	59
^{13}CO 2-1	0.17	0.10x0.08	0.6	25
C^{18}O 2-1	0.17	0.10x0.08	0.5	17
^{12}CO 3-2	0.21	0.12x0.09	1.7	192
^{12}CO 7-6	0.185	0.23x0.17	49.9	4116

5.2.3 Observational results

In Fig. 5.2 we present the continuum-subtracted intensity channels of the five CO lines in steps of three from the central channel and for the same channel spacing of $210\,\mathrm{m\,s^{-1}}$. The inner continuum ring is overlaid as dashed contours, showing that the gas disc is much more extended than the dust disc. As seen in the first three rows of Fig. 5.2, the ^{12}CO data appear elevated with the lower surface of

[1] `https://casadocs.readthedocs.io/en/stable/notebooks/data_weights.html`
[2] `https://github.com/richteague/keplerian_mask`

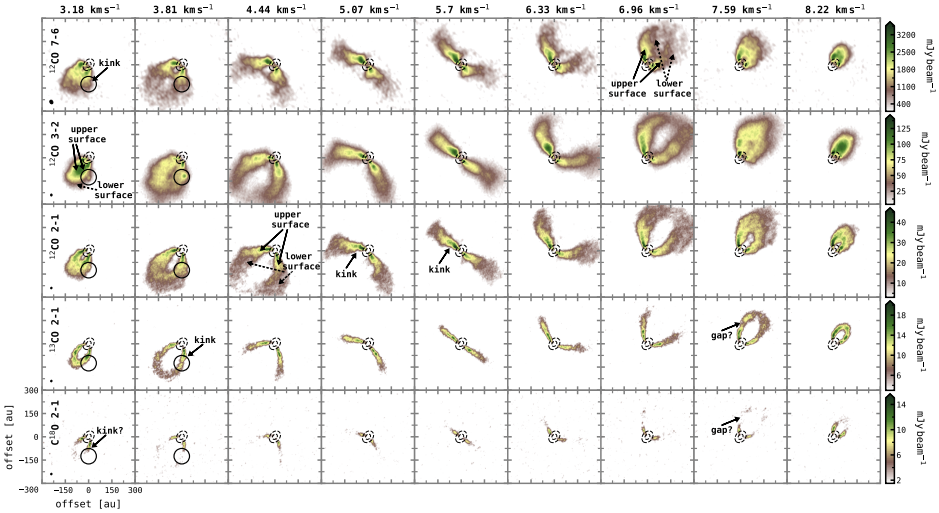

Figure 5.2: Examples of the intensity channels of the five CO lines, shown in steps or three from the central channel and for a velocity resolution of $210\,\mathrm{m\,s^{-1}}$. The inner ring of the millimetre continuum is overlaid as dashed contours. A localized feature is seen in some of the channels within the solid circle. The beam of the observation is indicated in the bottom left corner of the first column panels.

the disc being at least partly visible. The other two isotopologues, shown in the bottom two rows, on the other hand, appear rather flat and the lower surface can not be distinguished. This suggests that the emission from these molecules comes, as generally expected (Law et al. 2021b), from lower heights in the disc located closer to the midplane. For these rarer isotopologues, line wing emission may be missing due to sensitivity effects.

In the first two channels of the ^{12}CO 3-2 data, a bright spot is visible at a separation of $\sim 100\,\mathrm{au}$ to the south of the central star, highlighted by the solid black circle in Figs. 5.2 and 5.A.1. As those data represent a combination of ALMA Cycle 0 and Cycle 3 data, both time variations and a difference in the observational setups may lead to imaging artefacts. It could further be the result of a projection effect. However, looking at the other lines, a similar, yet much weaker spot is present in the ^{12}CO 2-1 data and a wiggle or break can be discerned in the corresponding ^{12}CO 7-6 and ^{13}CO 2-1 channels around this area. Altogether, this points towards the localized feature being real, but higher sensitivity data including both the long and the short baselines in the same observational setup are needed to support this claim. Continuum subtraction can be ruled out as a cause for the substructure as the continuum ring is located much closer to the star. A comparison of the combined data with the long- and short-baseline data is included in Appendix 5.A.

The channels of ^{12}CO 7-6 appear to be very asymmetric: the iso-velocity curves seem to be twisted in the centre with the two sides bending in opposite directions. Expected to come from the highest layers of the disc, this may result from interac-

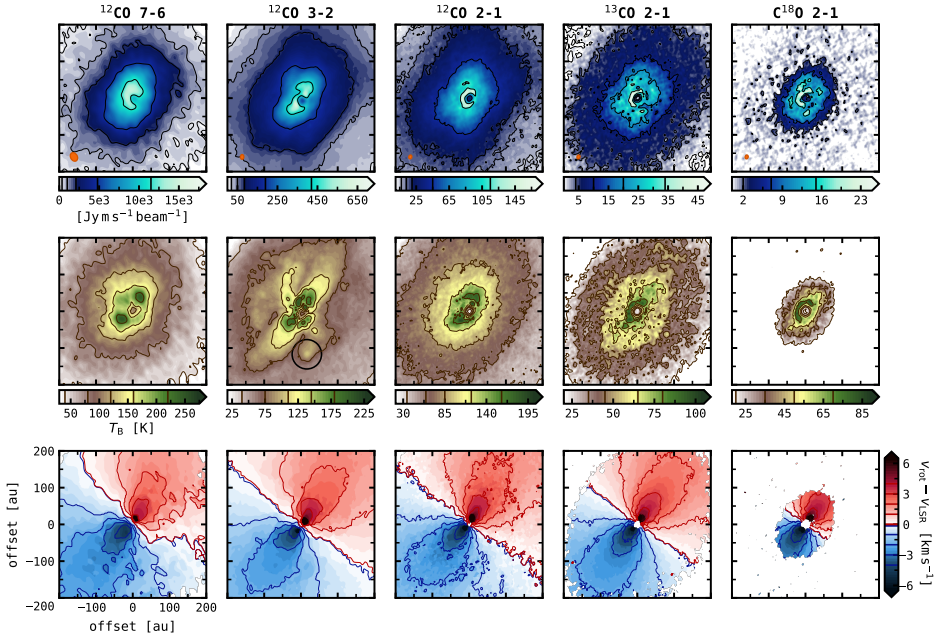

Figure 5.3: Integrated intensity (top), peak intensity (middle), and line-of-sight velocity (bottom) of the five CO lines studied here. A localized feature is seen in ^{12}CO 3-2 around 125 au, marked by the solid circle. Some contours are overlaid and their levels are indicated in the colour bars. The beam of the observation is shown in the bottom left corner of the first-row panels.

tions with material surrounding the disc but could also point towards misaligned disc regions (e.g., Walsh et al. 2017; Facchini et al. 2018). Furthermore, the north-east side of the disc appears to be brighter than the southwest side of the disc.

The ^{13}CO and C^{18}O data show tentative signs of an outer intensity gap in the disc, becoming most prominent for the 7.59 km s^{-1} channel, but higher sensitivity data are needed to confirm its presence. As mentioned in previous work (Pérez et al. 2020), several of the velocity channels are marked by wiggles or kink-like features in their profile, some of which are annotated in Fig. 5.2.

In Fig. 5.3 we show the integrated and peak intensity maps alongside the kinematics for all five lines. These maps were computed with the BETTERMOMENTS package (Teague & Foreman-Mackey 2018) and in case of the peak intensity converted to units of Kelvin with the Planck law. While the intensity maps were obtained with the standard moment 0 and 8 implementations, respectively, the kinematics were derived with the quadratic method. In this approach, a quadratic function is fitted to the brightest pixel in the spectrum as well as the two neighbouring pixels to find the centroid of the line in pixel coordinates. For the peak intensity, we used the non-continuum-subtracted data cube, for the other two quantities the continuum-subtracted data cube. For optically thick lines, continuum subtraction can remove part of the line emission and artificially lower the peak in-

tensity, as part of the underlying continuum is absorbed (e.g., Weaver et al. 2018; Rosotti et al. 2021; Bosman et al. 2021). While we did not apply any masking in the computation of the peak intensity maps, a Keplerian mask was included in the computation of the integrated intensity, and for the kinematics we selected a masking for regions below a certain SNR to reduce the noise at the disc's edge (between 4.5–5).

As seen in the intensity maps, an inner gas cavity ($< 20\,\mathrm{au}$) is present in all isotopologues and lines. At the same location as in the channel maps, a localized, however weak spot is seen in the peak intensity of ^{12}CO 3-2 (black circle in Figs. 5.3 and 5.A.2), the other lines are lacking a similar feature at this location. In general, the ^{12}CO 3-2 intensities appear to be very asymmetric, with a cross-like – or possibly spiral-like – structure extending towards the north and south. Again, caution should be exercised with regard to these substructures, as artefacts may have been introduced through the combination of data sets. In Fig. 5.A.2 we compare the intensity and kinematical maps for the different ^{12}CO 3-2 data sets. Even though the long-baseline observation may be lacking flux in some regions, the cross-like structure is also present in the short-baseline data, pointing towards a real substructure and suggesting that no strong artefacts have been introduced in the imaging process. With three years having passed between the two observations, some time variations can, however, not be ruled out. It is puzzling that no similar structures are found in the ^{12}CO 2-1 and ^{12}CO 7-6 data. While the lack of features in ^{12}CO 2-1 may be explained by temperature effects with the substructures becoming visible only at a certain height above the midplane, a similar pattern would at least be expected in ^{12}CO 7-6, which traces even higher disc layers. Interaction with material from the environment of the disc could, however, wash out substructures. Moreover, ^{12}CO 7-6 may be lacking flux in the outer disc regions. To get to the bottom of these peculiar substructures, it is crucial to obtain higher sensitivity data with a similar observational setup in the future.

On first look, the kinematics overall suggest an only mildly elevated disc: despite an inclination of $\sim 40\,^{\circ}$ only slight contributions from the back side of the disc are visible in ^{12}CO and no contributions are seen in ^{13}CO and C^{18}O. In the ^{12}CO 7-6 kinematics, the central velocity seems to be off by a few $100\,\mathrm{m\,s^{-1}}$ from the systemic velocity of the source at $5.7\,\mathrm{km\,s^{-1}}$. This is also seen in the according channel map in Fig. 5.2 which seems 'S-shaped' as the south wing is bent upwards compared to the north wing. The central channel of the other lines on the other hand appears more symmetric. Assuming that ^{12}CO 7-6 emission comes from a higher disc layer, the disc's surface may be distorted due to interactions with material from the environment. We analyse the kinematics in further detail in Sec. 5.3

Figure 5.4 presents normalized azimuthally averaged radial profiles of the integrated intensity for the lines of this analysis and the continuum emission. These profiles were obtained with the GOFISH package (Teague 2019) by shifting and stacking all line spectra to increase the SNR. This approach is based on the assumption that the disc is symmetric and Keplerian, which does not necessarily hold. Therefore, we compared the profiles to those obtained from simply azimuth-

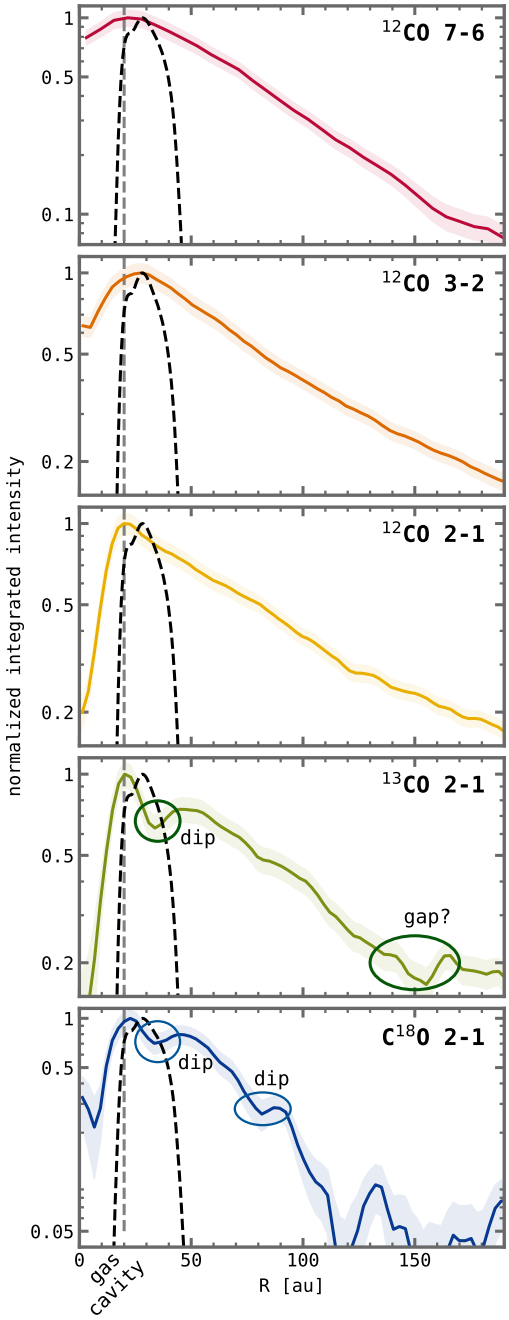

Figure 5.4: Azimuthally averaged and normalized radial integrated intensity profiles for the different CO lines. A radial profile of the Band 6 millimetre continuum is included as black dashed lines. The vertical grey dashed line marks the location inside which the gas emission rapidly drops (gas cavity). Some features of the profiles are annotated.

ally averaging the moment 0 maps, yielding similar results. By default, the widths of the annuli in the GOFISH package are given as one-fourth of the beam major axis. For the deprojection, we assume a disc geometry as obtained from the models presented in Sect. 5.3 and Table 5.4. The gas intensity significantly drops inside of ~ 20 au for all lines, thus just inside the dust cavity. We note the location of the drop as the gas cavity, but this represents an upper limit. To get a better estimate of the actual gas cavity, a more thorough analysis of the temperature structure across the cavity such as in Leemker et al. (2022) or a kinematical approach such as in Bosman et al. (2021) is required. In addition to the inner cavity, a prominent drop of emission is seen in ^{13}CO and C^{18}O at ~ 35 au. This intensity drop coincides with the continuum emission and thus may be caused by continuum absorption rather than representing a gas gap. Another intensity drop is observed in C^{18}O around 85 au and in ^{13}CO around 150 au, the C^{18}O emission is too noisy around this location. This dip corresponds to the gap tentatively detected in the channel maps. Continuum absorption is unlikely responsible for this substructure as it peaks around 200 au, but (particularly for C^{18}O) higher sensitivity data are needed to quantify a gas gap at these radii.

5.3 Analysis

5.3.1 Model setup

We use the DISCMINER code introduced in Izquierdo et al. (2021) to model the intensity channels (see Fig. 5.2) of the HD 100546 disc. In the following, we outline the basic modelling approach but refer the reader to Izquierdo et al. (2021) for the full details of the package. In the DISCMINER, parametric prescriptions are adopted to reproduce the intensity channel maps from molecular emission. The parameters used in this work are briefly summarized as follows (see Table 5.3).

To describe the orientation of the disc, we use the position angle PA, inclination i, and disc centre $(x_{\rm c}, y_{\rm c})$. For the rotation velocity we adopt a Keplerian rotation, using the stellar mass M_* and source systemic velocity $v_{\rm sys}$ to describe the background velocity. The upper and lower emission surfaces are controlled by the height z above and below the disc midplane. Here we use a power law with an exponential tapering. The line peak intensity, line width, and line slope across the disc radial and vertical extent are parameterized with simple power laws of the disc cylindrical coordinates (R, z). For the peak intensity we select a combination of two power laws, describing the intensity profile inside and outside a radius $R_{\rm break}$. By doing so, we are able to account for a decrease in intensity inside the gas cavity. For radii larger than the parameter $R_{\rm out}$, the peak intensity is set to zero.

Subsequently, the DISCMINER is coupled with the Markov chain Monte Carlo (MCMC) random sampler EMCEE (Foreman-Mackey et al. 2013) to find those model parameters that best recover the intensity of the observed data cube. The different physical and morphological properties of the disc are thus modelled simultaneously to give a comprehensive view of the gas substructures and kinematics.

From the disc attributes, a model for the line profiles and data channels is generated. The modelled intensity I_m is described by a generalized bell kernel

$$I_{\rm m}(R, z, v_{\rm ch}) = I_{\rm p} \left(1 + |\frac{v_{\rm ch} - v_{\rm K^{l.o.s}}}{L_{\rm w}}|^{2L_{\rm s}}\right)^{-1} \tag{5.1}$$

as a function of the disc cylindrical coordinates (R, z) and velocity channel $v_{\rm ch}$. $I_{\rm p}$ is the peak intensity, $L_{\rm w}$ half the line width at half power, $L_{\rm s}$ the line slope, and $v_{\rm K^{l.o.s}}$ the Keplerian line-of-sight velocity. The vertical coordinate z is determined by the height of both the upper and the lower disc surface, thus each property except for L_s has two descriptions. The contribution of the upper and lower emitting surfaces are merged into a single-line profile by selecting the highest intensity between bell profiles computed for both surfaces independently in each velocity channel and pixel.

Table 5.3: Parameterization adopted for the DISCMINER models in this work[(a)].

Attribute	Parameterization
Orientation	i, PA, $x_{\rm c}, y_{\rm c}$
Rotation velocity	$v_{\rm K} = \sqrt{GM_*/r^3} \cdot R$, $v_{\rm sys}$
Emission surface	$z_{u,l} = z_{u0,l0}(R/D_0)^p \cdot \exp\left[-(R/R_{\rm t})^q\right]$
Peak intensity	$I_{\rm p} = I_0(R/D_0)^{p0}(z/D_0)^q$, $R < R_{\rm break}$
	$I_{\rm p} = I_0(R/D_0)^{p1}(z/D_0)^q$, $R > R_{\rm break}$
	$I_{\rm p} = 0$, $R > R_{\rm out}$
Line width	$L_{\rm w} = L_{\rm w0}(R/D_0)^p(z/D_0)^q$
Line slope	$L_{\rm s} = L_{\rm s0}(R/D_0)^p$

Notes. [(a)] D_0 represents a normalization constant, set to 100 au, R and z are the disc cylindrical coordinates, and r the spherical radius. G is the gravitational constant, all other variables are left as free parameters.

5.3.2 Fitting procedure

To initialize the EMCEE sampler, we chose inclination, position angle, and stellar mass found by the models of Wölfer et al. (2023) and guessed the other parameters using the interactive prototyping tool of the DISCMINER, which allows to compare the morphology of the model and data channel maps as well as line profiles by eye. As a burn-in phase, the MCMC was then run with 256 walkers in two phases, first for 2000 steps and then for 5000 steps but using the fitting results from the previous run. Afterwards, we performed runs with the same number of walkers

and 10 000 steps until convergence was reached in all parameters. In each run, the posterior distribution was sampled from the last 1000 steps and used as initial parameters for the next step[3].

The noise of the data was taken into account in the fit: at each data pixel, the standard deviation of the residual intensities in line-free channels was calculated and adapted as a weighting factor for the likelihood function to be maximized by the sampler (see Izquierdo et al. 2021). To ensure that the noise of the individual pixels was approximately independent of their neighbouring pixels, we down-sampled the data with at least one beam while still ensuring that we had enough pixels left for the fit (> 50).

The HD 100546 disc has previously been proposed to be warped in the centre (Walsh et al. 2017). This could result in a temperature difference, potentially producing an elevation asymmetry, as it has been observed in CO emission of the Elias 2-27 disc (Paneque-Carreño et al. 2021). Moreover, the system is still surrounded by a diffuse envelope (Grady et al. 2001) and the infall of material from that envelope onto the disc could also result in such an asymmetry. To check for asymmetries between the blue- and redshifted sides of the disc, we conducted additional runs where only half of the channels of the according side were modelled instead of using the full cube. For $C^{18}O$ we switched off the lower surface in all runs since the channels appear to be very flat. Even though this is true also for ^{13}CO, we ran models fitting for both surfaces and models where the lower surface was not included, yielding similar results. In the following, we will thus use the models where both surfaces were modelled. In the case of ^{12}CO 7-6, only the models that accounted for the blue- and redshifted side separately converged, however, they failed for the lower surface of the blueshifted side. To model the full cube, we therefore conducted additional runs with the lower surface switched off, which converged fine and are thus used in our following results.

5.3.3 Fitting Results

The best-fit parameters are summarized in Table 5.4 for the models fitting the full cube and in Tables 5.B.1 and 5.B.2 for the models fitting the blue- and redshifted side separately. The retrieved orientation of the disc is very similar in all models, resulting in a mean inclination i and position angle PA of $42.71 \pm 1.48\,^{\circ}$ and $232.78 \pm 2.12\,^{\circ}$, respectively. A slightly larger, but still small scatter is found for the stellar mass ($2.14 \pm 0.15\,M_*$), which is relatively sensitive to changes in the model. For the Band 6 and Band 7 data, the systemic velocity is very close to the expected value of $5.7\,\mathrm{km\,s^{-1}}$, however, for the ^{12}CO 7-6 it is fitted as $5.4\,\mathrm{km\,s^{-1}}$. As mentioned before, this offset from the source velocity found in the literature (e.g., Walsh et al. 2014, 2017) can be seen in the channel and rotation maps. The trend of decreasing line width from ^{12}CO 7-6 to $C^{18}O$ is picked up by the DISCMINER. The radius R_{break}, where a switch in the peak intensity profiles is happening, generally increases towards $C^{18}O$ (exception is ^{12}CO 3-2). This can be explained by the inner gas cavity ($< 20\,\mathrm{au}$) becoming more pronounced in the more optically thin lines. We note however, that R_{break} marks the point where the

[3]For the ^{12}CO 7-6 model we doubled the number of steps in all stages.

Table 5.4: Best-fit results of the modelling of the full cubes with the DISCMINER.

Attribute	Parameter	Unit	^{12}CO 7-6	^{12}CO 3-2	^{12}CO 2-1	^{13}CO 2-1	C^{18}O 2-1
Orientation	i	$^\circ$	39.30	43.83	44.12	42.86	42.51
	PA	$^\circ$	230.95	233.37	233.37	234.45	234.34
	x_c	au	–0.44	10.29	2.11	0.23	2.61
	y_c	au	–2.20	–7.09	–2.34	–1.34	–3.11
Velocity	M_*	$M_\odot$	2.21	1.94	1.99	2.16	2.30
	v_{sys}	km s^{-1}	5.38	5.65	5.65	5.64	5.64
Upper surface	z_0	au	19.32	32.06	21.20	3.07	8.21
	p	-	0.85	0.49	0.71	0.02	0.22
	q	-	1.88	1.78	3.64	5.05	1.88
	R_t	au	292.86	303.21	324.06	212.80	161.45
Lower surface	z_0	au	-	15.32	23.93	43.72	-
	p	-	-	1.06	1.61	0.97	-
	q	-	-	1.02	1.01	2.46	-
	R_t	au	-	265.38	147.78	20.98	-
Intensity	I_0	Jy px^{-1}	7.04	5.56	0.21	0.06	0.009
	p_0	-	–0.97	0.79	–0.08	0.97	0.94
	p_1	-	–1.40	–0.58	–0.88	–0.41	–2.46
	q	-	0.83	0.59	0.55	0.32	0.001
	R_{break}	au	54.98	37.90	55.05	59.14	64.20
	R_{out}	au	322.04	372.79	369.84	326.29	253.61
Line width	L_W	km s^{-1}	2.01	1.03	0.66	0.29	0.02
	p	-	–0.90	–0.73	–0.59	–0.80	–1.28
	q	-	0.44	0.13	–0.002	–0.11	–0.87
Line slope	L_S	-	2.03	1.81	2.02	1.61	1.74
	p	-	0.29	0.11	0.26	0.08	–0.001

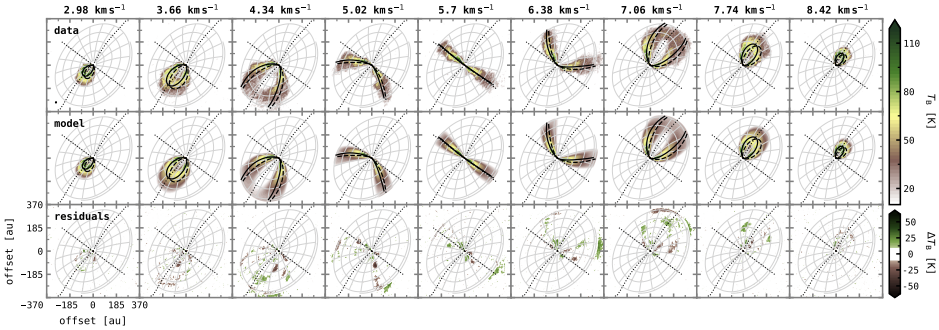

Figure 5.5: Examples of the intensity channels of ^{12}CO 2-1 (top), shown in steps of four around the central channel, alongside the best-fit model obtained with the DISCMINER (middle) and the corresponding residuals (bottom). The iso-velocity curves of the upper and lower surfaces are overlaid as solid and dashed lines, respectively. The emitting surface and disc axes are plotted in the background as grey contours and dotted lines, respectively. The beam of the observation is indicated in the bottom left corner of the first panel.

intensity is maximal and not the actual cavity radius, and other effects (such as temperature) influence its location.

5.3.3.1 Channel maps

In Fig. 5.5, we present a comparison of the data and best-fit model channels of ^{12}CO 2-1 alongside the residuals obtained from subtracting the model from the data. The channels are shown in steps of four around the central channel. The according plots of the other lines are included in Appendix 5.C. The overall morphology of the data channels is well reproduced by the models, except for ^{12}CO 7-6, where the lower surface could not be modelled properly.

The emission surfaces obtained from the models are overlaid as grey contours in the individual panels. For all lines, their morphology matches that of a rather flat and not very flared disc: the back side of the disc is barely visible and the azimuthal contours do not show any clear bending. While this is not unusual for ^{13}CO and C^{18}O, it is puzzling that we do not see a stronger manifestation of the vertical structure in ^{12}CO.

The surface of the disc is expected to become most visible in ^{12}CO 7-6. In Fig. 5.C.2, we therefore plot the channels as a combination of the models fitting only half of the cube. While the emission surface on the blueshifted side is still showing a flat morphology, the redshifted side appears much more elevated and flared. A similar exercise for the other ^{12}CO lines did not yield a significantly different emission surface compared to the one retrieved from the full cube. Another interesting point about the combined ^{12}CO 7-6 plot is that it shows that the vertical structure itself can produce apparent wiggles in the channels, which are nicely retrieved by the model, especially for the blueshifted side.

The residuals of the different lines partly reach high values, suggesting that

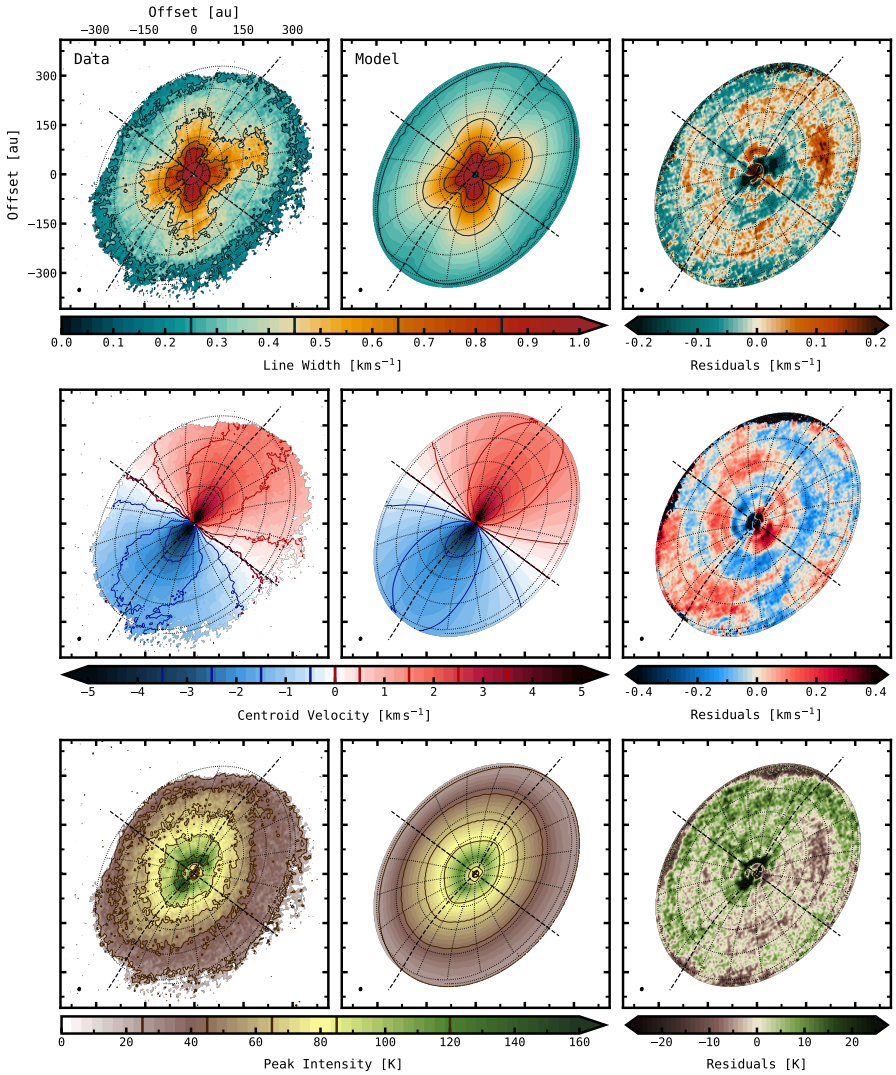

Figure 5.6: Observables extracted from the modelled line intensity, shown for ^{12}CO 2-1 as an example. Displayed are the line widths (top), centroid velocities (middle), and peak intensities (bottom) for the data and best-fit model. The residuals, showing the differences between the data and model, are included in the last column. Some contour levels, indicated in the colour bars, are included to ease comparison. The emission surface and disc axes are plotted as dotted and dashed lines, respectively.

a smooth Keplerian model cannot fully reproduce the data. These deviations from Keplerian rotation can be used to unveil the mechanisms being at play, including massive planets but also other physical processes such as disc winds, hydrodynamical instabilities, or turbulence.

5.3.3.2 Observables

From the line intensity profiles modelled by the DISCMINER, we extract three observables to search for substructures in the gas disc of HD 100546: the line width, centroid velocity, and peak intensity or brightness temperature. These are computed from Gaussian kernels which are fitted to both the data and the model and illustrated in Fig. 5.6 (left and middle panels) for the ^{12}CO 2-1 line. The residuals resulting from the deviations of the data from the model are depicted in the right panels. The different observables can be used to trace various physical properties of the disc. The line width and peak intensity are shaped by both the gas temperature and density, the line width can additionally be used to trace turbulent motions. The gas motions which manifest in the kinematics are driven by dynamical, and often coupled, processes, including the gravitational influence of embedded (massive) bodies. Using the vertical emission structure together with the orientation of the disc as modelled by the DISCMINER, the observables can be deprojected onto the disc's reference frame and their substructures can be analysed in terms of location, magnitude, and extent.

5.4 Results

5.4.1 Kinematics

In Fig. 5.7 we show the centroid velocity residuals for all five lines, ordered from the brightest to the faintest. It is striking, that prominent spiral features are visible in all maps: in ^{12}CO 7-6, a large coherent spiral runs from the inner disc around 50 au and 90 ° out to radii of 300 au, and possibly further, covering more than one full azimuth. In ^{12}CO 3-2, similar features can be discerned, yet they are not as connected. In ^{12}CO 2-1, which has a higher spatial resolution, the spiral seems to consist of several arms which are slightly more tightly wound than in ^{12}CO 7-6. In ^{13}CO and C^{18}O, the spirals become even more tightly wound. The anchoring point of the spiral substructures lies between 50 and 150 au and between 60 and 120 °.

To further analyse the spiral features we plot the binned residuals as radius versus azimuth in Fig. 5.8 and attempt to reproduce the morphology of the spirals (by eye) with different functional forms: an Archimedean or linear spiral

$$r = a + b\phi, \tag{5.2}$$

and a logarithmic spiral

$$r = ae^{b\phi}, \tag{5.3}$$

where r is the radius and ϕ the polar angle of the spiral. In Fig. 5.7 we overlay the obtained linear spirals, the logarithmic spirals are presented in Fig. 5.D.1. The overall morphology of the spiral substructures is well represented by both parameterizations, however, the logarithmic spirals tend to deviate more from the features in the outer disc, while they better reproduce the bending in the inner disc than the linear spiral, which can by definition not account for that. Connected

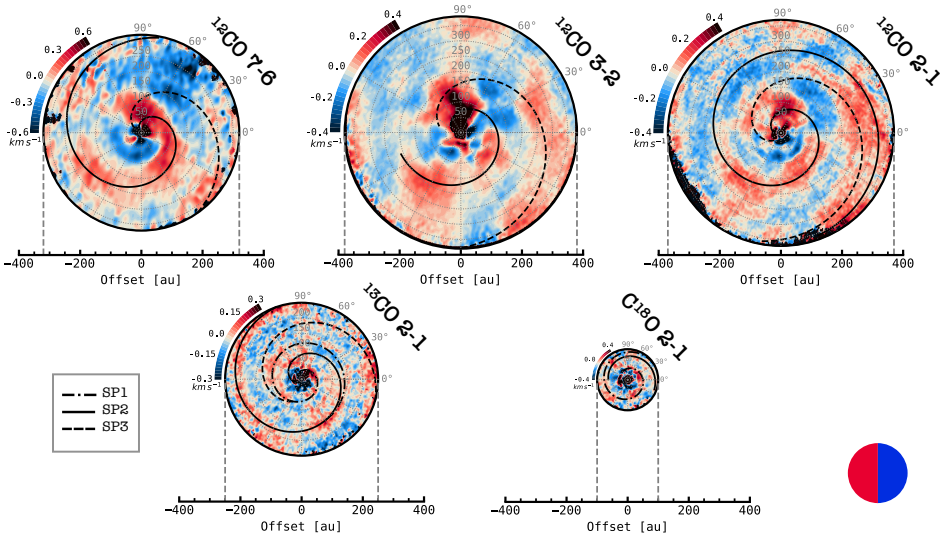

Figure 5.7: Centroid velocity residuals, shown for the five lines studied in this work. All lines exhibit extended spiral substructures. A linear (by-eye) parameterization of the spirals is overlaid as black lines. The spirals are labelled depending on their (increasing) radius as SP1, SP2, and SP3. The circle in the lower right corner indicates the blue- and redshifted sides of the disc.

to that, three linear spirals can account for the substructures seen in ^{13}CO 2-1, but only two logarithmic spirals are needed to match the pattern. The different spirals are labelled as SP1, SP2, and SP3 depending on their radial locations (i.e., SP1 is the spiral closest in, SP3 the farthest). We note that the second spiral is not really visible as a connected structure in ^{12}CO 7-6 but we have based this on the features seen in ^{12}CO 2-1.

Comparing the three ^{12}CO lines, it seems that a blue feature, separating the inner and outer parts of the spiral, is emerging more and more from ^{12}CO 2-1 to ^{12}CO 7-6. This suggests that other mechanisms shaping the kinematics may be coming into play, for example, interactions with the discs's environment (such as infall) which are adding a large velocity dispersion.

The parameters of the individual spiral prescriptions are presented in Table 5.5. They can be used to compute the opening angle or pitch angle β of the spirals with

$$\tan\beta = \left|\frac{dr}{d\phi}\right| \cdot \frac{1}{r}. \tag{5.4}$$

This results in a constant pitch angle for the logarithmic and a radially varying one for the linear spirals. The pitch angles are plotted in Fig. 5.9. For the linear spirals, the pitch angles are relatively small in the outer disc regions but rapidly increase inside of ~ 50 au. The constant pitch angles found from the logarithmic spirals have values below $20\,^{\circ}$. In both cases, the pitch angles decrease from ^{12}CO 7-6 to C^{18}O 2-1 and from SP3 to SP1, which is in agreement with the predictions of Juhász & Rosotti (2018) from modelling of thermal stratification.

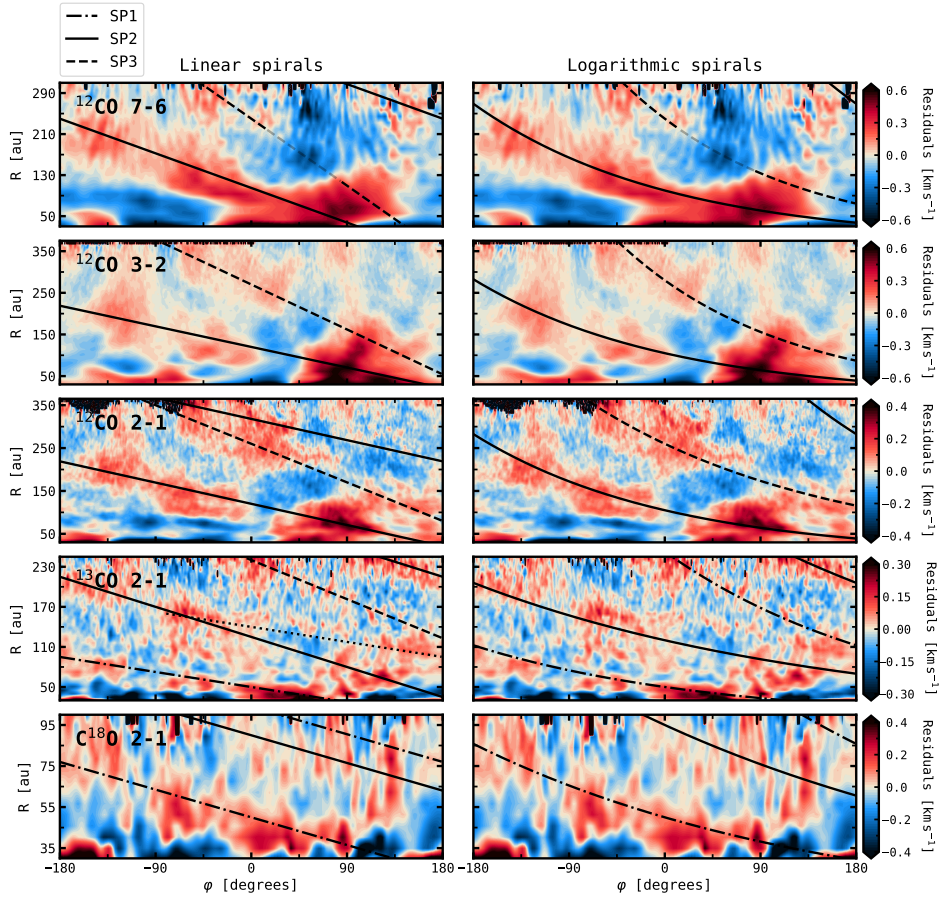

Figure 5.8: Azimuthal deprojection of the centroid velocity residuals of the five lines, shown with overlaid linear (left) and logarithmic (right) spirals. The spirals are labelled depending on their (increasing) radius as SP1, SP2, and SP3.

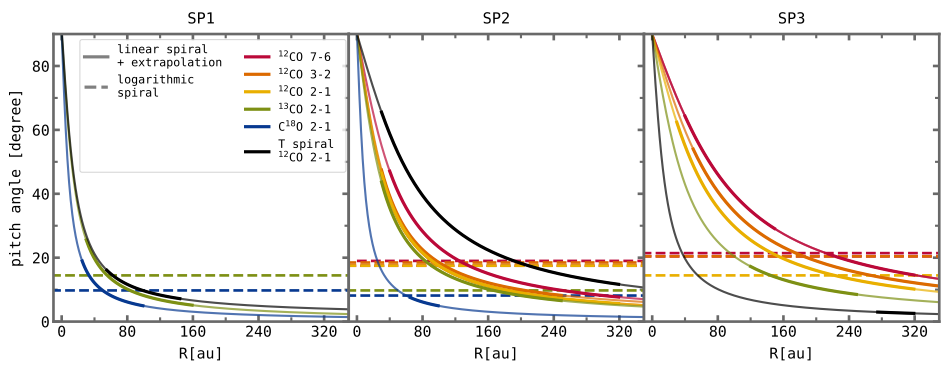

Figure 5.9: Pitch angles of the spirals observed in the kinematics (and peak intensity of ^{12}CO 2-1), obtained from a linear and a logarithmic prescription.

Table 5.5: Parameters to reproduce the spirals (by eye) with linear and logarithmic functions.

		Parameter	^{12}CO 7-6	^{12}CO 3-2	^{12}CO 2-1	^{13}CO 2-1	C^{18}O 2-1	^{12}CO 2-1 $T_{\rm B}$
Linear	SP1	a (au)	-	-	-	50	50	100
		b ($^\circ$ au^{-1})	-	-	-	–0.25	–0.15	–0.25
	SP2	a	105	120	120	125	90	90
		b	–0.75	–0.55	–0.55	–0.5	–0.15	–1.15
	SP3	a	240	270	260	240	–	290
		b	–1.45	–1.2	–1.0	–0.65	–	–0.25
Logarithmic	SP1	a (au)	-	-	-	50	50	-
		b ($^\circ$ au^{-1})	-	-	-	–0.0045	–0.003	-
	SP2	a	100	105	105	120	95	-
		b	–0.0055	–0.0055	–0.0055	–0.003	–0.0025	-
	SP3	a	240	280	260	-	-	-
		b	–0.0065	–0.0065	–0.0045	-	-	-

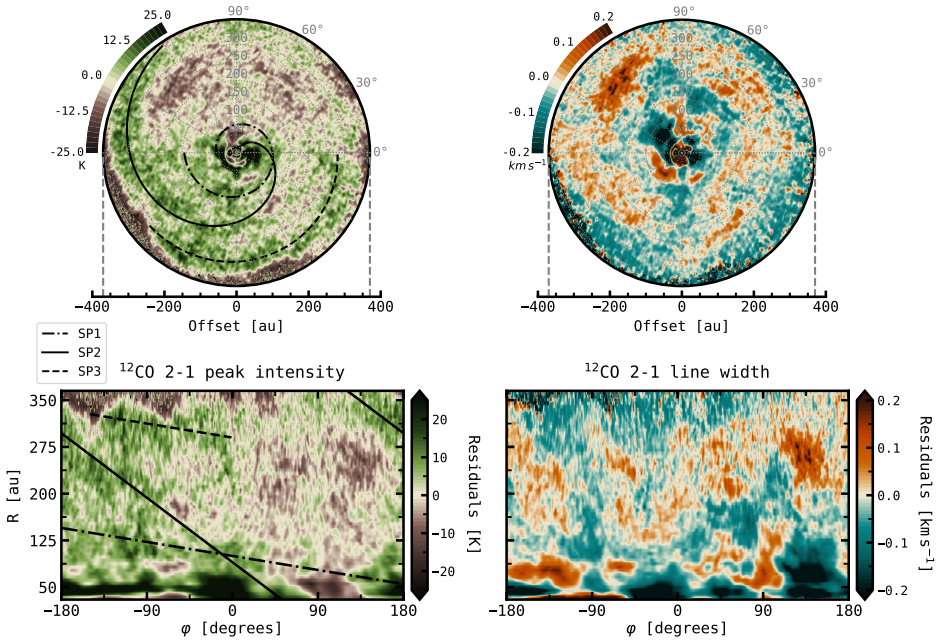

Figure 5.10: Peak intensity (left) and line width (right) residuals of ^{12}CO 2-1. Shown are the deprojected maps (top) and an azimuthal deprojection (bottom). In the peak intensity, three parameterizations of a linear spiral are overlaid.

5.4.2 Peak intensities and line widths

The residuals of the peak intensity and line widths are displayed in the Appendix in Figs. 5.E.1 and 5.E.2, again shown ordered from the brightest to the faintest line. The substructures in the peak intensity and line width are less clear than in the kinematics and no coherent spiral structures can be discerned. In ^{12}CO 7-6, the upper half of the disc (corresponding to the southwest side of the disc in disc coordinates) happens to be colder while the lower half is hotter. This corresponds to the brightness asymmetry mentioned before, which is seen in the channels. The line widths on the other hand are increased in the upper half of the disc, but they are decreased in the lower side. Together, this may suggest that the surface density is larger on the upper (south) side, thus broadening the line width and at the same time lowering the temperature. The additional material could be a result of infall processes, which do not only increase the density but also add a large velocity dispersion, which affects the shape of the line profile.

In ^{12}CO 3-2, peculiar wing- and cross-like structures are present in both the peak intensity and line width residuals, showing a very similar pattern, yet with opposite signs (i.e., enhanced temperatures correspond to decreased line widths). Another prominent feature is a localized temperature enhancement around 150 au and 60 °, which corresponds to the spot already seen in the channel maps. The features in ^{12}CO 3-2 are very hard to interpret and better resolution data (including

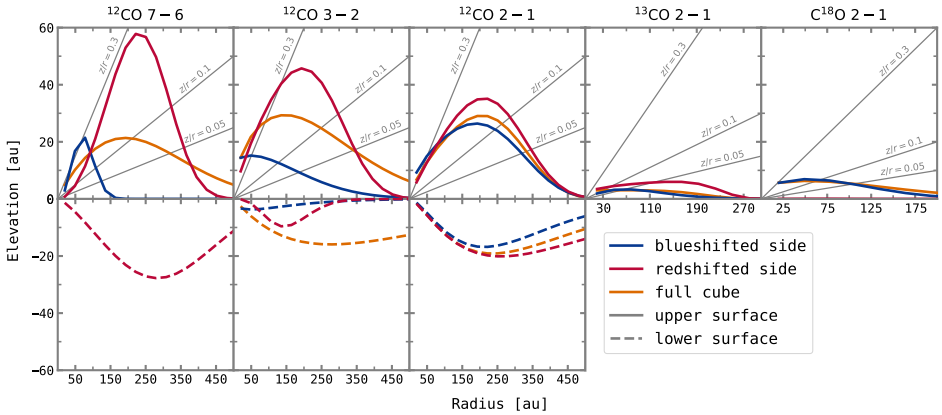

Figure 5.11: Upper (top) and lower (bottom) emission surfaces of the five molecular lines, shown for the fits of the full cube and the fit of the blue- and redshifted sides only.

the short and long baseline observations with the same setup) are needed to make any quantitative remarks. Similarly, higher sensitivity data are needed for ^{13}CO and C^{18}O, which show cross-like patterns in the line width residuals, resulting from the missing fit of the lower surface.

Somewhat clearer substructures can be discerned in ^{12}CO 2-1, for which we show the projected and polar-deprojected maps in Fig. 5.10. In the peak intensity, three tentative spiral- or arc-like structures are visible, which we reproduce with the linear function. The parameters and pitch angles obtained for these spirals are included in Table 5.5 and Fig. 5.9. We note that it is difficult to clearly disentangle the patterns seen in the ^{12}CO 2-1 peak-intensity residuals and their connection. Therefore, the parameterizations of the temperature spirals should be treated with caution. Furthermore, a prominent ring of enhanced line widths can be distinguished between $\approx 125 - 330$ au, showing a particularly bright region between 100–150 °. The ring co-locates with both low and high temperatures and it is thus difficult to say if the lines are broadened by temperature effects or density enhancements. The localized region on the other hand coincides with a low-temperature spot and may be tracing a region of dense gas material or turbulent motions rather than temperature.

5.4.3 Emission heights

In Fig. 5.11, we present the emission layers of the upper and, in case of ^{12}CO, lower surfaces of the disc, extracted from the DISCMINER models. Here we plot the profiles obtained from runs fitting for the full cube (orange) as well as the blue- and redshifted sides only. The curves show that while the optically thick ^{12}CO emission is coming from more elevated disc layers, particularly in the higher transitions, ^{13}CO and ^{18}CO originate from similar layers that are very close to the midplane. Furthermore, a clear asymmetry between the red- and blueshifted side

is revealed, which becomes particularly strong for ^{12}CO 7-6 and ^{12}CO 3-2: the emission of the redshifted side of the disc is coming from much higher disc layers ($\sim$ 30 au difference for ^{12}CO 7-6 and ^{12}CO 3-2) than that of the blueshifted side, which can already be seen in the channel maps (see for example Fig. 5.C.2). Such an asymmetry has been detected before only for the Elias 2-27 disc, a massive and gravitationally unstable disc, that may be affected by infall or an inner warp (Paneque-Carreño et al. 2021, 2022).

5.4.4 Azimuthal averages

In Fig. 5.12, we plot the azimuthally averaged residuals, including both the azimuthal and vertical velocity perturbations aside from the line width and peak intensity deviations. The former two are obtained by using either the simple subtraction of the DISCMINER model from data or subtracting absolute values. The derivation of the azimuthal and vertical velocities is detailed in Izquierdo et al. in submission. In Fig. 5.12, we mark the locations where planets have previously been proposed as well as the centres of the two observed dust rings (B28 and B200). We further annotate some trends seen in the profiles such as the sign of the velocity gradient in the azimuthal perturbations (tracing pressure minima and maxima), upwards and downwards meridional flows in the vertical perturbations, and local minima or maxima in the line width and peak intensity. We discuss some of the trends seen in the averages in the following, however, we note that their computation is based on the assumption of axisymmetry, which does not necessarily hold. In fact, the spiral structures seen in the kinematics suggest the perturbations to be non-symmetric. Nevertheless, the curves are still useful to get an indication of some general trends.

At the location of the dust rings, negative velocity gradients are seen in all lines except ^{12}CO 7-6, tracing pressure bumps which can account for the formation of the rings. In this context, the more optically thin lines tracing regions closer to the midplane can better constrain the underlying density profile than the optically thick lines which are affected by the temperature. Thus, it is not surprising that ^{12}CO 7-6 is showing an opposite trend. Inside the inner dust cavity, a strong positive gradient is present and downward meridional flows indicate the gas material falling into the cavity. However, close to the star, beam smearing and optical depth effects are becoming significant, resulting in large errors, and inside of $\sim$ 25 au the profiles have to be treated with caution. For the same reason, we are not able to draw any conclusions on the features seen around the innermost planet candidate at $\sim$ 15 au. Around the location of the second planet candidate at $\sim$ 53 au, both ^{13}CO and C^{18}O show strong positive gradients, supporting the presence of a gas gap that indeed may be carved by a massive companion. Again, an opposite trend is visible in ^{12}CO but as mentioned above, ^{13}CO and C^{18}O are more likely to trace pressure minima related to a low gas density. Just inside the planet candidate's location, downward meridional flows are seen in all lines, further supporting the presence of a companion. Moreover, there are line width minima (in ^{12}CO) that align well with the meridional flows. The brightness temperature shows strong fluctuations inside of $\sim$ 100 au, which are hard to put into context with the other

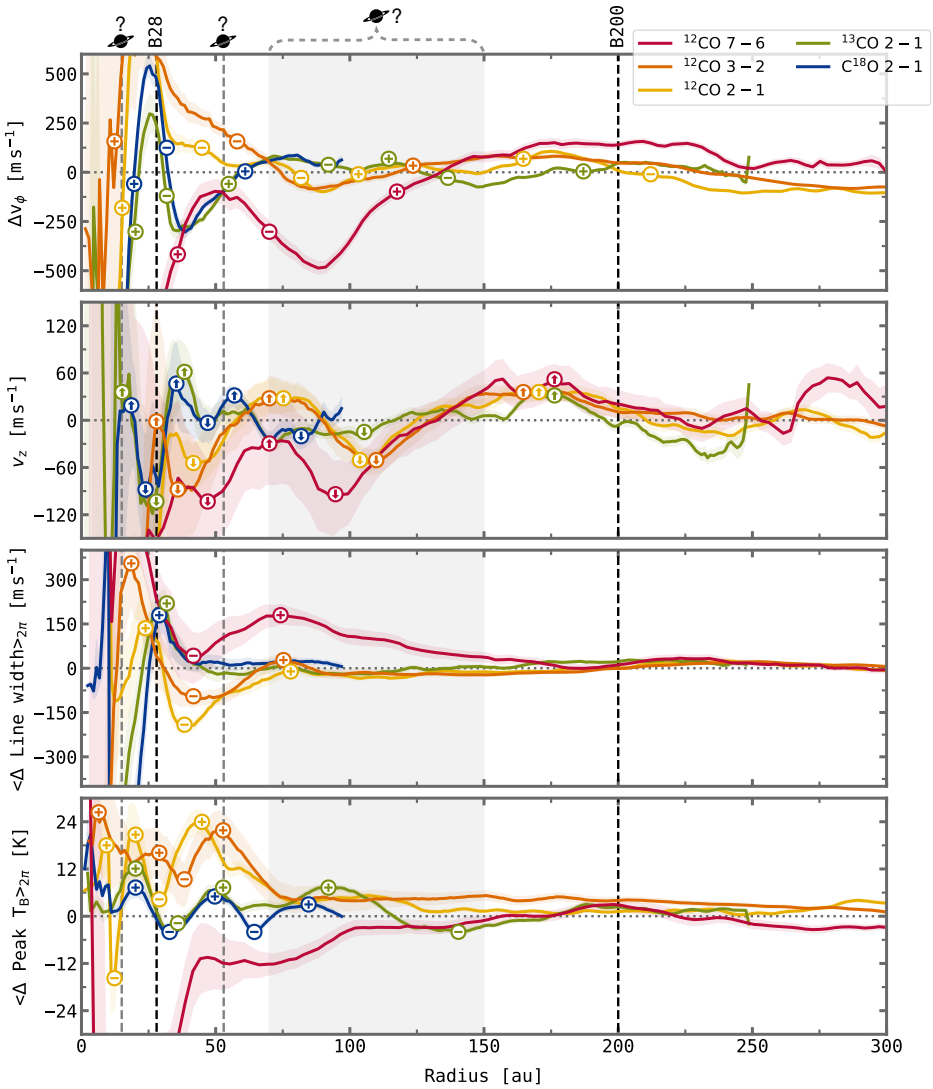

Figure 5.12: Azimuthally averaged profiles of the azimuthal and vertical velocity (top two panels), line width (third panel), and peak intensity (lower panel) residuals, shown for all five lines. The centres of the dust rings and locations of previously proposed planets are marked by dashed lines and a shaded region. In the top panel, the sign of the velocity gradient is indicated with plus and minus signs. In the second row, meridional flows hinting at gas moving away from and towards the disc midplane are highlighted as up and down arrows. Local line width and temperature maxima and minima are indicated with plus and minus signs.

substructures and their origin cannot really be assessed.

Except for $C^{18}O$, for which the emission is not as extended, positive azimuthal velocity gradients and significant downward meridional flows are present in all molecular tracers between 90–125 au, which coincides with the dust gap found by Fedele et al. (2021), the third proposed location of a planet candidate, the location of the bright spot in ^{12}CO 3-2, and the gap seen in the radial profile of ^{13}CO. For most of the radii, where the ring of enhanced line widths is observed in ^{12}CO 2-1 (see Fig. 5.10), a negative azimuthal velocity gradient is found, supporting that we are indeed tracing a gas ring.

5.5 Discussion

5.5.1 On the planet candidate at 50 au

All molecular tracers analysed in this study exhibit extended spiral structures in the kinematical residuals, which we reproduce (by eye) with linear and logarithmic functions (Figs. 5.7, 5.8). Their consistency suggests them to be real features tracing a common origin. The pitch angles of the linear spirals show small values at most radii but rapidly increase inside of ∼50 au. Such a behaviour is consistent with Lindblad-resonance-driven spiral wakes of a massive embedded companion (e.g., Ogilvie & Lubow 2002; Rafikov 2002; Bae & Zhu 2018a,b), which tend to increase only close to the location of the planet. The logarithmic spirals on the other hand show constant pitch angles below 20 °, which are more consistent with tightly wound spirals excited by a planet through buoyancy resonances (Bae et al. 2021). In both cases, the spirals support the presence of a companion inside of ~ 50 au and therefore provide additional evidence for the planet candidate HD 100546 b, even though also the candidate HD 100546 c could in principle explain the formation of the spirals. Furthermore, the possibility of a binary rather than a planetary companion, as invoked by Norfolk et al. (2022), cannot be ruled out with the present data. The HD 100546 disc has previously been suggested to be warped in the centre (Walsh et al. 2017), and a binary companion would provide a good explanation for both the extended spiral structures and the misaligned inner disc. Hydrodynamical simulations are needed to further distinguish between the Lindblad and buoyancy scenario and to make predictions on the companion mass and location.

While velocity spirals do not necessarily align with spiral features in the peak intensity, it is still puzzling that except for ^{12}CO 2-1, no counterpart of the kinematical spirals is found. Both in TW Hydra (Teague et al. 2019b, 2022a,b) and CQ Tau (Wölfer et al. 2021), temperature spirals have been observed that overlap at least partly with the spirals in the velocity residuals, suggesting that there may be a physical mechanism behind their connection. In the companion scenario, the spiral density waves lead to an increase in surface density and thus to a higher CO opacity. The $\tau = 1$ layer is moved to a larger altitude, where the temperature is generally higher, resulting in the observed spiral substructure in the gas temperature (Phuong et al. 2020a,b). The lack of temperature features in HD 100546 is therefore unexpected, however, velocity spirals are more easily detected than

those in the peak brightness temperature. The absence could therefore result from sensitivity effects and needs to be further investigated in the future.

Aside from dynamical interactions with a companion, spiral structures can also be a signpost of gravitational instability (GI; e.g., Rice et al. 2003). In that case, the pitch angles are expected to be comparable for the surface and the midplane layers, which are heated by shocks. On the other hand, the pitch angle is expected to increase towards the surface layers in the companion scenario if the disc is passively heated with a positive vertical temperature gradient (Juhász & Rosotti 2018). The spirals in HD 100546 indeed become more tightly wound towards the midplane, supporting the predictions by Juhász & Rosotti (2018) and dynamical interactions rather than GI as the underlying mechanism.

5.5.2 On the planet candidate between 70–150 au

To explain the ringed substructures in the dust, a planet orbiting at large separations between 70–150 au has previously been proposed (Walsh et al. 2014; Pinilla et al. 2015; Fedele et al. 2021; Pyerin et al. 2021). In this region, we observe vertical motions directed down towards the midplane around ~ 110 au in ^{12}CO 3-2, ^{12}CO 2-1, and ^{13}CO 2-1, and around ~ 95 au in ^{12}CO 7-6 (Fig. 5.12, panel two). This shift is not surprising as the lines trace different heights in the disc which are governed by different physical and chemical processes. Such meridional flows are commonly associated with forming planets and similar motions have been observed before by Teague et al. (2019a), possibly tracing a depletion of gas material carved by an embedded companion. The presence of a gas gap around 90–150 au is further supported by the positive sign of the azimuthal velocity gradient at these radii (Fig. 5.12), and tentative dips of emission in the azimuthally averaged radial intensity profiles of ^{13}CO (~ 150 au) and C^{18}O (~ 85 au) (Fig. 5.4). Lastly, a bright, localized spot stands out in the velocity channels and peak intensity map of ^{12}CO 3-2 around 125 and 150 au, respectively. Altogether, these features strongly support the presence of a massive planet in the outer disc. However, higher sensitivity data at high resolutions are needed to confirm the robustness of the substructures. Moreover, a comparison with hydrodynamical models is crucial to understand if they can indeed be explained by a massive embedded body.

5.5.3 Origin of the asymmetry in emission heights

The CO emission of HD 100546 is marked by an asymmetry between the blue- and redshifted halves of the disc, which is especially pronounced in ^{12}CO 7-6 and ^{12}CO 3-2 (Fig. 5.11). Such an asymmetry has previously been detected only for the Elias 2-27 disc (Paneque-Carreño et al. 2021, 2022). One explanation could be given by infall onto the redshifted side of the disc. Infalling material results in an increase of the surface density, and thus the emission becomes optically thick in higher disc layers. Moreover, the temperature is altered as shocks will heat the layers on which the material is accreted (Hennebelle et al. 2017). Observations of scattered light have indeed revealed that the disc is surrounded by a diffuse envelope (Grady et al. 2001; Ardila et al. 2007). Another scenario that may account for the asymmetry

is the presence of a warped inner disc casting a shadow over part of the outer disc, shielding it from stellar radiation and thus resulting in an azimuthal variation of the temperature, which has an immediate effect on the vertical structure of the disc. The northeast side of the disc indeed appears to be brighter, which is in agreement with a shadowing misaligned disc. A warped inner disc can in principle be triggered by binary interactions or a misaligned planet (e.g., Nealon et al. 2018) but also the infall of material may produce such a structure (Bate et al. 2010; Sakai et al. 2019).

5.6 Summary

In this work, we have modelled the molecular line emission of five CO lines observed with ALMA in the circumstellar disc around HD 100546. Our main results are summarized as follows.

- Extended spiral features are resolved in the kinematics of all five lines. The peak intensity also shows indications of spirals but only in ^{12}CO 2-1, likely due to limited sensitivity for the other lines. A ring and bright region of enhanced line widths are seen in the line width residuals of ^{12}CO 2-1.
- The spirals are well reproduced by a linear and/or a logarithmic function and show small pitch angles that are consistent with Lindblad or Buoyancy spirals driven by a companion.
- A rapid increase of the pitch angles inside of ~ 50 au suggests an upper limit for the companion location around this radius, which is consistent with the planet candidate HD 100546 b or HD 100546 c but may point to a binary companion rather than a planet as suggested by Norfolk et al. (2022).
- Several indications for a companion at larger separations (90–150 au) are present: meridional flows towards the midplane and pressure minima around this region suggest a gas-depleted ring that may be carved by an unseen planet. In the radial curves of the integrated intensity of ^{13}CO 2-1 and C^{18}O 2-1, tentative gas gaps are visible at 150 and 85 au, respectively, but they need to be confirmed with higher sensitivity data. Altogether, these features coincide with the dust gap observed by Fedele et al. (2021).
- The emission from the redshifted side appears more elevated compared to the blueshifted side of the disc. Such an asymmetry may result from infalling material on one side of the disc, thus increasing the density and lifting the optically thick emission layer. Temperature effects resulting from a warped inner disc casting a shadow over the disc represent an alternative explanation.

High-sensitivity multi-line and multi-isotopologue data (of different molecules) taken at high spectral and spatial resolution are of paramount importance to probe the full vertical and radial extent of protoplanetary discs. Mapping out their structures and kinematics may enable us to distinguish different disc-shaping mechanisms, including planet–disc interactions, and to link their properties to those of the mature exoplanet populations.

Acknowledgements

This paper makes use of the following ALMA data: 2011.0.00863.S, 2015.1.00806.S, 2016.1.00344.S, and 2018.1.00141.S. ALMA is a partnership of ESO (representing its member states), NSF (USA) and NINS (Japan), together with NRC (Canada) and NSC and ASIAA (Taiwan) and KASI (Republic of Korea), in cooperation with the Republic of Chile. The Joint ALMA Observatory is operated by ESO, auI/NRAO and NAOJ.

Appendix

5.A Comparison of the ^{12}CO 3-2 data sets

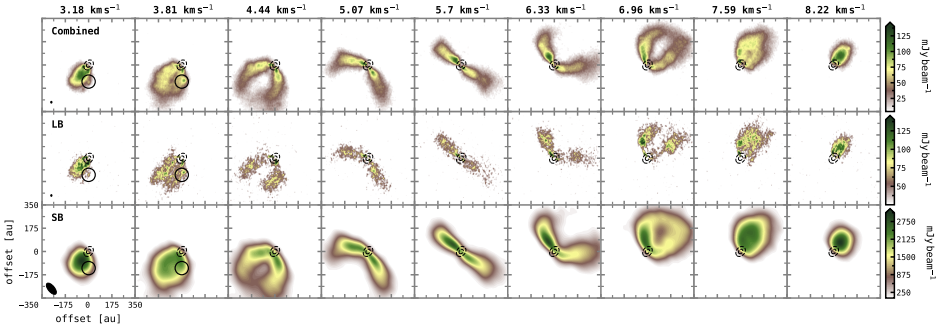

Figure 5.A.1: Comparison of the different ^{12}CO 3-2 data sets, with the combined data in the top row, the long-baseline data in the middle row, and the short-baseline data in the bottom row. Shown are the channels in steps or three from the central channel and for a velocity resolution of $210\,\mathrm{m\,s^{-1}}$. The inner millimetre continuum ring is overlaid as dashed contours. A localized feature is seen in some of the channels within the solid circle. The beam of the observation is indicated in the bottom left corner of the first panel of each row.

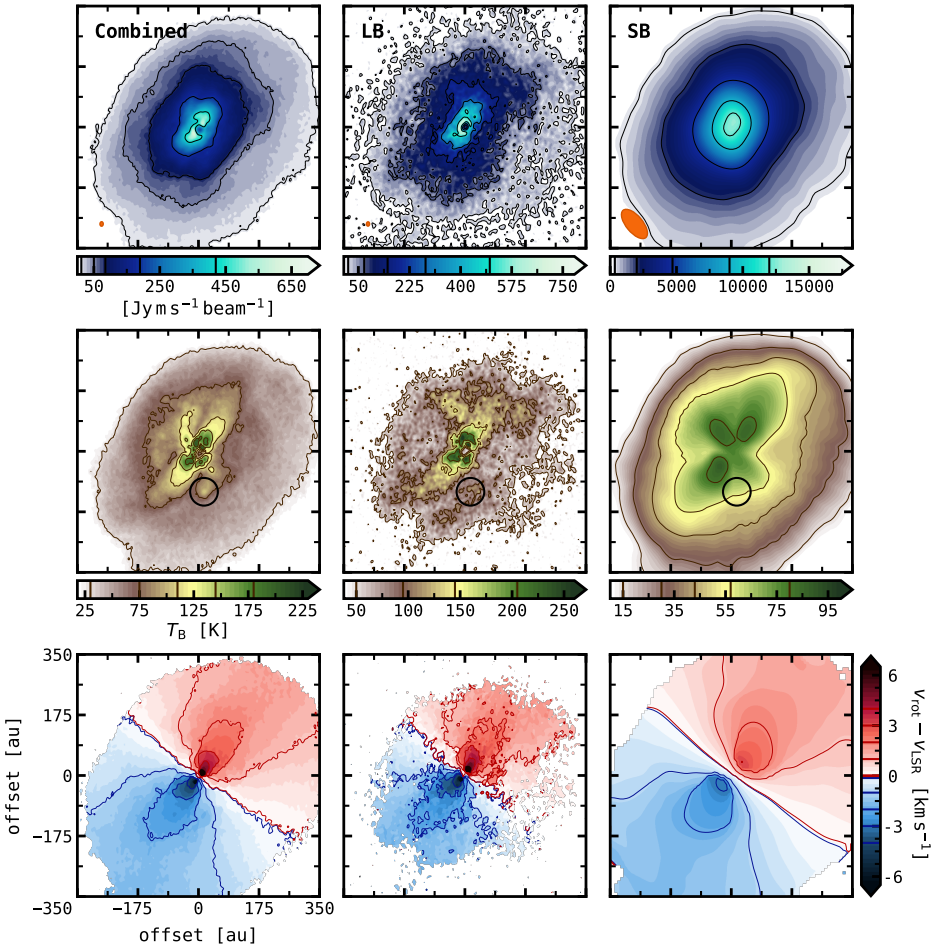

Figure 5.A.2: Comparison of the different ^{12}CO 3-2 data sets, with the combined data in the left column, the long-baseline data in the middle column, and the short-baseline data in the right column. Shown are the integrated intensity (top), peak intensity (middle), and line-of-sight velocity (bottom). A localized feature is seen within the solid circle. Some contours are overlaid and their levels are indicated in the colour bars. The beam of the observation is shown in the bottom left corner of the first-row panels.

5.B Best-fit parameters blue- and redshifted sides

Table 5.B.1: Best-fit results of the modelling of the blueshifted channels with the DISCMINER.

Attribute	Parameter	Unit	^{12}CO 7-6	^{12}CO 3-2	^{12}CO 2-1	^{13}CO 2-1	C^{18}O 2-1
Orientation	i	$^\circ$	41.88	42.06	44.06	41.88	42.06
	PA	$^\circ$	230.73	233.54	234.40	234.63	233.94
	x_c	au	0.45	4.29	3.11	0.08	3.12
	y_c	au	0.63	–6.32	–1.37	–1.42	–3.47
Velocity	M_*	$M_\odot$	2.12	1.99	2.12	2.25	2.40
	v_{sys}	km s^{-1}	5.41	5.64	5.70	5.66	5.68
Upper surface	z_0	au	146.40	17.65	21.94	7.80	10.60
	p	-	2.38	0.12	0.54	0.83	0.38
	q	-	2.27	1.78	3.44	1.65	2.02
	R_t	au	68.74	224.98	324.88	101.50	121.83
Lower surface	z_0	au	0.0	5.97	19.65	31.72	-
	p	-	0.06	0.30	1.63	1.14	-
	q	-	5.22	1.21	1.18	2.40	-
	R_t	au	116.38	149.38	161.36	21.41	-
Intensity	I_0	Jy px^{-1}	1.23	0.47	0.20	0.08	0.008
	p_0	-	–0.27	0.48	–0.08	0.65	0.81
	p_1	-	–0.90	–0.27	–0.83	–0.11	–2.49
	q	-	0.007	0.47	0.56	0.41	0.001
	R_{break}	au	55.14	39.67	59.18	59.69	65.16
	R_{out}	au	349.22	393.55	388.75	289.24	253.58
Line width	L_W	km s^{-1}	0.93	1.09	0.77	0.20	0.08
	p	-	–0.55	–0.66	–0.62	–0.94	–1.21
	q	-	0.005	0.09	0.06	–0.19	–0.44
Line slope	L_S	-	2.05	1.74	2.01	1.62	1.80
	p	-	0.21	0.14	0.23	0.07	0.03

Table 5.B.2: Best-fit results of the modelling of the redshifted channels with the DISCMINER.

Attribute	Parameter	Unit	^{12}CO 7-6	^{12}CO 3-2	^{12}CO 2-1	^{13}CO 2-1	C^{18}O 2-1
Orientation	i	$^\circ$	45.26	41.65	44.46	43.54	41.14
	PA	$^\circ$	226.83	230.16	232.74	234.05	234.17
	x_c	au	–7.22	7.93	1.12	0.28	–0.46
	y_c	au	1.61	–8.96	–3.29	–2.09	–3.12
Velocity	M_*	$M_\odot$	1.84	2.18	2.04	2.16	2.38
	v_{sys}	km s^{-1}	5.39	5.62	5.62	5.62	5.62
Upper surface	z_0	au	19.29	33.91	23.64	5.57	12.13
	p	-	2.02	0.78	0.87	0.29	3.78
	q	-	3.44	3.52	3.47	7.28	1.12
	R_t	au	269.93	299.48	313.99	234.89	21.46
Lower surface	z_0	au	11.82	21.17	27.43	2.52	-
	p	-	1.34	3.26	1.61	0.23	-
	q	-	2.48	1.67	0.87	3.07	-
	R_t	au	362.94	95.97	128.54	177.59	-
Intensity	I_0	Jy px^{-1}	7.63	0.52	0.21	0.05	0.009
	p_0	-	–1.22	0.97	0.06	0.90	1.28
	p_1	-	–2.10	–0.80	–0.89	–0.61	–2.40
	q	-	0.67	0.45	0.50	0.30	0.001
	R_{break}	au	56.69	40.33	50.56	61.69	60.35
	R_{out}	au	339.92	398.23	369.69	337.93	254.15
Line width	L_W	km s^{-1}	0.93	0.86	0.63	0.34	0.06
	p	-	–0.89	–0.63	–0.54	–0.67	–1.22
	q	-	0.12	0.01	0.02	–0.07	–0.19
Line slope	L_S	-	2.22	1.77	1.99	1.59	1.69
	p	-	0.32	0.20	0.27	0.09	0.07

5.C Comparison of the data and model channels

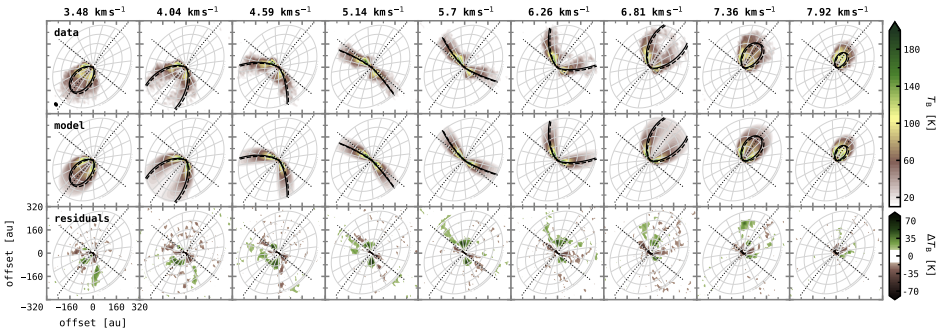

Figure 5.C.1: Same as in Fig. 5.5 but for ^{12}CO 7-6.

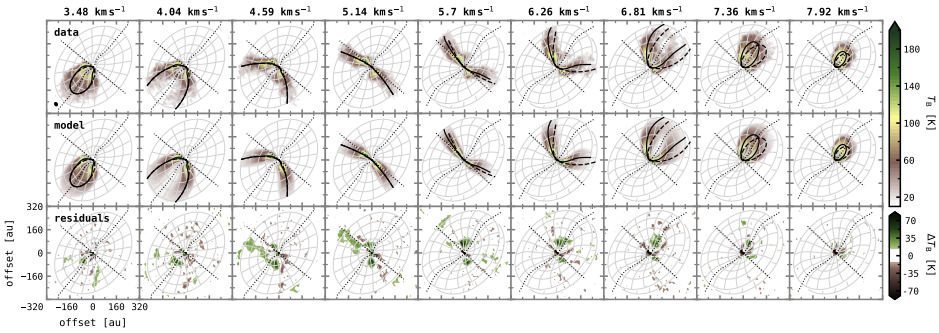

Figure 5.C.2: Same as in Fig. 5.5 but for ^{12}CO 7-6 and the blue- and redshifted sides being modelled separately.

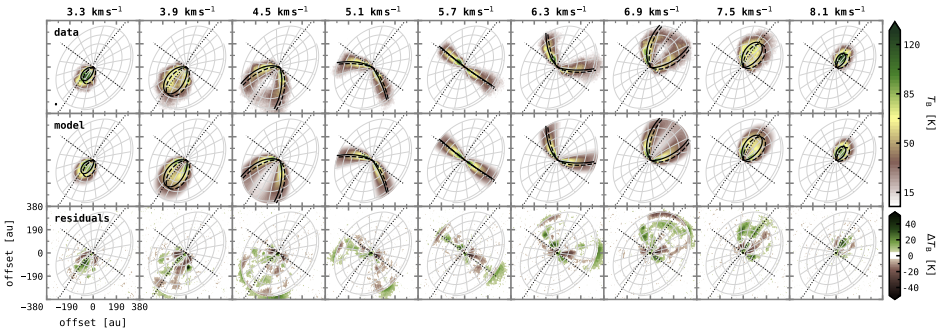

Figure 5.C.3: Same as in Fig. 5.5 but for ^{12}CO 3-2.

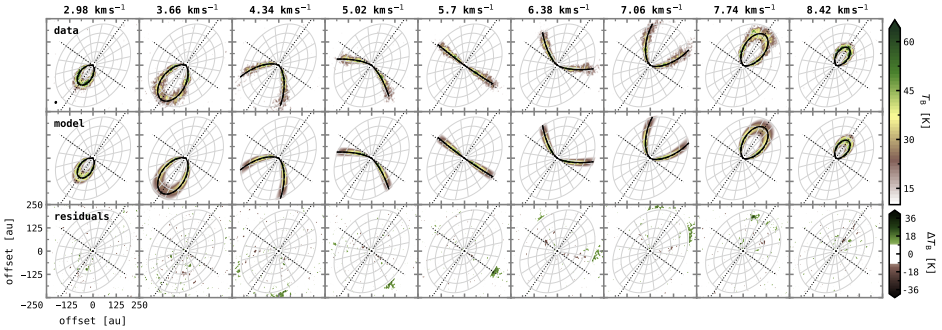

Figure 5.C.4: Same as in Fig. 5.5 but for ^{13}CO 2-1.

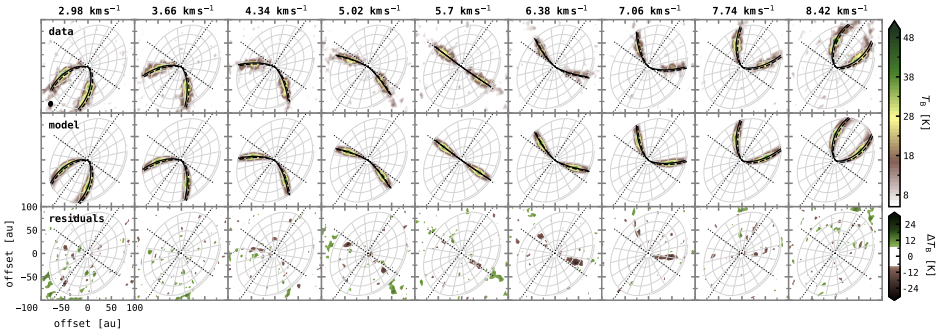

Figure 5.C.5: Same as in Fig. 5.5 but for C^{18}O 2-1.

5.D Logarithmic spirals

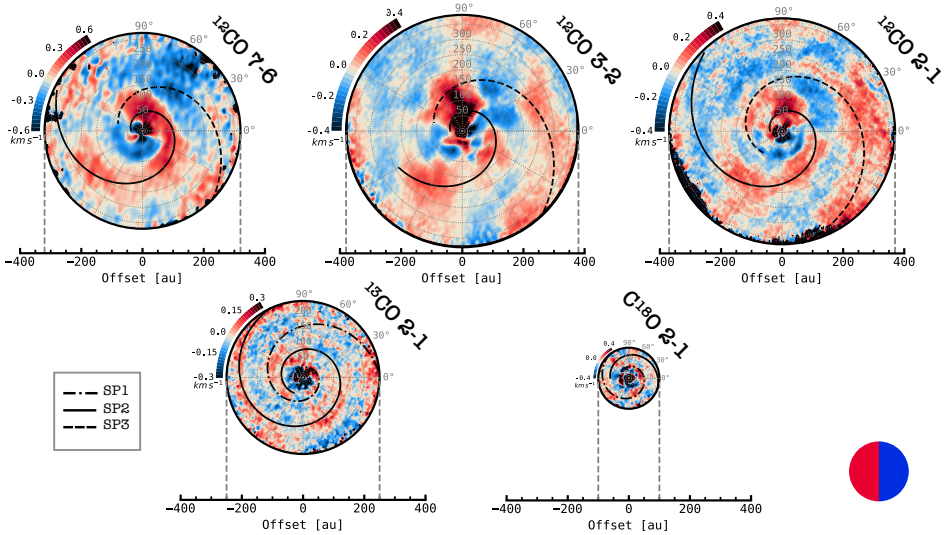

Figure 5.D.1: Same as in Fig. 5.7 but with overlaid logarithmic spirals.

5.E Peak intensity and line width residuals

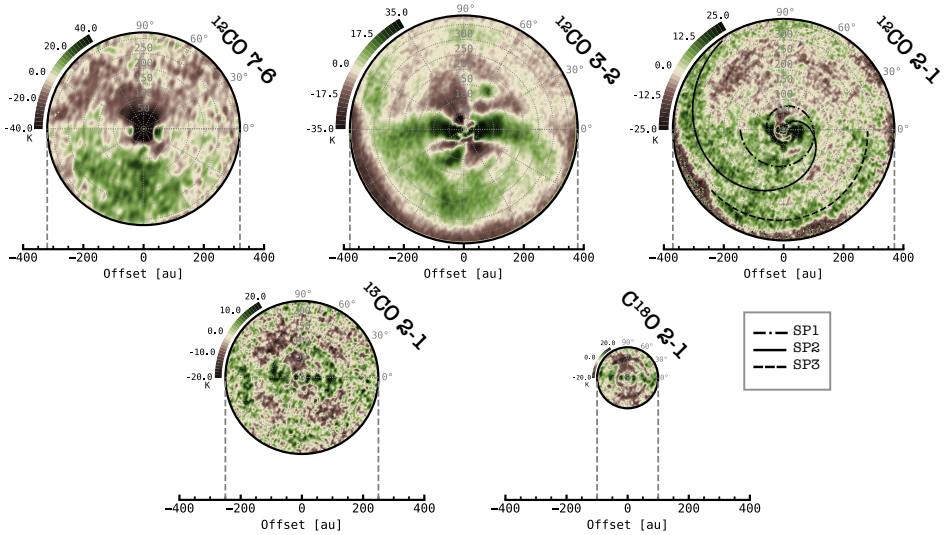

Figure 5.E.1: Peak intensity residuals, shown for the five lines studied in this work.

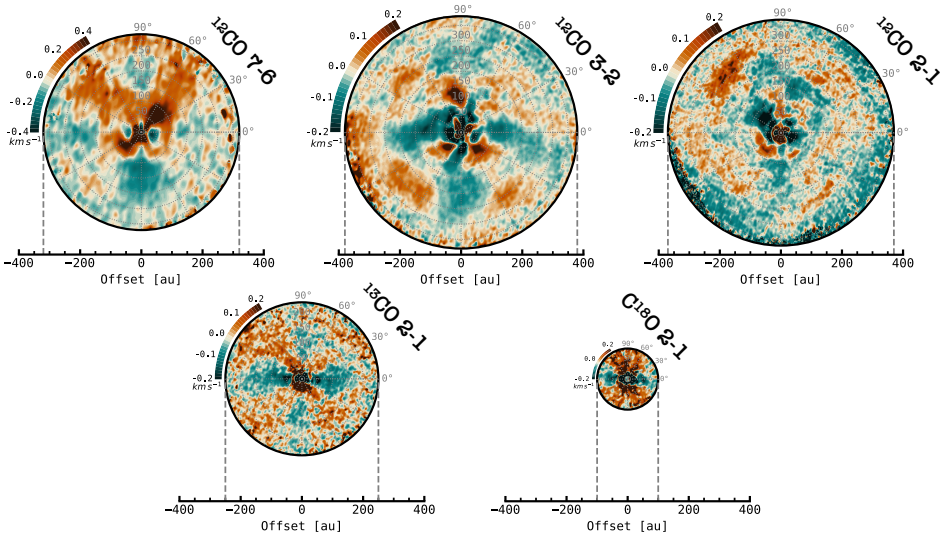

Figure 5.E.2: Line width residuals, shown for the five lines studied in this work.

Bibliography

Acke, B. & van den Ancker, M. E. 2006, A&A, 449, 267

Alarcón, F., Bergin, E. A., & Teague, R. 2022, ApJ, 941, L24

Alexander, R., Pascucci, I., Andrews, S., Armitage, P., & Cieza, L. 2014, in Protostars and Planets VI, ed. H. Beuther, R. S. Klessen, C. P. Dullemond, & T. Henning, 475

Alexander, R. D., Clarke, C. J., & Pringle, J. E. 2006a, MNRAS, 369, 216

Alexander, R. D., Clarke, C. J., & Pringle, J. E. 2006b, MNRAS, 369, 229

ALMA Partnership, Brogan, C. L., Pérez, L. M., et al. 2015, ApJ, 808, L3

André, P., Ward-Thompson, D., & Barsony, M. 1993, ApJ, 406, 122

Andrews, S. M. 2020, ARA&A, 58, 483

Andrews, S. M., Huang, J., Pérez, L. M., et al. 2018, ApJ, 869, L41

Ansdell, M., Williams, J. P., Manara, C. F., et al. 2017, AJ, 153, 240

Ansdell, M., Williams, J. P., van der Marel, N., et al. 2016, ApJ, 828, 46

Ardila, D. R., Golimowski, D. A., Krist, J. E., et al. 2007, ApJ, 665, 512

Armitage, P. J. 2019, Saas-Fee Advanced Course, 45, 1

Asplund, M., Grevesse, N., & Sauval, A. J. 2005, in Astronomical Society of the Pacific Conference Series, Vol. 336, Cosmic Abundances as Records of Stellar Evolution and Nucleosynthesis, ed. T. G. Barnes, III & F. N. Bash, 25

Avenhaus, H., Quanz, S. P., Garufi, A., et al. 2018, ApJ, 863, 44

Avenhaus, H., Quanz, S. P., Meyer, M. R., et al. 2014, ApJ, 790, 56

Bae, J., Hartmann, L., & Zhu, Z. 2015, ApJ, 805, 15

Bae, J., Isella, A., Zhu, Z., et al. 2022, arXiv e-prints, arXiv:2210.13314

Bae, J., Teague, R., & Zhu, Z. 2021, ApJ, 912, 56

Bae, J. & Zhu, Z. 2018a, ApJ, 859, 118

Bae, J. & Zhu, Z. 2018b, ApJ, 859, 119

Balbus, S. A. & Hawley, J. F. 1991, ApJ, 376, 214

Banzatti, A., Testi, L., Isella, A., et al. 2011, A&A, 525, A12

Barenfeld, S. A., Carpenter, J. M., Ricci, L., & Isella, A. 2016, ApJ, 827, 142

Barenfeld, S. A., Carpenter, J. M., Sargent, A. I., Isella, A., & Ricci, L. 2017, ApJ, 851, 85

Bate, M. R., Lodato, G., & Pringle, J. E. 2010, MNRAS, 401, 1505

Beckwith, S. V. W. & Sargent, A. I. 1993, ApJ, 402, 280

Benisty, M., Bae, J., Facchini, S., et al. 2021, ApJ, 916, L2

Benisty, M., Dominik, C., Follette, K., et al. 2022, arXiv e-prints, arXiv:2203.09991

Benisty, M., Juhasz, A., Boccaletti, A., et al. 2015, A&A, 578, L6

Benisty, M., Juhász, A., Facchini, S., et al. 2018, A&A, 619, A171

Benisty, M., Stolker, T., Pohl, A., et al. 2017, A&A, 597, A42

Béthune, W., Lesur, G., & Ferreira, J. 2017, A&A, 600, A75

Beuzit, J. L., Vigan, A., Mouillet, D., et al. 2019, A&A, 631, A155

Birnstiel, T., Klahr, H., & Ercolano, B. 2012, A&A, 539, A148

Birnstiel, T., Ricci, L., Trotta, F., et al. 2010, A&A, 516, L14

Blaes, O. M. & Balbus, S. A. 1994, ApJ, 421, 163

Blandford, R. D. & Payne, D. G. 1982, MNRAS, 199, 883

Blum, J., Gundlach, B., Mühle, S., & Trigo-Rodriguez, J. M. 2014, ICARUS, 235, 156

Blum, J. & Wurm, G. 2008, ARA&A, 46, 21

Boccaletti, A., Di Folco, E., Pantin, E., et al. 2020, A&A, 637, L5

Boccaletti, A., Pantin, E., Lagrange, A. M., et al. 2013, A&A, 560, A20

Boehler, Y., Ricci, L., Weaver, E., et al. 2018, ApJ, 853, 162

Bohn, A. J., Benisty, M., Perraut, K., et al. 2022, A&A, 658, A183

Boley, A. C. 2009, ApJ, 695, L53

Bollati, F., Lodato, G., Price, D. J., & Pinte, C. 2021, MNRAS, 504, 5444

Booth, A. S., Ilee, J. D., Walsh, C., et al. 2023, A&A, 669, A53

Booth, A. S., Walsh, C., Ilee, J. D., et al. 2019, ApJ, 882, L31

Booth, A. S., Walsh, C., Kama, M., et al. 2018, A&A, 611, A16

Bosman, A. D., Bergin, E. A., Loomis, R. A., et al. 2021, ApJS, 257, 15

Brauer, F., Henning, T., & Dullemond, C. P. 2008, A&A, 487, L1

Brittain, S. D., Carr, J. S., Najita, J. R., Quanz, S. P., & Meyer, M. R. 2014, ApJ, 791, 136

Brittain, S. D., Najita, J. R., & Carr, J. S. 2009, ApJ, 702, 85

Brittain, S. D., Najita, J. R., & Carr, J. S. 2019, ApJ, 883, 37

Brittain, S. D., Najita, J. R., Carr, J. S., et al. 2013, ApJ, 767, 159

Bruderer, S. 2013, A&A, 559, A46

Bruderer, S., van der Marel, N., van Dishoeck, E. F., & van Kempen, T. A. 2014, A&A, 562, A26

Bruderer, S., van Dishoeck, E. F., Doty, S. D., & Herczeg, G. J. 2012, A&A, 541, A91

Calcino, J., Hilder, T., Price, D. J., et al. 2022, ApJ, 929, L25

Calvet, N., D'Alessio, P., Watson, D. M., et al. 2005, ApJ, 630, L185

Casassus, S. 2016, PASA, 33, e013

Casassus, S., Avenhaus, H., Pérez, S., et al. 2018, MNRAS, 477, 5104

Casassus, S., Cárcamo, M., Hales, A., Weber, P., & Dent, B. 2022, ApJ, 933, L4

Casassus, S., Christiaens, V., Cárcamo, M., et al. 2021, MNRAS, 507, 3789

Casassus, S., Marino, S., Pérez, S., et al. 2015, ApJ, 811, 92

Casassus, S. & Pérez, S. 2019, ApJ, 883, L41

Cazzoletti, P., Manara, C. F., Liu, H. B., et al. 2019, A&A, 626, A11

Cazzoletti, P., van Dishoeck, E. F., Pinilla, P., et al. 2018, A&A, 619, A161

Chapillon, E., Guilloteau, S., Dutrey, A., & Piétu, V. 2008, A&A, 488, 565

Cieza, L. A., Ruíz-Rodríguez, D., Hales, A., et al. 2019, MNRAS, 482, 698

Clarke, C. 2011, in Physical Processes in Circumstellar Disks around Young Stars, ed. P. J. V. Garcia, 355–418

Claudi, R., Maire, A. L., Mesa, D., et al. 2019, A&A, 622, A96

Cleeves, L. I., Öberg, K. I., Wilner, D. J., et al. 2016, ApJ, 832, 110

Cossins, P., Lodato, G., & Clarke, C. J. 2009, MNRAS, 393, 1157

Cox, E. G., Harris, R. J., Looney, L. W., et al. 2017, ApJ, 851, 83

Crapsi, A., van Dishoeck, E. F., Hogerheijde, M. R., Pontoppidan, K. M., & Dullemond, C. P. 2008, A&A, 486, 245

Currie, T., Brittain, S., Grady, C. A., Kenyon, S. J., & Muto, T. 2017, Research Notes of the American Astronomical Society, 1, 40

Currie, T., Cloutier, R., Brittain, S., et al. 2015, ApJ, 814, L27

Czekala, I., Loomis, R. A., Teague, R., et al. 2021, ApJS, 257, 2

D'Alessio, P., Calvet, N., & Hartmann, L. 2001, ApJ, 553, 321

D'Alessio, P., Calvet, N., Hartmann, L., Lizano, S., & Cantó, J. 1999, ApJ, 527, 893

de Boer, J., Langlois, M., van Holstein, R. G., et al. 2020, A&A, 633, A63

Dipierro, G., Laibe, G., Price, D. J., & Lodato, G. 2016, MNRAS, 459, L1

Dipierro, G., Lodato, G., Testi, L., & de Gregorio Monsalvo, I. 2014, MNRAS, 444, 1919

Dominik, C. & Tielens, A. G. G. M. 1997, ApJ, 480, 647

Donehew, B. & Brittain, S. 2011, AJ, 141, 46

Dong, R., Fung, J., & Chiang, E. 2016, ApJ, 826, 75

Dong, R., Liu, S.-y., Eisner, J., et al. 2018, ApJ, 860, 124

Dong, R., Liu, S.-Y., & Fung, J. 2019, ApJ, 870, 72

Dong, R., van der Marel, N., Hashimoto, J., et al. 2017, ApJ, 836, 201

Dong, R., Zhu, Z., Rafikov, R. R., & Stone, J. M. 2015, ApJ, 809, L5

Draine, B. T. 2003, ARA&A, 41, 241

Draine, B. T. 2006, ApJ, 636, 1114

Drazin, P. G. & Reid, W. H. 1981, NASA STI/Recon Technical Report A, 82, 17950

Drazkowska, J., Bitsch, B., Lambrechts, M., et al. 2022, arXiv e-prints, arXiv:2203.09759

Du, F., Bergin, E. A., Hogerheijde, M., et al. 2017, ApJ, 842, 98

Dullemond, C. P., Küffmeier, M., Goicovic, F., et al. 2019, A&A, 628, A20

Dutrey, A., di Folco, E., Guilloteau, S., et al. 2014a, Nature, 514, 600

Dutrey, A., Semenov, D., Chapillon, E., et al. 2014b, in Protostars and Planets VI, ed. H. Beuther, R. S. Klessen, C. P. Dullemond, & T. Henning, 317

Ercolano, B., Barlow, M. J., & Storey, P. J. 2005, MNRAS, 362, 1038

Ercolano, B., Barlow, M. J., Storey, P. J., & Liu, X.-W. 2003, MNRAS, 340, 1136

Ercolano, B. & Clarke, C. J. 2010, MNRAS, 402, 2735

Ercolano, B., Clarke, C. J., & Drake, J. J. 2009, ApJ, 699, 1639

Ercolano, B., Drake, J. J., Raymond, J. C., & Clarke, C. C. 2008a, ApJ, 688, 398

Ercolano, B. & Pascucci, I. 2017, Royal Society Open Science, 4, 170114

Ercolano, B., Weber, M. L., & Owen, J. E. 2018, MNRAS, 473, L64

Ercolano, B., Young, P. R., Drake, J. J., & Raymond, J. C. 2008b, ApJS, 175, 534

Espaillat, C., Calvet, N., D'Alessio, P., et al. 2007, ApJ, 670, L135

Espaillat, C., Muzerolle, J., Najita, J., et al. 2014, in Protostars and Planets VI, ed. H. Beuther, R. S. Klessen, C. P. Dullemond, & T. Henning, 497

Evans, Neal J., I. 1999, ARA&A, 37, 311

Facchini, S., Birnstiel, T., Bruderer, S., & van Dishoeck, E. F. 2017, A&A, 605, A16

Facchini, S., Juhász, A., & Lodato, G. 2018, MNRAS, 473, 4459

Favre, C., Cleeves, L. I., Bergin, E. A., Qi, C., & Blake, G. A. 2013, ApJ, 776, L38

Fedele, D., Toci, C., Maud, L., & Lodato, G. 2021, A&A, 651, A90

Ferland, G. J. 1979, MNRAS, 188, 669

Ferreira, J., Dougados, C., & Cabrit, S. 2006, A&A, 453, 785

Flock, M., Nelson, R. P., Turner, N. J., et al. 2017, ApJ, 850, 131

Flock, M., Ruge, J. P., Dzyurkevich, N., et al. 2015, A&A, 574, A68

Follette, K. B., Rameau, J., Dong, R., et al. 2017, AJ, 153, 264

Foreman-Mackey, D., Hogg, D. W., Lang, D., & Goodman, J. 2013, PASP, 125, 306

Francis, L. & van der Marel, N. 2020, ApJ, 892, 111

Fung, J. & Chiang, E. 2016, ApJ, 832, 105

Gaia Collaboration, Brown, A. G. A., Vallenari, A., et al. 2018, A&A, 616, A1

Garcia Lopez, R., Natta, A., Testi, L., & Habart, E. 2006, A&A, 459, 837

Garg, H., Pinte, C., Christiaens, V., et al. 2021, MNRAS, 504, 782

Garufi, A., Benisty, M., Pinilla, P., et al. 2018, A&A, 620, A94

Garufi, A., Quanz, S. P., Schmid, H. M., et al. 2016, A&A, 588, A8

Ginski, C., Benisty, M., van Holstein, R. G., et al. 2018, A&A, 616, A79

Goldreich, P. & Tremaine, S. 1979, ApJ, 233, 857

Goldreich, P. & Tremaine, S. 1980, ApJ, 241, 425

Gorti, U., Dullemond, C. P., & Hollenbach, D. 2009, ApJ, 705, 1237

Gorti, U. & Hollenbach, D. 2009, ApJ, 690, 1539

Gorti, U., Hollenbach, D., & Dullemond, C. P. 2015, ApJ, 804, 29

Gorti, U., Liseau, R., Sándor, Z., & Clarke, C. 2016, Space Sci. Rev., 205, 125

Grady, C. A., Polomski, E. F., Henning, T., et al. 2001, AJ, 122, 3396

Gravity Collaboration, Abuter, R., Accardo, M., et al. 2017, A&A, 602, A94

Greene, T. P., Wilking, B. A., Andre, P., Young, E. T., & Lada, C. J. 1994, ApJ, 434, 614

Gundlach, B., Kilias, S., Beitz, E., & Blum, J. 2011, ICARUS, 214, 717

Güttler, C., Blum, J., Zsom, A., Ormel, C. W., & Dullemond, C. P. 2010, A&A, 513, A56

Haffert, S. Y., Bohn, A. J., de Boer, J., et al. 2019, Nature Astronomy, 3, 749

Hall, C., Dong, R., Teague, R., et al. 2020, ApJ, 904, 148

Harsono, D., Bjerkeli, P., van der Wiel, M. H. D., et al. 2018, Nature Astronomy, 2, 646

Hartmann, L., Calvet, N., Gullbring, E., & D'Alessio, P. 1998, ApJ, 495, 385

Helled, R., Bodenheimer, P., Podolak, M., et al. 2014, in Protostars and Planets VI, ed. H. Beuther, R. S. Klessen, C. P. Dullemond, & T. Henning, 643

Hennebelle, P., Lesur, G., & Fromang, S. 2017, A&A, 599, A86

Herbig, G. H. 1950, ApJ, 111, 11

Hogerheijde, M. R., Bergin, E. A., Brinch, C., et al. 2011, Science, 334, 338

Hollenbach, D. & Gorti, U. 2009, ApJ, 703, 1203

Hollenbach, D. J., Yorke, H. W., & Johnstone, D. 2000, in Protostars and Planets IV, ed. V. Mannings, A. P. Boss, & S. S. Russell, 401–428

Horne, K. & Marsh, T. R. 1986, MNRAS, 218, 761

Huang, J., Andrews, S. M., Pérez, L. M., et al. 2018, ApJ, 869, L43

Huang, J., Bergin, E. A., Öberg, K. I., et al. 2021, ApJS, 257, 19

Izidoro, A. & Raymond, S. N. 2018, in Handbook of Exoplanets, ed. H. J. Deeg & J. A. Belmonte, 142

Izquierdo, A. F., Facchini, S., Rosotti, G. P., van Dishoeck, E. F., & Testi, L. 2022, ApJ, 928, 2

Izquierdo, A. F., Testi, L., Facchini, S., Rosotti, G. P., & van Dishoeck, E. F. 2021, A&A, 650, A179

Johansen, A. & Lambrechts, M. 2017, Annual Review of Earth and Planetary Sciences, 45, 359

Johnson, J. A., Aller, K. M., Howard, A. W., & Crepp, J. R. 2010, PASP, 122, 905

Jorsater, S. & van Moorsel, G. A. 1995, AJ, 110, 2037

Jovanovic, N., Martinache, F., Guyon, O., et al. 2015, PASP, 127, 890

Juhász, A., Benisty, M., Pohl, A., et al. 2015, MNRAS, 451, 1147

Juhász, A. & Rosotti, G. P. 2018, MNRAS, 474, L32

Kama, M., Bruderer, S., van Dishoeck, E. F., et al. 2016, A&A, 592, A83

Kanagawa, K. D., Tanaka, H., Muto, T., Tanigawa, T., & Takeuchi, T. 2015, MNRAS, 448, 994

Kashyap, V. & Drake, J. J. 2000, Bulletin of the Astronomical Society of India, 28, 475

Keppler, M., Benisty, M., Müller, A., et al. 2018, A&A, 617, A44

Keppler, M., Penzlin, A., Benisty, M., et al. 2020, A&A, 639, A62

Keppler, M., Teague, R., Bae, J., et al. 2019, A&A, 625, A118

Klahr, H. & Bodenheimer, P. 2004, in IAU Symposium, Vol. 202, Planetary Systems in the Universe, ed. A. Penny, 350

Kley, W., D'Angelo, G., & Henning, T. 2001, ApJ, 547, 457

Kokubo, E. & Ida, S. 1996, ICARUS, 123, 180

Kothe, S., Güttler, C., & Blum, J. 2010, ApJ, 725, 1242

Kratter, K. & Lodato, G. 2016, ARA&A, 54, 271

Kratter, K. M., Murray-Clay, R. A., & Youdin, A. N. 2010, ApJ, 710, 1375

Kraus, S., Kreplin, A., Fukugawa, M., et al. 2017, ApJ, 848, L11

Krijt, S. & Kama, M. 2014, A&A, 566, L2

Krijt, S., Ormel, C. W., Dominik, C., & Tielens, A. G. G. M. 2015, A&A, 574, A83

Kwon, W., Looney, L. W., Mundy, L. G., Chiang, H.-F., & Kemball, A. J. 2009, ApJ, 696, 841

Lada, C. J. 1987, in Star Forming Regions, ed. M. Peimbert & J. Jugaku, Vol. 115, 1

Lambrechts, M. & Johansen, A. 2012, A&A, 544, A32

Langlois, M., Pohl, A., Lagrange, A. M., et al. 2018, A&A, 614, A88

Law, C. J., Loomis, R. A., Teague, R., et al. 2021a, ApJS, 257, 3

Law, C. J., Teague, R., Loomis, R. A., et al. 2021b, ApJS, 257, 4

Leemker, M., Booth, A. S., van Dishoeck, E. F., et al. 2022, A&A, 663, A23

Leinert, C., Haas, M., Mundt, R., Richichi, A., & Zinnecker, H. 1991, A&A, 250, 407

Lesur, G., Hennebelle, P., & Fromang, S. 2015, A&A, 582, L9

Li, H., Colgate, S. A., Wendroff, B., & Liska, R. 2001, ApJ, 551, 874

Li, H., Finn, J. M., Lovelace, R. V. E., & Colgate, S. A. 2000, ApJ, 533, 1023

Lin, D. N. C. & Papaloizou, J. 1979, MNRAS, 188, 191

Lin, D. N. C. & Papaloizou, J. 1986, ApJ, 309, 846

Lin, D. N. C. & Pringle, J. E. 1987, MNRAS, 225, 607

Lodato, G., Dipierro, G., Ragusa, E., et al. 2019, MNRAS, 486, 453

Long, F., Herczeg, G. J., Harsono, D., et al. 2019, ApJ, 882, 49

Long, F., Herczeg, G. J., Pascucci, I., et al. 2017, ApJ, 844, 99

Long, F., Pinilla, P., Herczeg, G. J., et al. 2018, ApJ, 869, 17

Lovelace, R. V. E., Li, H., Colgate, S. A., & Nelson, A. F. 1999, ApJ, 513, 805

Lubow, S. H. & Zhu, Z. 2014, ApJ, 785, 32

Lynden-Bell, D. & Pringle, J. E. 1974, MNRAS, 168, 603

Macintosh, B., Graham, J. R., Ingraham, P., et al. 2014, Proceedings of the National Academy of Science, 111, 12661

Maggio, A., Flaccomio, E., Favata, F., et al. 2007, ApJ, 660, 1462

Manara, C. F., Ansdell, M., Rosotti, G. P., et al. 2022, arXiv e-prints, arXiv:2203.09930

Manara, C. F., Morbidelli, A., & Guillot, T. 2018, A&A, 618, L3

Mannings, V. & Sargent, A. I. 1997, ApJ, 490, 792

Marino, S., Perez, S., & Casassus, S. 2015, ApJ, 798, L44

Maud, L. T., Cesaroni, R., Kumar, M. S. N., et al. 2019, A&A, 627, L6

Mayama, S., Akiyama, E., Panić, O., et al. 2018, ApJ, 868, L3

Mayor, M. & Queloz, D. 1995, Nature, 378, 355

McMullin, J. P., Waters, B., Schiebel, D., Young, W., & Golap, K. 2007, in Astronomical Society of the Pacific Conference Series, Vol. 376, Astronomical Data Analysis Software and Systems XVI, ed. R. A. Shaw, F. Hill, & D. J. Bell, 127

McNally, C. P., Nelson, R. P., Paardekooper, S.-J., Benítez-Llambay, P., & Gressel, O. 2020, MNRAS, 493, 4382

Ménard, F., Cuello, N., Ginski, C., et al. 2020, A&A, 639, L1

Mendigutía, I., Mora, A., Montesinos, B., et al. 2012, A&A, 543, A59

Mignone, A., Bodo, G., Massaglia, S., et al. 2007, ApJS, 170, 228

Miley, J. M., Panić, O., Haworth, T. J., et al. 2019, MNRAS, 485, 739

Miotello, A., Kamp, I., Birnstiel, T., Cleeves, L. I., & Kataoka, A. 2022, arXiv e-prints, arXiv:2203.09818

Miotello, A., Testi, L., Lodato, G., et al. 2014, A&A, 567, A32

Miotello, A., van Dishoeck, E. F., Williams, J. P., et al. 2017, A&A, 599, A113

Morbidelli, A., Szulágyi, J., Crida, A., et al. 2014, ICARUS, 232, 266

Muley, D., Dong, R., & Fung, J. 2021, AJ, 162, 129

Muro-Arena, G. A., Ginski, C., Dominik, C., et al. 2020, A&A, 636, L4

Nakatani, R., Hosokawa, T., Yoshida, N., Nomura, H., & Kuiper, R. 2018a, ApJ, 857, 57

Nakatani, R., Hosokawa, T., Yoshida, N., Nomura, H., & Kuiper, R. 2018b, ApJ, 865, 75

Natta, A., Grinin, V., & Mannings, V. 2000, in Protostars and Planets IV, ed. V. Mannings, A. P. Boss, & S. S. Russell, 559–588

Nealon, R., Dipierro, G., Alexander, R., Martin, R. G., & Nixon, C. 2018, MNRAS, 481, 20

Nelson, R. P., Gressel, O., & Umurhan, O. M. 2013, MNRAS, 435, 2610

Ney, E. P., Strecker, D. W., & Gehrz, R. D. 1973, ApJ, 180, 809

Nielsen, E. L., De Rosa, R. J., Macintosh, B., et al. 2019, AJ, 158, 13

Norfolk, B. J., Pinte, C., Calcino, J., et al. 2022, ApJ, 936, L4

Öberg, K. I., Guzmán, V. V., Walsh, C., et al. 2021, ApJS, 257, 1

O'dell, C. R. & Wen, Z. 1994, ApJ, 436, 194

O'dell, C. R. & Wong, K. 1996, AJ, 111, 846

Ogilvie, G. I. & Lubow, S. H. 2002, MNRAS, 330, 950

Ormel, C. W. & Klahr, H. H. 2010, A&A, 520, A43

Owen, J. E., Clarke, C. J., & Ercolano, B. 2012, MNRAS, 422, 1880

Owen, J. E., Ercolano, B., & Clarke, C. J. 2011, MNRAS, 412, 13

Owen, J. E., Ercolano, B., Clarke, C. J., & Alexander, R. D. 2010, MNRAS, 401, 1415

Paneque-Carreño, T., Miotello, A., van Dishoeck, E. F., et al. 2022, A&A, 666, A168

Paneque-Carreño, T., Miotello, A., van Dishoeck, E. F., et al. 2023, A&A, 669, A126

Paneque-Carreño, T., Pérez, L. M., Benisty, M., et al. 2021, ApJ, 914, 88

Panić, O., van Dishoeck, E. F., Hogerheijde, M. R., et al. 2010, A&A, 519, A110

Papaloizou, J. & Lin, D. N. C. 1984, ApJ, 285, 818

Pascucci, I., Cabrit, S., Edwards, S., et al. 2022, arXiv e-prints, arXiv:2203.10068

Pascucci, I., Testi, L., Herczeg, G. J., et al. 2016, ApJ, 831, 125

Paszun, D. & Dominik, C. 2009, A&A, 507, 1023

Pérez, L. M., Carpenter, J. M., Andrews, S. M., et al. 2016, Science, 353, 1519

Pérez, S., Casassus, S., & Benítez-Llambay, P. 2018, MNRAS, 480, L12

Pérez, S., Casassus, S., Hales, A., et al. 2020, ApJ, 889, L24

Perez, S., Casassus, S., Ménard, F., et al. 2015a, ApJ, 798, 85

Perez, S., Dunhill, A., Casassus, S., et al. 2015b, ApJ, 811, L5

Perraut, K. & Gravity Collaboration. 2021, in The 20.5th Cambridge Workshop on Cool Stars, Stellar Systems, and the Sun (CS20.5), Cambridge Workshop on Cool Stars, Stellar Systems, and the Sun, 334

Phuong, N. T., Dutrey, A., Di Folco, E., et al. 2020a, A&A, 635, L9

Phuong, N. T., Dutrey, A., Diep, P. N., et al. 2020b, A&A, 635, A12

Picogna, G., Ercolano, B., Owen, J. E., & Weber, M. L. 2019, MNRAS, 487, 691

Pineda, J. E., Szulágyi, J., Quanz, S. P., et al. 2019, ApJ, 871, 48

Pinilla, P., Benisty, M., & Birnstiel, T. 2012a, A&A, 545, A81

Pinilla, P., Birnstiel, T., Ricci, L., et al. 2012b, A&A, 538, A114

Pinilla, P., Birnstiel, T., & Walsh, C. 2015, A&A, 580, A105

Pinilla, P., Tazzari, M., Pascucci, I., et al. 2018, ApJ, 859, 32

Pinilla, P. & Youdin, A. 2017, in Astrophysics and Space Science Library, Vol. 445, Formation, Evolution, and Dynamics of Young Solar Systems, ed. M. Pessah & O. Gressel, 91

Pinte, C., Ménard, F., Duchêne, G., et al. 2018a, A&A, 609, A47

Pinte, C., Price, D. J., Ménard, F., et al. 2020, ApJ, 890, L9

Pinte, C., Price, D. J., Ménard, F., et al. 2018b, ApJ, 860, L13

Pinte, C., Teague, R., Flaherty, K., et al. 2022, arXiv e-prints, arXiv:2203.09528

Pinte, C., van der Plas, G., Ménard, F., et al. 2019, Nature Astronomy, 3, 1109

Pohl, A., Benisty, M., Pinilla, P., et al. 2017, ApJ, 850, 52

Pollack, J. B., Hubickyj, O., Bodenheimer, P., et al. 1996, ICARUS, 124, 62

Preibisch, T. & Feigelson, E. D. 2005, ApJS, 160, 390

Preibisch, T., Mehlhorn, M., Townsley, L., Broos, P., & Ratzka, T. 2014, A&A, 564, A120

Pringle, J. E. 1981, ARA&A, 19, 137

Pyerin, M. A., Delage, T. N., Kurtovic, N. T., et al. 2021, A&A, 656, A150

Quanz, S. P., Amara, A., Meyer, M. R., et al. 2015, ApJ, 807, 64

Quanz, S. P., Amara, A., Meyer, M. R., et al. 2013, ApJ, 766, L1

Rab, C., Kamp, I., Dominik, C., et al. 2020, A&A, 642, A165

Rab, C., Kamp, I., Ginski, C., et al. 2019, A&A, 624, A16

Rafikov, R. R. 2002, ApJ, 569, 997

Raymond, S. N., Izidoro, A., & Morbidelli, A. 2020, in Planetary Astrobiology, ed. V. S. Meadows, G. N. Arney, B. E. Schmidt, & D. J. Des Marais, 287

Rice, W. K. M., Armitage, P. J., Bate, M. R., & Bonnell, I. A. 2003, MNRAS, 338, 227

Richard, D. & Zahn, J.-P. 1999, A&A, 347, 734

Riols, A. & Lesur, G. 2019, A&A, 625, A108

Rosenfeld, K. A., Andrews, S. M., Hughes, A. M., Wilner, D. J., & Qi, C. 2013, ApJ, 774, 16

Rosenfeld, K. A., Andrews, S. M., Wilner, D. J., & Stempels, H. C. 2012, ApJ, 759, 119

Rosotti, G. P., Benisty, M., Juhász, A., et al. 2020a, MNRAS, 491, 1335

Rosotti, G. P., Ilee, J. D., Facchini, S., et al. 2021, MNRAS, 501, 3427

Rosotti, G. P., Teague, R., Dullemond, C., Booth, R. A., & Clarke, C. J. 2020b, MNRAS, 495, 173

Ruden, S. P. 1993, in Astronomical Society of the Pacific Conference Series, Vol. 36, Planets Around Pulsars, ed. J. A. Phillips, S. E. Thorsett, & S. R. Kulkarni, 197–215

Sakai, N., Hanawa, T., Zhang, Y., et al. 2019, Nature, 565, 206

Salz, M., Banerjee, R., Mignone, A., et al. 2015, A&A, 576, A21

Sanchis, E., Picogna, G., Ercolano, B., Testi, L., & Rosotti, G. 2020, MNRAS, 492, 3440

Sano, T. & Stone, J. M. 2002, ApJ, 570, 314

Savage, B. D. & Sembach, K. R. 1996, ApJ, 470, 893

Shakura, N. I. & Sunyaev, R. A. 1973, A&A, 24, 337

Shu, F. H., Adams, F. C., & Lizano, S. 1987, ARA&A, 25, 23

Sissa, E., Gratton, R., Garufi, A., et al. 2018, A&A, 619, A160

Skrutskie, M. F., Dutkevitch, D., Strom, S. E., et al. 1990, AJ, 99, 1187

Stadler, J., Benisty, M., Izquierdo, A., et al. 2023, A&A, 670, L1

Stempels, H. C. & Gahm, G. F. 2004, A&A, 421, 1159

Stolker, T., Dominik, C., Avenhaus, H., et al. 2016, A&A, 595, A113

Stoll, M. H. R. & Kley, W. 2014, A&A, 572, A77

Strom, K. M., Strom, S. E., Edwards, S., Cabrit, S., & Skrutskie, M. F. 1989, AJ, 97, 1451

Sturm, J. A., Rosotti, G. P., & Dominik, C. 2020, A&A, 643, A92

Szulágyi, J., Morbidelli, A., Crida, A., & Masset, F. 2014, ApJ, 782, 65

Tabone, B., Rosotti, G. P., Cridland, A. J., Armitage, P. J., & Lodato, G. 2022a, MNRAS, 512, 2290

Tabone, B., Rosotti, G. P., Lodato, G., et al. 2022b, MNRAS, 512, L74

Takami, M., Karr, J. L., Hashimoto, J., et al. 2013, ApJ, 772, 145

Tanaka, H. & Ida, S. 1999, ICARUS, 139, 350

Tanigawa, T., Ohtsuki, K., & Machida, M. N. 2012, ApJ, 747, 47

Tarter, C. B., Tucker, W. H., & Salpeter, E. E. 1969, ApJ, 156, 943

Teague, R. 2019, Journal of Open Source Software, 4, 1220

Teague, R. 2019, The Journal of Open Source Software, 4, 1632

Teague, R., Bae, J., Aikawa, Y., et al. 2021, ApJS, 257, 18

Teague, R., Bae, J., Andrews, S. M., et al. 2022a, ApJ, 936, 163

Teague, R., Bae, J., Benisty, M., et al. 2022b, ApJ, 930, 144

Teague, R., Bae, J., & Bergin, E. A. 2019a, Nature, 574, 378

Teague, R., Bae, J., Bergin, E. A., Birnstiel, T., & Foreman-Mackey, D. 2018a, ApJ, 860, L12

Teague, R., Bae, J., Birnstiel, T., & Bergin, E. A. 2018b, ApJ, 868, 113

Teague, R., Bae, J., Huang, J., & Bergin, E. A. 2019b, ApJ, 884, L56

Teague, R. & Foreman-Mackey, D. 2018, Research Notes of the American Astronomical Society, 2, 173

Teague, R., Guilloteau, S., Semenov, D., et al. 2016, A&A, 592, A49

Teague, R., Henning, T., Guilloteau, S., et al. 2018c, ApJ, 864, 133

Terebey, S., Shu, F. H., & Cassen, P. 1984, ApJ, 286, 529

Testi, L., Natta, A., Shepherd, D. S., & Wilner, D. J. 2001, ApJ, 554, 1087

Testi, L., Natta, A., Shepherd, D. S., & Wilner, D. J. 2003, A&A, 403, 323

Thalmann, C., Janson, M., Garufi, A., et al. 2016, ApJ, 828, L17

Thies, I., Kroupa, P., Goodwin, S. P., Stamatellos, D., & Whitworth, A. P. 2011, MNRAS, 417, 1817

Thommes, E. W., Duncan, M. J., & Levison, H. F. 2003, ICARUS, 161, 431

Trapman, L., Facchini, S., Hogerheijde, M. R., van Dishoeck, E. F., & Bruderer, S. 2019, A&A, 629, A79

Tripathi, A., Andrews, S. M., Birnstiel, T., & Wilner, D. J. 2017, ApJ, 845, 44

Trotta, F., Testi, L., Natta, A., Isella, A., & Ricci, L. 2013, A&A, 558, A64

Tsukagoshi, T., Momose, M., Hashimoto, J., et al. 2014, ApJ, 783, 90

Tsukagoshi, T., Momose, M., Kitamura, Y., et al. 2019, ApJ, 871, 5

Turner, N. J., Carballido, A., & Sano, T. 2010, ApJ, 708, 188

Tychoniec, Ł., Tobin, J. J., Karska, A., et al. 2018, ApJS, 238, 19

Ubeira Gabellini, M. G., Miotello, A., Facchini, S., et al. 2019, MNRAS, 486, 4638

Uribe, A., Matsakos, T., & Konigl, A. 2015, in Cambridge Workshop on Cool Stars, Stellar Systems, and the Sun, Vol. 18, 18th Cambridge Workshop on Cool Stars, Stellar Systems, and the Sun, 739–742

Uyama, T., Muto, T., Mawet, D., et al. 2020, AJ, 159, 118

van der Marel, N., Birnstiel, T., Garufi, A., et al. 2021, AJ, 161, 33

van der Marel, N. & Mulders, G. D. 2021, AJ, 162, 28

van der Marel, N., van Dishoeck, E. F., Bruderer, S., et al. 2016, A&A, 585, A58

van der Marel, N., van Dishoeck, E. F., Bruderer, S., et al. 2013, Science, 340, 1199

Villenave, M., Benisty, M., Dent, W. R. F., et al. 2019, A&A, 624, A7

Wada, K., Tanaka, H., Suyama, T., Kimura, H., & Yamamoto, T. 2008, ApJ, 677, 1296

Wagner, K., Apai, D., Kasper, M., & Robberto, M. 2015, ApJ, 813, L2

Wagner, K., Follete, K. B., Close, L. M., et al. 2018, ApJ, 863, L8

Walsh, C., Daley, C., Facchini, S., & Juhász, A. 2017, A&A, 607, A114

Walsh, C., Juhász, A., Pinilla, P., et al. 2014, ApJ, 791, L6

Wang, L. & Goodman, J. 2017, ApJ, 847, 11

Ward-Duong, K., Patience, J., Bulger, J., et al. 2018, AJ, 155, 54

Weaver, E., Isella, A., & Boehler, Y. 2018, ApJ, 853, 113

Weidenschilling, S. J. 1977, MNRAS, 180, 57

Weidling, R., Güttler, C., & Blum, J. 2012, ICARUS, 218, 688

Whipple, F. L. 1972, in From Plasma to Planet, ed. A. Elvius, 211

Williams, J. P., Cieza, L., Hales, A., et al. 2019, ApJ, 875, L9

Wölfer, L., Facchini, S., Kurtovic, N. T., et al. 2021, A&A, 648, A19

Wölfer, L., Facchini, S., van der Marel, N., et al. 2023, A&A, 670, A154

Wolszczan, A. & Frail, D. A. 1992, Nature, 355, 145

Yen, H.-W. & Gu, P.-G. 2020, ApJ, 905, 89

Yorke, H. W., Bodenheimer, P., & Laughlin, G. 1993, ApJ, 411, 274

Yu, H., Teague, R., Bae, J., & Öberg, K. 2021, ApJ, 920, L33

Zhang, S., Zhu, Z., Huang, J., et al. 2018, ApJ, 869, L47

Zhu, Z. & Stone, J. M. 2018, ApJ, 857, 34

Zhu, Z., Stone, J. M., & Bai, X.-N. 2015, ApJ, 801, 81

Zhu, Z., Stone, J. M., & Rafikov, R. R. 2012, ApJ, 758, L42

Ik weet niets met zekerheid,
maar de aanblik van de sterren
doet me dromen.

Vincent van Gogh

Nederlandse samenvatting

Al sinds de vroegste geschiedenis kijkt de mensheid naar de nachthemel gevuld met sterren en vraagt men zich af hoe deze tot stand zijn gekomen. De vraag naar de oorsprong van de aarde en diens plaats in het universum houdt de mensheid al gedurende zijn hele bestaan bezig en heeft uiteindelijk geleid tot de ontwikkeling van telescopen die vele malen verder kunnen kijken dan het menselijk oog. Deze instrumenten worden geleidelijk verbeterd en zorgen er daarmee voor dat wetenschappers alle hoeken van de kosmos in steeds groter detail kunnen bestuderen. Dit brengt ons dichterbij het beantwoorden van dezelfde vragen die al lang geleden gesteld zijn.

Één specifiek interessante vraag is die van de oorsprong van leven. Hedendaags kennen we slechts één plek in het universum waar leven mogelijk is: de aarde. Ongeveer 30 jaar geleden werd echter de eerste planeet in een baan rond een andere ster ontdekt, een zogeheten exoplaneet. Dit heeft de deur geopend naar een nieuw tijdperk in de astronomie waar de mogelijkheid tot leven op andere werelden een realiteit is. Tegenwoordig zijn er meer dan 5000 exoplaneten bevestigd en dit aantal groeit nog elke dag. Statistisch gezien draait er om elke ster één planeet. Ook al zijn planeten gewone inwoners van de kosmos, ze laten een grote diversiteit zien: planeetstelsels laten een grote verscheidenheid zien, zowel in termen van stellaire en planetaire massas als in de structuren van de systemen zoals het aantal planeten, de samenstelling en de distributie in het planeetstelsel.

Om deze grote diversiteit te verklaren en om uiteindelijk de vraag te beantwoorden of er leven mogelijk is op andere planeten moeten we eerst begrijpen hoe planeten worden gevormd, zowel vanuit een fysisch als vanuit een chemisch perspectief. Om dit te bewerkstelligen moeten we naar hun geboorteplekken kijken. Deze bevinden zich in de zogeheten protoplanetaire of planeet-vormende schijven, bestaande uit stof en gas, rond de nieuwgevormde ster. Deze schijven evolueren en vergaan uiteindelijk. De evolutionaire processen bepalen zowel het uiterlijk van de schijven en hoe de planeten zich vormen. Tegelijkertijd hebben vormende planeten interactie met hun omgeving gedurende de groei van kleine stofkorrels tot kiezels, planetesimalen en uiteindelijk rotsachtige planeten en de kernen van gasreuzen, veranderen ze de structuur van hun schijf, en veranderen ze diens evolutionaire pad.

Dit proefschrift focusseert zich op de interpretatie van substructuren in schij-

Figuur 1: Afbeelding van de zuilen van creatie, een stervormingsgevield in de Adelaarsnevel, genomen met de James Webb Ruimtetelescoop. Afbeelding van: NASA, ESA, CSA, and STScI.

ven in termen van schijfwinden en planeet-schijf interacties. Het modelleren van dynamische processen in schijven alsmede het karakteriseren van de waargenomen substructuren vormen essentiële stukjes bij het samenstellen van de planeetvormingspuzzel. Dit proefschrift draagt bij aan het begrijpen van hoe algemeen substructuren zijn en of deze bepaalde patronen volgen.

Jonge stellaire systemen

Sterren worden gevormd in langzaam roterende gigantische moleculaire wolken, enorme opeenhopingen van interstellair materiaal dat voornamelijk bestaat uit gas en kleine stofkorrels. Een voorbeeld van zo'n stervormingsgebied is weergegeven in Fig. 1. Onder bepaalde voorwaarden kunnen de meest dichte en koude regio's (kernen) van de wolk ineenstorten onder hun eigen zwaartekracht, resulterend in een verhoging van de dichtheid en de temperatuur en de vorming van een jonge (proto-)ster in het centrum. Tegelijkertijd moet het draaimoment van de wolk behouden blijven en het materiaal met het hoogste draaimoment (dat de nieuwgeboren ster uit elkaar zou laten draaien) verspreidt zich in een circumstellaire accretieschijf waaruit de ster zich de eerste paar miljoen jaar van zijn leven voedt.

De evolutie van jonge stellaire objecten is schematisch weergegeven in Fig. 2. Na het ineenstorten van het centrum van de moleculaire wolk vormt zich een prestellaire kern. Deze stort vervolgens verder ineen tot een protoster omgeven door een ineenstortend omhulsel. Op dit punt wordt er al een schijf gevormd rondom

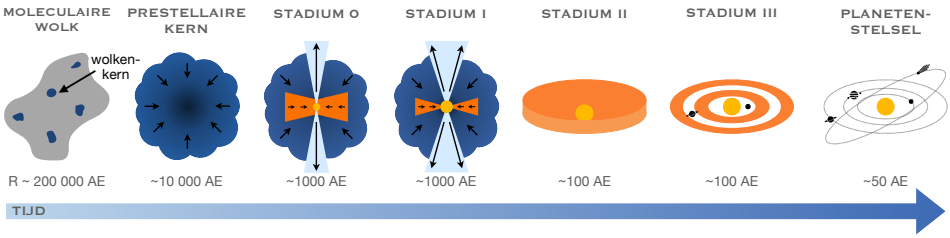

Figuur 2: Schematisch overzicht van de verschillende stadia van stervorming. De focus van dit proefschrift ligt op de stadium II objecten, ook wel bekend als protoplanetaire schijven. Één astronomische eenheid, ook wel aangeduid met AE, is gelijk aan de gemiddelde afstand tussen de aarde en de zon.

de protoster, maar deze bevindt zich nog diep in de wolk (stadia 0 en I). Gedurende deze stadia verdwijnt het omliggende omhulsel in 100 000 tot één miljoen jaar door accretie van het omhulsel op de schijf en naar buiten vloeiend materiaal totdat er op ten duur een ster met een gasrijke protoplanetaire schijf overblijft die direct kan worden waargenomen (stadium II). In de volgende miljoen tot tien miljoen jaar verdwijnt het materiaal de schijf of wordt het gebruikt om planeten en kleinere objecten te bouwen waardoor er een ster overblijft die omgeven is door een gasarme puinschijf (stadium III). Uiteindelijk verdwijnt de schijf volledig en wordt er een nieuw planetenstelsel zoals ons zonnestelsel geboren. De focus van dit proefschrift ligt op de systemen die zich in stadium II bevinden en de substructuren van het gas welke direct kunnen worden waargenomen met de Atacama Large Millimeter/submillimeter Array (ALMA).

Evolutie van de schijf

Een circumstellaire schijf moet zijn draaimoment ofwel verliezen ofwel herdistribueren om te kunnen evolueren. Anders zou het materiaal in de schijf voor eeuwig in dezelfde baan rond de ster blijven draaien. De twee belangrijkste manieren, die elkaar niet uitsluiten, voorgesteld om het draaimoment te verminderen en de evolutie van de schijf te beheersen zijn: schijfwinden en viscositeit. In een schijf die door viscositeit evolueert wordt het draaimoment geherdistribueerd door een wrijvingskracht tussen gas deeltjes die ervoor zorgt dat een deeltje naar binnen beweegt doordat deze draaimoment verliest aan het andere deeltje dat op zijn beurt naar buiten beweegt. De exacte oorsprong van viscositeit blijft nog onbekend en wordt nog actief onderzocht maar turbulentie wordt vaak aangevoerd om evolutie door viscositeit te verklaren. Aan de andere kant brengen schijfwinden een manier om draaimoment uit het systeem te verwijderen zonder dat turbulentie nodig is. In de aanwezigheid van een magnetisch veld kan een magnetisch-aangedreven wind gelanceerd worden van de oppervlakte van de schijf die draaimoment met zich mee draagt. Derhalve moet het materiaal dat in de schijf blijft draaimoment verliezen en beweegt het richting de ster.

In het simpele beeld van evolutie door viscositeit is het verdwijnen van een

protoplanetaire schijf een langdurig proces waar de schijf gestaag en homogeen vervaagt. Er is echter geen bewijs van zulke langzaam vervagende schijven en dus moet er een alternatieve manier aanwezig zijn om schijven in latere stadia snel te laten verdwijnen. Één manier die mogelijk een rol speelt in het snel laten verdwijnen van schijven is fotoverdamping. Fotoverdamping beschrijft de bestraling van materiaal in de schijf met hoog-energetische stellaire fotonen die de bovenste lagen van de schijf verwarmen tot een hogere energie dan de energie van de zwaartekracht, resulterend in het lanceren van een fotoverdampende wind. Gedurende het grootste deel van de levensduur van de schijf wordt de evolutie gedomineerd door viscositeit en is het verlies van massa door een fotoverdampende wind nihil. Na verloop van tijd nemen de instroom van materiaal op de ster en de oppervlaktedichtheid van de schijf echter af en kunnen de fotonen doordringen in diepere lagen van de schijf. Zodra de accretiesnelheden dalen tot onder het verlies van massa door de wind, begint fotoverdamping de evolutie van de schijf te domineren. Naar binnen stromend materiaal wordt door de wind weggeblazen in plaats van dat het op de ster valt, en er ontstaat een ringvormig gat dat de binnenste en buitenste delen van de schijf van elkaar scheidt. Zonder de aanvoer van materiaal uit de buitenste schijf valt het binnenste deel van de schijf snel op de ster en verdwijnt het buitenste deel van de schijf, dat nu direct bestraalt wordt door de ster, snel van binnenuit.

In de context van gaten en holtes in protoplanetaire schijven moet ook de term „overgangsschijf" worden genoemd. Overgangsschijven worden gekenmerkt doordat hun binnendeel compleet ontdaan is van stof (en mogelijk gas). Ze zijn in eerste instantie geïdentificeerd in waarnemingen door de aanwezigheid van een infraroodexces in de spectrale energie distributie van jonge stellaire objecten. Als natuurlijke uitkomst van fotoverdamping werd gedacht dat deze schijven op het punt stonden om te verdwijnen en dat deze daarmee een brug vormden tussen optisch dikke schijven en puinschijven. Vanuit een waarneemperspectief zijn overgangsschijven een diverse groep van objecten en worden ze gekenmerkt door een scala aan substructuren die verschillende vormingsmechanismes suggereren. In het bijzonder kunnen vooral schijven met grote gaten die tegelijkertijd nog heel veel accretie op de ster laten zien moeilijk worden verklaard door fotoverdamping. Planeet-schijf interacties bieden een alternatieve oplossing en in ieder geval van een aantal van de waargenomen gaten in schijven wordt gedacht dat deze resulteren door dynamisch leegruimen door een planeet in plaats van dat deze gaten een evolutionair stadium representeren. Overgangsschijven bieden ons fantastische laboratoria om schijven en planeetvorming te bestuderen en kunnen ons misschien zelfs in staat stellen om planeetvorming in actie te zien. Dit proefschrift besteedt daarom speciale aandacht aan deze intrigerende klasse van objecten.

Waarnemingen van schijven

Tot ongeveer een decennium geleden kon het circumstellaire materiaal niet ruimtelijk worden opgelost vanwege een gebrek aan resolutie van oudere generatie telescopen. Waarnemingen toonden vlakke en gladde structuren die symmetrisch

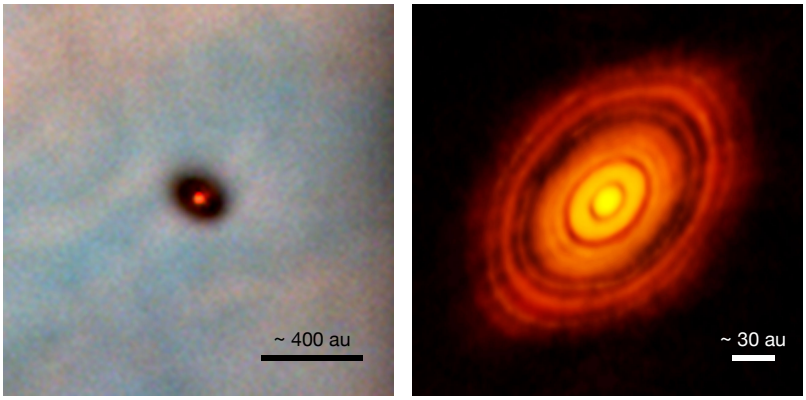

Figuur 3: Links: optische HST afbeelding van een protoplanetaire schijf in de Orionnevelcluster. Afbeelding van: Mark McCaughrean (MPIA), C. Robert O'Dell (Rice University) en NASA/ESA. Rechts: een ALMA afbeelding van de schijf van HL Tau op mm-golflengten. Afbeelding van:ALMA (ESO/NAOJ/NRAO).

rond de centrale ster leken te zijn. Het was pas sinds de opkomst van ALMA en de Spectro-Polarimetric High-contrast Exoplanet REsearch (SPHERE) op ESO's Very Large Telescope (VLT) dat verbazingwekkende substructuren werden waargenomen (vergelijk Fig. 3).

Het millimeter bereik van het spectrum is bijzonder geschikt om protoplanetaire schijven waar te nemen aangezien het koude moleculaire gas en stof voornamelijk op deze golflengten licht uitzendt en omdat de distributie van het stof gedomineerd wordt door stofkorrels ter grote van een millimeter. De beste faciliteit om straling met millimeter golflengten waar te nemen is ALMA omdat het de gevoeligheid, spectrale resolutie en het ruimtelijk oplossend vermogen biedt die nodig zijn om individuele schijven in detail in kaart te brengen. Tegelijkertijd heeft ALMA ook studies van grote populaties mogelijk gemaakt. Gecombineerd hebben deze waarnemingen ons geleerd dat protoplanetaire schijven gekenmerkt worden door een grote variëteit in substructuren zoals gaten en holtes, ringen, spiraalarmen en azimutale asymmetrieën. Dit proefschrift richt zich op het gas in schijven, wat als voordeel heeft dat het informatie geeft over de schijfdynamica of kinematica: moleculaire lijn emissie van roterend gas is rood- of blauwverschoven afhankelijk van of de geprojecteerde snelheid van ons af of naar ons toe is gericht.

Schijfkinematica

Het ultieme doel is om planeten in schijven direct waar te nemen en zo de link met waargenomen substructuren te bevestigen, maar de dichte en ondoorzichtige omgeving rondom jonge planeten maakt dit moeilijk. Het is dus geen verrassing dat de enige tot nu toe robuust gedetecteerde jonge planeten zich bevinden in het PDS 70 systeem. Er zijn daarom indirecte detectietechnieken bedacht en één veelbelovende techniek is om het snelheidsveld van het roterende gas te bestuderen

met waarnemingen van moleculaire lijnen. Het zoeken naar afwijkingen van Kepleriaanse rotatie kunnen zo gebruikt worden om te begrijpen welke processen, die elk hun eigen voetafdruk achterlaten in de kinematica, de schijf zijn vorm geven. De kinematische kenmerken die worden veroorzaakt door planeet-schijf interacties zijn specifiek interessant aangezien de amplitude en morfologie van deze verstoringen afhankelijk zijn van de positie en de massa van de planeet, maar ook van de structuur van de schijf. Ook al zijn meerdere waarnemingen van kinematische afwijkingen zoals niet-Kepleriaanse spiraalarmen, meridionale stromen of knikken in verband gebracht met de aanwezigheid van planeten blijft het moeilijk om deze te onderscheiden van andere onderliggende mechanismes. Om de individuele bijdragen beter te begrijpen zijn speciale modelleer inspanningen nodig in combinatie met uitzonderlijk gevoelige waarnemingen met een hoge spectrale resolutie en ruimtelijk oplossend vermogen. Zulke waarnemingen komen met hoge kosten qua waarneemtijd en daarom is er slechts een beperkt aantal bronnen waarvoor de kinematica in detail bestudeerd is. Het veld van kinimatica staat dus nog in zijn kinderschoenen maar brengt de mogelijkheid om jonge en nog steeds vormende planeten te vinden die niet zijn waar te nemen met klassieke methodes. De eigenschappen van deze planeten leveren belangrijke conclusies voor planeetvorming en migratiemodellen, en de tijdschalen van deze processen helpen om ze te linken aan de eigenschappen van de populatie van reeds gevormde exoplaneten.

Dit proefschrift

In dit proefschrift wordt het gas in protoplanetaire schijven en diens substructuren bestudeerd in de context van zowel schijfwinden als planeet-schijf interacties. De variëteit in waargenomen substructuren, in combinatie met het ontbreken van direct waargenomen planeten in schijven, heeft geleid tot de volgende hoofdvragen die in dit proefschrift worden behandeld:

1. Zijn de diverse substructuren zoals waargenomen in schijven het resultaat van planeet-schijf interacties of van andere mechanismes?

2. Als ze veroorzaakt worden door planeten, wat kunnen dan leren over deze planeten, bijvoorbeeld in termen van positie of massa, en wat kunnen we leren over de schijf als ze niet veroorzaakt worden door planeten?

3. Wat drijft het transport van draaimoment in de schijf en het verdwijnen van de schijf, hetgeen de levensduur beïnvloedt en dus de tijd om planeten te bouwen?

De volgende paragrafen bieden een korte samenvatting van alle hoofdstukken en hun belangrijkste resultaten.

Hoofdstuk 2 onderzoekt we de effecten van verdamping via röntgenstraling van protoplanetaire schijven die arm zijn in koolstof in de gasfase, een eigenschap die vaak wordt waargenomen. Aangezien koolstof één van de belangrijkste bijdragen levert aan de opaciteit in het röntgengolflengtegebied kan verwacht worden dat

koolstofarm gas ervoor zorgt dat röntgenstraling dieper in de schijf kan penetreren. Onderzocht wordt hoe dit de sterkte van het fotoverdampende massaverlies en de vorming van holtes beïnvloedt. Hiervoor worden berekeningen van stralingsoverdracht en hydrodynamische modellen van schijven die worden bestraald door interne röntgen en extreem-ultraviolette straling voor verschillende maten van koolstofverarming gecombineerd. De resultaten laten zien dat fotoverdampende winden sterker zijn voor zulke koolstofarme schijven vergeleken met schijven met evenveel zware elementen als de zon. Dit resulteert in verhoogd massaverlies dat zich uitstrekt tot grotere stralen. Deze resultaten kunnen een groter aantal waargenomen overgangsschijven verklaren. Tevens kan het extreem koolstofarm zijn van het gas een mechanisme zijn om de schijf snel te laten verdwijnen tegen het einde van diens levensduur.

Hoofdstuk 3 presenteert hoge-resolutie Band 6 ALMA waarnemingen van de circumstellaire schijf rond CQ Tau. Drie CO isotopologen, ^{12}CO, ^{13}CO en C^{18}O, zijn geanalyseerd in termen van zowel hun kinematica als hun helderheidstemperatuur. Door het fitten van een Kepleriaans schijfmodel aan het snelheidveld hebben wordt gezocht naar zowel afwijkingen van Kepleriaanse rotatie als variaties in de temperatuurstructuur. De resultaten laten een significante spiraalstructuur zien in de residuen van zowel de snelheid als de gas temperatuur nadat het model van de data is afgetrokken. De snelheid- en temperatuur spiralen komen deels met elkaar overeen wat een gemeenschappelijke oorsprong suggereert. Hun morfologie, aantal en hellingshoeken ondersteunen een dynamisch vormingsscenario. Tezamen met de (bijna overeenkomende) spiralen in nabij-infrarode waarnemingen en een diep gas en stof holte suggereren ze dat een massief lichaam zoals een planeet of een tweede ster aanwezig is binnen ongeveer 25 AE.

In hoofdstuk 4 wordt de analyse van gas kinematica en helderheidstemperaturen zoals uitgevoerd in het vorige hoofdstuk uit naar 36 overgangsschijven met grote holtes uitgebreid, waarmee de beschikbare ALMA waarnemingen tot het uiterste worden gedreven. Voor de analyse worden CO data uit het archief gebruikt die zijn waargenomen in verschillende cycli in Band 6 en Band 7. Voor het eerst worden voor een groot aantal bronnen de substructuren zoals gevonden in de kinematica en temperatuur residuen vergeleken met andere indicatoren voor de aanwezigheid van planeten. De resultaten leveren sterke structuren zoals bogen en spiralen op in 20 % van de bronnen die mogelijk geassocieerd kunnen worden met de aanwezigheid van planeten of tweede sterren, terwijl de meeste bronnen geen sterke structuren laten zien. Bijna alle schijven die spiralen tonen in waarnemingen van verstrooid licht op nabij-infrarode golflengten laten hiervoor ook indicaties zien in de CO data.

Hoofdstuk 5 presenteert een onderzoek met meerdere spectraallijnen van de schijf rondom de Herbig ster HD 100546, een bijzonder interessant systeem in termen van planeet-schijf interacties. Voor de analyse worden ALMA waarnemingen in Band 6, 7 en 10 met hoge spectrale resolutie en hoog ruimtelijk oplossend vermogen van meerdere lijnen van CO gebruikt. Om deze lijn-emissie te modelleren voor elke snelheidsdataset wordt gebruik gemaakt een kanaal-kaart fitting pakket. De analyse laat uitgerekte spiraalstructuren zien in de kinematische residuen van alle lijnen en hun morfologie wordt goed gereproduceerd door lineaire en logarit-

mische functies. Ze komen overeen met spiralen die worden aangedreven door een ingebedde planeet binnen 50 AE. Aanwijzingen voor een tweede compagnon die zich verder weg bevindt op een afstand van 90-150 au zijn te zien als meridionale stromen richting het middenvlak van de schijf en drukminima, alsmede in een mogelijk gat in de meer optisch dunne moleculen. Een asymmetrie in de emissiehoogtes van de blauw- en roodverschoven kant van de schijf kan een indicatie zijn van invallend materiaal aan de roodverschoven zijde of een kromgetrokken binnenschijf, die een schaduw over het buitenste deel van schijf werpt.

Toekomstperspectief

ALMA heeft onze kijk op planeetvormende schijven getransformeerd en een schat aan substructuren blootgelegd. We zijn echter nog maar net begonnen om de verschillende mechanismen die een rol spelen van elkaar te onderscheiden. De oorsprong van de substructuren blijft een belangrijke open vraag. Tegelijkertijd hebben we nu een tijd bereikt waarin zowel met ALMA als met JWST nieuwe en spannende nieuwe mogelijkheden ontstaan door de hoge gevoeligheid en resolutie van deze telescopen die alle eerdere waarnemingen overtreffen.

ALMA waarnemingen van moleculaire gasemissie hebben het voordeel dat we de gasstroom door de schijf heen in kaart kunnen brengen, en met voldoende gevoeligheid en resolutie opent dit een unieke nieuwe manier om planeten in de schijf te detecteren en fysische processen te onderzoeken. Het veld van schijfkinematica is pas recent ontstaan en zeer diepe lijnwaarnemingen zullen ons in staat stellen om ook planeten met een kleinere massa in kortere banen om hun ster te detecteren.

Een ultiem doel is om de eigenschappen van schijven en hun jonge planeten te koppelen aan de zeer diverse populatie van volwassen exoplaneten. Daarom zijn systematische en uitgebreide programmas voor een groot aantal schijven nodig, waaronder ook de kleinere schijven waarvan algemeen wordt aangenomen dat ze minder gestructureerd zijn, als complement voor de massieve en heldere schijven die doorgaans in detail worden bestudeerd. Dit is een essentiële stap om te begrijpen of er systematische verschillen zijn tussen deze groepen en of met name Herbig Ae/Be of T Tauri schijven verschillende patronen volgen. Tot nu toe hebben kinematische studies zich vooral gericht op de helderdere CO lijnen, maar om de mechanismen achter de waargenomen substructuren echt te ontrafelen is het van cruciaal belang om ze over de volledige radiële en verticale omvang van de schijf te bestuderen. Dit vereist waarnemingen van veel verschillende moleculen die op hun beurt ook de mogelijkheid bieden om de chemische kenmerken van vormende planeten te begrijpen.

Om de waarnemingen te begrijpen is ook fundamenteel onderzoek nodig vanuit een theoretisch perspectief. Toegewijde modellen zijn nodig om te begrijpen welke afdrukken planeet-schijf interacties of andere schijfvormende mechanismes zoals schijfwinden en gravitatie-instabiliteiten zullen achterlaten in de kinematica of temperatuurstructuren. Dit is cruciaal om te begrijpen welke rol de verschillende processen spelen in de planeetvormingspuzzel en zal ons helpen om te bepalen welke schijven het meest geschikt zijn om directe afbeeldingen van te maken met

JWST en de toekomstige Extremely Large Telescope (ELT). Samen met ALMA zullen deze baanbrekende faciliteiten ons in staat stellen om de verbinding te leggen tussen de van binnenste en buitenste schijfstructuren, wat hedendaags nog niet volledig worden begrepen, en de weg vrij te maken voor een uitgebreide karakterisering van de jongste exoplaneten.

The true sign of intelligence is
not knowledge but imagination.

Albert Einstein

English summary

Since the earliest history of mankind, people have gazed at the night sky studded with stars and wondered how they came to be. The question of the origin of the earth and its place in the universe has accompanied humans throughout all centuries and eventually triggered the development of telescopes reaching far beyond the human eye. These instruments are steadily improved, enabling scientists to study all corners of the cosmos in greater and greater detail, and bring us closer to answering the same questions raised long before.

One particularly interesting question is that of the origin of life. To date, we know only one place in the universe where life is possible: The Earth. About 30 years ago however, the discovery of the first planet orbiting another star than our Sun, an exoplanet, opened the door to a new era in Astronomy, making the possibility of life on other worlds a reality. Nowadays, more than 5000 exoplanets have been confirmed, a number that is growing each day and statistically speaking each star is on average orbited by one planet. While planets may be common inhabitants of the cosmos, they do exhibit a great deal of variety: planetary systems show a large scatter in terms of stellar and planetary mass and size as well as in system architectures such as the number, species, or distribution of planets.

In order to explain such diversity and ultimately to address the question of whether life is possible on other planets, we must first understand how planets are formed both from a physical and chemical point of view. To do so, we need to look at their birthplaces. These reside in the dusty and gaseous material surrounding a newborn star and are also called protoplanetary or planet-forming discs. They evolve and ultimately disperse over time, with the evolutionary processes shaping both the disc's appearance and the planet-formation mechanisms. At the same time, forming planets interact with their environment, while they grow from tiny grains to pebbles, planetesimals, and finally rocky planets and cores of gas giants, and they alter the structure of their host disc and influence its evolutionary path.

This dissertation focuses on the interpretation of disc substructures in terms of disc winds and planet–disc interactions. Modelling the dynamical processes in discs and characterizing the observed substructures represent key pieces in assembling the planet-formation puzzle and this thesis contributes to the understanding of how common substructures are and if they follow certain patterns.

Figure 1: Image of the pillars of creation, a star-forming region in the Eagle Nebula, taken with the James Webb Space Telescope. Credits: NASA, ESA, CSA, and STScI.

Young stellar systems

Stars are formed in slowly rotating giant molecular clouds, massive accumulations of interstellar material, predominantly containing molecular gas and some tiny dust particles. An example of such a star-forming region is shown in Fig. 1. Under certain conditions, the densest and coldest regions (cloud cores) can collapse under their own gravity and as density and temperature rise, young (proto-) stars are formed in the centre. At the same time, angular momentum needs to be conserved and the highest angular momentum material (which would break up the newly formed star) distributes into a circumstellar accretion disc from which the star is feeding during the first few million years of its lifetime.

The evolution of young stellar objects is illustrated in Fig. 2. After the collapse of a molecular cloud core and the formation of a prestellar core, the latter further collapses into a protostar surrounded by an infalling envelope. Already at this point, a disc is formed around the protostar, but remains deeply embedded (Stage 0 and I). Throughout these stages, accretion and outflows result in the envelope dissipating within 100 000 to a million years and left is a star surrounded by a gas-rich protoplanetary disc, which can directly be observed (Stage II). During another million to ten million years, disc material is either dispersed or assembled into planets and smaller bodies and the star is left with a gas-poor debris disc (Stage III). Eventually, the disc fully vanishes and a new planetary system such as our Solar System is born. The focus of this thesis are Stage II systems and their gas substructures, which can be observed directly with the Atacama Large Millimeter/submillimeter Array (ALMA).

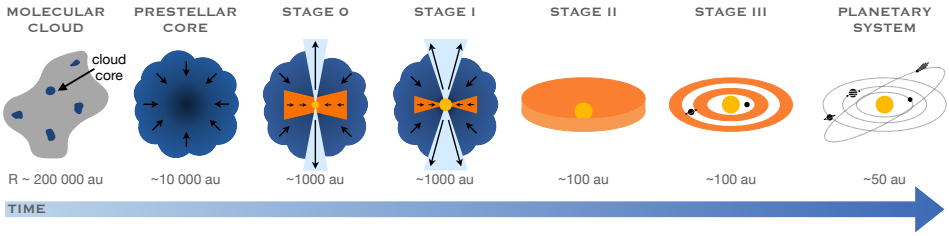

Figure 2: Schematic overview of the different stages of star formation. The focus of this thesis are Stage II objects, also known as protoplanetary discs. One astronomical unit, written here as au, represents the average distance between the Earth and the Sun.

Disc evolution

In order for a circumstellar disc to evolve, angular momentum needs to be either lost or redistributed. Otherwise, the disc material would continue to orbit the star at the same radius for all eternity. Two main mechanisms, which are not mutually exclusive, have been proposed to decrease angular momentum and govern disc evolution: disc winds and viscosity. In a viscously evolving disc, angular momentum is redistributed as a shear between gas particles causes one particle to move inwards by losing angular momentum to the other particle, which moves outwards. The exact source of viscosity remains a topic of active research, but turbulence is commonly invoked to account for viscous evolution. Disc winds on the other hand provide a way to remove angular momentum from the disc without the need for it to be turbulent. In the presence of a magnetic field, magnetically-driven winds can be launched from the disc surface, carrying away angular momentum. Consequently, the remaining material needs to lose angular momentum and moves towards the star where it is accreted.

In the simple picture of viscous evolution, the dispersal of a protoplanetary disc is predicted as a long-lasting process, where the disc is steadily and homogeneously fading. There is no evidence for such slowly draining discs and thus an alternative mechanism is required to rapidly disperse the disc at later stages. One mechanism which is proposed to play a significant role in that regard is photoevaporation. Photoevaporation describes the irradiation of disc material with highly energetic stellar photons, which heat up the upper disc layers to energies larger than the gravitational binding energy, launching a photoevaporative wind. For most of the disc's lifetime, the evolution is governed by viscosity and the mass loss due to photoevaporation is negligible. Over time, however, the accretion onto the star and the surface density of the disc decrease and the photons can penetrate into deeper disc layers. Once the accretion rates drop below the wind mass-loss rates, photoevaporation starts to dominate disc evolution. Inwards-flowing parcels are blown away with the wind rather than being accreted, and an annular gap which detaches the inner and outer disc regions from each other is formed. Without the resupply of matter from the outer disc, the inner disc rapidly drains on the star

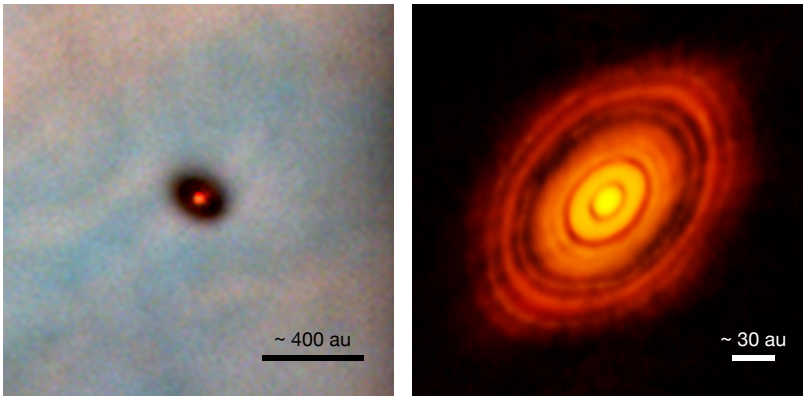

Figure 3: Left: Optical image of a protoplanetary disc in the Orion Nebula Cluster, taken with the Hubble Space Telescope. Credit: Mark McCaughrean (MPIA), C. Robert O'Dell (Rice University), and NASA/ESA. Right: ALMA image of the HL Tau disc at millimetre-wavelengths. Credit: ALMA (ESO/NAOJ/NRAO).

and the outer disc, now directly illuminated, experiences a fast inside-out clearing.

In the context of gaps and cavities in protoplanetary discs, the term 'transition disc' is to be noted. Transition discs are characterized by inner regions depleted in dust (and possibly gas) and were first identified observationally through a lack of infrared excess in the spectral energy distribution of young stellar objects. Being a natural outcome of photoevaporation, they were initially thought to be on the verge of dispersal, representing a transitioning phase between an optically thick and a debris disc. However, from an observational point of view, transition discs present to be a diverse group of objects and are marked by various substructures, which suggests different formation mechanisms. Especially those discs that exhibit large cavities and simultaneously vigorous accretion can hardly be explained by photoevaporation. Planet–disc interactions provide an alternative explanation and at least some of the observed cavities are expected to result from dynamical clearing rather than representing an evolutionary state. Transition discs provide us with great laboratories to study disc evolution and planet formation and may even enable us to catch planet formation in action. This dissertation, therefore, sets a special focus on this intriguing class of objects.

Disc observations

Until a decade ago, the circumstellar material could not be resolved in detail due to a lack of resolution of the former-generation telescopes. Observations showed flat and smooth structures which appeared to be symmetric around the central star, and it was not until the advancement of ALMA or the Spectro-Polarimetric High-contrast Exoplanet REsearch (SPHERE) on ESO's Very Large Telescope(VLT) that astonishing substructures were captured (see Fig. 3).

To study protoplanetary discs, the millimetre regime is particularly well suited,

as the cold molecular gas emits predominantly at these wavelengths and the dust distribution is dominated by millimetre-sized grains. The best facility to observe millimetre emission is ALMA because it provides the sensitivity, spectral resolution, and spatial resolution needed to map out individual discs in detail. At the same time, it has also allowed for large population studies. Altogether these observations have revealed that protoplanetary discs are marked by a large variety of substructures, including gaps or cavities, rings, spiral arms, and azimuthal asymmetries. This dissertation focuses on the gas content of discs, which yields the advantage of having information on the disc dynamics or kinematics: molecular line emission of rotating gas is red- and blueshifted, depending on whether the gas moves away from or towards us.

Disc kinematics

While the ultimate goal is to directly image embedded planets and thus confirm their link with the observed substructures, the dense and opaque environment surrounding young planets makes such a task very challenging. It is not surprising that to date, the only robust detections of embedded planets are those of the PDS 70 system. Therefore, more indirect detection techniques have been developed and a particularly promising one is to study the velocity field of the rotating gas, accessible with molecular line observations. Searching for deviations from Keplerian rotation can be used to understand which processes, all leaving their individual fingerprints in the kinematics, are shaping the disc. The kinematical features induced by planet–disc interactions are particularly exciting, with the amplitude and morphology of these perturbations depending on the location and mass of the planet, but also the disc structure. While several observations of kinematical deviations such as non-Keplerian spirals, meridional flows, or kink features have been linked to the presence of planets, it remains difficult to distinguish them from other underlying mechanisms. To better understand the individual contributions, dedicated modelling efforts are needed in combination with exceptionally sensitive observations at high spectral and spatial resolution. Such observations come at high observational costs and there are limited sources for which the kinematics have been thoroughly analysed. The field of kinematics is thus still in its infancy but brings the opportunity to find young, still forming planets, which escape the classical detection techniques. The properties of these planets yield important implications for planet-formation and -migration models and the timescales of these processes. Linking these properties to those of the mature exoplanet populations is crucial to solve the planet-formation puzzle.

This thesis

In this dissertation, the gas content of protoplanetary discs and their substructures are studied in the context of disc winds as well as planet–disc interactions. The variety of observed substructures, coupled with the lack of directly observed planets in discs, has triggered the following main questions which are tackled in this thesis:

1. Are the diverse substructures observed in discs the result of planet–disc interactions or other mechanisms?
2. If planets are the cause, what can we learn about these planets, for example in terms of location or mass, and if not planet-driven, what can we learn about the disc?
3. What modulates angular momentum transport in the disc as well as disc dispersal, influencing its lifetime and thus the time available to build planets?

The following paragraphs provide a brief summary of the individual chapters and their main results.

Chapter 2 investigates the effects of X-ray photoevaporation, acting in protoplanetary discs in which, as commonly observed, volatile carbon is depleted. Being one of the main contributors to the X-ray opacity, a gas-phase depletion of carbon is expected to enable larger X-ray penetration depths and here it is explored how this influences the strength of the photoevaporative mass loss and the formation of cavities. For this purpose, radiative transfer calculations and hydrodynamical models are combined, modelling discs irradiated by internal X-ray+EUV radiation and with different degrees of carbon depletion. The results show that photoevaporative winds are - with respect to solar metallicity discs - stronger in such carbon-depleted discs, resulting in enhanced mass-loss rates and mass-loss profiles that extend to larger radii. These results may explain a larger number of the observed transition discs. Additionally, very high carbon depletion may represent a mechanism of very fast disc dispersal towards the end of the lifetime of a disc.

Chapter 3 presents high-resolution Band 6 ALMA observations of the circumstellar disc around CQ Tau. Three CO isotopologues ^{12}CO, ^{13}CO, and C^{18}O are analysed both in terms of their kinematics and brightness temperatures. A Keplerian disc model is fitted to the velocity field to search for deviations from Keplerian rotation and variations in the temperature structure. The analysis yields significant spiral features in the residuals of both the velocity and gas brightness temperature after the model is subtracted from the data. The velocity and temperature spirals are partly aligned, suggesting a common origin. Their morphology, number, and pitch angles support a dynamical formation scenario. Together with (co-locating) spirals observed in the near-infrared and an observed deep gas and dust cavity, the spirals point towards a massive body such as a planet or binary companion located inside of about 25 au.

In chapter 4, the analysis of the gas kinematics and brightness temperatures conducted in the previous chapter is expanded to a sample of 36 large cavity transition discs, pushing the available ALMA observations to their limits. For the analysis, archival CO data taken in different cycles in Band 6 and Band 7 are used. For the first time, the substructures found in the kinematics and brightness temperature residuals are compared with other indicators for the presence of planets for a large sample of sources. The results yield strong features such as arcs or spirals, possibly associated with the presence of planets or companions, in about

20 % of discs, while the majority of the sources do not present as clear signatures. Almost all discs that exhibit spirals in near-infrared scattered light show at least tentative features in the CO data.

Chapter 5 presents a multi-line study of the disc surrounding the Herbig star HD 100546, which represents a particularly interesting target in terms of planet–disc interactions. For the analysis, several CO lines observed at high spectral and spatial resolution with ALMA in Band 6, 7, and 10 are used. To model the line emission for each intensity cube, a channel-map fitting package is used. The analysis reveals extended spiral structures in the kinematical residuals of all lines and their overall morphology is well reproduced by linear and logarithmic functions. They are consistent with spirals driven by an embedded planet or stellar companion inside of 50 au. Indications of a second companion, located further out at around 90-150 au are seen in the form of meridional flows towards the midplane and pressure minima, as well as a tentative gap in the more optically thin tracers. An asymmetry in the emission heights of the blue- and redshifted sides may indicate infalling material on the redshifted side of the disc or an inner warped disc, casting a shadow over the outer disc.

Future outlook

ALMA has transformed our view of planet-forming discs, revealing a wealth of substructures. However, we have only just started to really disentangle the different mechanisms being at play and the origin of the substructures remains a burning open question. At the same time, we have now reached a stage where new and exciting opportunities are opening up both with ALMA and JWST, providing a sensitivity and resolution exceeding all previous observations.

ALMA observations of molecular gas emission bring the advantage of allowing one to map the gas flow throughout the disc, and with sufficient sensitivity and resolution, this opens up a unique new window to detect embedded planets and probe physical processes in the disc. The field of disc kinematics has just started to emerge, and very deep line observations will allow us to also detect smaller mass planets at shorter periods.

One ultimate goal is to link the properties of discs and their young planets to the mature and very diverse exoplanet populations. Therefore, systematic and comprehensive surveys of a large number of discs are needed, including also the smaller ones, generally thought to be less structured, in addition to the massive and bright discs that are typically studied in detail. This is an essential step to understand if there are systematic differences between these groups and if in particular Herbig Ae/Be or T Tauri discs follow different patterns. So far, kinematic studies have mostly focused on the brighter CO lines but to really disentangle the mechanisms behind the observed substructures, it is crucial to trace them throughout the full radial and vertical extent of the disc. This requires observations of a range of molecular tracers, which also brings the opportunity to understand the chemical signatures of planets.

To interpret the observations, fundamental work is also required on the theo-

retical side. Dedicated modelling efforts are needed to understand which imprints planet–disc interactions or other disc-shaping mechanisms, such as disc winds or gravitational instabilities, leave in the kinematics or temperature structure. This is crucial to understand which role the individual processes play in the planet-formation puzzle and will help us to assess which targets are best suited for direct imaging programs with JWST and the future Extremely Large Telescope (ELT). Together with ALMA, these ground-breaking facilities will enable us to access the connection of inner and outer disc structures, which is so far not fully understood. They will pave the way for a comprehensive characterization of the youngest exoplanets.

Ihr Lichter, die ich nicht auf Erden satt kann schauen
Ihr Fackeln, die ihr stets das weite Firmament
Mit euren Flammen ziert, und ohn Auffhören brennt
Ihr Blumen, die ihr schmückt des großen Himmels Auen

Andreas Gryphius, An die Sternen

Deutsche Zusammenfassung

Seit den frühesten Anfängen ihrer Geschichte hat die Menschheit in den mit Sternen übersäten Nachthimmel geblickt und sich gefragt, wie diese wohl entstanden sind. Fragen wie die nach dem Ursprung der Erde oder ihrem Platz im Universum haben die Menschen dabei durch alle Jahrhunderte hinweg begleitet und schließlich zu der Entwicklung von Teleskopen geführt, die weit über das menschliche Auge hinausreichen. Diese Instrumente werden stetig verbessert und ermöglichen es den Wissenschaftler*innen alle Winkel des Kosmos immer genauer zu erforschen. Dabei bringen sie uns der Beantwortung derselben Fragen näher, die wir uns schon vor langer Zeit gestellt haben.

Eine besonders interessante Frage ist die nach dem Ursprung des Lebens. Bis heute kennen wir nur einen einzigen Ort im Universum, an dem Leben mit Sicherheit möglich ist: die Erde. Vor etwa 30 Jahren leitete die Entdeckung des ersten Planeten, der einen anderen Stern als unsere Sonne umkreist – eines Exoplaneten – jedoch eine neue Ära in der Astronomie ein und ließ die Möglichkeit von Leben auf anderen Welten zur Realität werden. Inzwischen sind mehr als 5000 Exoplaneten bekannt, eine Zahl, die täglich wächst, und die Statistik sagt uns, dass im Durchschnitt jeder Stern von mindestens einem Planeten umkreist wird. Planeten mögen zwar häufige Bewohner des Kosmos sein, dabei stellen sie jedoch keinesfalls eine homogene Gruppe dar. Vielmehr weisen sie eine große Vielfalt auf, sowohl in Bezug auf ihre Masse und Größe und die ihrer Heimatsterne, als auch in Bezug auf die Anzahl, Art oder Verteilung der Planeten im jeweiligen Sternsystem.

Um eine solche Vielfalt zu erklären - und letztlich die Frage zu beantworten, ob Leben auf anderen Planeten möglich ist - müssen wir zunächst verstehen, wie sich Planeten bilden und welche physikalischen sowie chemischen Prozesse dabei eine Rolle spielen. Dazu ist es sinnvoll die Orte zu betrachten, an denen Planeten geboren werden. Sie befinden sich im staub- und gasförmigen Material, das neugeborenen Sterne umgibt und werden auch protoplanetare oder planetenbildenende Scheiben genannt. Diese Scheiben verändern sich im Laufe der Zeit, wobei die dort stattfindenden Mechanismen sowohl die Struktur der Scheibe als auch die Planetenbildung beeinflussen. Gleichzeitig interagieren auch die sich formenden Planeten mit ihrer Umgebung, während sie von winzigen Körnern zu Kieselsteinen, Planetesimalen und schließlich zu Gesteinsplaneten und Kernen von Gasriesen heranwachsen. Dabei verändern sie ebenfalls die Struktur der Scheibe und beein-

Abbildung 1: Aufnahme der sogenannten Säulen der Schöpfung, ein Sternentstehungsgebiet im Adler Nebel. Aufgenommen mit dem James Webb Space Telescope. Credits: NASA, ESA, CSA und STScI.

flussen wiederum deren Entwicklungsprozesse.

Die vorliegende Dissertation befasst sich mit der Interpretation von Strukturen in protoplanetaren Scheiben im Kontext von Scheibenwinden und Wechselwirkungen zwischen Planeten und Scheiben. Die Modellierung der dynamischen Prozesse und Charakterisierung der beobachteten Strukturen in protoplanetaren Scheiben stellt dabei ein wichtiges Puzzleteil der Planetenentstehung dar. Diese Arbeit trägt dazu bei zu verstehen, mit welcher Häufigkeit Substrukturen auftreten und ob sie dabei bestimmten Mustern folgen.

Junge Sternsysteme

Sterne entstehen in riesigen, langsam rotierenden Molekülwolken, welche große Ansammlungen von interstellarem Material darstellen, das überwiegend aus molekularem Gas und einigen kleinen Staubteilchen zusammengesetzt ist. Ein Beispiel für eine solche Sternentstehungsregion ist in Abb. 1 dargestellt. Unter bestimmten Bedingungen können die dichtesten und kältesten Regionen der Wolke (Wolkenkerne) unter ihrer eigenen Gravitation kollabieren. Die dabei ansteigende Dichte und Temperatur im Zentrum führen zu der Bildung eines jungen Protosterns. Außerdem verteilt sich aufgrund der Drehimpulserhaltung das Material mit dem größten Drehimpuls (welches den neu geformten Stern wieder zerreißen würde) in eine zirkumstellare Akkretionsscheibe, die den Stern in den ersten paar Millionen Jahren seiner Lebenszeit mit Nahrung versorgt.

Die Entwicklung junger stellarer Objekte ist in Abb. 2 dargestellt. Im An-

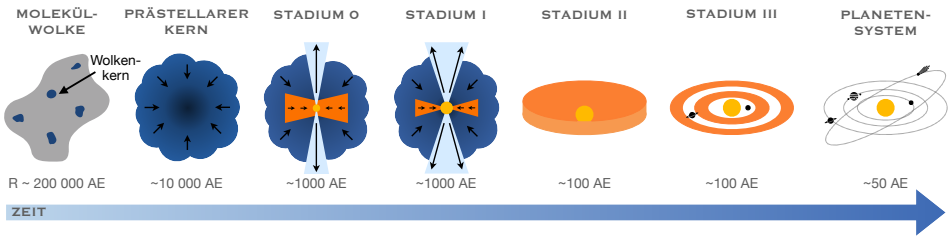

Abbildung 2: Schematische Übersicht der verschiedenen Stadien der Sternentstehung. Der Schwerpunkt dieser Arbeit liegt auf Objekten des Stadiums II, die auch als protoplanetare Scheiben bezeichnet werden. Eine astronomische Einheit, hier AE, entspricht der durchschnittlichen Entfernung zwischen Erde und Sonne.

schluss an den Kollaps eines Molekülwolkenkerns und die Bildung eines prästellaren Kerns kollabiert dieser weiter zu einem Protostern, welcher von einer nach innen fallenden Hülle umgeben ist. Bereits zu diesem Zeitpunkt bildet sich eine - jedoch tief eingebettete - Scheibe um den Protostern (Stadium 0 und I). Akkretion und Ausströmungen führen in diesen Stadien dazu, dass sich die Hülle innerhalb von 100.000 bis einer Millionen Jahren auflöst. Es bleibt ein Stern übrig, der von einer gasreichen protoplanetaren Scheibe umgeben ist, die nun direkt beobachtet werden kann (Stadium II). Im Laufe von weiteren eine Millionen bis zehn Millionen Jahren wird das meiste Material der Scheibe entweder zerstreut oder zu Planeten und Kleinkörpern zusammengesetzt, der Stern bleibt mit einer gasarmen Trümmerscheibe zurück (Stadium III). Schlussendlich löst sich die Scheibe vollständig auf und ein neues Planetensystem, wie unser Sonnensystem eines ist, ist geboren. Der Fokus dieser Arbeit liegt auf Systemen des Stadiums II und ihren Gasstrukturen, welche mit dem Atacama Large Millimeter/submillimeter Array (ALMA) direkt beobachtet werden können.

Entwicklung von Scheiben

Damit sich eine zirkumstellare Scheibe entwickelt, muss Drehimpuls entweder gänzlich aus dem System verloren gehen oder sich neu in der Scheibe verteilen. Andernfalls würden die Teilchen den Stern bis in alle Zeit auf dem gleichen Orbit umkreisen. In diesem Zusammenhang wurden zwei, sich nicht ausschließende Mechanismen vorgeschlagen, hauptsächlich verantwortlich zu sein für die Verringerung des Drehimpulses und die Steuerung der Scheibenentwicklung: Scheibenwinde und Viskosität. In einer sich viskos entwickelnden Scheibe wird der Drehimpuls dadurch umverteilt, dass Reibung zwischen den Gasteilchen dazu führt, dass sich ein Teilchen nach innen bewegt, Drehimpuls an das andere Teilchen abgibt, welches sich infolgedessen nach außen bewegt. Die genaue Ursache der Viskosität ist nach wie vor Gegenstand aktiver Forschung, jedoch werden häufig Turbulenzen angenommen, um eine viskose Entwicklung zu erklären. Auf der anderen Seite bieten Winde, die die Scheibe verlassen, eine Möglichkeit ihr Drehimpuls zu entziehen, ohne dass sie dabei turbulent sein muss. Unter dem Einfluss eines Magnetfeldes

können Winde von der Scheibenoberfläche ausgehen, welche Drehimpuls mit sich tragen. Als Konsequenz muss das verbleibende Material Drehimpuls verlieren und bewegt sich folglich in Richtung des Sternes, wo es schließlich akkretiert werden kann.

Das einfache Konzept der viskosen Entwicklung sagt das Auflösen der Scheibe als lang anhaltenden Prozess voraus, bei dem die Scheibe kontinuierlich und homogen verblasst und schließlich verschwindet. Da jedoch keine Nachweise für solche sich langsam zerstreuenden Scheiben existieren, ist ein alternativer Mechanismus erforderlich, der in späteren Stadien zu einem schnellen Auflösen führt. In dieser Hinsicht könnte die sogenannte Photoevaporation - die Verdampfung durch Licht - eine wichtige Rolle spielen. Photoevaporation beschreibt einen Prozess, bei dem hochenergetische, stellare Photonen die oberen Schichten der Scheibe auf Energien aufheizen, welche die gravitative Bindungsenergie überschreiten und einen photoevaporativen Wind auslösen. Für einen Großteil ihrer Lebensdauer wird die Entwicklung der Scheibe durch Viskosität bestimmt, der Massenverlust durch Photoevaporation bleibt vernachlässigbar. Wenn allerdings mit der Zeit die Akkretion auf den Stern und die Oberflächendichte der Scheibe abnehmen, können die Photonen in immer tiefere Schichten der Scheibe eindringen. Sobald die Akkretionsrate unter die Rate des durch den Wind verursachten Massenverlustes sinkt, beginnt die Photoevaporation die Scheibenentwicklung zu dominieren. Nach innen strömende Teilchen werden nun mit dem Wind davongetragen anstatt akkretiert zu werden. Es bildet sich eine ringförmige Lücke, welche die inneren und äußeren Regionen voneinander trennt. Ohne Materienachschub aus der äußeren Scheibe wird die innere Scheibe in kurzer Zeit auf den Stern akkretiert und die äußere Scheibe, die nun direkt beleuchtet wird, erfährt eine schnelle, von innen nach außen gerichtete Auflösung.

Im Zusammenhang mit Lücken oder gar Löchern in protoplanetaren Scheiben ist der Begriff „Übergangsscheibe" von besonderer Bedeutung. Übergangsscheiben zeichnen sich durch innere staub- und möglicherweise gasfreie Regionen aus. Sie wurden erstmals durch Beobachtungen junger stellarer Objekte identifiziert, deren spektrale Energieverteilung keinen Infrarotüberschuss aufwies. Da Übergangsscheiben eine natürliche Folge der Photoevaporation darstellen, wurde zunächst angenommen, dass sie kurz davor stehen sich aufzulösen und eine Übergangsphase zwischen einer gasreichen und einer Trümmerscheibe darstellen. Beobachtungen haben jedoch gezeigt, dass es sich bei den Übergangsscheiben um eine vielfältige Gruppe von Objekten handelt, die durch verschiedene Strukturen gekennzeichnet ist. Dies lässt auf unterschiedliche Entstehungsmechanismen schließen. Insbesondere jene Scheiben, die große Löcher und gleichzeitig eine starke stellare Akkretion aufweisen lassen sich kaum allein durch Photoevaporation erklären. Hier bieten Wechselwirkungen zwischen Planeten und der Scheibe eine alternative Erklärung. Es ist zu erwarten, dass zumindest einige der beobachteten Löcher eher das Ergebnis solcher dynamischen Prozesse sind, als dass sie einen evolutionären Zustand darstellen. Übergangsscheiben bieten uns großartige Laboratorien um die Scheibenentwicklung und Planetenentstehung zu untersuchen und letztere womöglich sogar in Aktion zu beobachten. In dieser Dissertation wird daher ein besonderer Schwerpunkt auf diese faszinierende Klasse von Objekten gelegt.

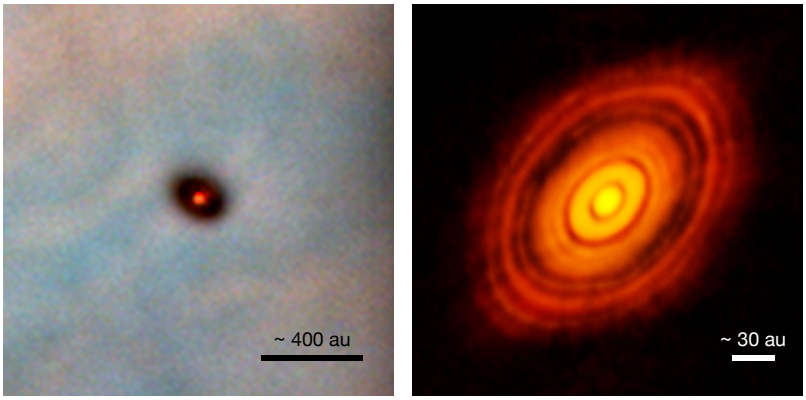

Abbildung 3: Links: Optische Aufnahme einer protoplanetaren Scheibe im Orion Nebel, beobachtet mit dem Hubble Space Telescope. Credit: Mark McCaughrean (MPIA), C. Robert O'Dell (Rice University) und NASA/ESA. Rechts: ALMA Aufnahme der HL Tau Scheibe im Millimeter-Wellenlängenbereich. Credit: ALMA (ESO/NAOJ/NRAO).

Beobachtungen von Scheiben

Bis noch vor einem Jahrzehnt konnte das zirkumstellare Material aufgrund der mangelnden Auflösung der früheren Teleskope nicht im Detail aufgenommen werden. Beobachtungen zeigten flache und homogene Strukturen, die symmetrisch um den Zentralstern angeordnet zu sein schienen. Erst mit der Entwicklung von ALMA oder dem Spectro-Polarimetric High-contrast Exoplanet REsearch (SPHERE) am Very Large Telescope (VLT) der ESO konnten erstaunliche Substrukturen eingefangen werden (vgl. Abb. 3).

Der Millimeter-Wellenlängenbereich eignet sich besonders gut für die Untersuchung protoplanetarer Scheiben, da das kalte molekulare Gas vorwiegend bei diesen Wellenlängen emittiert und die Staubverteilung von millimetergroßen Teilchen dominiert wird. Das beste Instrument für die Beobachtung von Emissionen im Millimeterbereich stellt dabei das ALMA Teleskop dar, welches sowohl die Sensitivität als auch die spektrale und räumliche Auflösung bietet, die für eine detaillierte Untersuchung einzelner Scheiben erforderlich ist. Gleichzeitig ermöglicht es außerdem die Durchführung großer Populationsstudien. Insgesamt haben die bisherigen Beobachtungen gezeigt, dass protoplanetare Scheiben durch eine enorme Vielfalt an Substrukturen gekennzeichnet sind, darunter Lücken oder Löcher, Ringe, Spiralarme und azimutale Asymmetrien. Der Schwerpunkt dieser Dissertation liegt auf dem Gasmaterial der Scheibe. Dies bietet den Vorteil, dass die Beobachtungen zusätzlich Informationen über die Dynamik - oder auch Kinematik - der Scheibe enthalten: Je nachdem, ob sich das rotierende Gas von uns weg oder auf uns zu bewegt, ist die Molekülinienemission rot- oder blauverschoben.

Die Kinematik von Scheiben

Um eine Verbindung zwischen den beobachteten Strukturen und sich bildenden Planeten nachzuweisen, ist es schlussendlich notwendig diese noch eingebetteten Planeten direkt zu beobachten. Aufgrund der dichten und undurchsichtigen Umgebung junger Planeten stellt sich eine solche Aufgabe jedoch als große Herausforderung dar. Es ist daher auch nicht verwunderlich, dass die Entdeckung solcher jungen Planeten im PDS 70 System die bisher einzige robuste Beobachtung darstellt. Aus diesem Grund wurden andere, indirekte Nachweismethoden entwickelt, von denen eine besonders vielversprechende die der Untersuchung der Geschwindigkeit des rotierenden Gases ist, die über Molekülinienbeobachtungen zugänglich gemacht werden kann. Dabei können Abweichungen von der Keplerschen Geschwindigkeit genutzt werden, um zu verstehen, welche Prozesse die Scheibe beeinflussen, da diese alle einen individuellen Fingerabdruck in der Kinematik hinterlassen. Besonders spannend sind kinematischen Signaturen, welche durch die Wechselwirkungen zwischen Planeten und der Scheibe hervorgerufen werden, wobei die Amplitude und die Morphologie dieser Störungen von der Position und der Masse des Planeten, aber auch von der Scheibenstruktur selbst abhängen. Obwohl bereits verschiedene Beobachtungen kinematischer Abweichungen, wie z.B. Spiralen, meridionale Strömungen oder sogenannte „Knickmerkmale", mit der Anwesenheit von Planeten in Verbindung gebracht wurden, stellt es sich nach wie vor als schwierig dar, diese von anderen zugrunde liegenden Mechanismen zu unterscheiden. Um die individuellen Beiträge dieser Prozesse besser zu verstehen, sind sowohl gezielte Modelle als auch äußerst empfindliche Beobachtungen erforderlich, die eine hohe spektrale und räumliche Auflösung aufweisen. Solche Beobachtungen sind mit einem großen Zeitaufwand verbunden und daher ist die Scheibenkinematik bisher nur für wenige Objekte detailliert analysiert worden. Das Forschungsfeld der Kinematik protoplanetarer Scheiben steckt somit noch in den Kinderschuhen, bietet jedoch die Möglichkeit junge, sich noch bildende Planeten zu entdecken, welche den klassischen Nachweismethoden entgehen. Die Eigenschaften dieser Planeten haben wichtige Auswirkungen auf die Modelle der Planetenentstehung und der Planetenmigration sowie auf die Zeitskalen, innerhalb welcher diese Prozesse stattfinden können. Ihre Charakterisierung trägt dazu bei, junge Planeten in Verbindung zu den vielfältigen, voll geformten Exoplanetenpopulationen zu setzen.

Diese Dissertation

In der vorliegenden Arbeit wird das gasförmige Material protoplanetarer Scheiben und dessen Struktur im Zusammenhang mit Scheibenwinden und Wechselwirkungen zwischen Planeten und Scheiben untersucht. Die Vielfalt der beobachteten Strukturen, zusammen mit dem Fehlen eines direkten Nachweises vom Planeten in den Scheiben, hat folgenden Fragen aufgeworfen, welche in dieser Dissertation behandelt werden.

1. Sind die vielfältigen beobachteten Strukturen in protoplanetaren Scheiben das Ergebnis von Planet-Scheibe-Wechselwirkungen oder anderen Mechanismen?

2. Falls sie durch Planeten verursacht werden, was können wir dann über diese lernen, z.B. über ihre Masse oder ihren Orbit. Und falls sie nicht durch Planeten entstanden sind, was können wir dann über die Scheibe lernen?

3. Wodurch wird der Transport des Drehimpulses in der Scheibe sowie ihre Auflösung bestimmt, was sich wiederum auf ihre Lebensdauer und damit auf die mögliche Zeitspanne für die Bildung von Planeten auswirkt?

In den folgenden Abschnitten wird eine kurze Zusammenfassung der individuellen Kapitel und ihrer wichtigsten Ergebnisse gegeben.

Im zweiten Kapitel werden die Auswirkungen von Photoevaporation durch Röntgenstrahlen auf protoplanetare Scheiben untersucht, in denen die Menge an gasförmigem Kohlenstoff reduziert ist, eine Eigenschaft, die regelmäßig beobachtet wurde. Da gasförmiger Kohlenstoff einen großen Teil der Opazität gegenüber Röntgenstrahlung ausmacht, ist zu erwarten, dass eine Verringerung zu einer größeren Eindringtiefe der Photonen führt. Es wird untersucht, wie dies die Stärke des photoevoparativen Massenverlustes sowie die Ausbildung von Löchern beeinflusst. Zu diesem Zweck werden Rechnungen des Strahlungstransfers mit hydrodynamischen Simulationen verknüpft, bei denen die Scheibe interner Röntgen- und UV-Strahlung ausgesetzt ist, wobei verschiedene Abstufungen von reduziertem Kohlenstoff angenommen werden. Die Ergebnisse zeigen, dass sich im Vergleich zu Scheiben solarer Metallizität stärkere photoevaporative Winde in Scheiben mit verringertem Kohlenstoffgehalt ausbilden. Dies führt zu einem gesteigerten Massenverlust und Massenverlustprofilen, die bis zu größeren Radien reichen. Diese Ergebnisse können möglicherweise einen größeren Teil der beobachteten Übergangsscheiben erklären. Darüber hinaus könnte ein sehr hoher Grad an Kohlenstoffverringerung ein Mechanismus für eine sehr schnelle Auflösung der Scheibe gegen Ende ihrer Lebensdauer darstellen.

Kapitel 3 präsentiert hochauflösende Beobachtung der zirkumstellaren Scheibe im CQ Tau System, aufgenommen im Band 6 mit dem ALMA Teleskop. Drei CO-Isotopologe ^{12}CO, ^{13}CO und C^{18}O werden sowohl im Hinblick auf ihre Kinematik als auch auf ihre Helligkeitstemperaturen analysiert. Die Rotationsgeschwindigkeit wird mithilfe eines Keplerschen Scheibenmodels modelliert und es wird nach Abweichungen von der Keplerschen Rotation sowie nach Variationen in der Temperaturstruktur gesucht. Nachdem das Model von den Daten subtrahiert wurde, ergeben sich signifikante spiralförmige Muster sowohl in der Geschwindigkeit als auch in der Helligkeitstemperatur des Gases. Die Geschwindigkeits- und Temperaturspiralen sind teilweise überlappend, was auf einen gemeinsamen Ursprung hindeutet. Die Morphologie, Anzahl und der Öffnungswinkel der Spiralen sprechen für ein dynamisches Entstehungsszenario. Zusammen mit den im nahen Infrarot beobachteten Spiralen und einem beobachteten, großen Gas- und Staubloch deuten sie auf einen massereichen Körper wie einen Planeten oder einen stellaren Begleiter hin, der sich innerhalb von etwa 25 AE befindet.

In Kapitel 4 wird die im vorigen Kapitel durchgeführte Analyse der Gaskinematik und der Helligkeitstemperaturen auf 36 Übergangsscheiben ausgedehnt, welche große innere Hohlräume aufweisen. Dabei werden die Möglichkeiten der verfügbaren ALMA-Beobachtungen an ihre Grenzen gebracht. Für die Analyse werden archivierte CO-Daten verwendet, die in verschiedenen ALMA-Zyklen im Band 6 und Band 7 aufgenommen wurden. Zum ersten Mal werden die in den Residuen der Kinematik und der Helligkeitstemperatur gefundenen Substrukturen mit anderen Indikatoren für das Vorhandensein von Planeten für eine große Anzahl an Objekten verglichen. Die Ergebnisse zeigen, dass signifikante Merkmale wie Bögen oder Spiralen, die möglicherweise mit der Anwesenheit von Planeten oder stellaren Begleitern in Zusammenhang stehen, in etwa 20 % der Scheiben vorhanden sind, während die Mehrheit der Objekte keine eindeutigen Strukturen aufweist. Fast alle Scheiben, die im nahen Infrarot Spiralen aufweisen, zeigen zumindest ansatzweise Merkmale in den CO-Daten.

Kapitel 5 präsentiert eine Studie mehrerer Emissionslinien, welche in der Scheibe um den Herbig-Stern HD 100546 beobachtet wurden. Mit Hinblick auf Planet-Scheibe-Wechselwirkungen handelt es sich dabei um ein besonders interessantes Beobachtungsobjekt. Es werden mehrere CO-Linien analysiert, welche mit einer hohen spektralen und räumlichen Auflösung mit dem ALMA Teleskop in den Bändern 6, 7 und 10 beobachtet wurden. Um die Linienemission für jeden Geschwindigkeitsdatensatz (genannt Channel) zu modellieren, wird eine sogenannte Channel-Map-Fitting Software verwendet. Die Analyse zeigt ausgedehnte spiralförmige Strukturen in den kinematischen Residuen aller Linien auf, deren globale Morphologie durch lineare und logarithmische Funktionen gut wiedergegeben werden kann. Diese Spiralen stimmen mit solchen überein, welche durch einen eingebetteten Planeten oder stellaren Begleiter erzeugt werden können, der sich innerhalb von etwa 50 AE befindet. Es finden sich außerdem Hinweise auf einen zweiten Begleiter, der sich weiter außen zwischen 90–150 AE befindet: Meridionale Strömungen in Richtung der Mittelebene der Scheibe und Druckminima sowie eine mögliche Lücke in den optisch dünneren Molekülinien sind in dieser Region zu erkennen. Weiterhin findet sich eine Asymmetrie in den Emissionshöhen der blau- und rotverschobenen Seiten. Dies könnte auf einfallendes Material auf der rotverschobenen Seite der Scheibe oder auf eine verdrehte innere Scheibe, welche einen Schatten auf die äußere Scheibe wirft, hinweisen.

Ausblick

Aufgrund von ALMA wurde unsere Sicht auf planetenbildende Scheiben verändert und eine Fülle von Substrukturen enthüllt. Dabei haben Wissenschaftler*innen gerade erst damit begonnen, die verschiedenen Mechanismen, welche die Scheibe beeinflussen, zu entschlüsseln: Der Ursprung der Substrukturen stellt nach wie vor eine der wichtigsten offenen Frage dar. Gleichzeitig eröffnen sich nun neue und aufregende Möglichkeiten für Beobachtungen mit ALMA und JWST, welche eine Empfindlichkeit und Auflösung bieten, die alle bisherigen Beobachtungen übertrifft.

ALMA-Beobachtungen von Molekülgasemissionen bieten den Vorteil, dass der Gasfluss durch die Scheibe kartiert werden kann. Bei ausreichender Empfindlichkeit und Auflösung eröffnet dies eine einzigartige neue Möglichkeit Planeten in der Scheibe zu entdecken und physikalische Prozesse zu untersuchen. Das Gebiet der Scheibenkinematik ist dabei erst kürzlich entstanden. Tief reichende Linienbeobachtungen werden es uns in Zukunft ermöglichen, auch Planeten mit kleineren Massen, welche sich auf engeren Orbits um ihren Stern drehen, zu entdecken.

Schlussendliche ist es das Ziel, die Eigenschaften von Scheiben und ihren jungen Planeten in den Kontext derer der äußerst vielfältigen Populationen fertig geformter Exoplaneten zu setzen. Dazu sind systematische und umfassende Beobachtungen einer großen Anzahl von Scheiben erforderlich, welche in Ergänzung zu den massereichen und hellen Scheiben, die normalerweise im Detail untersucht werden, auch kleineren Scheiben enthalten, von denen man im Allgemeinen annimmt, dass sie weniger strukturiert sind. Dies stellt einen wesentlichen Schritt dar, um zu verstehen, ob es systematische Unterschiede zwischen diesen Gruppen gibt und ob insbesondere Herbig-Ae/Be- und T-Tauri-Scheiben verschiedenen Mustern folgen. Kinematische Studien haben sich bisher hauptsächlich auf die helleren CO-Linien konzentriert. Um jedoch die Mechanismen hinter den beobachteten Substrukturen wirklich zu entschlüsseln, ist es entscheidend, sie über die gesamte radiale und vertikale Ausdehnung der Scheibe zu untersuchen. Dies erfordert die Beobachtung vieler verschiedener Moleküle, was wiederum auch die Möglichkeit bietet, die chemischen Eigenschaften der sich bildenden Planeten zu verstehen.

Um die Beobachtungen zu interpretieren ist auch auf der theoretischen Seite grundlegende Forschung erforderlich: Gezielte Modellierungsansätze sind nötig, um zu verstehen, welche Spuren die Wechselwirkungen zwischen Planeten und Scheiben, aber auch andere Mechanismen wie Scheibenwinde oder gravitative Instabilitäten, in der Kinematik oder der Temperaturstruktur hinterlassen. Dies ist von entscheidender Bedeutung, um zu verstehen, welche Rolle die einzelnen Prozesse im sogenannten Puzzle der Planetenbildung spielen. Weiterhin kann so besser beurteilt werden, welche Objekte sich am besten für direkte Beobachtungen mit JWST und dem zukünftigen Extremely Large Telescope (ELT) eignen. Zusammen mit ALMA ermöglichen es diese bahnbrechenden Einrichtungen, die bisher nicht vollständig verstandene Verbindung der Strukturen in den inneren und äußeren Scheibenregionen zu erforschen. Sie ebnen den Weg für eine umfassende Charakterisierung der jüngsten Exoplaneten.

Publications

First-author publications

Refereed

Kinematics and brightness temperatures of transition discs. A survey of gas substructures as seen with ALMA
Wölfer, L., Facchini, S., van der Marel, N., van Dishoeck, E. F., Benisty, M., Bohn, A. J., Francis, L., Izquierdo, A. F., Teague, R., 2023, Astronomy & Astrophysics, 670, A154.

A highly non-Keplerian protoplanetary disc. Spiral structure in the gas disc of CQ Tau.
Wölfer, L., Facchini, S., Kurtovic, N. T., Teague, R., van Dishoeck, E. F., Benisty, M., Ercolano, B., Lodato, G., Miotello, A., Rosotti, G., Testi, L., Ubeira Gabellini, M. G., 2021, Astronomy & Astrophysics, 648, A19.

Radiation-hydrodynamical models of X-ray photoevaporation in carbon-depleted circumstellar discs
Wölfer, L., Picogna, G., Ercolano, B., van Dishoeck, E. F., 2019, Monthly Notices of the Royal Astronomical Society, 490, 5596.

Submitted

Spirals and meridional flows in the planet-forming disc around HD 100546. A multi-line study of its gas kinematics.
Wölfer, L., Izquierdo, A. F., Booth, A., Facchini, S., van Dishoeck, E. F., Paneque-Carreño, T., Dent, B., submitted to Astronomy & Astrophysics.

Co-author publications

Refereed

Probing inner and outer disk misalignments in transition disks. Constraints from VLTI/GRAVITY and ALMA observations.
Bohn, A. J., Benisty, M., Perraut, K., van der Marel, N., **Wölfer, L.**, van Dishoeck, E. F., Facchini, S., Manara, C. F., Teague, R., Francis, L., Berger, J. P., Garcia-Lopez, R., Ginski, C., Henning, T., Kenworthy, M., Kraus, S., Ménard, F., Mérand, A., Pérez, L. M., 2022, Astronomy & Astrophysics, 658, A183.

Submitted

The Disc Miner II: Revealing gas substructure and kinematic signatures of planet-disc interaction through line profile analysis.
Izquierdo, A. F., Testi, L., Facchini, S., Rosotti, G. P., van Dishoeck, E. F., **Wölfer, L.**, Paneque-Carreño, T., submitted to Astronomy & Astrophysics.

It is our choices, that show what we truly are, far more than our abilities.

Dumbledore, Harry Potter and the Chamber of Secrets

Curriculum Vitae

I was born on August 1st 1993 to Annette Schneider and Wilhelm Wölfer in Münster, a city located deep in the west of Germany and known for both its rainy weather and an immense amount of bicycles. While indeed 1.7 bikes come per person, Münster does not live up to its reputation of being particularly rainy[4] but in fact represents a rather average German city in that regard. Being born on a Sunday, I was told that I was a child of good fortune and I can say that I was at least lucky enough to grow up with two wonderful sisters: Helen, who is two years younger and Anne who is eight years younger than me. As the oldest sibling, I learned from a young age to take responsibility, but coupled with my already well-developed perfectionism and love for detail, I would sometimes drive both my sisters and parents crazy. However, these characteristics were very useful for my interest in creative activities (such as creative writing, drawing, and handcrafting) and triggered my desire to understand things in their entirety. I grew a particular passion for two topics, dinosaurs and the universe, and the latter eventually developed into my profession.

But first, I attended the Thomas-Morus-Schule, an elementary school close to my home, and later the Annette-von-Droste Hülshoff Gymnasium, a high school only a 20-minute bike ride away. While I already had a tendency towards natural sciences and mathematics at that time, I must admit that I was one of those weird students who liked most subjects, perhaps not entirely surprising with both of my parents being teachers. In my senior years it was therefore particularly difficult for me to drop some of my classes and when I had to choose what to focus on – linguistic, scientific or social science subjects – I decided to go with all of them at first. In the end, however, I decided to keep physics and chose math and chemistry as my majors, while I had to give up two of the foreign languages and art with a heavy heart. But of course there were also subjects I wasn't really keen on. In geography, my poor sense of orientation could be quite inconvenient and most of the time I didn't enjoy the gym classes (which unfortunately I was forced to keep until the end): I hated running, was too small for basketball, and fouled too much for football.

After school, I decided to stay in my home town, where my family and best friends were still living, to study physics with chemistry as a minor at the West-

[4] „Entweder regnet es in Münster, oder es läuten die Glocken" - Westfälisches Sprichwort

fälische Wilhelms-Universität. Even though I enjoyed my studies, I very quickly had to realize that the astrophysics component, which interested me most, was virtually non-existent. The only astronomy class offered included not much more than looking at pretty pictures of the universe, which were so large that it was nearly impossible to download the lecture notes, let alone print them. After finishing my Bachelor's project in nuclear physics under the supervision of Prof. Dr. Alfons Khoukaz it was therefore clear to me that I would leave for another university. In 2016, I moved to the southeast of Germany to Munich, where I started a Master of Astrophysics at the Ludwig-Maximillians Universität. Although it was hard at first to leave my friends and family behind and although everybody else in class had much more astrophysical knowledge from their Bachelor programs than me, this turned out to be one of the best decisions in my life, as I could finally study what I enjoyed most. However, an old problem of mine came back when I had to choose a Master's project because I didn't know how to decide which area interested me most. In the end, I decided on a theoretical project in planetary sciences with Prof. Dr. Barbara Ercolano. I very much enjoyed this year of research and I decided to pursue a scientific career by applying to PhD positions in astronomy.

During the PhD interviews, I got particularly excited about the projects of prof. dr. Ewine van Dishoeck and when students got offered positions from Leiden Observatory, I was very disappointed not to be among them. I wrote to Ewine to ask if there was still a chance for me, and I could not have been happier when she replied that my offer would actually come in the next few days through the Max Planck Institute for Extraterrestrial Physics rather than Leiden Observatory. Looking back, I recall that my project was supposed to be more on the theoretical side but as customary in Ewine's group, I also started to work on some observations. Not only did this research turn out to be more than the side project it was initially intended to be but also as very exciting and in the end a large part of my thesis is observational.

During my three years at MPE in Garching and my final year at Leiden Observatory, I had the privilege to meet many great people and to travel to interesting conferences. I am very grateful for the experiences I made during my PhD and although at times it could be very stressful, these experiences convinced me to continue in science. My next stop will now take me to Boston, where I will start a postdoctoral position with Dr. Richard Teague at the Massachusetts Institute of Technology.

Quand tu regarderas le ciel, la nuit,
puisque j'habiterai dans l'une d'elles,
puisque je rirai dans l'une d'elles,
alors ce sera pour toi
comme si riaient toutes les étoiles.
Tu auras, toi, des étoiles qui savent rire.

Antoine de Saint-Exupéry, Le Petit Prince

Acknowledgements

Now that this adventure called PhD is coming to an end, I would like to take the time to thank the people (apologies if I have forgotten anyone!), who did not only accompany me on this journey but also gave me a great deal of support in times when my feet wouldn't carry me any further. As it lies in the nature of adventures, my path led me via several detours and was marked by many ups and downs, but these are exactly the ingredients that make a story interesting.

First of all, I would like to express my gratitude to you Ewine, for making it possible for me to start my journey in the first place. Thank you for believing in me and for the huge amount of time and support you have granted me over the past years. I find both your scientific insights and your joy for science inspiring! I also would like to thank my co-supervisors: Barbara, who always had kind words for me and found the time to help me with various issues. I admire your positive attitude and thank you for sparking my interest in planetary sciences. And Stefano, for introducing me to the world of observations and taking the time to explain even the more basic things. I really appreciate all the help you have given me!

I was lucky enough to be part of a big research group, with very cool and unique characters both on the Garching and Leiden side. Paolo, Yao, Andrés, Teresa, Sierra, and Giulio, all of you have been great colleagues in Garching! I always enjoyed chatting with you about both science and life in general. Alex, I am glad that we had some overlap in Garching, it was cool to see your excitement in scientific discussions! Margot, thank you for the joint online lunches during the pandemic, for helping me with dutch bureaucracy, and for being there for me when I was struggling. You are a very sweet and considerate person! Alice, you have been the best office mate! Thank you for taking care of me and cheering me up, I could not have made it through the last year without you. I love your fun and down-to-earth personality. See you in Boston! Pooneh, thank you for finding the kindest words for me when I was doubting myself. Your cheerful and enthusiastic nature is contagious! Martijn, I really like your relaxed and humorous way of approaching things! Thanks for all your help with the formalities, including travel forms and thesis formats, and with the nederlandse samenvatting. Lucas and Ardjan, you have been great colleagues! Nienke, I got a lot of good advice from you. Pranjal, talking to you was always very interesting, especially during stressful times. Merel, Arthur, Sierk, Leon, Łukaz, Giovanni, Benoît, Jeroen, and

Michał, most of the time you were on the other side of the screen, but I always enjoyed our meetings and valued your input a lot! Yuan, Katie, Marissa, Milou, Nashanty, Danny, and Logan, it was really great meeting you!

I also would like to thank my friends outside the observatory. First, my best friends Hilke and Sandra: Hilke, you have been like family to me for almost 30 years. You are a warm and welcoming and overall just lovely person, and the only one who is allowed to call me "Lieschen". Ever since we were little, you took care of me and I know that I can always rely on you. Sandra, we could not be more different but you have always accepted me for who I am and defended me against all odds. You believed in me when I didn't and were never afraid to tell me the truth. Sophia, there is no one else I enjoy taking a walk with as much as with you. I love engaging in hour-long and very unique conversations with you and I appreciate that you showed so much interest in my work. Answering your question was sometimes challenging but helped me to understand my research better. Sebi, you have been a great friend (and dancing partner!) and I especially like looking back at our fun times during the Bachelor. Camilla, Lukas, and Geray, you are what made my move to Munich and my Master studies most enjoyable. And even though our PhDs brought us to different corners of the world, you stayed amazing and supporting friends. Katja, our regular gatherings kept me going during my PhD in Garching and I was thrilled to hear that you and Dominik would also move to Leiden. I think the four of us make a good team! You are not only an impressive scientist but also a genuine and caring person.

I also would like to thank my family, we are a bit of a chaotic bunch, but I would not be where I am today without them. Papa, you claim that it was you who sparked my interest in astronomy when you showed me the full moon as a baby. I appreciate that you tried to answer my many, sometimes weird and difficult questions, and maybe one day I will learn: "Il faut cultiver notre jardin". Mama, thank you for all your support and love, which I did not always appreciate as much as I should have. Helen, growing up with you, my days were often filled with adventures, magic, and fantasy. You are my fellow dinosaur lover, my fashion advisor and my fellow "Die Drei Fragezeichen"-listener. Thanks for staying calm during times I panicked. Anne, when you were very little you once told me that growing up you would like to be like me. But it was actually me who learned a great deal of things from you! You are a wonderful and most kind person and I am grateful that you were always there for me when I felt lonely. Oma, ich weiß dir ist nicht ganz klar, was genau ich eigentlich mache, aber deine Liebe und Unterstützung haben mich stets begleitet! Elias, I love that you share my interest in science, one day Wölfer & Wölfer will come!

And my biggest thanks goes to you David, for being my rock, making me laugh every day and convincing me that it was worth it. I have always admired your optimism and I never would have made it to the finish line without you. I appreciate you accompanying me to different places and I know that with you by my side nothing can really go wrong. Our adventure has just begun!

Don't adventures ever have an end? I suppose not. Someone else always has to carry on the story.

J.R.R. Tolkien, The Lord of the Rings